

THE OPTIMUM DESIGN OF A VACUUM-COMPATIBLE MANIPULATOR TO
CALIBRATE SPACE BASED ULTRAVIOLET IMAGERS

A Thesis

presented to

the Faculty of California Polytechnic State University,

San Luis Obispo

In Partial Fulfillment

of the Requirements for the Degree

Master of Science in Mechanical Engineering

by

Jason L. Grillo

January 2020

© 2020
Jason L. Grillo
ALL RIGHTS RESERVED

COMMITTEE MEMBERSHIP

TITLE: The Optimum Design of a Vacuum-
Compatible Manipulator to Calibrate
Space Based Ultraviolet Imagers

AUTHOR: Jason L. Grillo

DATE SUBMITTED: January 2020

COMMITTEE CHAIR: Eltahry Elghandour, Ph.D.
Associate Professor of Mechanical Engineering

COMMITTEE MEMBER: John Ridgely, Ph.D.
Professor of Mechanical Engineering

COMMITTEE MEMBER: Jim Widmann, Ph.D.
Professor and Chair of Mechanical Engineering

COMMITTEE MEMBER: Kodi Rider
UC Berkeley Space Sciences Laboratory
Senior Aerospace Engineer

ABSTRACT

The Optimum Design of a Vacuum-Compatible Manipulator to Calibrate Space Based Ultraviolet Imagers

Jason L. Grillo

Recent discoveries in geospace science have necessitated the design of compact UV imaging instruments to make space-based observations from multiple vantage points. The miniaturized ultraviolet imager (MUVI) instrument from the Space Sciences Laboratory (SSL) at UC Berkeley is under development to facilitate such discoveries on a wider scale. This thesis documents the design, integration, and characterization of a vacuum compatible manipulator to calibrate the MUVI instrument inside the UV thermal vacuum chamber at SSL. Precision linear and rotation stages were implemented with custom mounting plates to achieve four degrees of freedom. Optical components were installed to imitate the MUVI instrument for testing purposes. A customized PCB was fabricated to control the stages and receive position feedback data. A Graphical User Interface was programmed and utilized to position the manipulator during experimental validation. Field of View sweeps were conducted using visible light and a monochromatic CMOS sensor to track the coordinates of a laser's centroid. An analytical model of the optics assembly was developed and later refined from the experimental results. Using this model, the translation stages successfully compensated for optical misalignments. Analysis of the performance data showed the pointing resolution of the manipulator was less than 1 arcmin, which satisfied the calibration requirement for the MUVI imager.

Keywords: Ultraviolet, Imager, Space, Vacuum, Manipulator

ACKNOWLEDGMENTS

This work was supported by the NASA Science Mission Directorate, Heliophysics Division through contract 80NSSC19K0494.

Dr. Eltahry Elghandour, thank you for mentoring me and pushing me to reach new limits. Your commitment to your students is unparalleled.

Kodi Rider, thank you for your time and guidance throughout this project. Your expertise and assistance was invaluable.

Dr. John Ridgely and Dr. Jim Widmann, thank you both for being on my committee.

Dr. Steve Gibson, I appreciated the time you took to help me understand the imaging effects of the collimated light through the optics GSE assembly.

I would like to thank the Space Sciences Laboratory at UC Berkeley for enabling me to work at their facility.

Furthermore, I would like to recognize my two senior project partners, Brady Hill and Troy Hajjar, who worked with me to design and test the front optics assembly of the MUVI instrument.

To all of my family and friends, thank you for your continual support. Special thanks to my parents and siblings for their abundant encouragement and passion for my success.

TABLE OF CONTENTS

	Page
LIST OF TABLES	x
LIST OF FIGURES	xi
LIST OF NOMENCLATURE	xix
CHAPTER	
1 Introduction	1
1.1 Need	2
1.2 Background Research	3
1.3 Objective	5
1.4 Thesis Scope	5
2 System Overview	7
2.1 Integrated Vacuum-Compatible Robotic Manipulator	7
2.2 Concept of Operation	9
3 Concept Development	11
3.1 Optical Requirements	11
3.1.1 Pointing Resolution	12
3.1.2 Periscope Simulation	12
3.2 Manipulator Requirements	17
3.2.1 Vacuum Compatibility	18
3.2.2 Instrument Interface	19
3.2.3 Remote Operation	19
3.3 Modularity	20
4 Hardware Design	21

4.1	Mechanical System	21
4.1.1	Stage Selection	21
4.1.2	Mechanical Interfaces	26
4.1.3	Optics Assembly	30
4.1.4	Stage Clearance	33
4.1.5	Test Configurations	34
4.1.5.1	Visible - Atmospheric	35
4.1.5.2	Ultraviolet - Vacuum Chamber	36
4.2	Electrical System	37
4.2.1	Architecture	37
4.2.2	Component Selection	38
4.2.2.1	Microcontroller	38
4.2.2.2	Stepper Drivers	39
4.2.2.3	Motor Connectors	40
4.2.2.4	Differential Signal Receivers	40
4.2.3	Breadboard Test	42
4.2.4	Custom PCB	43
4.2.5	Enclosure and Power Management	44
5	Software Design	46
5.1	Microcontroller RTOS	46
5.1.1	Hub Task	48
5.1.2	Motor Task	49
5.1.3	Feedback Task	50
5.2	Graphical User Interface	51
6	Integration of the Manipulator	55

6.1	Mechanical Integration	55
6.2	Electrical Integration	59
6.3	Lessons Learned	61
7	Performance Evaluation Methodology	65
7.1	Strategy	65
7.1.1	Optical Alignment	65
7.1.2	Position Repeatability	67
7.2	Test Schedule	69
8	Analytical Results	70
8.1	Backlash Mitigation	70
8.2	Ramp Profile Algorithm	72
8.3	Translation Compensation	79
9	Experimental Results	85
9.1	Optical Alignment	86
9.1.1	Mechanical Registration	86
9.1.2	FARO Laser Tracker Measurements	87
9.1.3	Defining the Quaternions	92
9.2	Finding the Spot Centroid	98
9.3	Boresight Test	101
9.4	Field of View Sweep Test	105
10	Comparison of Results	109
10.1	Adjustment for Systematic Errors	109
10.1.1	Detector Plane Offset	109
10.1.2	Center of Rotation	112
10.2	Post-Adjustment Test Results	113

11 Conclusion	115
11.1 Future Work	116
BIBLIOGRAPHY	118
APPENDICES	
A Manipulator User’s Manual	121
B Mechanical Drawings	134
C Electrical Schematics	150
D Software	154
E Bill of Materials	172
F FARO Laser Tracker Report	175

LIST OF TABLES

Table		Page
3.1	CMOS imager observational requirements and performance.	11
4.1	Performance specifications of the vacuum-compatible stages.	25
4.2	Performance specifications of the non-vacuum stages.	26
8.1	Vectors defining the 3D location and orientation of the top and bottom mirrors with respect to the iris center.	80
9.1	Quaternions that defined the 3D location and orientation of the top and bottom mirrors with respect to the iris center.	98
9.2	Position data for the boresight locations from various tests.	104
9.3	Position data of the spot location during the 7° FOV sweep.	107
10.1	Errors between the theoretical and measured spot locations before the center of rotation adjustment was applied.	113

LIST OF FIGURES

Figure		Page
1.1	Conceptual diagram of the Miniaturized UV Imager that will be developed.	2
2.1	The four vacuum-compatible stages with the bare optical ground support test equipment installed.	8
2.2	The defined coordinate system including stage definitions.	8
3.1	CAD model of the MUVI instrument in two configurations [21]. The stowed configuration is shown with a concept of the optical taper, CMOS detector, and power and signal PCBs (left). The deployed configuration is shown with the 30° FOV in yellow and the nearest PCB hidden for clarity (right).	13
3.2	2D ray trace sketch that illustrates the geometry of the multilayer turn mirrors from the deployable cover design. Note: the detector plane for the optical GSE is located at the point of ray convergence because there are no lenses to focus incoming light. During instrument tests, the lenses will focus the UV light approximately 90 mm behind the iris plane.	14
3.3	Zemax ray trace diagram of the MUVI instrument with different field angles (0°, 7.5°, and 15°).	15
3.4	3D ray trace of the MUVI instrument with 9 field angles shown. . .	15
3.5	Illustration of the iris projection on the detector plane at Boresight (left) and when the instrument is pitched downwards by 7° (right). The compression of the projection is exaggerated for effect.	16
3.6	Translation compensation illustrated for the pitch axis using a 2D ray trace sketch. The pitch axis was used to define the compensation limits because its optical lever arm was larger than that of the yaw axis.	17
4.1	Schematic of a Goniometer stage sold by Thorlabs [25].	22

4.2	Schematic of the instrument and manipulator concept in the UV vacuum chamber oriented at boresight.	23
4.3	2D representation of the instrument and manipulator concept in the UV vacuum chamber oriented at -15° pitch.	23
4.4	Three actuator types used in precision positioning applications. A stepper motor is shown on the left [23], a servo motor is shown in the middle [22], and a linear direct drive motor is shown on the right [7].	24
4.5	Load characteristics of the Newmark RM-5 stage [19].	27
4.6	Load characteristics of the Newmark NLS4 stage [18].	27
4.7	Load analysis for the Newmark Stages.	28
4.8	Gusset interface composed of three adapters to connect the Z stage to the X stage.	29
4.9	Adapter plate to connect the θ stage to the Z stage.	29
4.10	Angled gusset interface to connect the ψ stage to the θ stage.	30
4.11	Optical GSE assembly with labeled components.	31
4.12	Bottom mirror mount that was designed to fit the KC2 kinematic mount.	32
4.13	Two C-mount retaining rings secure the iris inside the camera.	32
4.14	The Phoenix 200S camera mount that mated to the optics datum.	33
4.15	Clearance of the manipulator when pitched up by 30°	33
4.16	Clearance of the manipulator when yawed $+24^\circ$ (top) and -30° (bottom).	34
4.17	A movable cart was designed out of 8020 aluminum stock for visible-atmospheric test purposes.	35
4.18	Sufficient clearance is observed between the vacuum chamber walls and the manipulator when the linear stages are located at their end of travel.	36
4.19	CAD of the manipulator inside the UV vacuum chamber at SSL. The manipulator is placed such that the stages are located at their mid-range of travel when the manipulator is oriented at boresight.	37

4.20	Diagram of the electrical system architecture.	38
4.21	Diagram of the TMC2160 stepper driver features [27].	39
4.22	Diagram of the TMC5072 stepper driver features [26].	40
4.23	Pinout of the connectors for the NLS4 stage [18].	41
4.24	Pinout of the connectors for the RM-5 stage [19].	41
4.25	Breadboard test of the manipulator electronics.	42
4.26	Conceptual layout of the custom PCB designed for the MUVI ma- nipulator.	43
4.27	PCB designed for the MUVI manipulator.	44
4.28	Electrical enclosure that housed the PCB and 24V power supply.	45
5.1	Task diagram of the manipulator RTOS that is run on the Nucleo microcontroller.	47
5.2	State machine for the hub task.	49
5.3	State machine for the motor task.	50
5.4	State machine for the feedback task.	51
5.5	Conceptual diagram of the manipulator GUI.	53
5.6	The finalized GUI that was designed to operate the MUVI manipulator.	54
6.1	The linear stages were integrated with the Z gusset assembly.	56
6.2	The θ stage was connected to the Z stage by the NLS4 to RM-5 adapter plate.	56
6.3	The angle gusset assembly was attached to the θ stage before mount- ing the ψ stage.	57
6.4	The ψ stage was mounted to the manipulator.	57
6.5	The optics datum was placed onto the ψ stage and the CCD PoE injector was mounted to the side.	58
6.6	SMR targets were hotglued to the optics datum to secure them in place.	58

6.7	Image of the PCB with components soldered (left) and integrated with the microcontroller and stepper driver boards (right).	59
6.8	The motor power and feedback harnesses were strain relieved to the GSE cart.	60
6.9	Limit switches for the θ stage were connected to the stationary side. A bracket connected to the rotational platform that contacted the limit switch at the end of travel.	60
6.10	A burn mark was seen on the fried microcontroller after a limit switch wire accidentally contacted a motor power pin.	63
6.11	A noise spike was observed on the SPI chip select line during data transfer. Capacitors were added to the CSN lines after this anomaly was detected.	64
7.1	Illustration of the optical alignment strategy. Perpendicularity of the GSE with respect to the laser beam will be established first (top) and then the periscope will be tuned (bottom).	66
7.2	FARO laser tracker (left) and its corresponding SMR targets (right).	67
7.3	Rectangular 7° FOV sweep comprised of 9 cardinal points to characterize the manipulator's repeatability.	68
7.4	Circular 7° FOV sweep to fit all 9 cardinal points onto the field angle border. The unit circle, shown on the right, shows the necessary angle multiplication factors for a given point on the field angle.	68
8.1	Diagram of the zeroing approach and the stage moving to a position that is in the positive coordinate direction.	71
8.2	Diagram of the stage moving to a position that is in the negative coordinate direction.	72
8.3	Five acceleration and deceleration scenarios in the ramp profile algorithm [20].	73
8.4	Ramp profile test featuring the velocity response of the X stage moving from 0.0000 mm to 11.1153 mm.	75
8.5	Ramp profile test featuring the position response of the X stage moving from 0.0000 mm to 11.1153 mm.	75

8.6	Ramp profile test featuring the velocity response of the Z stage moving from 0.0000 mm to 12.3857 mm. Aliasing could be the source of the two distinct steady state velocities.	76
8.7	Ramp profile test featuring the position response of the Z stage moving from 0.0000 mm to 12.3857 mm.	76
8.8	Ramp profile test featuring the velocity response of the ψ stage moving from 0.0000° to 15.0000°.	77
8.9	Ramp profile test featuring the position response of the ψ stage moving from 0.0000° to 15.0000°.	77
8.10	Ramp profile test featuring the velocity response of the θ stage moving from 0.0000° to 15.0000°.	78
8.11	Ramp profile test featuring the position response of the θ stage moving from 0.0000° to 15.0000°.	78
8.12	Labels of the points used to define the mirror vectors with respect to the iris center.	79
8.13	Optical simulation of the manipulator rotated in pitch by 15°. A positive vertical compensation of 12.3056 mm was calculated. Black represents the initial position of the optics at boresight, Red represents the optics after rotation, and Blue represents the optics after rotation and translation.	82
8.14	Optical simulation of the manipulator rotated in pitch by -15°. A negative vertical compensation of 10.0942 mm was calculated. Black represents the initial position of the optics at boresight, Red represents the optics after rotation, and Blue represents the optics after rotation and translation.	83
8.15	Optical simulation of the manipulator rotated in yaw by 15°. A positive horizontal compensation of 11.1999 mm was calculated. Black represents the initial position of the optics at boresight, Red represents the optics after rotation, and Blue represents the optics after rotation and translation.	83
8.16	Optical simulation of the manipulator rotated in yaw by -15°. A negative vertical compensation of 12.3056 mm was calculated. Black represents the initial position of the optics at boresight, Red represents the optics after rotation, and Blue represents the optics after rotation and translation.	84

8.17	Matlab simulation of the optical GSE rotating about the iris 10.606° in both pitch and yaw. Black represents the initial position of the optics at boresight, Red represents the optics after rotation, and Blue represents the optics after rotation and translation.	84
9.1	Experimental test setup of the manipulator on the GSE cart.	85
9.2	The iris was shimmed in the back and held in place by a C-Mount retaining ring. The distance from the front of the CCD flange to the iris plane was measured to be 6.75 mm, which implies the FOV would theoretically be a little smaller than 30°	86
9.3	The CCD mount and bracket were aligned using a jig on the optical breadboard and precision gauge blocks.	87
9.4	CAD measurements for the Thorlabs tip/tilt stages that were set using gauge blocks.	88
9.5	The bottom mirror base mount was first squared to the CCD mount (left) and then the distance from the bottom mirror T-slot mount to the CCD mount was set (right).	89
9.6	Image of the FARO laser tracker (left) and a view of the optical GSE with the laser tracker in the background (right).	90
9.7	Image of the SMR target placed in a magnetic mount on the optics datum.	90
9.8	Illustration of the working coordinate frame that was defined by metrology. The yellow circles represent the SMR target positions that were used to define the frame.	91
9.9	Measurement of the reflected spot during the alignment process for the top mirror. The measurement was used to calculate the required tip/tilt adjustment of the mirror stage.	92
9.10	Diagram of the X CSYS and Z CSYS measurements taken to locate the iris center with respect to the origin. The Z CSYS component (top) was 42.47 mm and the X CSYS component (bottom) was 145.26 mm.	93
9.11	Diagram of the ψ CSYS measurements taken to locate the iris center with respect to the origin. The ψ CSYS component was 50.84 mm.	94
9.12	Diagram of the Z CSYS (top) and X CSYS (bottom) measurements taken to locate the 3 bottom mirror points with respect to the origin.	94

9.13	Diagram of the ψ CSYS measurements taken to locate the 3 bottom mirror points with respect to the origin.	95
9.14	Diagram of the Z CSYS and X CSYS measurements taken to locate the 3 top mirror points with respect to the origin.	95
9.15	Diagram of the simplified Z CSYS and X CSYS measurements of the top mirror points with respect to the origin.	96
9.16	Diagram of the ψ CSYS measurements taken to locate the 3 top mirror points with respect to the origin.	97
9.17	The bottom mirror plane was incorrectly defined by the Spacial Analyzer program. The bottom mirror plane was translated by 12.7 mm along its normal vector to properly establish the location of the bottom mirror in 3D space.	98
9.18	Point spread function (PSF) of the laser spot and encircled energy with indication of 68%, 95%, and 99% of the total energy contained in the PSF.	99
9.19	Sensitivity of the X centroid calculation with respect to 1σ , 2σ , 3σ , and 4σ of encircled energy.	100
9.20	Sensitivity of the Z centroid calculation with respect to 1σ , 2σ , 3σ , and 4σ of encircled energy.	100
9.21	Illustration of the algorithm using 95% encircled energy to calculate the centroid of the spot. Note: the Phoenix 200S camera resolution was $2.4\mu\text{m}/\text{pixel}$	101
9.22	Assortment of images of the boresight location for the various field angle tests (left) and the centroid location overlaid on the initial boresight image (right).	102
9.23	Deviation of the boresight spot location in the X axis.	103
9.24	Deviation of the boresight spot location in the Z axis.	103
9.25	Assortment of images for the 7° field angle sweep test.	106
9.26	X spot location during the first 7° FOV sweep.	108
9.27	Z spot location during the first 7° FOV sweep.	108
10.1	Illustration of the spot shift along the X axis for a positive field angle.	110

10.2	Illustration of the spot shift along the X axis for a negative field angle.	110
10.3	Deviations along the X spot location were used to characterize the detector plane offset.	111
10.4	Deviations along the Z axis were used to characterize the center of rotation.	112
10.5	X spot location before and after the adjustment for systematic errors.	114
10.6	Z spot location before and after the adjustment for systematic errors.	114

LIST OF NOMENCLATURE

Acronyms

2D Two Dimensional

2U Two Unit CubeSat (10 cm x 10 cm x 22.70 cm)

3D Three Dimensional

CAD Computer-Aided Design

CCD Charge-Coupled Device

CMOS Complementary MetalOxideSemiconductor

CSYS Coordinate System

DOF Degrees of Freedom

FOV Field of View

GSE Ground Support Equipment

GUI Graphical User Interface

MUVI Miniaturized Ultraviolet Imager

PCB Printed Circuit Board

RTOS Real Time Operating System

SMR Spherically Mounted Retroreflector

UV Ultraviolet

Symbols

ψ, Y Yaw Rotation

θ, P Pitch Rotation

X X Translation

Z Z Translation

Chapter 1

INTRODUCTION

The Space Sciences Laboratory (SSL) at UC Berkeley fosters research in space-related sciences and focuses on experiments and observations carried out in space. A few examples of their research projects include MAVEN (Mars Atmosphere and Volatile EvolutionN Mission [12]), THEMIS (Time History of Events and Macroscale Interactions during Substorms [1]), and, most recently, ICON (Ionospheric Connection Explorer [11]). ICON aims to better understand the mysterious outermost layer of Earth's atmosphere, by utilizing UV imaging technology to measure the density ratio of neutral nitrogen and oxygen constituents in the ionosphere [15]. Space-based UV imaging has propelled discoveries in geospace science, and there is a compelling scientific design for future NASA science missions to make space-based observations from multiple vantage points. Recent changes in the commercialized space industry, including the miniaturization of avionics, expansion of Cubesat form-factor payloads, and ride-sharing opportunities with multiple orbit insertions, have inspired SSL to develop a low-complexity and miniaturized UV imager (MUVI) that can be rapidly deployed into space to support the next generation of Heliophysics missions. Fundamentally, MUVI is being developed as a small, 2U prototype for geospace applications with a CMOS detector and high spatial resolution with photon counting capability.

MUVI is beginning its third year of instrument development in the form of Senior Capstone projects through the Mechanical Engineering department at California Polytechnic University in San Luis Obispo. The planned phases of student-contributed development are:

1. Design and qualify the front optical assembly (Completed, 2018 [8])
2. Design and implement a remotely deployable cover to protect the optics (Initiated, 2019 [21])
3. Integrate the CMOS-based detector system (Ongoing, 2020)

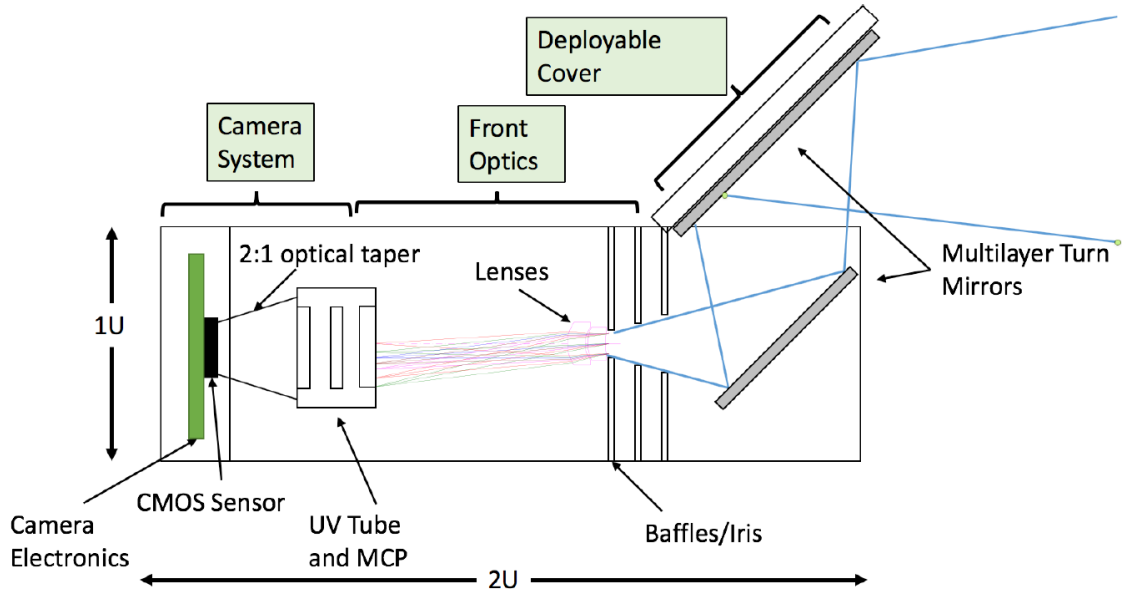


Figure 1.1: Conceptual diagram of the Miniaturized UV Imager that will be developed.

1.1 Need

As the instrument reaches the point of system-level integration and test, the optical calibration of the MUVI instrument requires specific ground support equipment (GSE). All the UV illumination operations have to be performed under vacuum, since UV light inherently reacts with atmospheric oxygen and scatters upon emission [16]. Optical calibration, which needs to be done close to its operational conditions, will take place inside the thermal UV vacuum chamber at SSL [17]. During these tests

the static, collimated UV beam will enter the aperture and illuminate the 30° FOV of the instrument.

One method of calibrating an instrument of this type is to steer the incoming beam into the instrument by manipulating the orientation of the light source. However, the light source is fixed in the UV chamber facility at SSL. Therefore, MUVI needs to be placed on tip and tilt rotation stages to rotate the instrument about its entrance pupil beyond the entire FOV. This calibration routine, known as stray light rejection, verifies that incoming light from stray sources do not interfere with the parent image. Furthermore, misalignment between the optical components may be quantified by measuring the centroid deviation of the UV source on the detector focal plane when the incoming light source enters the pupil at a given field angle inside the nominal FOV.

1.2 Background Research

Automated positioning stages are commonly found in complex imaging systems. They are implemented where manual positioning is impossible, such as inside a vacuum chamber or on spacecraft. Insight on previous vacuum-compatible manipulators was gathered to understand various approaches and results. *Characterization and calibration of the James Webb space telescope mirror actuators fine stage motion* discussed the methodology of characterizing hexapod actuation stages that were driven by cryo-rated stepper motors [6]. A deflectometer was used to measure the location of two low-power 635nm laser beams after reflecting onto two adjacent optical surfaces. The centroid position of the test beam and reference beam were tracked while each linear actuator was moved through its fine range in 30 increments of 130 fine steps. Out

of 108 actuators, data analysis found three discrepant actuators that lied outside the acceptable error limit.

Piezo-based motion stages for heavy duty operation in clean environments discussed a different actuation approach for use in high vacuum clean environments [14]. For applications sensitive to magnetic fields, ultrasonic motors may be used that were found to have 100 nm positioning resolution. The stages have high motion stiffness and no gear mechanism, high energy efficiency, no energy consumption when holding position, non-magnetic properties, unlimited travel and high vacuum compatibility. These stages were specifically designed for the semiconductor industry because of the material's sensitivity to oscillating magnetic fields.

X-Ray Test Facilities At Max-Planck- Institut Garching described various aspects of the instrument calibration chamber that housed vacuum-compatible manipulators [2]. The manipulator, driven by stepper motors, could be mounted directly to the interior of the chamber or on a marble optical bench. A high precision manipulator built for testing imaging X -ray telescopes of up to 1 m diameter allowed adjustment with an accuracy of a few arc seconds. Similarly, in *The Berkeley Extreme Ultraviolet Calibration Facility* the authors indicate the SSL UV vacuum chamber was equipped with a 4-axis manipulator with angular resolution of 1 arcsec and could accommodate payloads that weighed up to 500 kg. The drive system of the manipulator consisted of vacuum rated stepper motors on all axes. An interesting note in the paper recommended the use of dichronite (modified tungsten disulphide) as the lubricant on bearing surfaces because of its excellent high vacuum properties.

Both *Alignment and calibration of the ICON-FUV instrument: development of a vacuum UV facility* and *V-UV spectrographic imager (FUV) for Icon mission: from optical design to vacuum calibration* document the calibration of the FUV instrument developed by SSL for the ICON mission [16][15]. The manipulator, which was

designed and fabricated by Centre Spatial de Liege at the University of Liege in Belgium, was comprised of three linear actuators on which a rotation table was placed. The absolute accuracy and repeatability of the manipulator was measured to be 3 arcsec, which was fine enough to calibrate each field of the instrument. The clever design of this manipulator was that the instantaneous rotation center could be modified because of the tripod arrangement in combination with the rotation table. Therefore, the manipulator configuration was generic enough to be used for future instruments with different optical setups.

1.3 Objective

The objective of this thesis was to design, integrate, and characterize a vacuum-compatible robotic manipulator to calibrate the 2U MUVI instrument inside the UV vacuum chamber at SSL. The manipulator will be used to orient the instrument beyond its nominal 30° FOV to demonstrate successful rejection of out-of-field light, while simultaneously quantifying the relative alignment of the optical components. In addition to the manipulator, optical ground support equipment was needed to measure the performance of the manipulator and simulate the instrument's optical assembly using a visible light source. In a few years, the instrument will be ready for UV calibration and will directly interface with the manipulator, but until then a simulated optics assembly was required to characterize the manipulator prior to system level calibration.

1.4 Thesis Scope

This document details the development, integration, analytical and experimental methodologies, and characterization of the vacuum compatible manipulator for the

MUVI instrument. Chapter 2 presents an overview of the integrated manipulator and provides the reader context for the basis of its operation. The details of the requirements and performance factors are described in Chapter 3, which explains how the design form and evaluation metrics were established. Chapter 4 is the first detailed design section that presents the mechanical and electrical systems and their associated design decisions. Chapter 5 outlines the control software architecture for both the motor control board and GUI. Chapter 6 presents the integrated manipulator and explains the lessons learned during the assembly process. Next, Chapter 7 begins the testing and evaluation sections by describing the methodology to evaluate the performance of the manipulator. Chapter 8 contains the analytical results that includes a detailed simulation of the optical system. The experimental results are presented in Chapter 9, where images taken with the optical ground support equipment are analyzed to track the location of the laser spot. Chapter 10 compares the experimental and analytical results, which quantified the optical component alignment and removed systematic errors. Finally, Chapter 11 concludes the work and presents recommendations for next steps.

Chapter 2

SYSTEM OVERVIEW

This chapter presents an overview of the final manipulator design and build. The final manipulator consisted of two linear stages and two rotary stages for a total of four degrees of freedom. The vacuum-compatible stages and optical GSE components were purchased off the shelf. The manipulator's concept of operation is described in this chapter as well.

2.1 Integrated Vacuum-Compatible Robotic Manipulator

The finalized configuration of the manipulator is comprised of two translation stages with 100 mm of travel and two rotary stages with infinite travel. Both stages, manufactured by Newmark Systems, are designed to be vacuum-compatible down to 10^{-7} Torr [18][19]. Together, the stages provide 4 degrees of freedom and can orient the instrument $\pm 30^\circ$ in pitch and $\pm 24^\circ$ in yaw, which is nearly twice the FOV specification for MUVI. As shown in Figure 2.1, the optical test equipment is installed on top the ψ stage.

The most critical feature about this manipulator design is that the center-point of the entrance pupil is located at the intersection of the axes of rotation for the ψ and θ stages. Thus, collimated light effectively rotates about the aperture in the view of the detector. Reference Figure 2.2 for the stage definitions and labeled coordinate system.

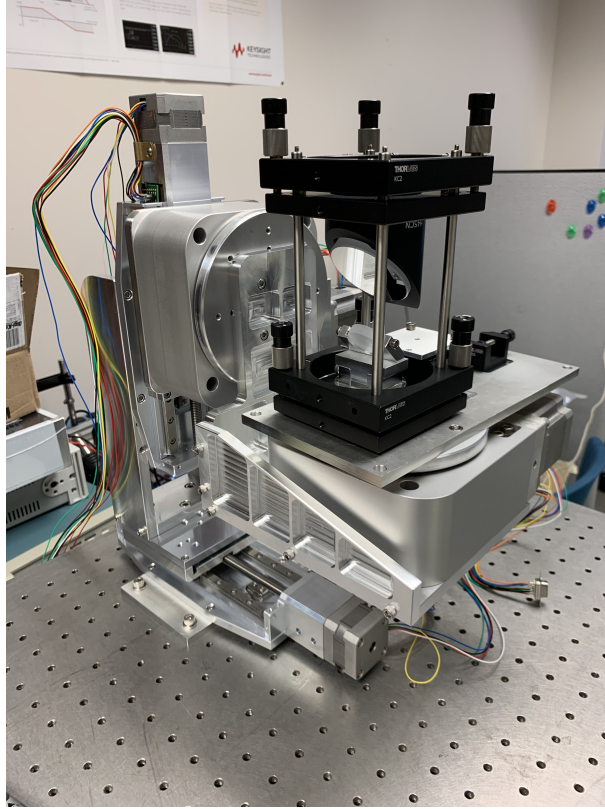


Figure 2.1: The four vacuum-compatible stages with the bare optical ground support test equipment installed.

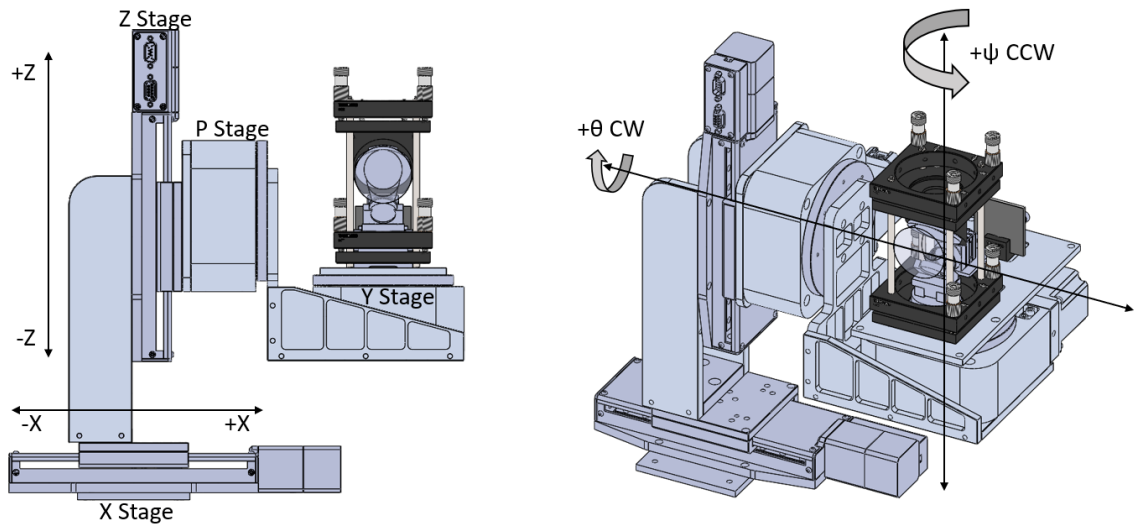


Figure 2.2: The defined coordinate system including stage definitions.

Translation compensation is required in this configuration because the mirrors are located at a lever arm with respect to the aperture, and they consequently translate in space as the instrument rotates about the iris. The X and Z stages accommodate translation effects from the ψ and θ stages, respectively. Although optical lever arms may be accounted for using a goniometer-style manipulator, these manipulators require unique interface plates specific to the exact optical lever arm and fail to accommodate variations in the opto-mechanical design. Thus, by placing the rotation point at the intersection of the ψ and θ axes, the optical lever arm may be accounted for purely in the translation stages, which is a software configuration instead of a hardware constraint.

2.2 Concept of Operation

In the MUVI calibration configuration, the manipulator is mounted inside the vacuum chamber and operated remotely. Commands to control the orientation of the manipulator are sent from a GUI that runs on a host computer and displays the status of the stages. The GUI is designed with three sections: the top section displays the encoder and limit switch feedback data, the middle section is the control hub for sending individual stage commands, and the bottom section contains test-specific commands with a pitch and yaw control panel that automatically calculates the required translation compensation for a composite field orientation. On a high level, the parameters for each of the stages are defined in a configuration file and uploaded to the GUI. This parameter definition method decouples the GUI from the hardware configuration, which may change for different manipulator applications. A more detailed description of the GUI may be found in Section 5.2.

The manipulator may be run in two different ways. The first method is to control each stage independently by using the GUI control panel. This method is most convenient when zeroing the stages to establish boresight, or when operating the manipulator in a stand-alone mode. The second control method is to use the test panel, where auto-sequences may be run. Although the auto-sequences themselves are not written, the framework is established for their use during extensive instrument calibration tests where repeated FOV sweeps may be run without continuous user feedback.

Chapter 3

CONCEPT DEVELOPMENT

This chapter introduces the design requirements and the resulting analysis that drove various design decisions. The optical parameters were established from the MUVI instrument-level science targets, which drove the required pointing resolution for the manipulator. A simulation of the light reflecting through the instrument's 2 mirror periscope system is shown to illustrate how the travel range requirements were defined. Vacuum-compatibility is defined in this chapter, along with the interface methodology for mounting the MUVI instrument onto the manipulator. Finally, the modularity requirements of the manipulator are described.

3.1 Optical Requirements

MUVI is primarily designed to stare at the earth in a Geosynchronous orbit to study the earth's ionosphere. The latitudinal science resolution requirement is 100 km per pixel, among other requirements listed in Table 3.1.

Table 3.1: CMOS imager observational requirements and performance.

Observing Requirement		Performance	
Parameter	Requirement	CCD Imager	CMOS Imager w/ Door
Resolution	100 km ² @ nadir	50 km ² samples = 100 km resolution	50 km ² samples = 90 km resolution
Wavelength	130.4 nm and/or 135.6 nm	123-154 nm	135.6 ± 2 nm
FOV	-	20°	20°
Aperture	-	0.7 cm ²	0.7 cm ²

3.1.1 Pointing Resolution

The heritage ICON FUV camera will be used to initially test the MUVI instrument. It has a 1024x1024 native readout, and on-chip binning to lower resolutions: a 256x256 mode results in pixels that are naturally about 50 km in size when projected out to the terrestrial target through a 20° FOV imager. As stated previously, the manipulator is conservatively designed to accommodate an instrument FOV of 30° or smaller. Assuming a 30° FOV, a readout of 1024 pixels, and 12 μm per pixel, the equivalent pixel size in angle space is 6.82 $\mu\text{m}/\text{arcmin}$. Furthermore, the tolerance of the placement of the lens from the imaging tube is important, as the crystal structure of the lens material has an index of refraction that changes depending upon the angle of incident light from the optical axis of the lens. The real risk in a future flight design is not the tolerance of the system to initial focus errors, but the defocusing of the system under vibration or thermal variations. Therefore, the optical calibration procedure must be able to verify the focus errors in the system are still within margin to meet the 50 km pixel size target.

To meet the science resolution requirement, the instrument must be aligned and oriented within 10 arcmin. Therefore, the target science requirement is 5 arcmin, which accounts for manufacturing alignment tolerances. For a 5 arcmin instrument pointing requirement, the manipulator must position itself within at least 1 arcmin to adequately measure and calibrate the instrument. Therefore, the pointing resolution target shall be less than 1 arcmin, and desirably 30 arcsec or better.

3.1.2 Periscope Simulation

The most recent state of the MUVI assembly, shown in Figure 3.1, is nearing the instrument integration phase. The front optics assembly was designed and tested in

2018 by the Cal Poly senior project team [8]. Integrating the deployable door cover and CMOS detector will commence once the deployable door design is assembled and preliminarily tested.

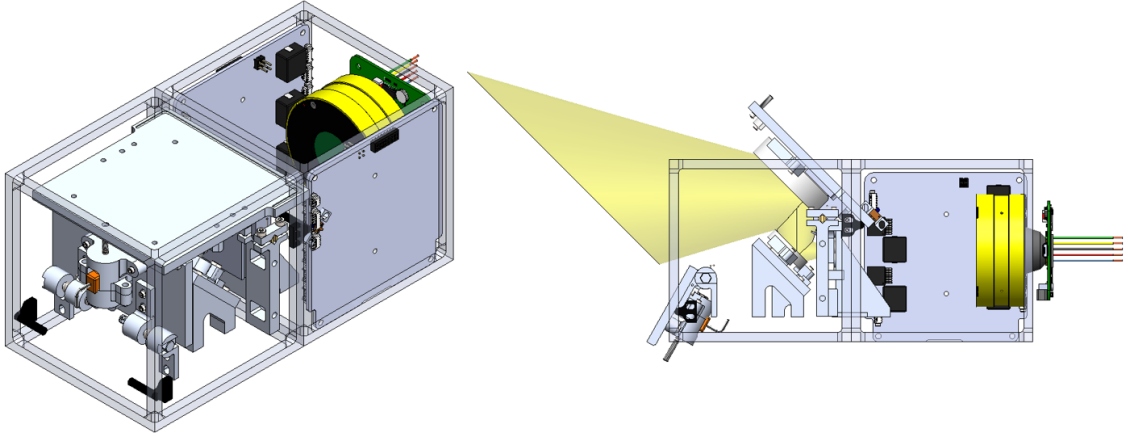


Figure 3.1: CAD model of the MUVI instrument in two configurations [21]. The stowed configuration is shown with a concept of the optical taper, CMOS detector, and power and signal PCBs (left). The deployed configuration is shown with the 30° FOV in yellow and the nearest PCB hidden for clarity (right).

The MUVI instrument is comprised of two multilayer turn mirrors that direct the FOV into the entrance pupil, which is mounted in front of two lenses. Although the positioning of these mirrors relative to the pupil is not crucial as they just steer the FOV, it is vital that the mirrors remain parallel relative to each other within 1 arcmin or better. Standard 1 and 2 inch mirrors were chosen for the bottom and top mirrors, respectively, because of their cost efficiency and availability. Ultimately, the diameters of the two mirrors were the driving factor for the location of the mirrors in the door cover subassembly, which is shown in Figure 3.2.

It is important to discuss the relevance of ray convergence in the 2D ray trace and how it pertains to the optical GSE tests. When lenses are present to focus the light onto the detector plane, each focused spot on the focal plane represents a given input angle filling the iris. As light is injected at further off angles, the rays refracted by

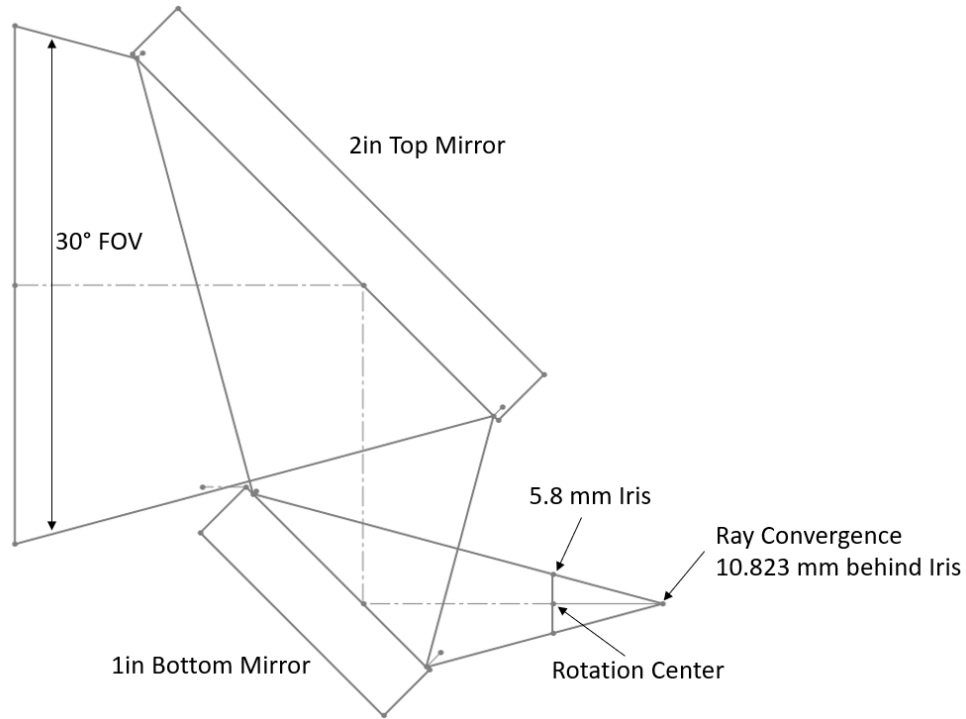


Figure 3.2: 2D ray trace sketch that illustrates the geometry of the multilayer turn mirrors from the deployable cover design. Note: the detector plane for the optical GSE is located at the point of ray convergence because there are no lenses to focus incoming light. During instrument tests, the lenses will focus the UV light approximately 90 mm behind the iris plane.

the lenses produce a translated spot of roughly the same size and shape as the on axis spot but translated spatially along the detector focal plane. This effect is shown in the ray trace diagrams in Figure 3.3 and Figure 3.4.

Since lenses are absent in the optical GSE to characterize the manipulator, only the projection of collimated light entering the pupil is captured by the detector. Consequently, as light enters the aperture at different field angles, the collimated light is projected through a slanted circle that compresses the image of the iris. An illustration of this phenomenon is shown in Figure 3.5, where the projection of the iris on the detector shrinks in height and translates downward.

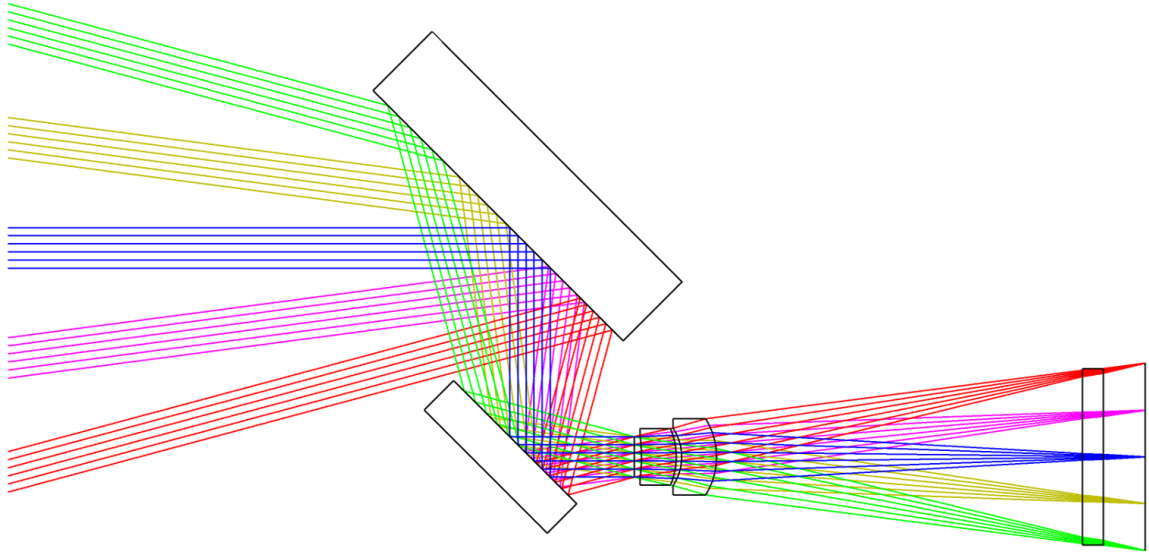


Figure 3.3: Zemax ray trace diagram of the MUVI instrument with different field angles (0° , 7.5° , and 15°).

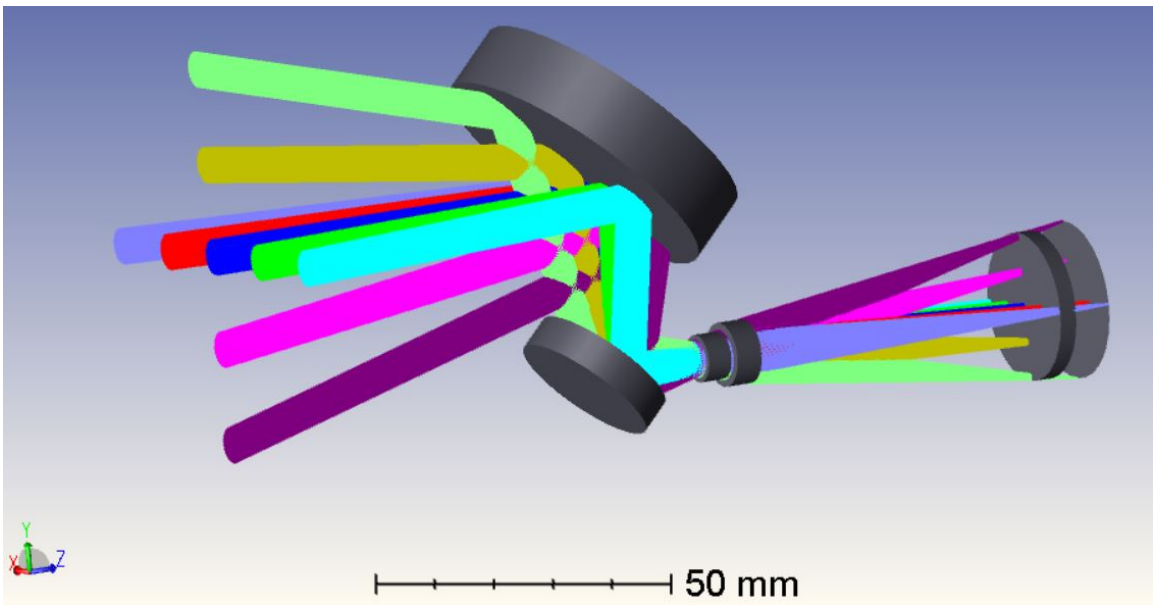


Figure 3.4: 3D ray trace of the MUVI instrument with 9 field angles shown.

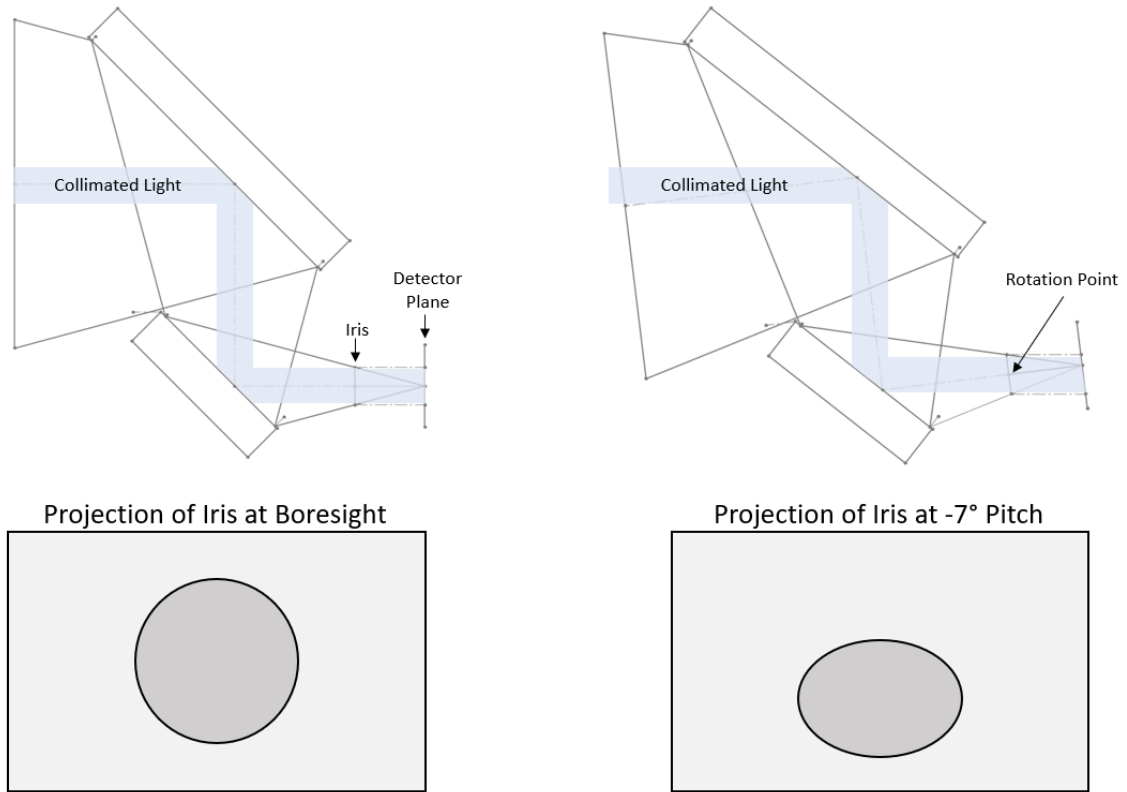


Figure 3.5: Illustration of the iris projection on the detector plane at Boresight (left) and when the instrument is pitched downwards by 7° (right). The compression of the projection is exaggerated for effect.

Instead of looking at the shape and location of the projected iris to characterize the manipulator, the optical GSE will take an image of a laser spot and track the location of its centroid. By positioning the detector plane on the point where the rays converge, the laser spot centroid would remain stationary at all times regardless of the angle of incidence of the incoming beam. Intrinsicly, any optical misalignment would be measured by a translation of the laser's centroid on the detector.

In addition to understanding the characterization methodology, the 2D FOV sketch shown previously in Figure 3.2 was used to find the required X and Z compensation for the manipulator. Translation compensation is required to inject the laser spot at the correct field angle with respect to pupil. Otherwise, the light beam would

be offset from the detector because the mirrors translate about the iris when the angular position of the instrument changes. The mirror translation is dictated by the distance the mirror is located from the point of rotation, which is referred to as the optical lever arm. Although the optical lever arm is truly defined upon assembly, a close approximation of the mirror translation may be obtained using this model. The estimate of the maximum required translation compensation is on the order of 13-15 mm, which was determined by pitching the 2D optical model $\pm 15^\circ$, as shown in Figure 3.6. The vertical translation compensation is not symmetric because the FOV is defined by rays diverging from the iris at 15° , respectively.

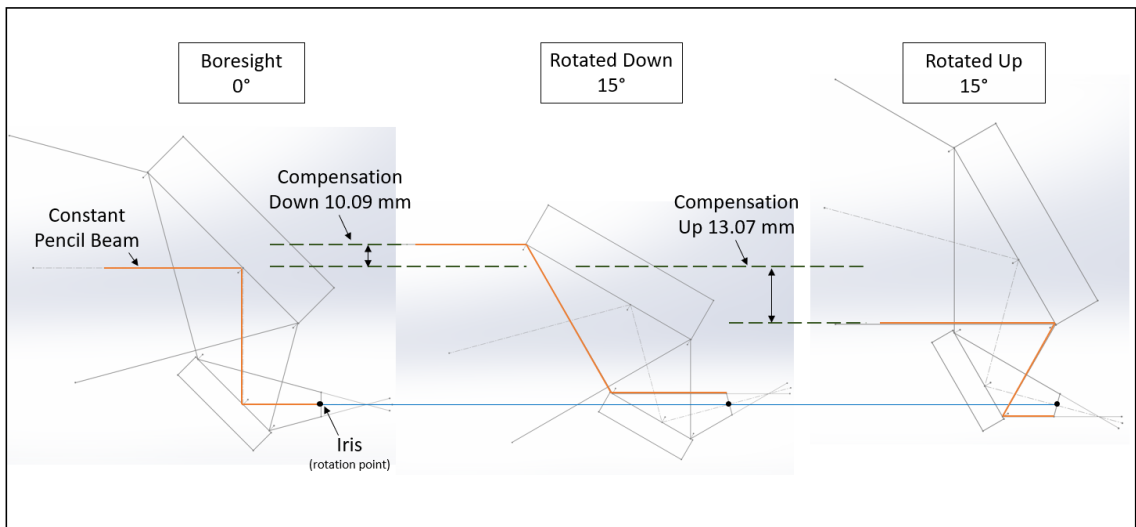


Figure 3.6: Translation compensation illustrated for the pitch axis using a 2D ray trace sketch. The pitch axis was used to define the compensation limits because its optical lever arm was larger than that of the yaw axis.

3.2 Manipulator Requirements

Other requirements for the manipulator include its ability to survive a vacuum environment and how it will interface with the instrument. The following sections describe these requirements.

3.2.1 Vacuum Compatibility

Outgassing, contamination, and cooling are all areas of concern when operating hardware in a vacuum environment. Thus, vacuum suitability extends beyond just material choice. Although material selection is important, especially for UV imaging applications, a few fundamental design principles must be followed. The first vacuum design principle is to avoid blind holes, or to use vented fasteners where they are unavoidable. Trapped volumes of air between a screw and the bottom of a blind hole drain very slowly under vacuum and lead to prolonged outgassing. This is observed as a virtual leak and must be avoided.

Contamination of the hardware is a result of outgassing materials. In a mechanical system under vacuum, lubricants in the bearings vaporize and the insulation materials of the motor and cable will also evaporate. These materials migrate to cold surfaces in the vacuum chamber and condense. Condensation of these materials on optical elements (mirrors, lenses, detectors) are a concern as that they adversely impact the efficiency (throughput) of the optical system. UV imaging surfaces are even more restrictive when it comes to contamination, since UV transmission is immensely reduced by volatile deposits [4]. Accordingly, the second design principle is that materials utilized in high vacuum for a UV application must have a Total Mass Loss (TML) of less than 1%, and a Collected Volatile Condensable Material (CVCM) under 0.1% [5].

Lastly, heat dissipation in a vacuum environment is restricted to conduction and radiation modes. Since convection is absent, motors nominally run hotter in a vacuum. Consequentially, it is imperative to monitor the temperature of the motors as heat is generated when current runs through the motor coils. If the motors exceed their designed operating temperature, the coil insulation material and other parts of the

motor may begin to outgas more contaminants, resulting in additional contamination and reduced throughput of the imager. Only vacuum-compatible motors are acceptable for this application.

3.2.2 Instrument Interface

The manipulator must accommodate a 2U-sized instrument with a maximum weight of 2.66 kg. Joining methods must securely attach the instrument onto the manipulator such that changes in the gravitational vector do not dislodge or shift the instrument. Evidently, this requirement drives the need to fasten the instrument against a hard-stop that is mounted on the manipulator. A kinematic mount is recommended for this interface to ensure accurate and repeatable positioning of the instrument onto the manipulator. Although the instrument interface design is not included within the scope of this thesis, it is imperative that the design ensures a rigid connection to the manipulator and proper knowledge of the rotation point about the instrument's iris.

3.2.3 Remote Operation

Another requirement for the manipulator is that it must be able to operate remotely without visual feedback required from the operator. Because the sealed vacuum chamber eliminates visual feedback from the user control loop, there must be built-in features to help the user calibrate and position the manipulator without visual aid. Furthermore, appropriate warnings or errors should be communicated to the user if the manipulator hardware is not correctly responding to user commands.

3.3 Modularity

Another requirement for the manipulator design is that it needs to account for various types of optical lever arms. As stated previously in 1.4, goniometer-style manipulators will be avoided for the reason that they are only designed for a fixed optical lever arm. The ability to use this manipulator in different instrument configurations is desirable, especially since the instrument optics may change slightly depending on future instrument development campaigns. The idea is that the final manipulator build may be recycled or adapted to future instruments with minor modifications.

Chapter 4

HARDWARE DESIGN

This chapter documents the design of the mechanical and electrical systems. The mechanical design process included selecting the actuators, interfacing the components, and design of an optical GSE test apparatus. The electrical design process consisted of device selection, routing and fabricating a custom PCB, and design of an enclosure system.

4.1 Mechanical System

4.1.1 Stage Selection

The manipulator's stage design was required to accommodate different optical lever arms to meet the modularity requirement defined in Section 3.3. It was stated without explanation that goniometer stages would be avoided because of this requirement. As seen in Figure 4.1, the point of rotation for a goniometer stage is fixed and relies on the mechanical interface between the base and platform to define its rotation radius. This is not an issue for one-off manipulator designs; however, the goniometer stages quickly become obsolete after slight changes in the optical assembly. For this reason, goniometer manipulators require specific mounting adapters that are unique to each instrument for which they are intended, which makes recycling the stages for different applications very difficult without significant mechanical redesign. Thus, the selected stage system needed to be generic enough to allow for variations in the point of rotation without modifying the mechanical adapters.

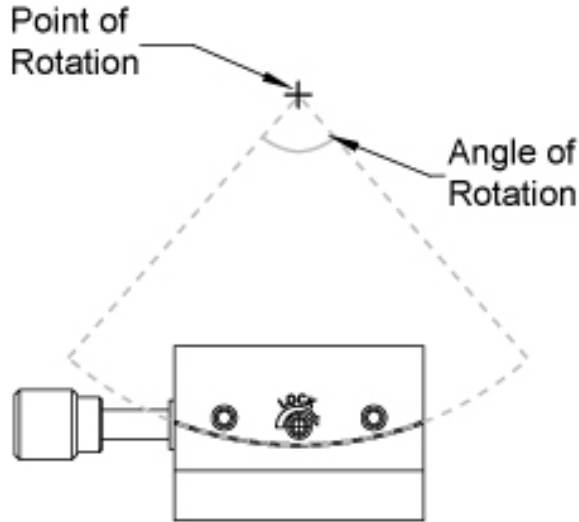


Figure 4.1: Schematic of a Goniometer stage sold by Thorlabs [25].

Rotation about a fixed point is comprised of a rotation and translation component, and both may be treated independently. Ultimately, this concept drove the stage selection process to use a combination of linear and rotation stages for a total of four degrees of freedom (DOF). Four DOF allows the manipulator to orient the instrument at various field angles using pitch and yaw components. Translation along the beam line was unnecessary, as well as rotation in the roll axis. Illustrations of the required manipulator movement are shown in Figures 4.2 and 4.3, where the instrument is oriented at boresight and -15° pitch inside the UV vacuum chamber, respectively. One may observe the subtle decoupling of rotation and translation components in these two figures.

There are a few different types of precision positioning actuators. The first, which is low-cost and widely implemented, is the stepper motor. Stepper motors have a series of toothed electromagnets. A bipolar stepper motor has two separate coil windings, typically distinguished A and B, which energize at various levels to orient the shaft at discrete angles. By alternating the sequence at which the phases energize, the motor shaft rotates. Stepper motors may be used in open loop positioning control because

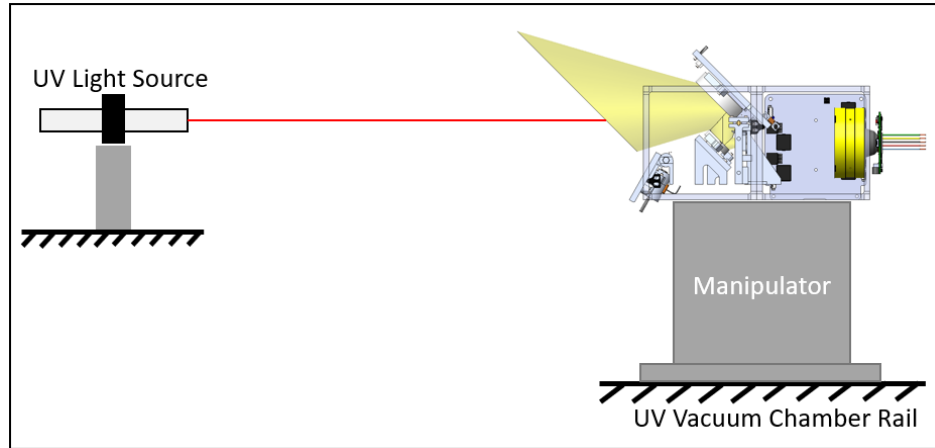


Figure 4.2: Schematic of the instrument and manipulator concept in the UV vacuum chamber oriented at boresight.

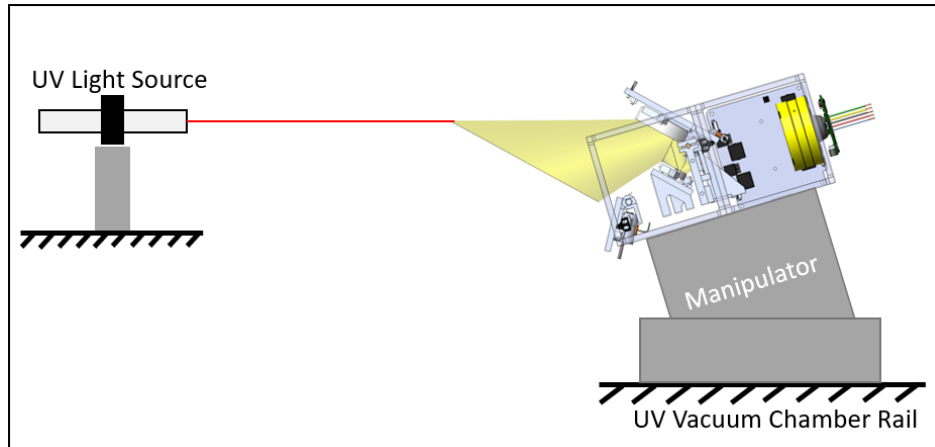


Figure 4.3: 2D representation of the instrument and manipulator concept in the UV vacuum chamber oriented at -15° pitch.

the shaft position is dependent on the step angle. One downside to implementing open loop control with stepper motors is the position may be lost if the difference between the mechanical load angle and electrical load angle exceeds 90° , resulting in lost steps. The servo motor is another commonly used actuator for positioning applications. The servo motor has less poles than a stepper motor, which results in more consistent torque at higher speeds. However, servo motors require closed-loop control that results in an increase of cost and complexity. Lastly, direct drive linear

motors may be used for precision applications. Iron core direct drives contain two outer layers of permanent magnets on the stator and three coils wound about the forcer. The forcer is driven by alternating the current through the windings. The three motor types that were considered for the vacuum-compatible manipulator are shown side by side in Figure 4.4.

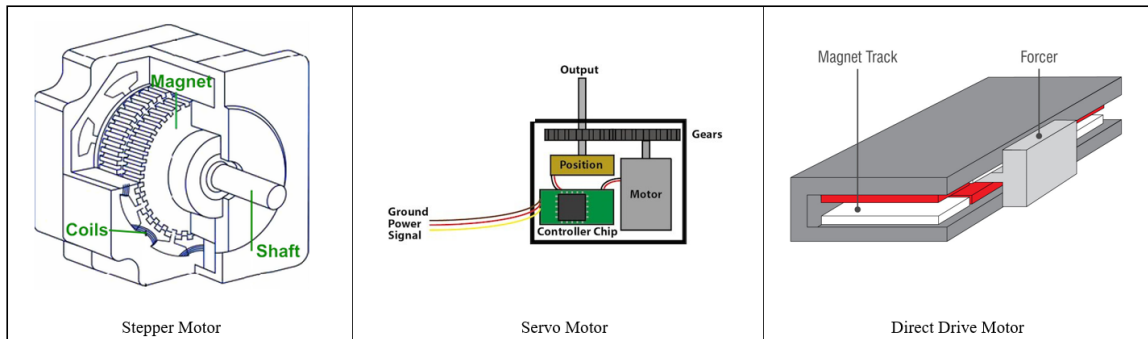


Figure 4.4: Three actuator types used in precision positioning applications. A stepper motor is shown on the left [23], a servo motor is shown in the middle [22], and a linear direct drive motor is shown on the right [7].

A few advantages and disadvantages of the three actuation methods are noteworthy to discuss. First, direct drive motors outperform traditional leadscrew driven positioning systems in acceleration, maximum travel speed, and accuracy. Furthermore, the resolution of direct drive stages is on the order of nanometers and the system is free of backlash. However, direct drive stages are expensive and they are difficult to find in vacuum-compatible versions off the shelf. Although stepper and servo motors are less expensive than direct drive motors, they both require leadscrew drive trains that induces backlash into the system. Despite this downside, backlash may be accounted for and is not a significant disadvantage. Servo motors are more expensive than stepper motors due to their inherent complexity. Stepper motors are more suitable in a vacuum environment because they contain fewer components that outgas compared to servo motors. Taking these considerations into account, it was decided

to select positioning stages driven by stepper motors because stepper motors were most effective in terms of vacuum-compatibility and cost.

Many online vendors sell vacuum-compatible stages driven by stepper motors, but only three reputable vendors were considered. Quotes from Newmark Systems and Standa were compared against each other and their stage specifications were compared with products from Velmex. The cost of vacuum-compatible stages from Newmark and Standa were similar. Separate quotes for non-vacuum hardware were used to approximate the additional cost for vacuum-compatible hardware, which came out to be 2.5 times more expensive. Because the cost of the stages was comparable across vendors, the stage specifications were then compared. Table 4.1 and Table 4.2 contain a list of basic performance specifications for the vacuum-compatible and non-vacuum configurations, respectively. As shown in these tables, the range of travel and resolution match well; however, the maximum load differs dramatically between vendors. After communication with Standa application engineers, it was decided that their products were insufficient to support the 2.66 kg instrument mass requirement in the desired configuration. Similarly, the Velmex stages would not be able to handle the application given the load constraints. Thus, the linear and rotary stages from Newmark Systems were selected for their superior load capacity.

Table 4.1: Performance specifications of the vacuum-compatible stages.

VENDOR	PART NUMBER	TYPE	TRAVEL RANGE	RESOLUTION	MAX LOAD
Newmark	NLS4-4-12V	Linear Stage	100 mm	0.03 μm	50 lb
Newmark	RM-5-111-V	Rotatary Stage	360°	4.5 arc-sec	100 lb
Standa	8MT175V-100-VSS42-VC9F-FT	Linear Stage	100 mm	0.01 μm	3 kg (6.6 lb)
Standa	8MVT120V-25-VSS43-VC9F-FT	Vertical Stage	25.4 mm	0.02 μm	10 kg (22 lb)
Standa	8MR190V-2-VSS42-VC9F-FT	Rotatary Stage	360°	36 arc-sec	2 kg (4.4 lb)

Table 4.2: Performance specifications of the non-vacuum stages.

VENDOR	PART NUMBER	TYPE	TRAVEL RANGE	RESOLUTION	MAX LOAD
Newmark	NLS4-4-12	Linear Stage	100 mm	0.04 μm	50 lb
Newmark	RM-5-111	Rotatory Stage	360°	0.36 arc-sec	100 lb
Standa	8MT175-100-MEN1	Linear Stage	100 mm	0.01 μm	3 kg (6.6 lb)
Standa	8MVT120-25-4247-MEN1	Vertical Stage	25.4 mm	0.02 μm	10 kg (22 lb)
Standa	8MR190-2-28-MEN1	Rotatory Stage	360°	36 arc-sec	2 kg (4.4 lb)
Velmex	MN10-0050-E01-21	Linear Stage	127 mm	0.15 μm	3 kg (6.6 lb)
Velmex	B4872TS-BK	Rotatory Stage	360°	100 arc-sec	25 lb

4.1.2 Mechanical Interfaces

The mechanical hardware consisted of two NSL4 linear positioning stages and two RM-5 rotary stages from Newmark Systems. Load analysis was performed before designing the hardware to understand the design constraints imposed by the stages' load capacities. Figures 4.5 and 4.6 show the load characteristics of the RM-5 and NLS4 stages, respectively. As seen in Figure 4.7, a 2.66 kg load was assumed as the payload mass and the mass of interfacing brackets was assumed to be 1 kg. Starting at analysis point 4, a normal load of 26 N was calculated on the ψ stage. Continuing to point 3, the payload and ψ stage weight imposed about a 10.6 Nm moment on the θ stage, with a 71 N shear component. At point 2, the combined loads from the rotation stages resulted in about a 14.2 Nm moment and an axial load of 109 N. The axial load on the Z stage was the equivalent of 11.1 kg, which was near the 11.3 kg limit. Moving on to point 1, the equivalent normal load was about 130 N and the transferred moment was 14.2 Nm. All four stages were capable of supporting the loads in the configuration.

Normal Load (Fz)	90.7 kg (200 lbs)
Moment Load (Ma)	54.2 Nm (40 lb-ft)
Max. Torque (Tz)	12.5 Nm (9.2 lb-ft)

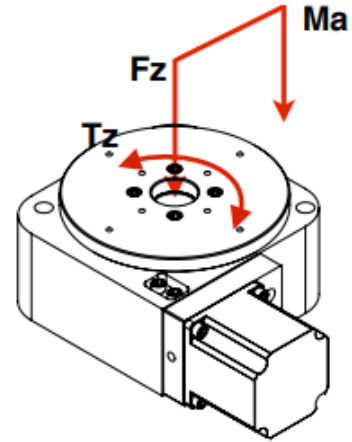


Figure 4.5: Load characteristics of the Newmark RM-5 stage [19].

Axial Load Fa	11.3 kg (25 lbs)
Normal Load Fz	22.6 kg (50 lbs)
Moment Load Ma	20.3 Nm (15 lb-ft)
Moment Load Mc	20.3 Nm (15 lb-ft)

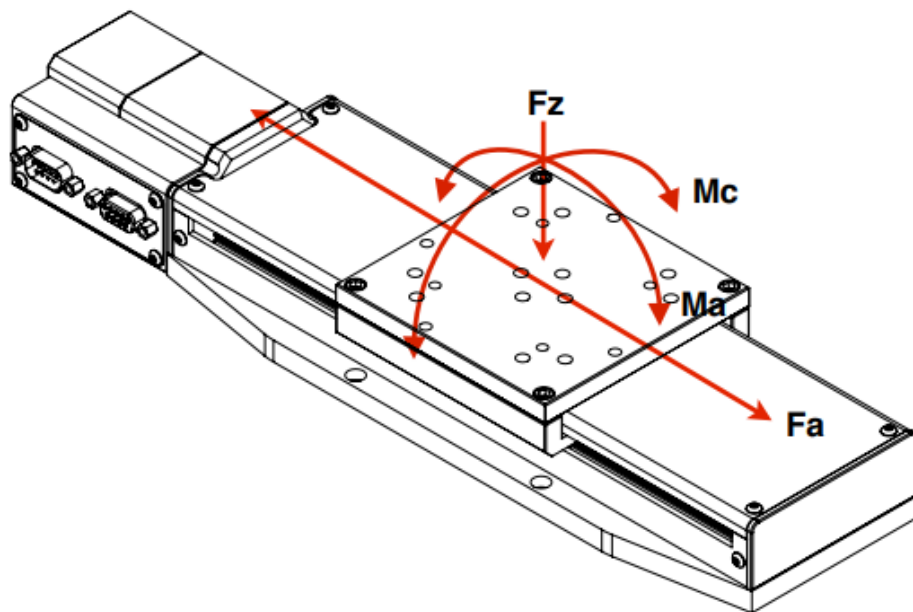


Figure 4.6: Load characteristics of the Newmark NLS4 stage [18].

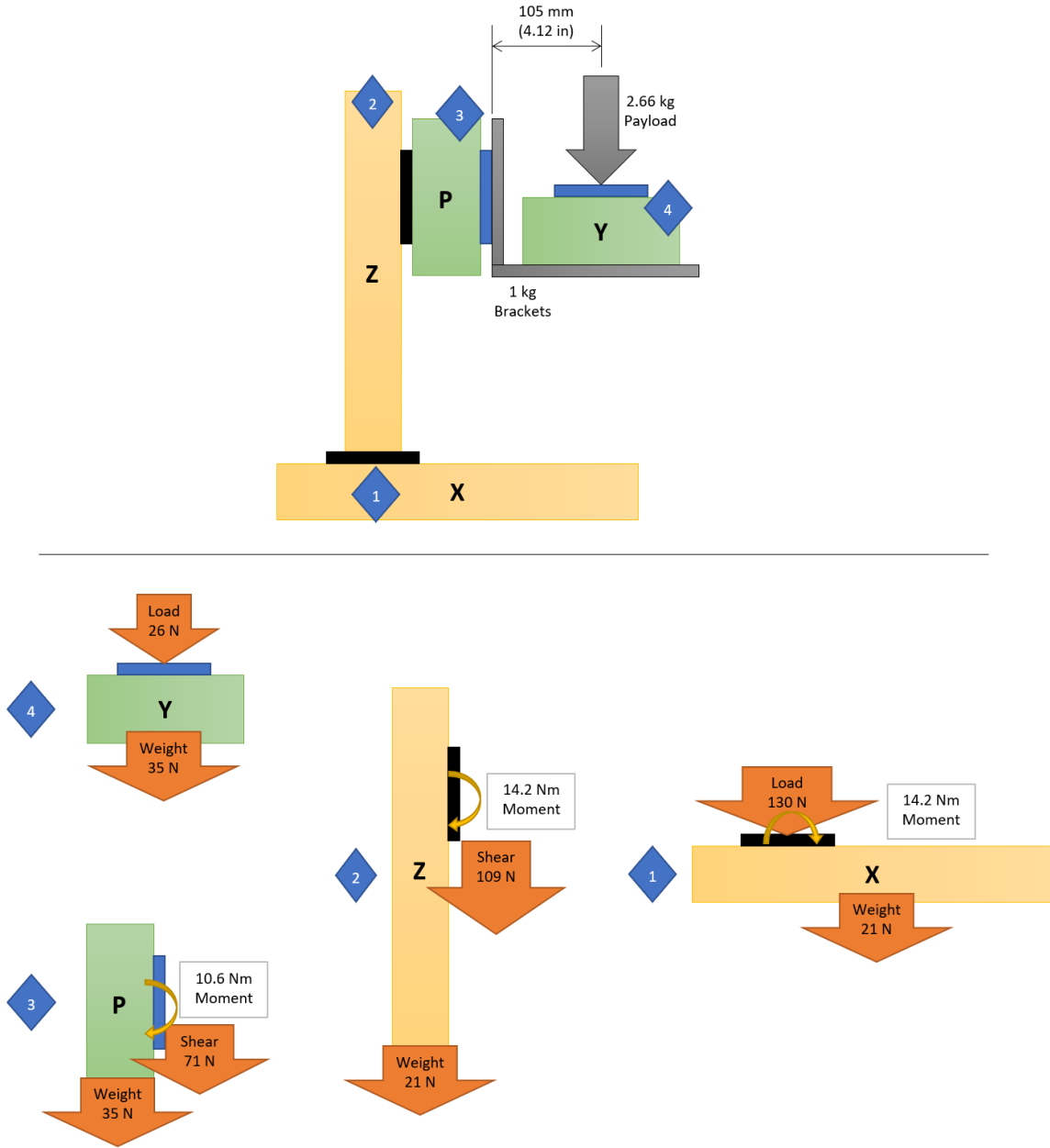


Figure 4.7: Load analysis for the Newmark Stages.

A total of eight mounting adapters were designed to interface the stages together. Two vertical beams secured the Z stage to the X stage, as shown in Figure 4.8. Then, a flat plate connected the θ stage to the Z stage, which is seen in Figure 4.9. The ψ stage interfaced to the θ stage through a customized shelf. The shelf was supported

by angle brackets to relieve the moment load on the plates. The ψ stage interface adapters may be seen in Figure 4.10. The interface components were light-weight to meet the axial load restriction of the Z stage.

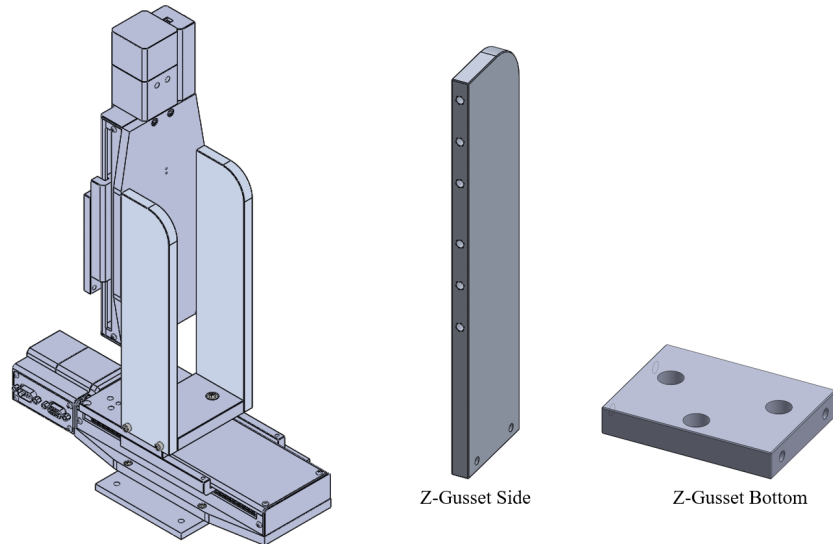


Figure 4.8: Gusset interface composed of three adapters to connect the Z stage to the X stage.

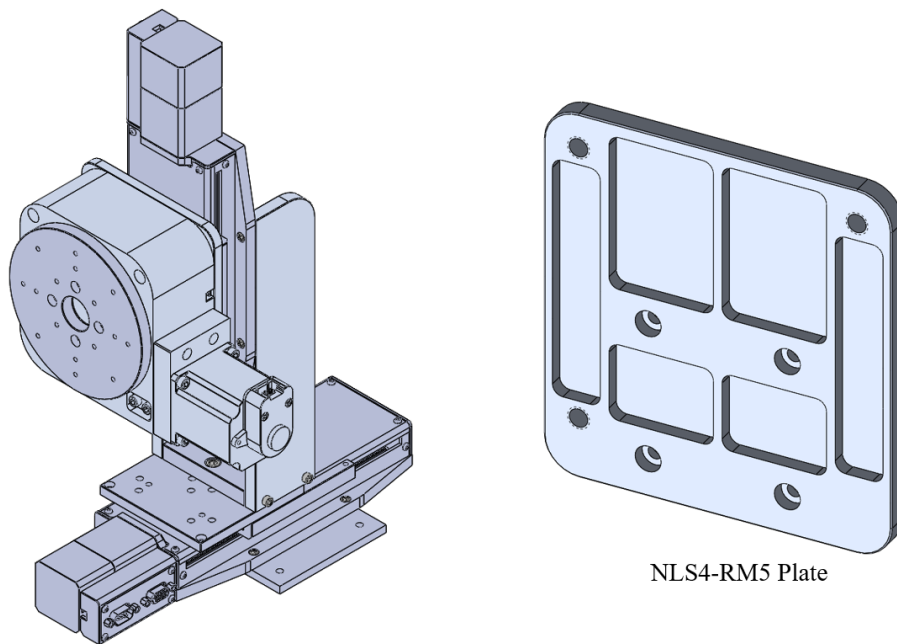


Figure 4.9: Adapter plate to connect the θ stage to the Z stage.

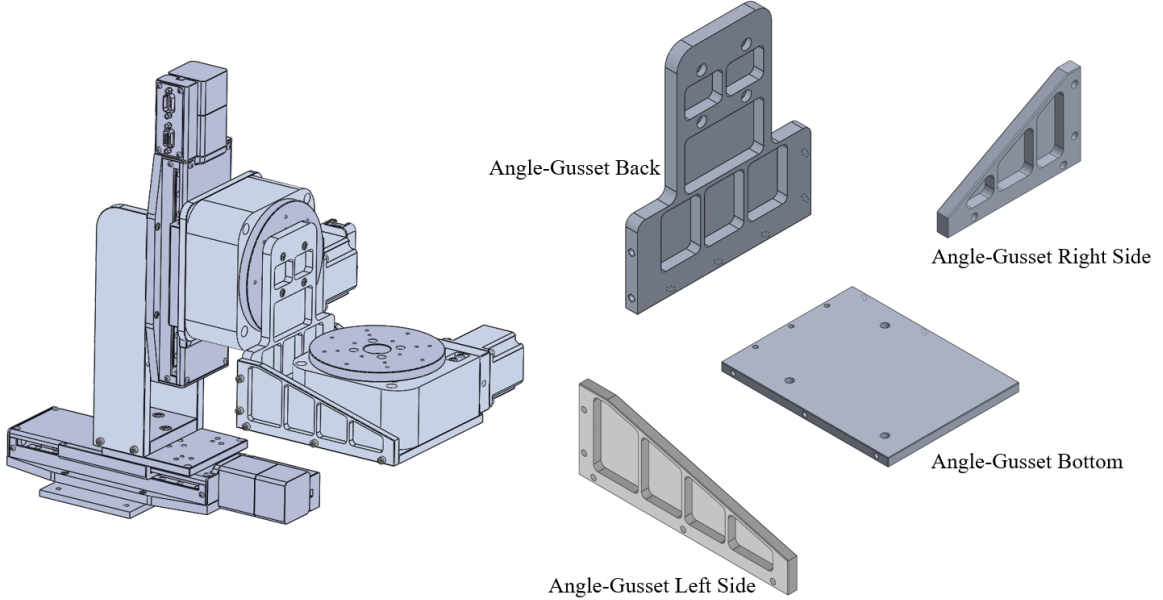


Figure 4.10: Angled gusset interface to connect the ψ stage to the θ stage.

4.1.3 Optics Assembly

The optical GSE was designed to simulate the MUVI instrument optics as close as possible. Many optical design iterations were performed, which resulted in the final design shown in Figure 4.11. Two Thorlabs KC2 kinematic mounts, constrained by four ER6 cage rods, were used to mount the 2 inch and 1 inch round mirrors. The 60 mm cage system permitted for height adjustment of the two mirrors relative to each other. The top mirror was mounted in Thorlab’s H45CN mirror mount, whereas the bottom mirror was secured by a customized mount. The custom bottom mirror mount consisted of three components, as seen in Figure 4.12. The 1 in round mirror mated to the 45° adapter, which then mated to the T-slot slider, which was connected to the bottom mirror mount. The slider was designed to adjust the horizontal distance between the mirror and the camera. The bottom mirror mount subassembly mated into the KC2 kinematic mount for fine angular adjustment. The Phoenix 200s GigE camera from LUCID Vision Labs was selected for the application and had a resolution

of 5472 x 3648 px, pixel size of $2.4\mu\text{m}$, and a sensor size of 15.86 mm (Type 1). As seen in Figure 4.14, the CMOS camera was mounted on a flat plate that was slotted to allow for horizontal adjustment of the camera. This adapter was then secured onto the camera mount bracket, which was secured to the optics datum. The optics datum plate contained two reliefs that registered the camera mount and alignment mirror to each other. The iris was mounted inside the camera C-mount section by two retaining rings, as shown in Figure 4.13. Lastly, a flat plane mirror, which was included to establish boresight, was mounted to the optics datum via the Thorlabs FP01 plate mount. A bill of materials for the optical GSE may be referenced in Appendix E.

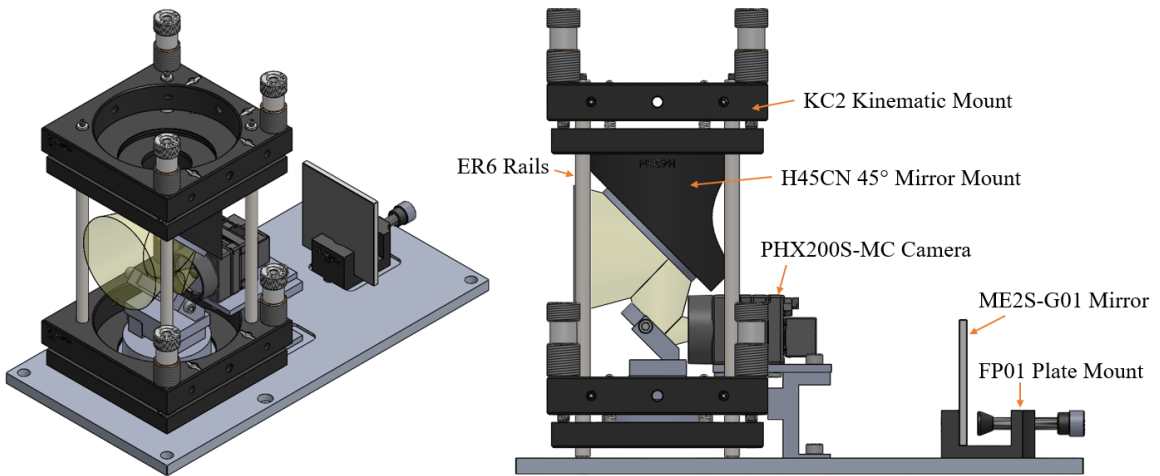


Figure 4.11: Optical GSE assembly with labeled components.

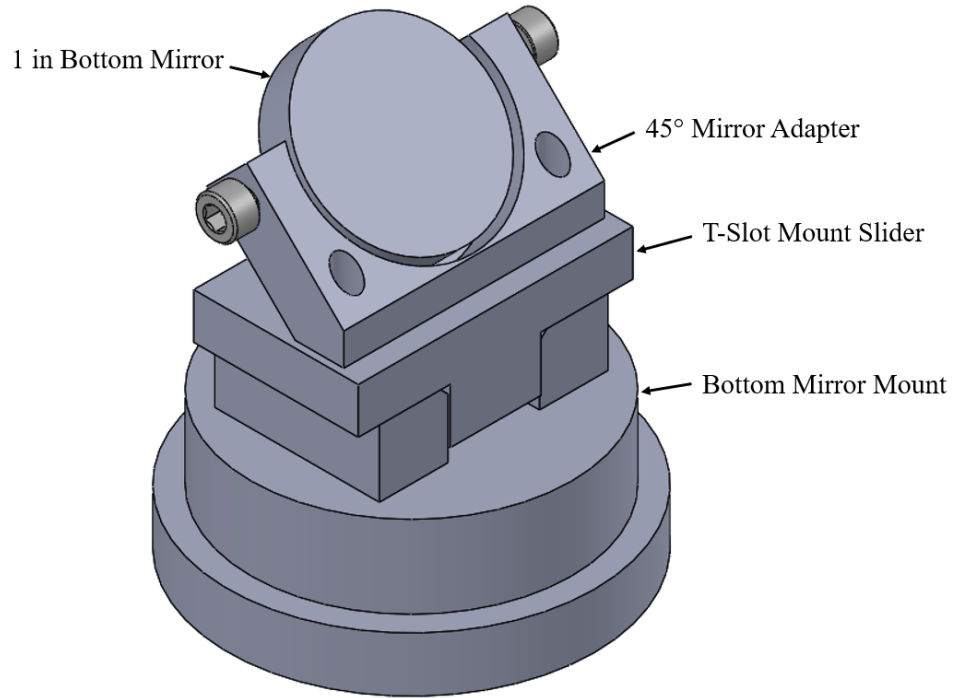


Figure 4.12: Bottom mirror mount that was designed to fit the KC2 kinematic mount.

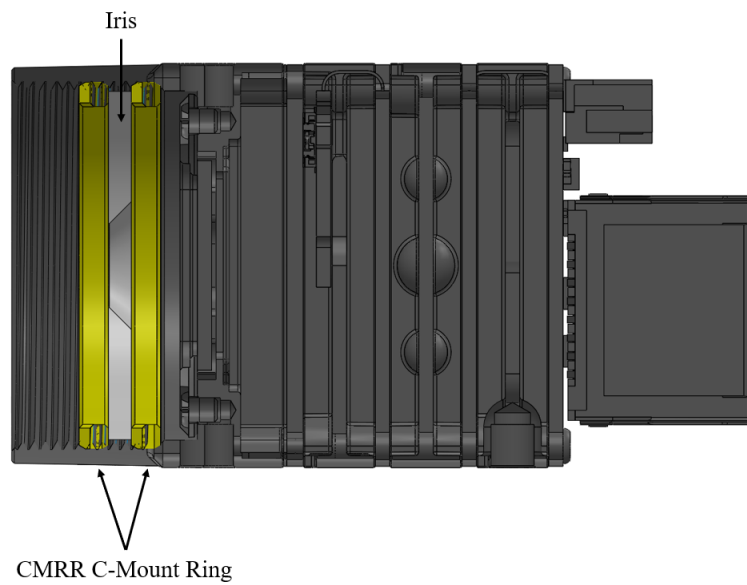


Figure 4.13: Two C-mount retaining rings secure the iris inside the camera.

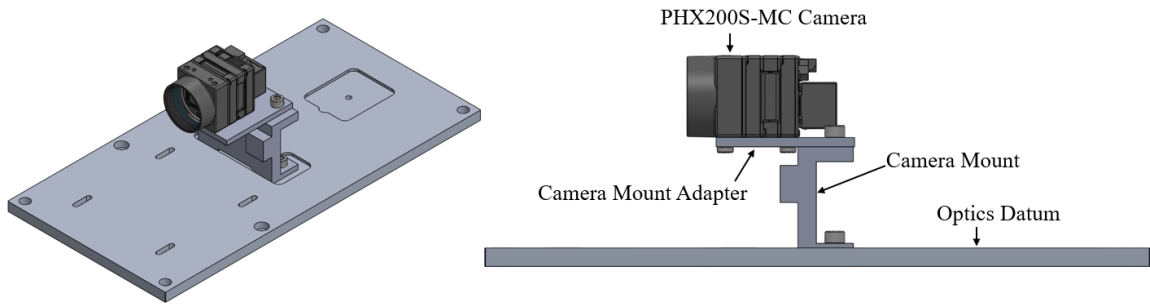


Figure 4.14: The Phoenix 200S camera mount that mated to the optics datum.

4.1.4 Stage Clearance

A clearance study was performed to ensure the stages did not interfere with each other. As seen in Figure 4.15, there is about 0.5 inches of clearance between the angle gusset bottom plate and the X stage when the θ stage is pitched up by 30° .

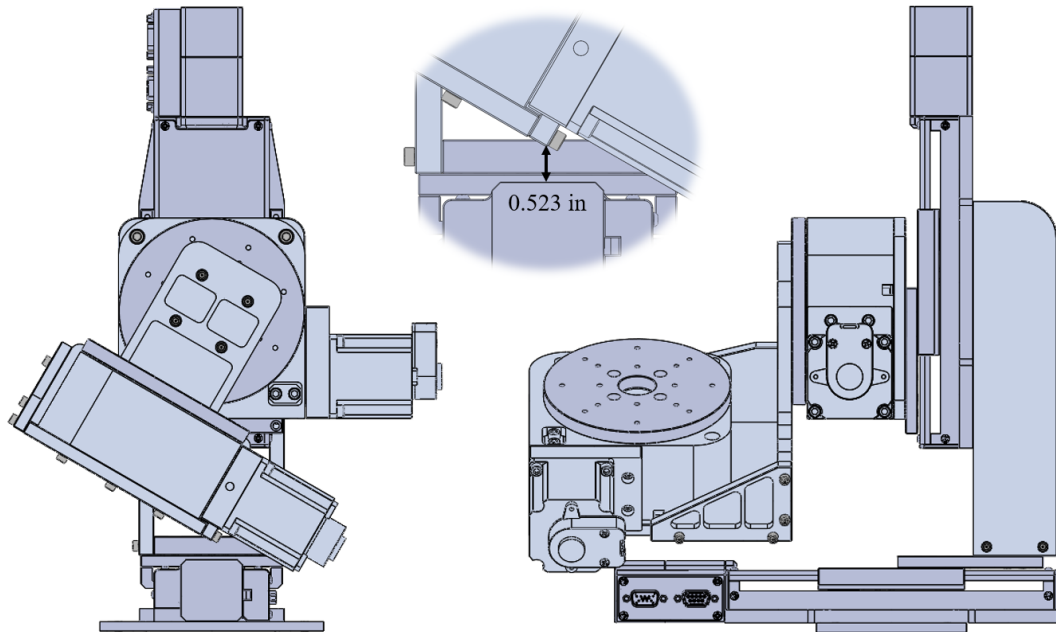


Figure 4.15: Clearance of the manipulator when pitched up by 30° .

Plenty of margin was observed when the yaw stage was rotated negative 30° . However, the corner of the instrument datum plate interferes with the θ stage motor around positive 24° of yaw, which is shown in Figure 4.16. This slight interference is not of concern because 24° of rotation far exceeds the one-sided 15° movement required for the 30° FOV.

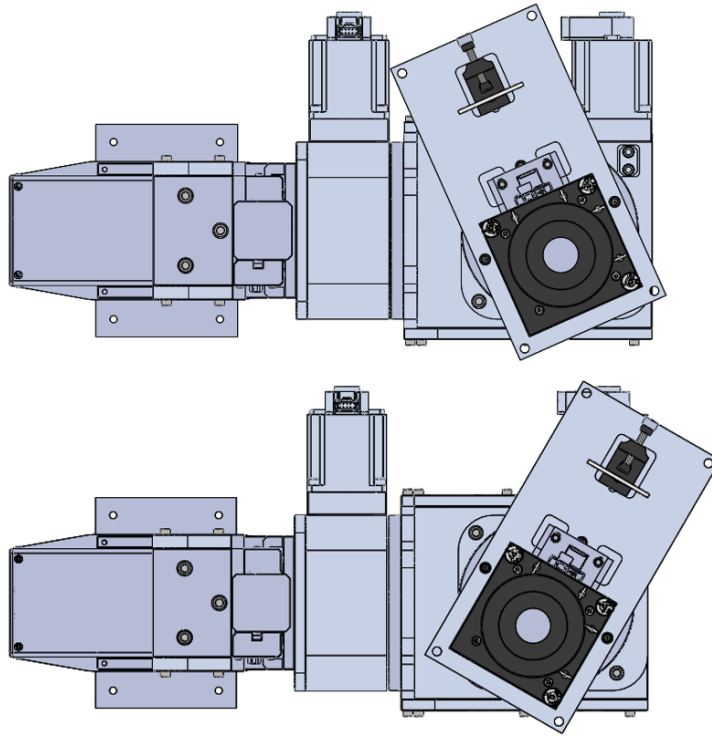


Figure 4.16: Clearance of the manipulator when yawed $+24^\circ$ (top) and -30° (bottom).

4.1.5 Test Configurations

The manipulator will be used in both visible light and UV-vacuum configurations. The following sections describe these configurations in detail.

4.1.5.1 Visible - Atmospheric

The visible-atmospheric test configuration was designed for two purposes. First, evaluation of the manipulator's performance was best conducted with maximum access to the hardware. Secondly, various components of the MUVI instrument may be initially tested in visible light before entering the UV vacuum chamber. These purposes drove the need for maneuverability of the test stand. A custom GSE cart was designed from extruded aluminum stock. An optical breadboard was placed on top of rubber mounts that were secured to the cart. Wheels below the cart allowed for quick movement around the lab, and leveling mounts ensured secure placement once the cart was placed in the desired location. The design of the visible light test stand is shown in Figure 4.17.

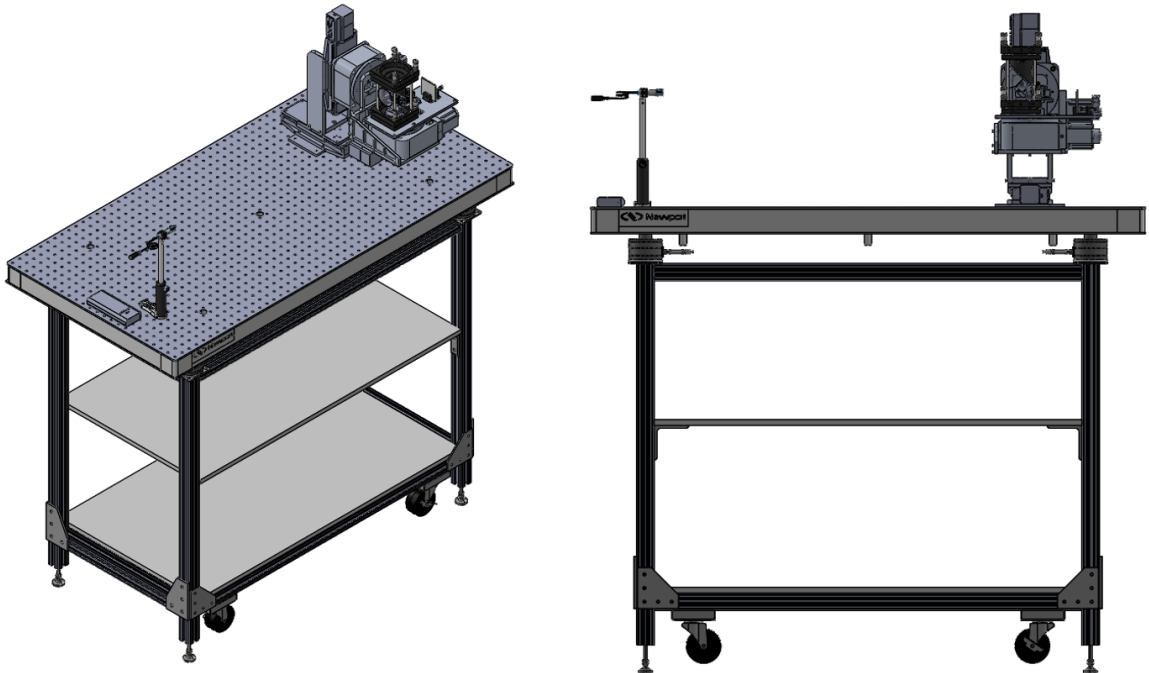


Figure 4.17: A movable cart was designed out of 8020 aluminum stock for visible-atmospheric test purposes.

4.1.5.2 Ultraviolet - Vacuum Chamber

Preliminary design of the UV-vacuum chamber test configuration was conducted. Although there are a few details to work out, such as designing an interface between the manipulator and chamber rails, the configuration shown in Figure 4.19 was useful to establish confidence of manipulator operation inside the chamber. Sufficient clearance was observed when the manipulator was oriented at its maximum range of travel nearest the chamber wall, as seen in Figure 4.18.

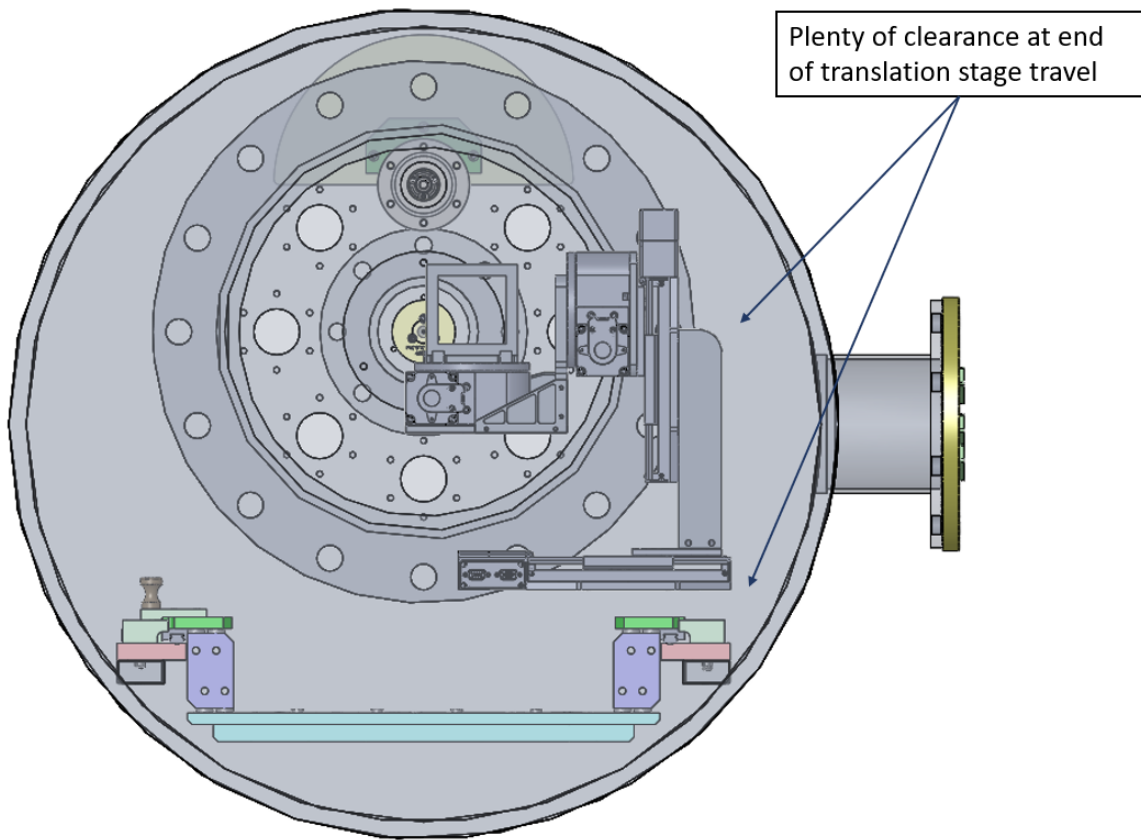


Figure 4.18: Sufficient clearance is observed between the vacuum chamber walls and the manipulator when the linear stages are located at their end of travel.

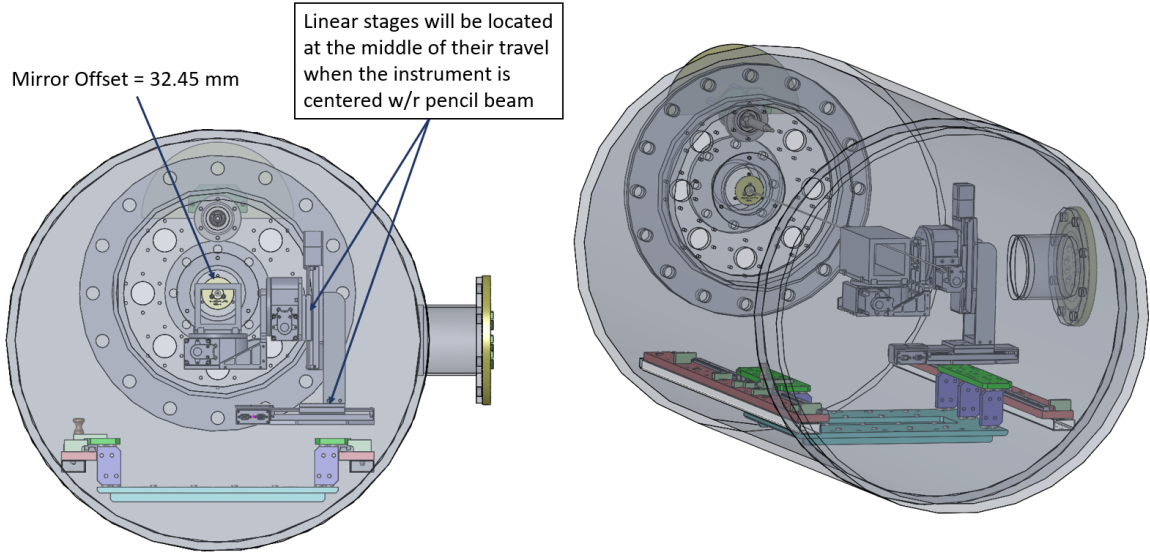


Figure 4.19: CAD of the manipulator inside the UV vacuum chamber at SSL. The manipulator is placed such that the stages are located at their mid-range of travel when the manipulator is oriented at boresight.

4.2 Electrical System

4.2.1 Architecture

The architecture of the electrical system is shown in Figure 4.20. A custom GUI, which is described in Chapter 5, sends serial commands to the microcontroller. The microcontroller, which runs a RTOS, handles the inputs and sends SPI commands through the custom PCB to the stepper motor drivers. The microcontroller also receives feedback data from the motor encoders and end of travel limit switches.

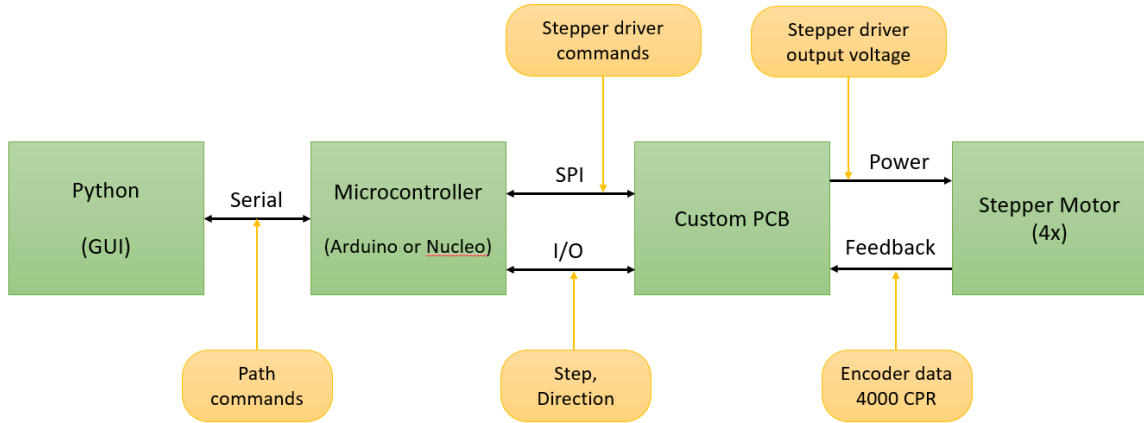


Figure 4.20: Diagram of the electrical system architecture.

4.2.2 Component Selection

4.2.2.1 Microcontroller

The microcontroller is a crucial element for the operation of the manipulator. Several factors, such as clock speed, memory size, and number of I/O ports, have a direct impact on the performance of the manipulator. However, an important factor that influenced the microcontroller selection the most was consideration for the development and maintenance of hardware by various engineers throughout the MUVI campaign. Arduino and STM32 brands of microcontrollers were considered for their popularity and reliable performance. Furthermore, most engineers with mechatronic experience are familiar with developing on these platforms. Although it was a close comparison, the Nucleo STM32-L476RG was selected instead of the Arduino ATmega for the following two reasons. First, the Nucleo was compatible with both C/C++ and MicroPython environments. Developing a system and GUI in the Python language would be straightforward for other engineers to pick up, especially when compared to the nuances of the C language. And second, the Nucleo STM32 had the correct

number of internal timers with built-in quadrature encoder counters. Overall, the peripherals were better matched on the Nucleo than the Arduino board.

4.2.2.2 Stepper Drivers

Stepper drivers come in a number of different styles, ranging from integrated circuit breakout boards to fully developed multi-axis CNC boards. CNC motion control boards were not considered for the application due to the "Learn by Doing" Cal Poly motto. Diving into stepper motor control details was beneficial to the learning process in this aspect of the thesis. Stepper drivers from Trinamic were considered for their superior performance and advanced features compared to other standard stepper drivers. The TMC2160 driver was compared against the TMC5072 driver. As seen in Figure 4.21, the TMC2160 single motor driver featured SPI configuration, a step/direction interface, and a 256 microstep sequencer. As seen in Figure 4.22, the TMC5072 featured dual motor control, UART and SPI configuration interface, an integrated motion controller, built-in encoder counter, and 256 microstep sequencer. Although the TMC5072 had more advanced features, the TMC2160 was selected for the application.

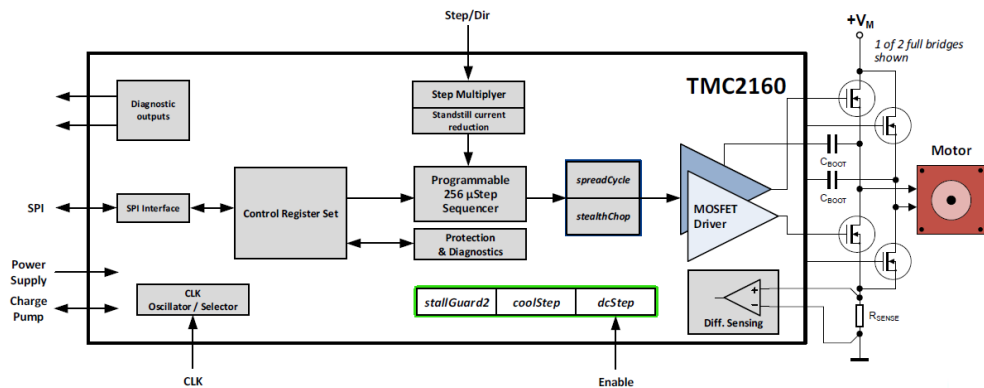


Figure 4.21: Diagram of the TMC2160 stepper driver features [27].

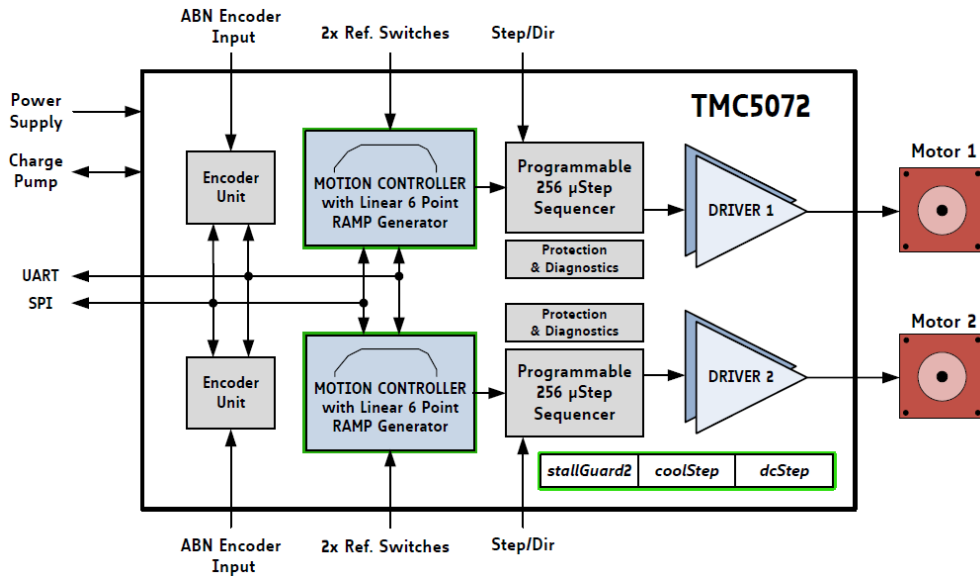


Figure 4.22: Diagram of the TMC5072 stepper driver features [26].

4.2.2.3 Motor Connectors

The harnesses for the Newmark stages came in D-Sub 9 and High-Density D-Sub 15 connections for the motor power and feedback signals, respectively. The pinouts for the linear stage connectors are shown in Figure, and the pinouts for the rotary stage connectors are shown in Figure.

4.2.2.4 Differential Signal Receivers

The encoder signals from the Newmark stages were specified to be differential output, which required a differential signal receiver to read the encoders. The SN65LVDS349 quad high-speed differential receiver IC from Texas Instruments was selected for the application [24].

Motor Connector

DB-9 Male	Description
1.	Phase A
2.	Phase A'
3.	Phase B
4.	Phase B'
5.	Phase A Center
6.	Phase B Center

Signals Connector (Encoder Option)

HD-15 Female	Description
1.	+ Limit Switch
2.	- Limit Switch
3.	Limit Switch Ground
4.	Encoder Ground
5.	+5V Encoder Power
6.	Ch. A
7.	Ch. A-
8.	Ch. B
9.	Ch. B-
10.	Index +
11.	Index -

Figure 4.23: Pinout of the connectors for the NLS4 stage [18].

Motor

DB-9 Male	Description
1.	Phase A
2.	Phase A'
3.	Phase B
4.	Phase B'

Signals (Encoder Option)

HD-15 Female	Description
1.	N.C.
2.	N.C.
3.	N.C.
4.	Encoder Ground
5.	+5V Encoder Power
6.	Ch. A
7.	Ch. A-
8.	Ch. B
9.	Ch. B-
10.	Index +
11.	Index -

Figure 4.24: Pinout of the connectors for the RM-5 stage [19].

4.2.3 Breadboard Test

A preliminary test of the electronics assembly was conducted using a couple of breadboards, jumper wires, and LEDs. Reference Figure 4.25 for the test setup. The first program that was run on the Nucleo tested the functionality of the digital pins. A few issues were discovered, such as Micropython firmware deficiencies for certain pin assignments, and the microcontroller pin assignments were redefined until all of the supported pins were functional. Afterwards, the breadboard setup was used to write, debug, and commission the ramp profile step generator for the motor drivers, in addition to troubleshooting the serial peripheral interface (SPI) communication between the microcontroller and the TMC2160 stepper drivers. The custom PCB design was finalized and ordered after the components were tested and working properly. The breadboard testing was invaluable, as many issues were resolved before the PCB was fabricated.

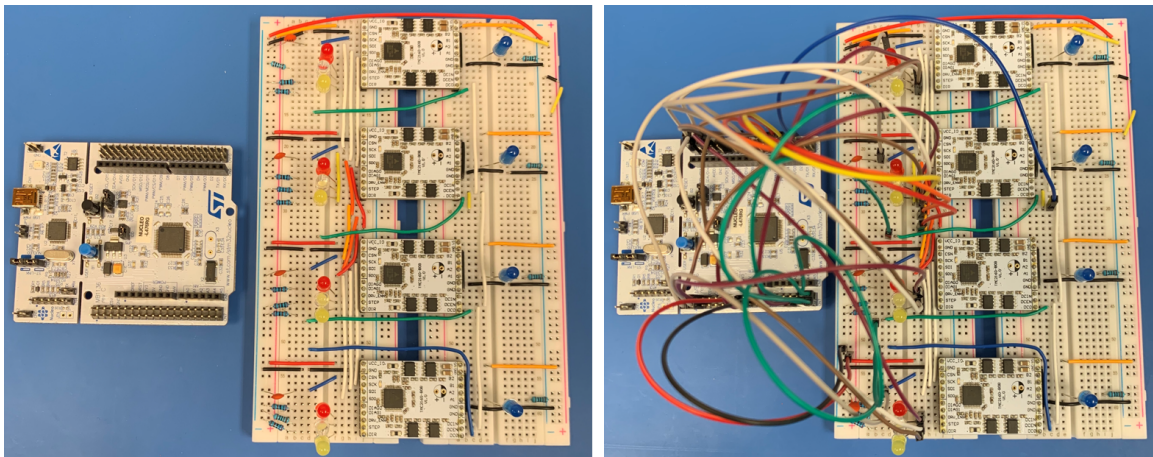


Figure 4.25: Breadboard test of the manipulator electronics.

4.2.4 Custom PCB

A custom PCB was designed for the application using the Eagle software package. A conceptual diagram of the PCB layout is shown in Figure 4.26. The basic components of the PCB consisted of the microcontroller, four HD-15 connectors, four DB9 connectors, four stepper driver boards, and a connection for motor power. A rendering of the final PCB design is displayed in Figure 4.27. The differential receivers were placed close to the HD-15 connectors to minimize the signal trace length for electrical noise purposes. Trace widths of 0.012 in and 0.075 in were used for the signal and power lines, respectively. Polygon traces were used for the power supply bank, and vias were scattered about the board to connect the top and bottom ground planes. The schematics for the PCB design may be found in Appendix C.

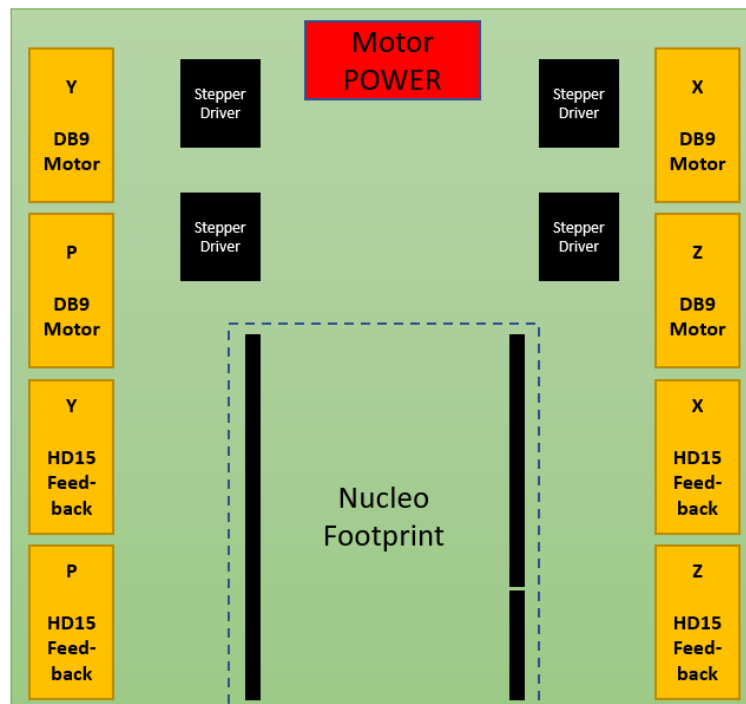


Figure 4.26: Conceptual layout of the custom PCB designed for the MUVI manipulator.

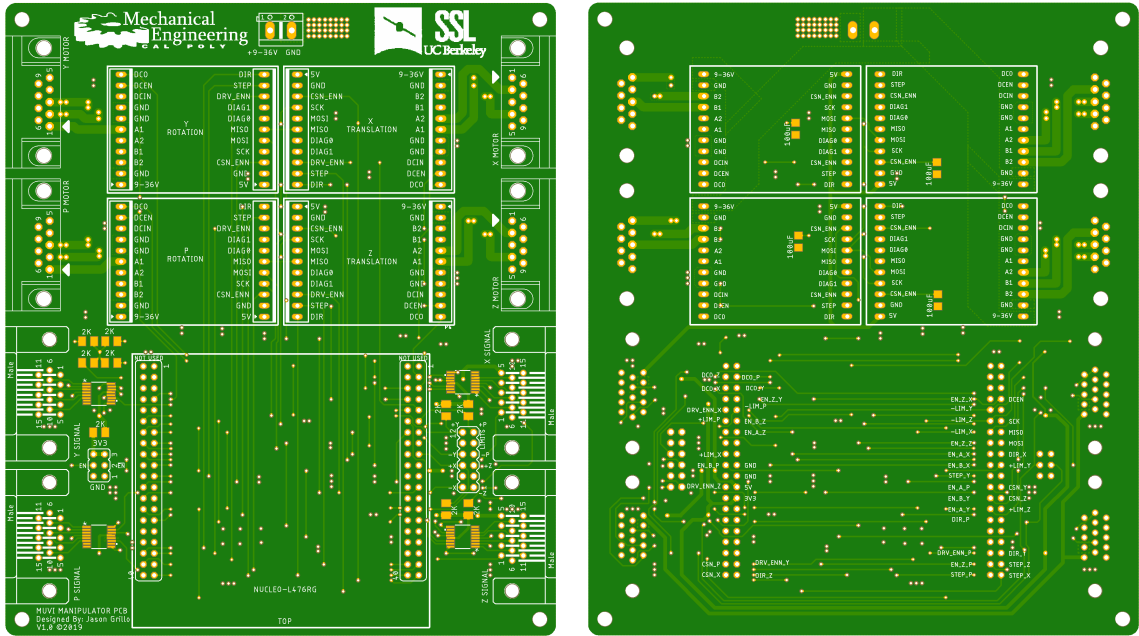


Figure 4.27: PCB designed for the MUVI manipulator.

4.2.5 Enclosure and Power Management

An electrical enclosure was designed to house the 24V power supply and custom PCB, which is shown in Figure 4.28. The Alitove 24VDC 15A 360W Power Supply was specified for the application. A cooling fan was placed inside the enclosure to aid in convective heat transfer to keep the stepper driver boards from over-heating during continuous use. The enclosure was designed using a 12x12x4 inch 5052 H-32 aluminum junction box from Hammond Manufacturing.

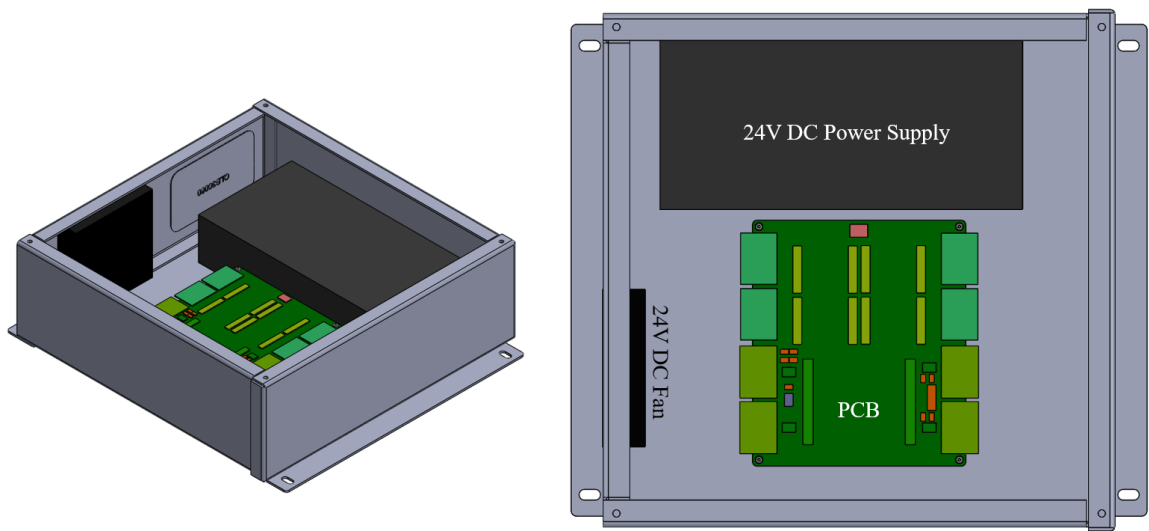


Figure 4.28: Electrical enclosure that housed the PCB and 24V power supply.

Chapter 5

SOFTWARE DESIGN

This chapter documents the software written to control the manipulator. The structure of the code was built using a multi-tasking strategy, which was most appropriate for executing the complex mechanical control system. The task scheduler python module was written and kindly provided by Professor John Ridgeley of Cal Poly. First, the Real-Time Operating System, state machine diagrams, and task diagrams implemented on the microcontroller are described. Next, the development of the GUI and its operation is discussed.

5.1 Microcontroller RTOS

A Real-Time Operating System was implemented in MicroPython on the Nucleo STM32-L476RG board using a cooperative multitasking environment. The approach for the software implementation was to develop modular code with efficient use of object-oriented programming. Thus, the tasks and hardware drivers were written as classes, and the inter-task communication variables for the task classes were passed through as parameters in the constructor. A diagram of the tasks is shown in Figure 5.1. The RTOS consisted of three different tasks that were implemented for each stage, totaling nine tasks. The hub task handled the input serial commands, updated the shared task data, and transmitted feedback data back to the GUI. The motor task handled the motion control of each stage to specific positions, and the feedback task read the encoder and limit switch data.

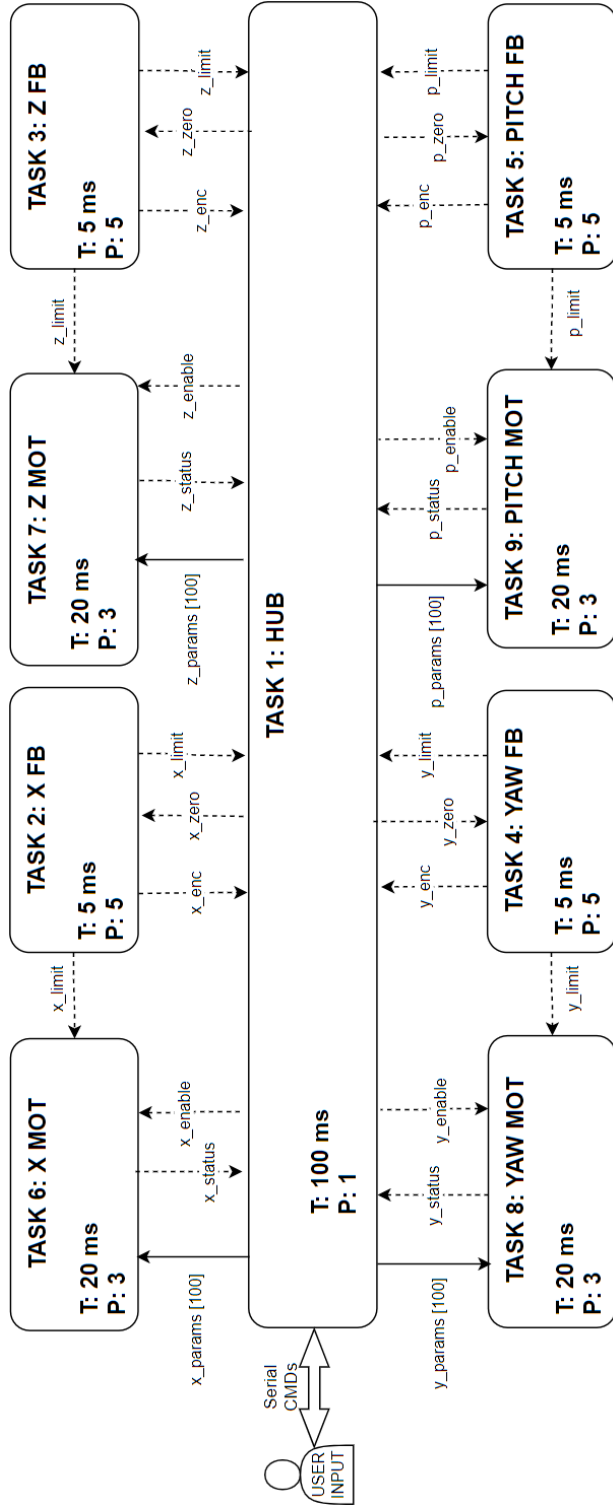


Figure 5.1: Task diagram of the manipulator RTOS that is run on the Nucleo microcontroller.

The priority and period of the tasks are defined upon RTOS initialization, and the priority scheduler executes the various tasks when they are ready to be run. The justification for the timing and priority of each task is as follows. Task 1 (Hub) must respond to GUI commands, and the time response of user input may be as quick as 200 ms if buttons are repeatedly clicked. Thus, the Hub task must run 2x as fast, or 100 ms, for margin. User input is the least priority task because the user may send a command again if the input was not initially received. Tasks 2-5 (Feedback) must read data around 10 Hz to not miss encoder counts at max speed. Thus, the Feedback tasks must run at 200 Hz, or 5 ms, for plenty of margin. Feedback is the highest priority because data may be lost if it is not executed on time. Tasks 6-9 (Motor) were experimentally found to operate reliably below 30 ms. Thus, the Motor tasks must run at 20 ms for margin. Motor control is a medium priority task with respect to the Hub and Feedback tasks.

5.1.1 Hub Task

The hub task was responsible for relaying information to and from the GUI. A state machine diagram for the hub task is shown in Figure 5.2. This task had five states:

State 1: Wait for command. In this state, the manipulator hub printed feedback data and waited for GUI movement commands. The exit condition for this state was a movement command to one of the stages.

State 2: Moving Yaw. If the ψ stage was enabled and a new ψ position was received, the hub entered this state. Feedback data was also printed in this state. If the ψ stage was disabled or a limit switch was triggered or the ψ stage reached its position, the hub exited and returned to State 1.

State 3: Moving Pitch. Similar conditions as State 2, but applied to the θ stage.

State 4: Moving Z. Similar conditions as State 2, but applied to the Z stage.

State 5: Moving X. Similar conditions as State 2, but applied to the X stage.

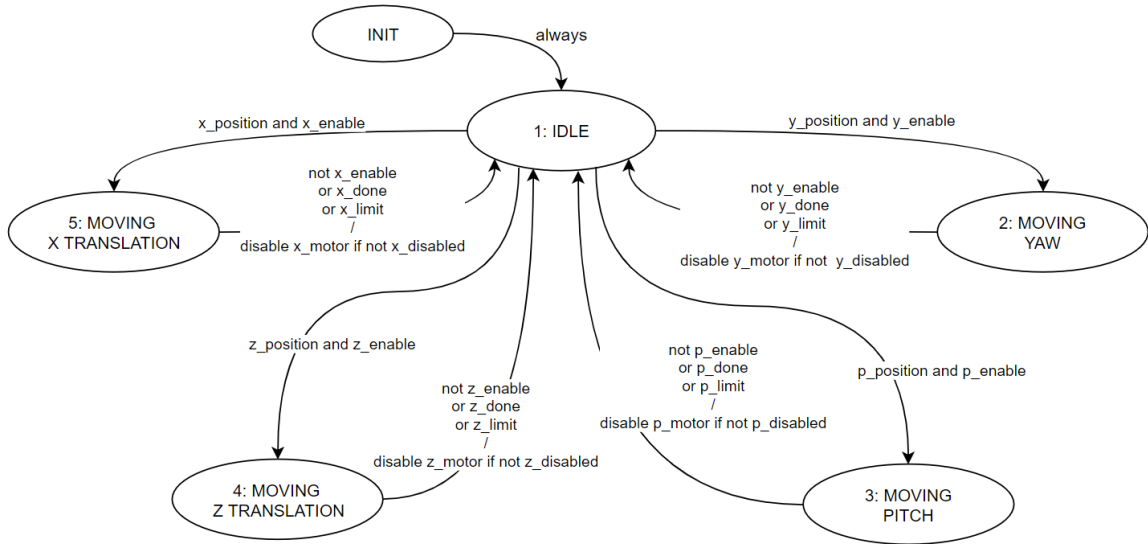


Figure 5.2: State machine for the hub task.

5.1.2 Motor Task

The motor task was responsible for controlling the stepper motors for both the linear and rotation stages. A state machine diagram for the motor task is shown in Figure 5.3. This task had two states:

State 1: Wait for move command. In this state, the stage waited for a new position command from the hub task. The exit condition for this state was a movement command, but only if the stage was enabled.

State 2: Moving Stage. The ramp profile step generator was started upon entrance to this state. If the stage was disabled or a limit switch was triggered or the stage reached its position, the task indicated that movement was done and returned to State 1.

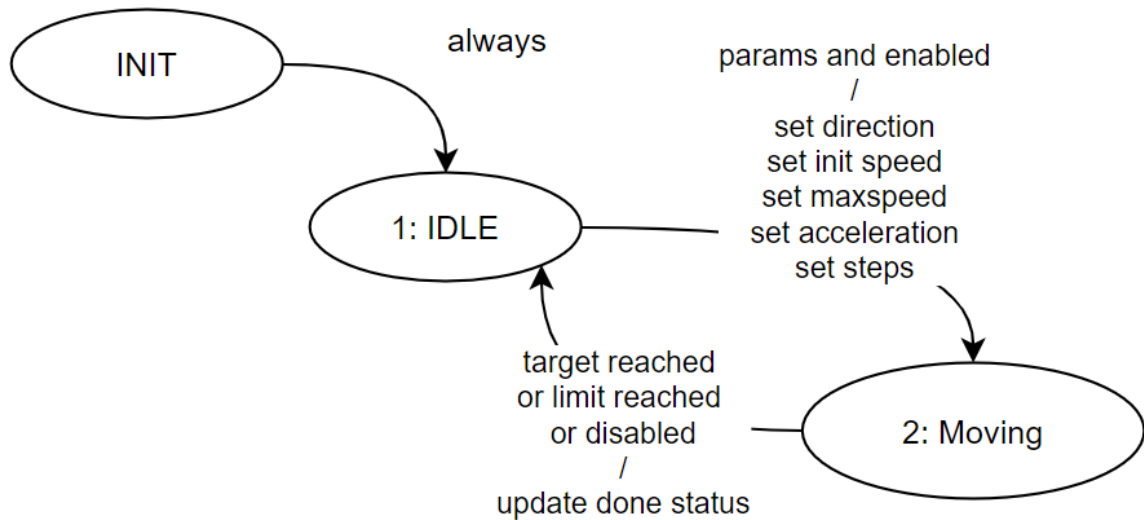


Figure 5.3: State machine for the motor task.

5.1.3 Feedback Task

The feedback task was responsible for reading the encoder and limit switches. A state machine diagram for the feedback task is shown in Figure 5.4. This task had two states:

State 1: Transmit feedback. In this state, the limit switch pins and the encoder timer counter were read and their shared variables were updated. The exit condition for this state was a command to zero the encoder.

State 2: Zero encoder. This state reset the encoder counter. The task returned to State 1 after the encoder was zeroed.

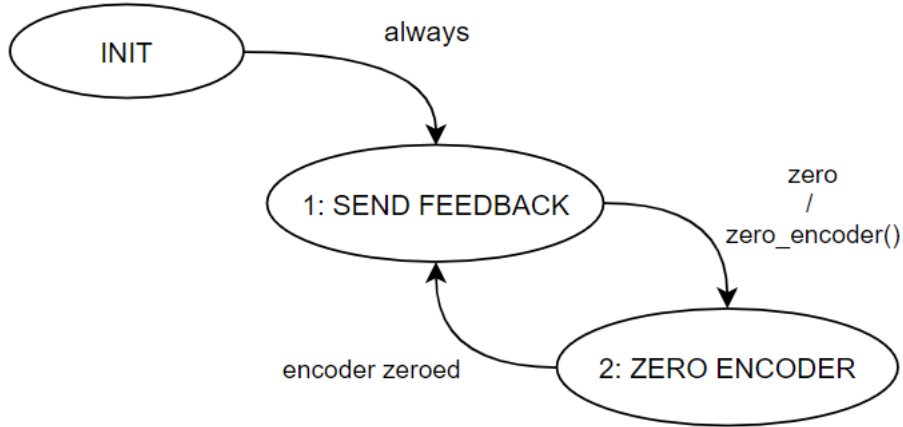


Figure 5.4: State machine for the feedback task.

5.2 Graphical User Interface

A GUI was written in Python to satisfy the requirement of using a serial interface between a computer and the Nucleo STM microcontroller. The Tkinter module was used to implement the GUI. The conceptual layout of the GUI is presented below in Figure 5.5, and the finalized version of the GUI is shown in Figure 5.6. The GUI was implemented with five main sections, which may be further explored in the Manipulator’s User Manual found in Appendix A:

Status Panel: In this section, live data streams were displayed from the encoders and limit switches of each stage. If live data was received from the serial port, the encoder readings were displayed in the position boxes and the stages’ speed were calculated by a simple two-point estimation. If a limit switch was triggered, the GUI changed the color from grey (inactive) to red (active). A user could also establish a reference position for later use by marking a stage’s position.

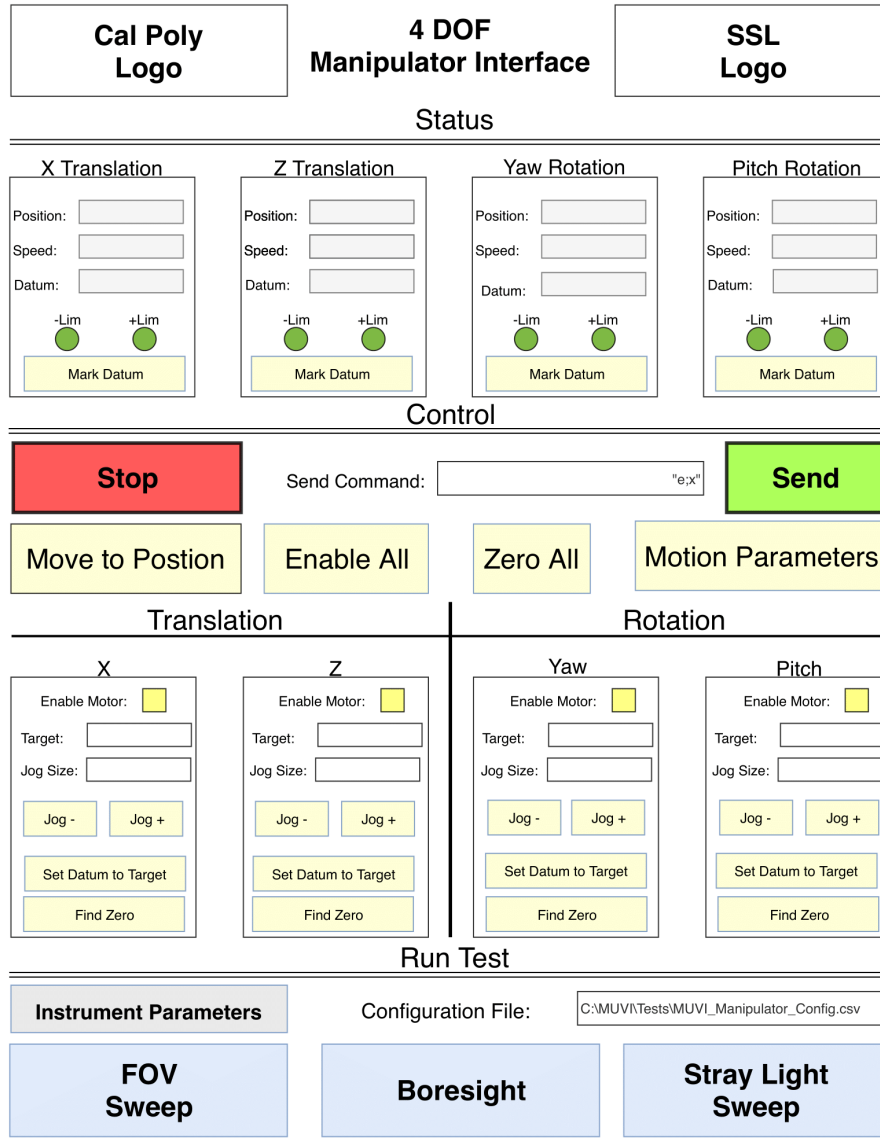
Control Panel: The control panel contained functions that enabled, zeroed, moved, and stopped the stages. A command line was included that would send user-

written serial commands to the microcontroller. The stages were enabled by clicking the "Enable" button, which was color coded red for "OFF" and green for "ON". To specify a new target position for the stage, the user would simply type the absolute position of the stage relative to its calibrated datum into the "Target" box. The target value could be automatically incremented (Jog +) or decremented (Jog -) by the value specified in the Jog Size input box. This feature removed the need of an external calculator when the target needed to be adjusted. The user could then move the stage and stop all motion if required.

Test Panel: In this section, the user could load configuration files that defined the motion parameters for each stage and the instrument configuration. The idea behind such configuration files was to decouple the software from the hardware, making the software variables easily modifiable without opening source code. Functions to run automated test scripts were included in this panel, but were not implemented due to time restrictions during commissioning. The input boxes labeled Pitch (θ) and Yaw (ψ) could be used to specify the field angle orientation of the manipulator. Once the Move Instrument button was pressed, the field angle target was fed through the translation compensation algorithm (translated to Python from Matlab), and the individual stage targets were returned. The user would then press the Capture Image button to take an image once the manipulator was at the field angle.

Manipulator Log: The Manipulator Log contained the print statements from the microcontroller. A timestamp was included for documentation purposes for when the data was saved to a CSV file. Because the microcontroller continuously printed its feedback data, the Manipulator Log was designed to not print duplicate lines.

GUI Log: The GUI Log documented the status of the GUI during automated sequences and printed the commands issued to the microcontroller. The timestamp of the GUI Log and Manipulator Log was consistent.



Created By: Jason Grillo
Cal Poly Mechanical Engineering, 2019

Figure 5.5: Conceptual diagram of the manipulator GUI.

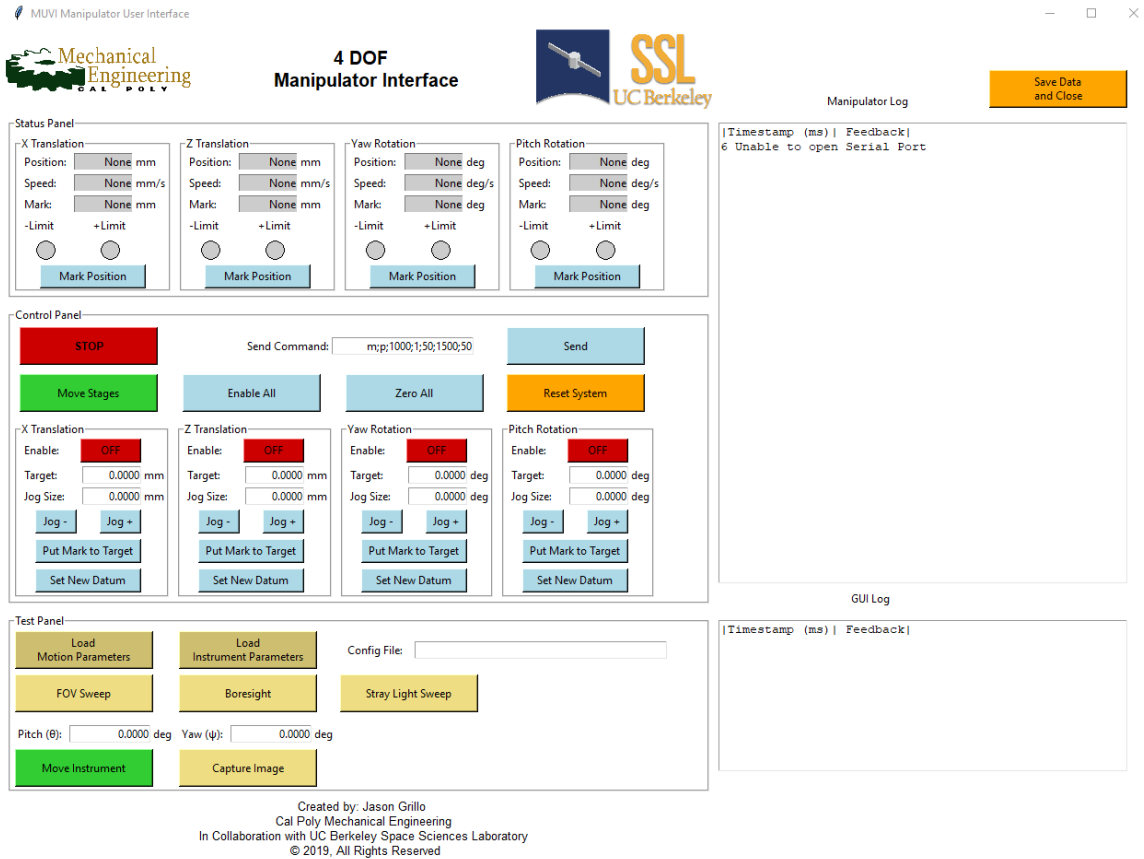


Figure 5.6: The finalized GUI that was designed to operate the MUVI manipulator.

Chapter 6

INTEGRATION OF THE MANIPULATOR

The results of fabrication and integration of the manipulator are documented in this chapter. At the end of the chapter, issues that arose during the build are documented and improvements are suggested for future iterations of the hardware.

6.1 Mechanical Integration

Nitronic 60 helicoils were installed in the adapter plates after they were machined. The parts were then wiped clean with Acetone and rinsed with Isopropyl alcohol. To remove machining lubricants from the threads, the parts were submerged in an ultrasonic bath of Simple Green degreaser for 30 minutes. Afterwards, they were rinsed in the same ultrasonic tub with a solution of Isopropyl alcohol and deionized water. Once the parts were properly cleaned, the manipulator was integrated on the GSE cart. First, the two linear stages were connected to each other using the Z gusset assembly, as shown in Figure 6.1. The position of the linear stages on the GSE cart was approximated based on the CAD model. Next, the NLS4-RM5 adapter plate was installed, and the θ stage was connected to the Z stage. Figure 6.2 shows the result of the θ stage integration. Afterwards, the angle gusset bracket was installed to the θ stage rotor, which may be seen in Figure 6.3. Finally, the ψ stage was mounted to the angle gusset bracket to finalize the stage integration, as seen in Figure 6.4. After the stages were integrated, the optics GSE subassembly was mounted to the ψ stage. The Power over Ethernet (PoE) injector needed to be mounted to the side of the ψ stage due to the length of the camera's PoE cable, as shown in Figure 6.5. As shown

in Figure 6.6, the SMR target holders were temporarily glued to the optics datum to secure them in place for the test campaign.

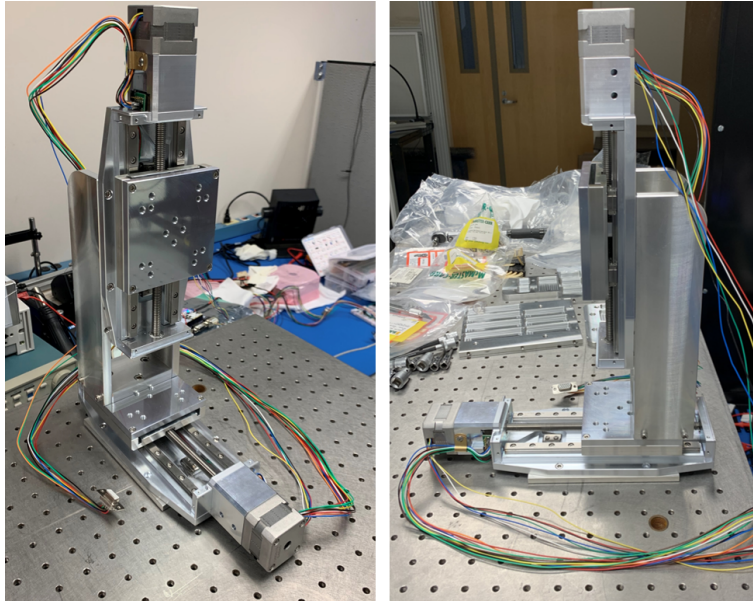


Figure 6.1: The linear stages were integrated with the Z gusset assembly.

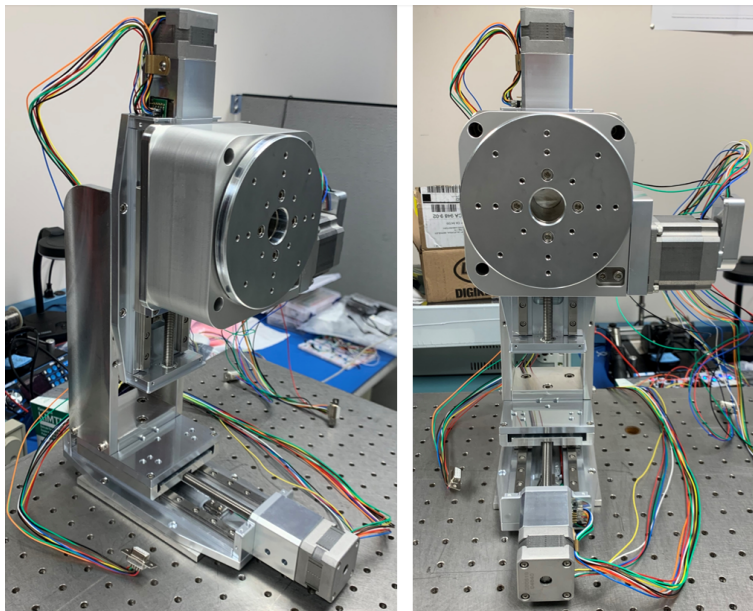


Figure 6.2: The θ stage was connected to the Z stage by the NLS4 to RM-5 adapter plate.

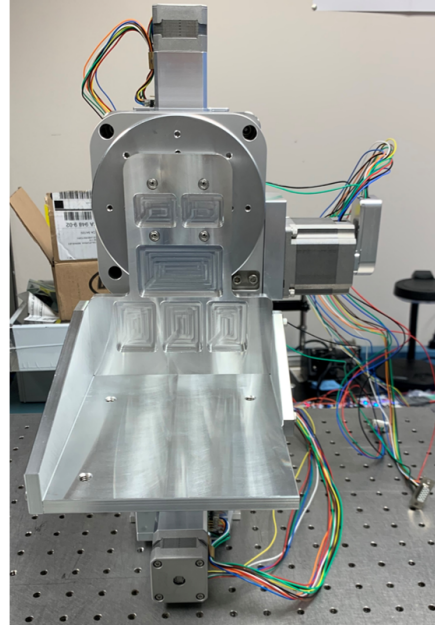
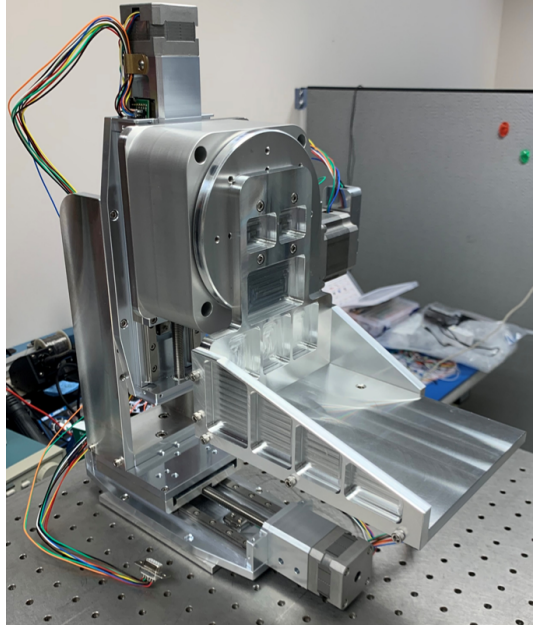


Figure 6.3: The angle gusset assembly was attached to the θ stage before mounting the ψ stage.

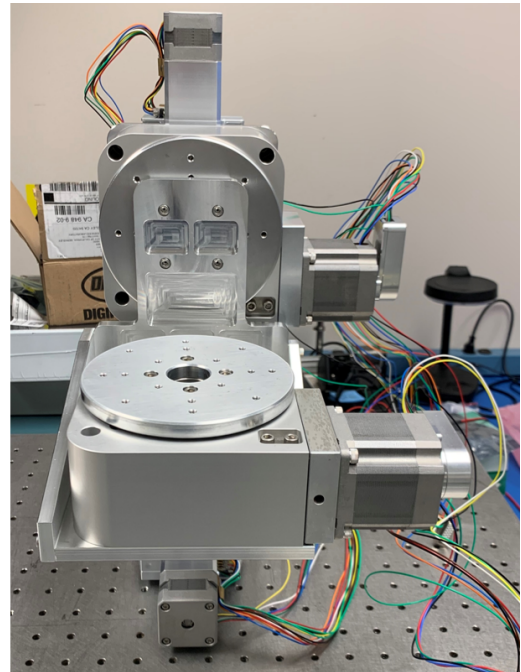
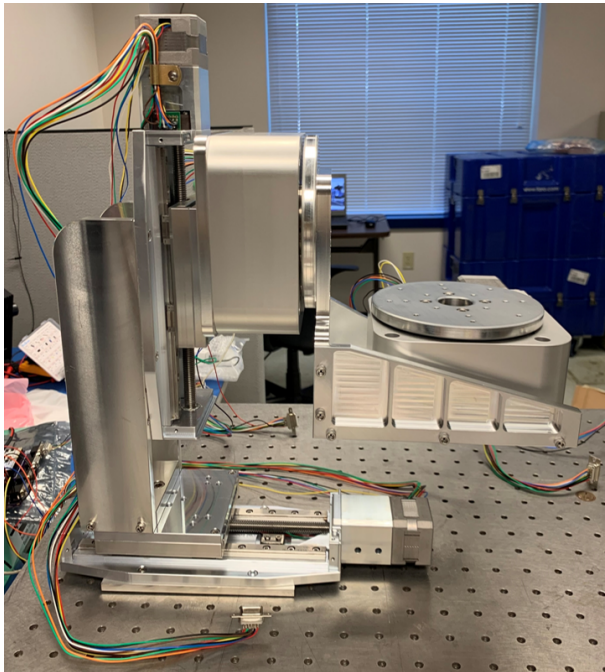


Figure 6.4: The ψ stage was mounted to the manipulator.

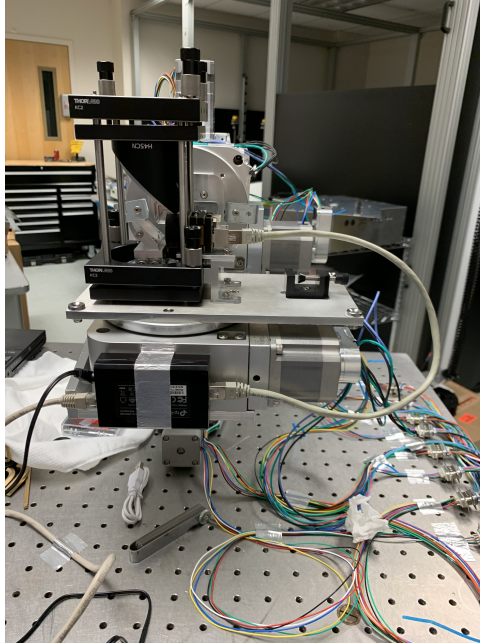


Figure 6.5: The optics datum was placed onto the ψ stage and the CCD PoE injector was mounted to the side.

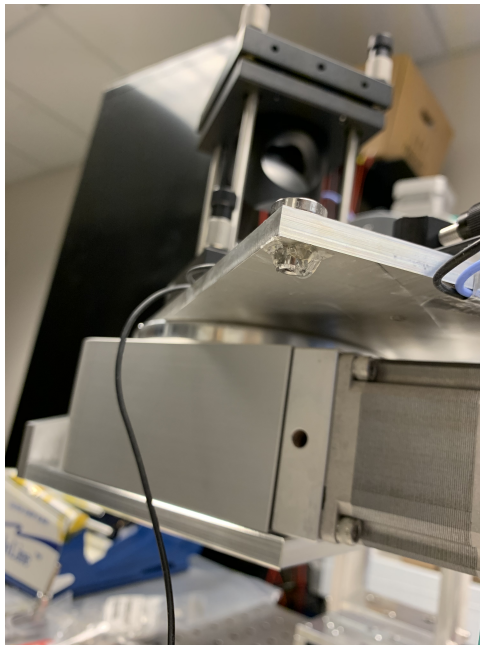


Figure 6.6: SMR targets were hotglued to the optics datum to secure them in place.

6.2 Electrical Integration

The electrical integration consisted of three parts - soldering the PCB, fabricating harnesses, and mounting the rotary stage limit switches. The soldered PCB, shown in Figure 6.7, consisted of the motor and signal connectors, the motor power supply terminal, header pins, and the differential signal receivers. Harnesses were fabricated using solder-style D-sub connectors and generic 24-gauge wire to extend the distance of the manipulator and electronics enclosure. The harnesses, shown in Figure 6.8, were strain-relieved to the GSE cart and connected to the PCB. Although the linear stages contained built-in vacuum-compatible limit switches, the rotary stages did not come with any. Temporary non-vacuum limit switches were mounted to the side of the rotary stages using hotglue and aluminum tape. An example of the limit switches defining end of travel for the θ stage is shown in Figure 6.9.

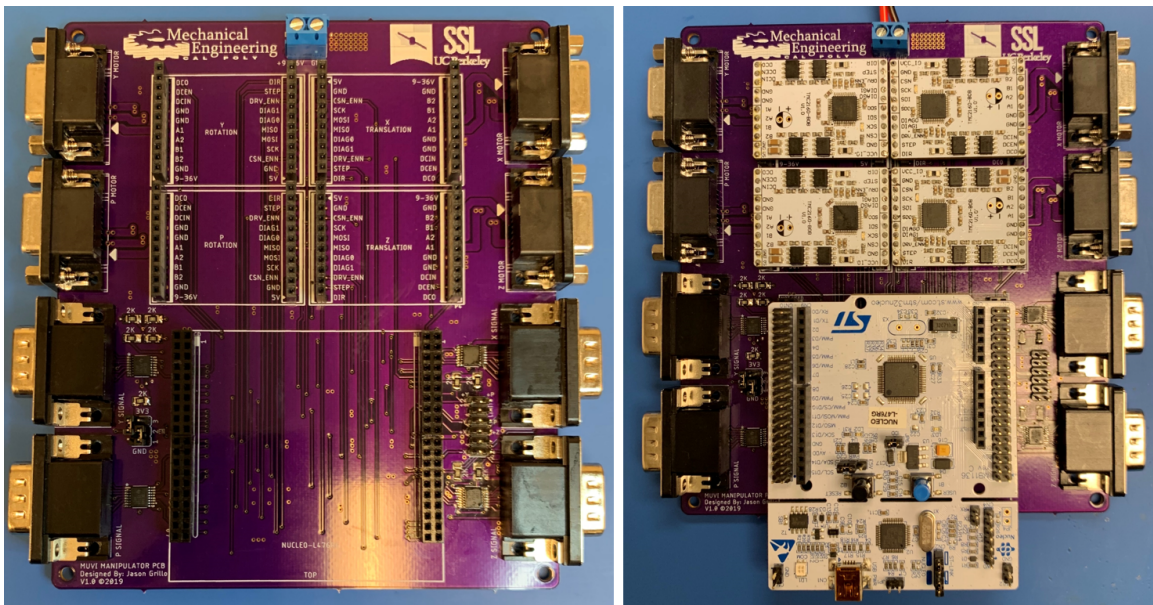


Figure 6.7: Image of the PCB with components soldered (left) and integrated with the microcontroller and stepper driver boards (right).

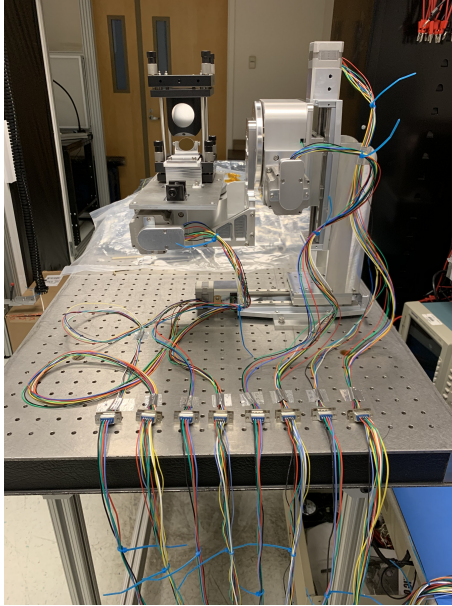


Figure 6.8: The motor power and feedback harnesses were strain relieved to the GSE cart.

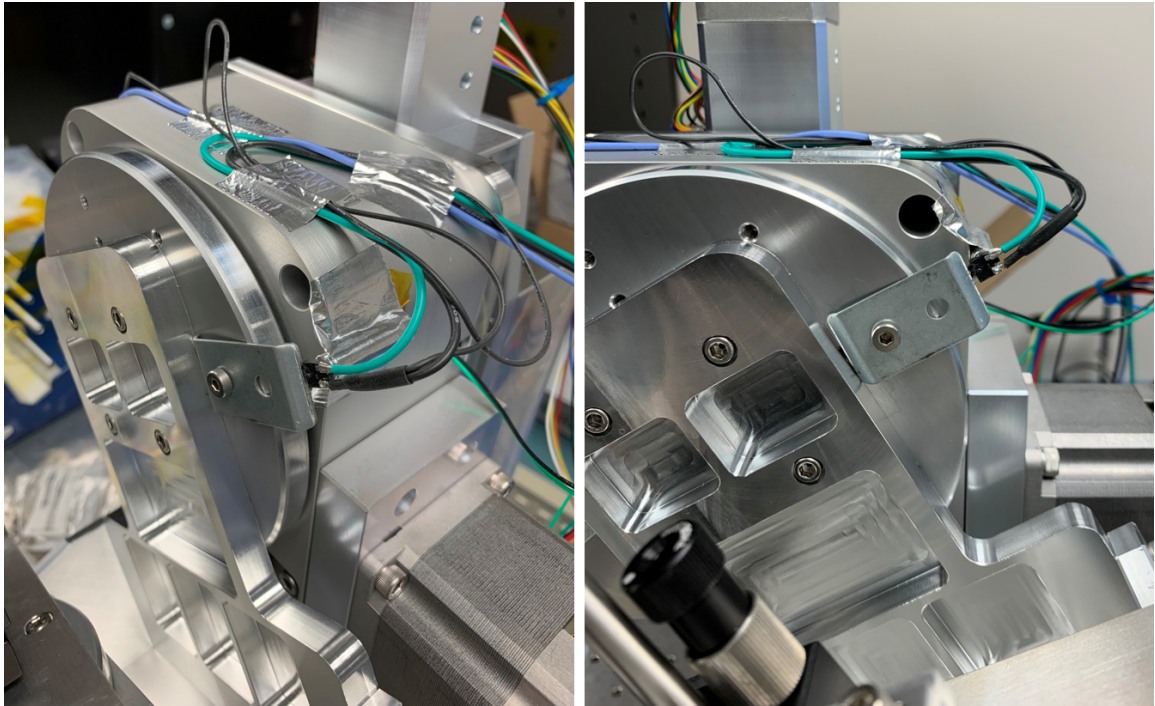


Figure 6.9: Limit switches for the θ stage were connected to the stationary side. A bracket connected to the rotational platform that contacted the limit switch at the end of travel.

6.3 Lessons Learned

During the course of the build and test of the manipulator, several lessons were learned and a few improvements were implemented. This section presents and describes a list of these changes.

Not Enough Timers

When the Nucleo and stepper drivers were tested on the breadboard, it was noticed that the microcontroller could not generate independent ramp profiles because the different channels all referenced the same timer frequency. Because the encoders also required timer peripherals, the Nucleo quickly became timer-limited. The solution to the problem was to assign all of the step pins to Timer 8 and only control one stage at a time. Although the Nucleo had enough pins for the application, a microcontroller with more timers would have been more suitable for the application.

Encoder and Limit Switch Crosstalk

Crosstalk between the limit switch and encoder traces on the PCB was evident when the HD-15 feedback harnesses were unplugged from the PCB. The issue was discovered when the X and Z limit switches were opened and closed consecutively, and voltage spikes were observed on the X and Z encoder lines. This resulted in false position increments whenever the limit switches changed state. Crosstalk was present because the encoder traces were floating, and were sensitive to the slight changes in magnetic field induced by the current flowing through the limit switch traces. Fortunately, crosstalk was not evident when the HD-15 connector was plugged into the PCB and the encoder traces were no longer floating.

SPI Data Latch

SPI communication between the microcontroller and TMC stepper drivers was not reliable because the chip select line was held low for multiple commands. On the TMC drivers, data latches after the chip select line is toggled high. Therefore, the chip select line was toggled after every individual command.

Stepper Driver Vcc

The TMC2160 may be supplied by either 5V or 3v3. As such, the logic reference voltage is set depending on the Vcc supply. It was found after the PCB was manufactured that the Nucleo's SPI bus operated at 3v3 logic, but the stepper drivers' Vcc trace was connected to the 5V pin on the board. Thus, the header pins between the 5V supply trace and stepper drivers were disconnected and a jumper wire was soldered to the 3v3 pin instead.

Limit Switches Prevent Programming and Startup

It was found that the Nucleo was unable to soft-reset when a limit switch was activated. Furthermore, the GUI was unable to establish a serial connection with the microcontroller during this condition. The solution was to disconnect the limit switch wires from the PCB if the stages are located at the end of their travel when a soft-reset is required.

Unresponsive Nucleo During Operation

If GUI commands were sent too quickly, or if general input timing was out of sync, the microcontroller would error into an unknown state. The only method that resolved the issue was to hard-reset the microcontroller by pressing the black reset button on the board.

Too Many Enabled Stages

The linear stages drew about 0.9 A of current when they idled, and upwards of 2.2 A during operation. If both linear stages were enabled while another stage was moving, the bench supply would reach its current limit and the supply voltage would rapidly drop. Ultimately, this was a benchtop power supply limitation and won't be an issue when using the box power supply. Only one linear stage should be enabled at a time if the benchtop supply is the power source.

Fried Nucleo

One of the Nucleo boards released white smoke when a limit switch wire momentarily contacted the +24V motor supply pin. The damage to the Nucleo may be seen in Figure 6.10. All loose wires were secured before applying power to the PCB after that incident.

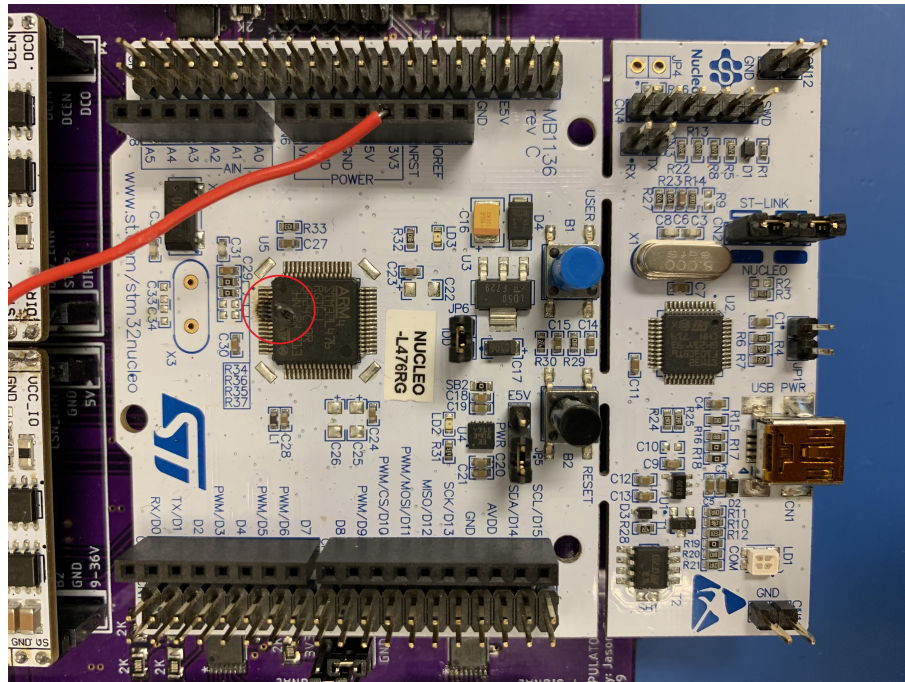


Figure 6.10: A burn mark was seen on the fried microcontroller after a limit switch wire accidentally contacted a motor power pin.

Noise on the SPI Chip Select Line

When troubleshooting the SPI communication, noise spikes on the chip select line interfered with the command interpretation on the stepper drivers. An example of the spike is shown in Figure 6.11. Using a logic analyzer, these spikes were measured and ceramic capacitors were installed between the chip select line and GND to stabilize the CSN line.

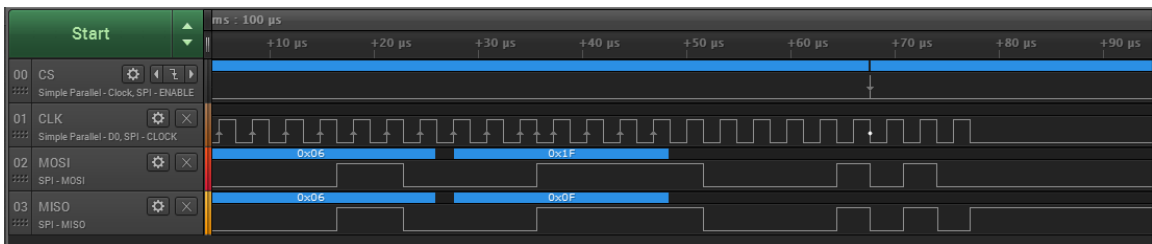


Figure 6.11: A noise spike was observed on the SPI chip select line during data transfer. Capacitors were added to the CSN lines after this anomaly was detected.

Chapter 7

PERFORMANCE EVALUATION METHODOLOGY

This chapter discusses the methodology to evaluate the performance of the manipulator. First, the strategy to align the optical components is discussed. Next, the approach to evaluate the positioning repeatability of the manipulator stages is explained. Finally, the order of the tests is described.

7.1 Strategy

The strategy to evaluate the manipulator's performance is comprised of two parts. The first part is ensuring that the optical components themselves are aligned within tolerance. After the optics are aligned, the positioning repeatability of the manipulator may be characterized. The characterization itself is composed of encoder feedback and image analysis.

7.1.1 Optical Alignment

A large portion of the manipulator characterization depends on the positioning and alignment of the optics. The first step in the alignment process is to establish boresight with the laser. First, the manipulator is roughly oriented close to 0° pitch and 0° yaw, and the translation stages are adjusted such that the laser reflects off the back plane mirror that defines the perpendicularity of the GSE plate. Next, the θ and ψ stages are finely adjusted until the reflection is collinear with the incident beam. Once perpendicularity is established with respect to the light source, the current angles of

the θ and ψ stages are marked as the new datum. The final result of this process is illustrated in the top view of Figure 7.1.

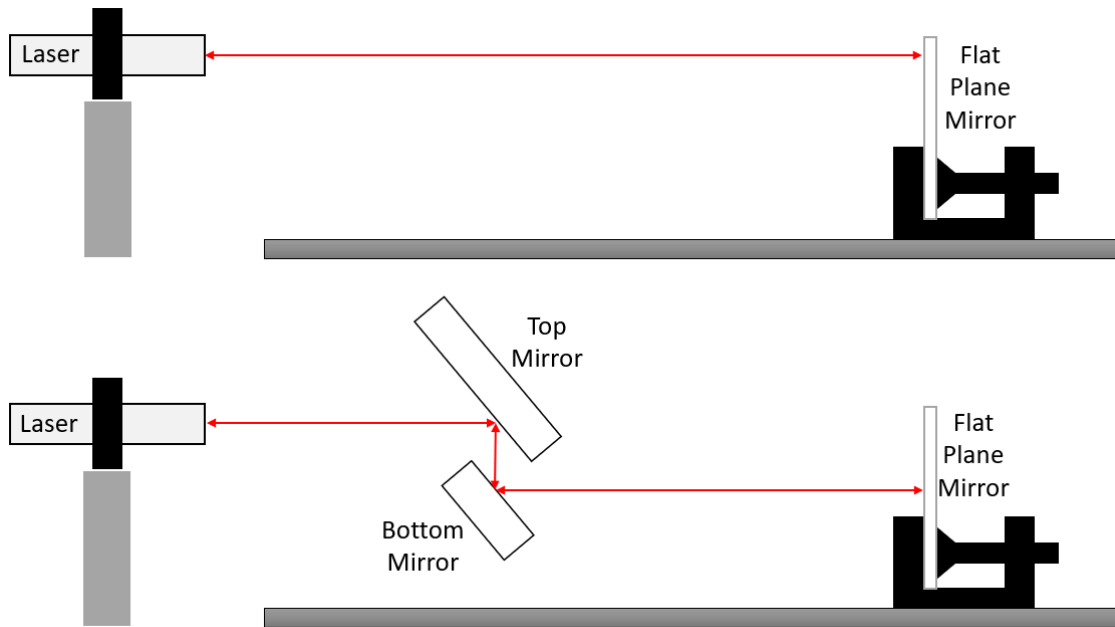


Figure 7.1: Illustration of the optical alignment strategy. Perpendicularity of the GSE with respect to the laser beam will be established first (top) and then the periscope will be tuned (bottom).

After perpendicularity is established, the X and Z stages are adjusted such that light is shined through the periscope. The remaining alignment procedure utilizes metrology equipment to measure the orientation of the mirrors. This equipment, presented in Figure 7.2, consists of a FARO laser tracker that emits a laser beam that is reflected back from a Spherically Mounted Retroreflector (SMR), allowing the system's computer to draw and record the 3D measurements within 20 microns.

First, the working coordinate system for the optical GSE is established by picking up the SMR target points on the GSE plate. Next, the orientation of the top mirror is measured by the laser tracker with respect to the defined working coordinate system, and iterated until its orientation is tilted by 45° and perpendicular to the other coordinate axes. After the top mirror is defined by metrology, the tip/tilt mount of

the bottom mirror is adjusted until the reflection of the laser is collinear with the incident beam.



Figure 7.2: FARO laser tracker (left) and its corresponding SMR targets (right).

7.1.2 Position Repeatability

Manipulator performance will be characterized by utilizing the feedback of the stages' encoders in combination with the images captured during the calibration test. The manipulator will orient itself to the cardinal points shown in Figure 7.3, the encoder position will be recorded, and an image of the laser spot will be captured. Optical misalignment may be determined by analyzing the centroidal position of the laser spot in the image and quantified by translation drift. The repeatability of the manipulator position will be characterized by homing the manipulator to boresight in between each cardinal point capture.

It is important to distinguish the difference between two types of FOV sweeps. A rectangular FOV sweep, which is the simplest type and shown in Figure 7.3, consists of a rectangular grid and treats the pitch and yaw axes independently. On the contrary,

the circular FOV, which is shown in Figure 7.4, contains dependent pitch and yaw axes. For example, to point the instrument North West on a 7° field angle ($3\pi/4$ on the unit circle), the required yaw and pitch angles would be $-7^\circ \times \sqrt{2}/2$ and $7^\circ \times \sqrt{2}/2$, respectively.

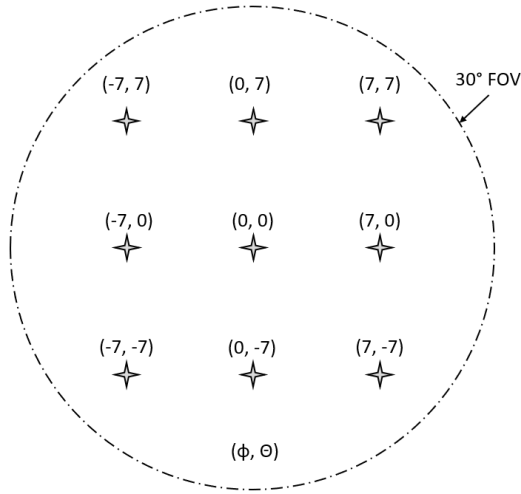


Figure 7.3: Rectangular 7° FOV sweep comprised of 9 cardinal points to characterize the manipulator's repeatability.

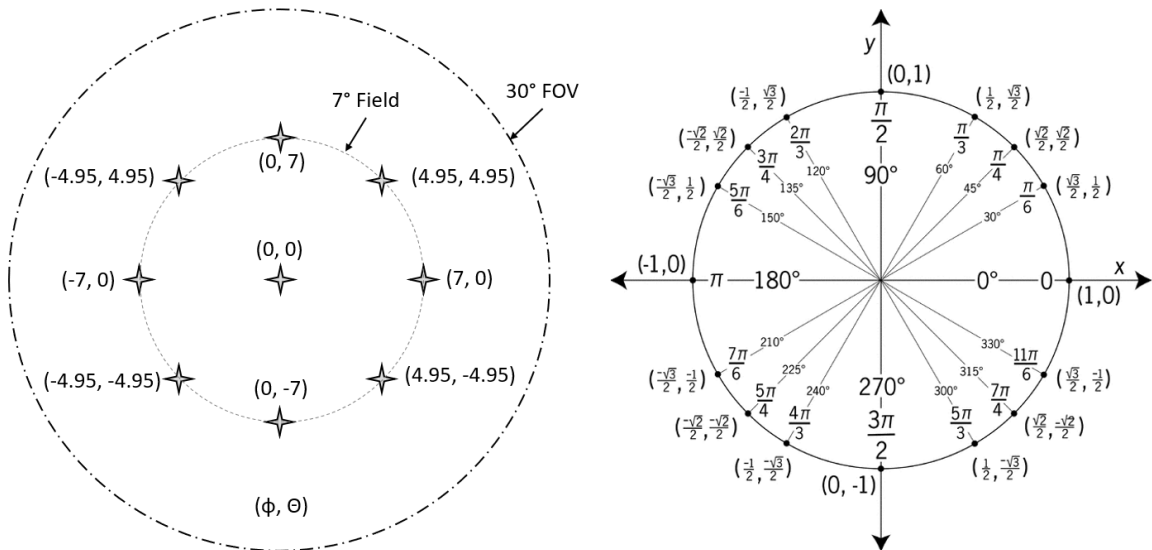


Figure 7.4: Circular 7° FOV sweep to fit all 9 cardinal points onto the field angle border. The unit circle, shown on the right, shows the necessary angle multiplication factors for a given point on the field angle.

7.2 Test Schedule

After the GSE optics are aligned, a boresight image will be taken to establish the initial reference image. All future boresight images will be compared to this reference as a repeatability assessment. Afterwards, two FOV sweeps will be conducted; the first one with 5 cardinal points at 15° and the second one with 9 cardinal points at 7° . After comparing the analytical and experimental data, a final FOV sweep with 9 cardinal points at 7° will be conducted in an attempt to remove systematic errors. A stray light rejection test will not be completed using the optical GSE because it is an instrument-level performance test and therefore independent to the manipulator's characterization.

Chapter 8

ANALYTICAL RESULTS

Understanding the manipulator's performance from an analytical perspective was achieved in three steps before collecting test data. First, a simulation of the methodology behind mechanical backlash mitigation was conducted. Second, a ramp profile algorithm was created that gradually brings the stage actuators up to full speed. This was necessary to prevent the motor's electrical field angle from surpassing the mechanical load angle due to the system's inertia. And third, a 3D optical model was generated to calculate and illustrate the required translation compensation for the characterization. The following sections of this chapter describe these methods in more detail.

8.1 Backlash Mitigation

Backlash is the mechanical tolerance in a driving mechanism that results in dead play upon reversing motions. Although necessary to prevent sticking, backlash is undesirable for high performance positioning applications where accurate positioning is limited to the tolerance of the mating drives. However, accurate positioning may still be achieved despite backlash as long as the actuator approaches the final position from its calibrated side. Using the linear stages as an example, if the X stage is zeroed from its left side (negative coordinate), then all future positioning should approach the desired coordinate from the right side. An illustration of an arbitrary stage moving to a target in the positive direction is found in Figure 8.1, and a similar illustration of the stage moving to a target in the negative direction is found in Figure 8.2. In

each of these diagrams, because the stage zeroed itself using the left (negative) hard stop, the stage approaches the setpoint from the right.

A conservative estimate for the backlash in each stage should be used to ensure all of the backlash is accounted for. If the positioning overshoot is insufficient to overcome the backlash, then the stepper motor will rotate the driving gear without actually moving the stage. According to Berg (1965), typical backlash in worm-gear systems is anywhere between 5-30 min of arc [3]. Therefore, assuming the worst case of 30 arcmin of backlash, it is required to overshoot the stepper motors by 0.5° . This corresponds to an equivalent stage displacement of 0.0022 mm for the linear stages and 0.0069° for the rotary stages.

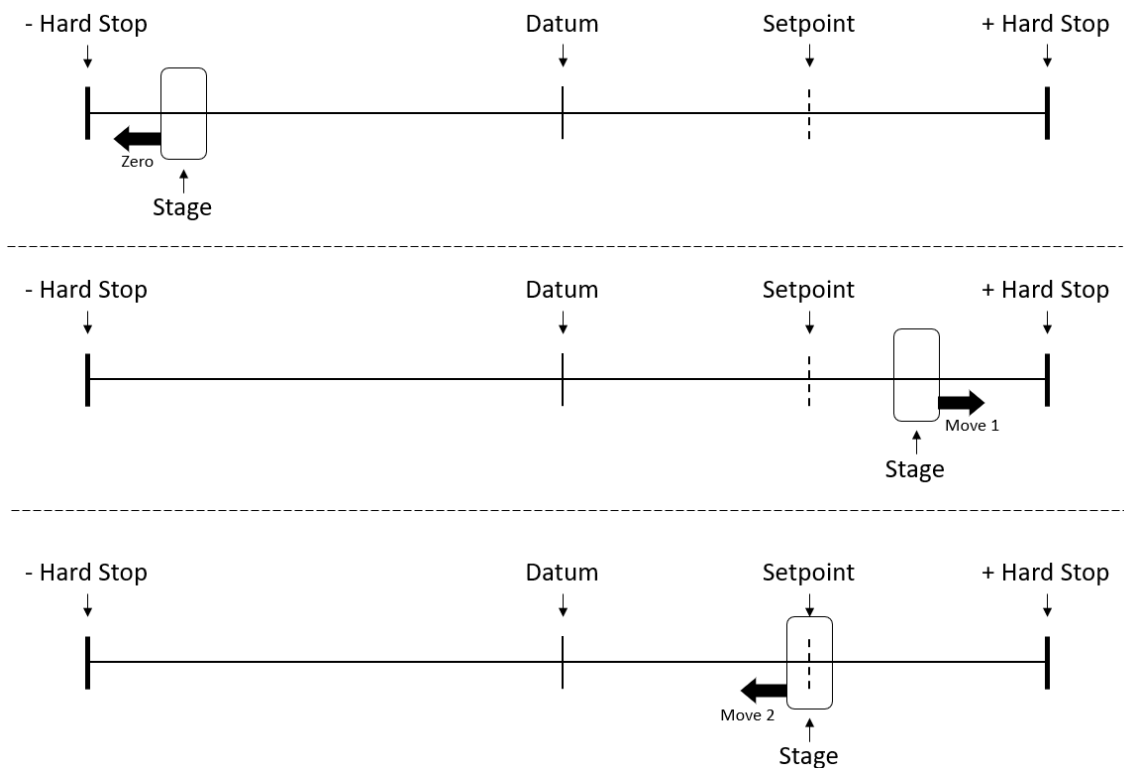


Figure 8.1: Diagram of the zeroing approach and the stage moving to a position that is in the positive coordinate direction.

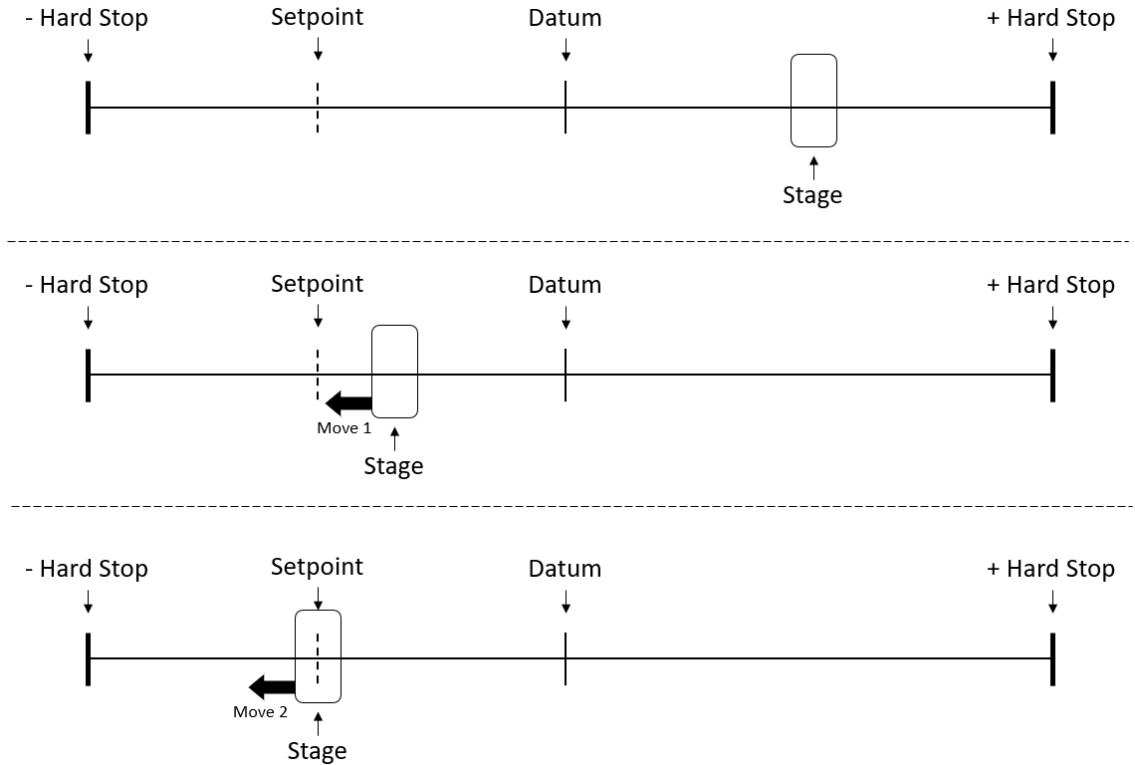


Figure 8.2: Diagram of the stage moving to a position that is in the negative coordinate direction.

8.2 Ramp Profile Algorithm

A ramp motion control profile was implemented to accelerate and decelerate the stepper motors. Although other intricate profiles are higher performing, like the S-shaped profile, their value added compared to their complexity was not high enough to make the trade. If such profiles are required for future applications, they may be implemented by modifying the stepper motor software script in the manipulator RTOS package. A ramp profile, otherwise known as a trapezoidal velocity profile, works in the following manner. In the first segment of motion, the motor speed is incremented at a constant rate until one of two things happen: either the maximum allowed speed is reached or the acceleration segment ends. In the second segment, the

motor speed remains constant until it reaches the point of deceleration. During the final segment, the motor speed is decremented until the motor reaches the end of the profile, or until the motor speed is equal to its initial speed and remains there until the profile ends. Illustrations of the ramp profile and various operational scenarios that Jose Quinones describes in his application guide are shown in Figure 8.3 [20]. Scenario 4 is the ideal operating case, where the stepper motor stops as soon as the stopping speed is reached at its destination.

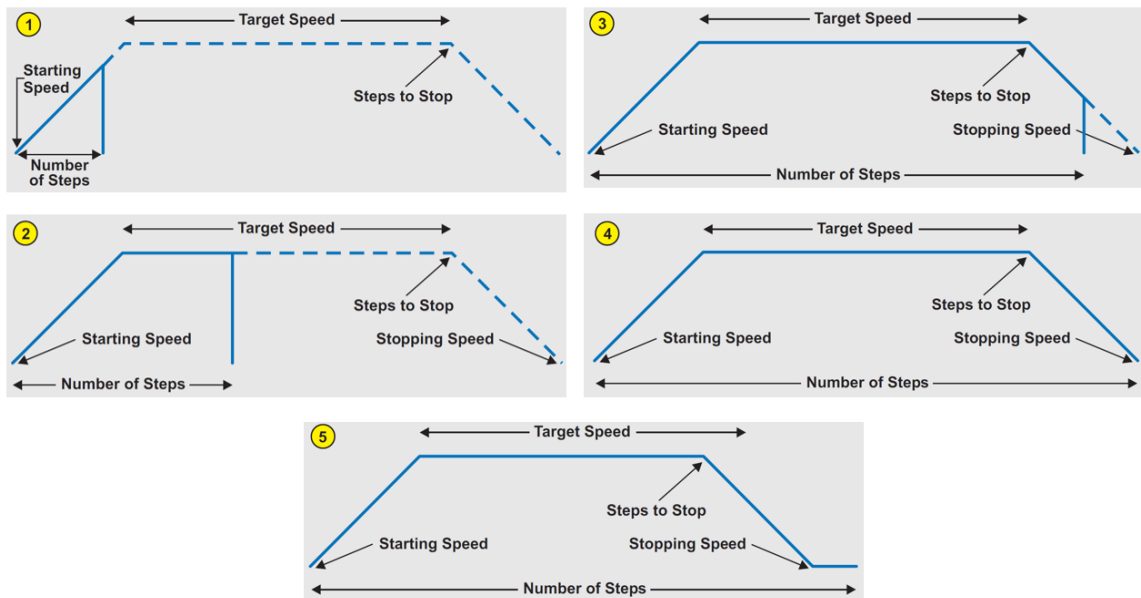


Figure 8.3: Five acceleration and deceleration scenarios in the ramp profile algorithm [20].

The ramp profile algorithm was implemented by utilizing two timers on the microcontroller. The first timer controlled the step generator frequency and the second timer was used to accelerate the step generator frequency at a fixed rate. A maximum frequency limit was defined to prevent motor speeds faster than the maximum allowable stage speed that was specified by the manufacturer. The acceleration and deceleration phases consisted of 20% of the total number of steps in the profile, as recommended by Quinones [20]. The number of steps defining these acceleration phases

were calculated by

$$accel\ steps = smallest\ of \begin{cases} steps * 0.20 \\ \frac{max\ speed * init\ speed}{accel\ rate} \end{cases} \quad (8.1)$$

where steps is the total number of steps to move the stepper motor, max speed is the maximum frequency limit of the step generator in Hz, init speed is the initial speed of the step generator in Hz, and accel rate is the acceleration rate of the step generator in Hz/s.

The algorithm was verified by plotting the theoretical step generator results and superimposing the encoder data for various stage movements. The stages' velocity was estimated by calculating the difference in the current and previous positions divided by the difference in time. As seen in Figure 8.4, the velocity data of the X stage closely matches the shape of the step generator frequency. Figure 8.5 shows a plot of the X stage position during the motion. The delay of data points towards the end of the position curve was a result of the backlash mitigation approach discussed in Section 8.1. Velocity and position curves for the Z stage are shown in Figure 8.6 and Figure 8.7, respectively. Two distinct populations of velocity data are prevalent at steady state velocity for the linear stages. Acoustic noise was observed from these stages when they operated, implying that aliasing of the sampling frequency could be the source of the distinct trends. Velocity and position curves for the ψ stage are shown in Figure 8.8 and Figure 8.9, respectively. Finally, velocity and position curves for the θ stage are shown in Figure 8.10 and Figure 8.11, respectively. Close agreement between the real-time data and theoretical data validated the ramp profile algorithm for its implementation.

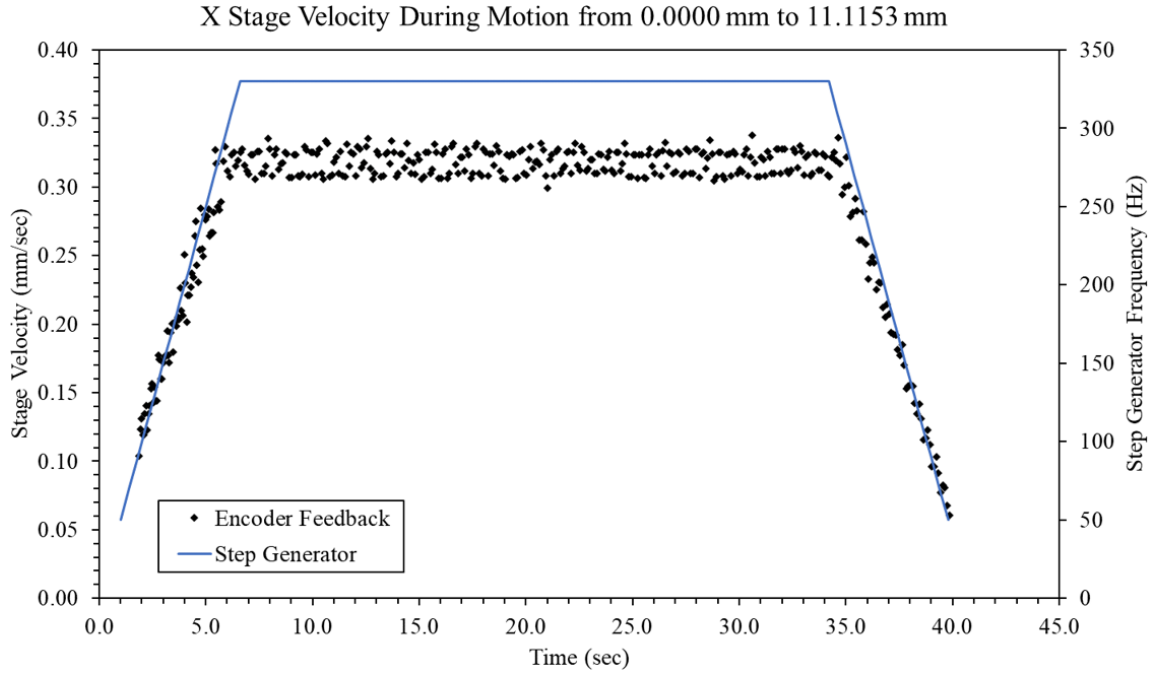


Figure 8.4: Ramp profile test featuring the velocity response of the X stage moving from 0.0000 mm to 11.1153 mm.

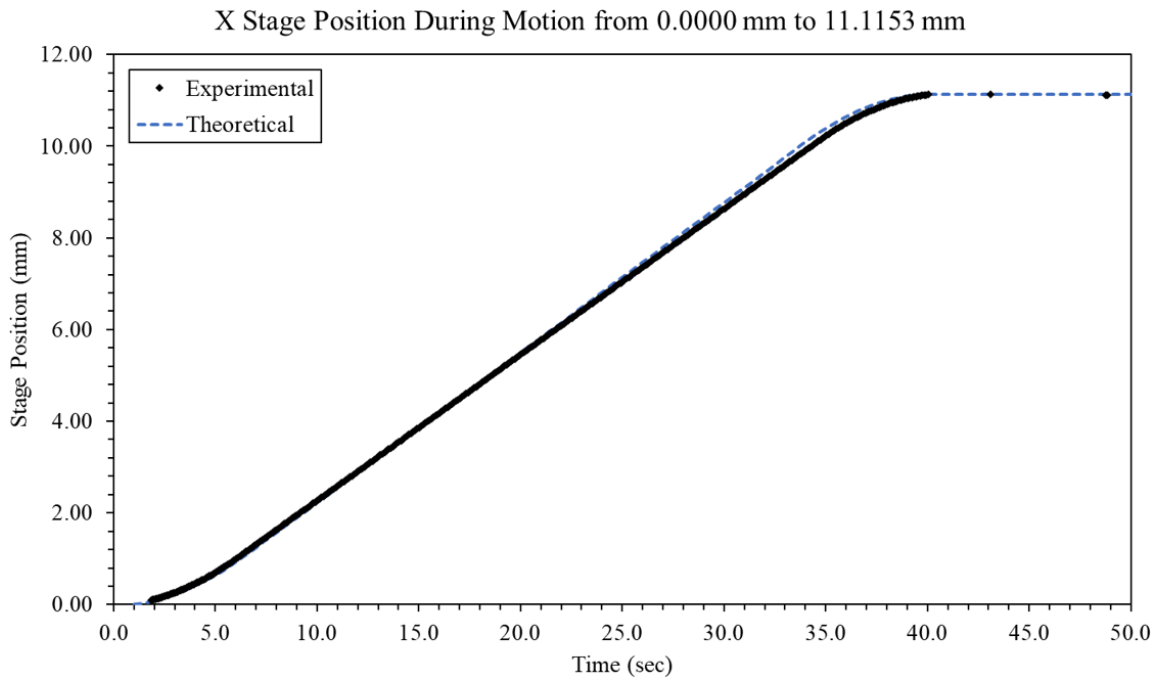


Figure 8.5: Ramp profile test featuring the position response of the X stage moving from 0.0000 mm to 11.1153 mm.

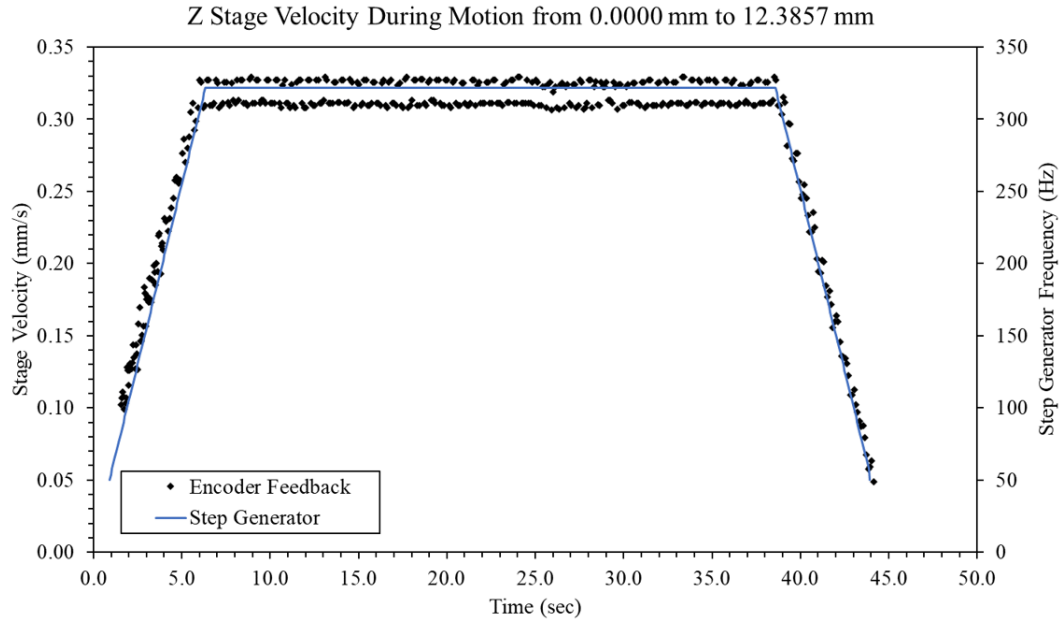


Figure 8.6: Ramp profile test featuring the velocity response of the Z stage moving from 0.0000 mm to 12.3857 mm. Aliasing could be the source of the two distinct steady state velocities.

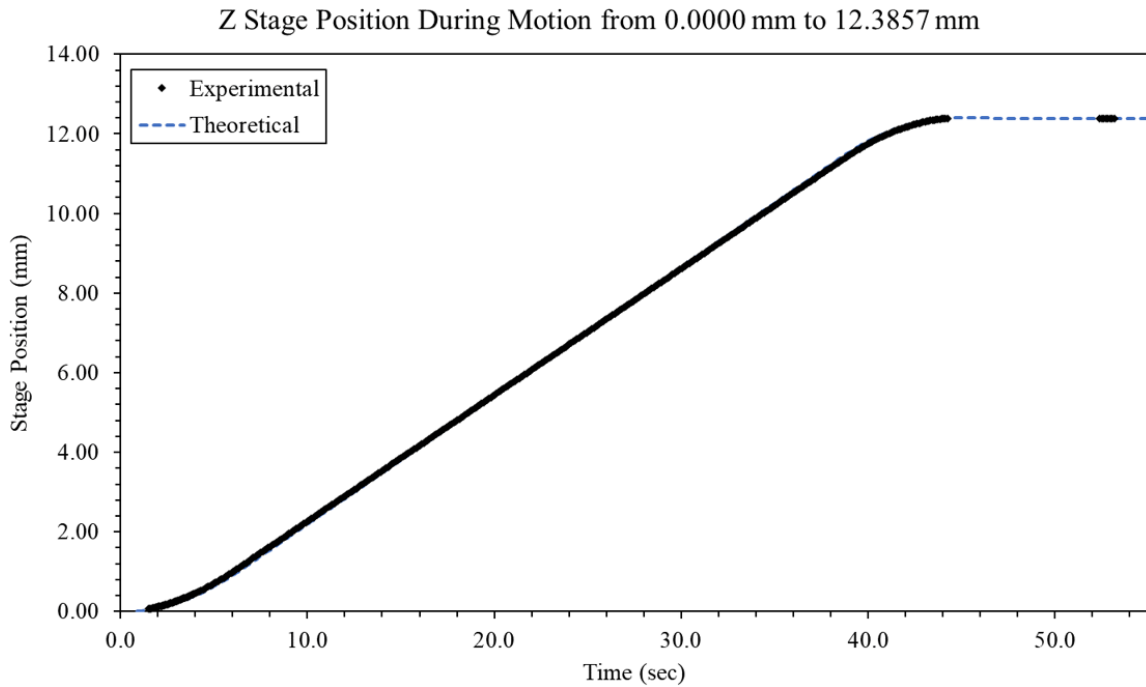


Figure 8.7: Ramp profile test featuring the position response of the Z stage moving from 0.0000 mm to 12.3857 mm.

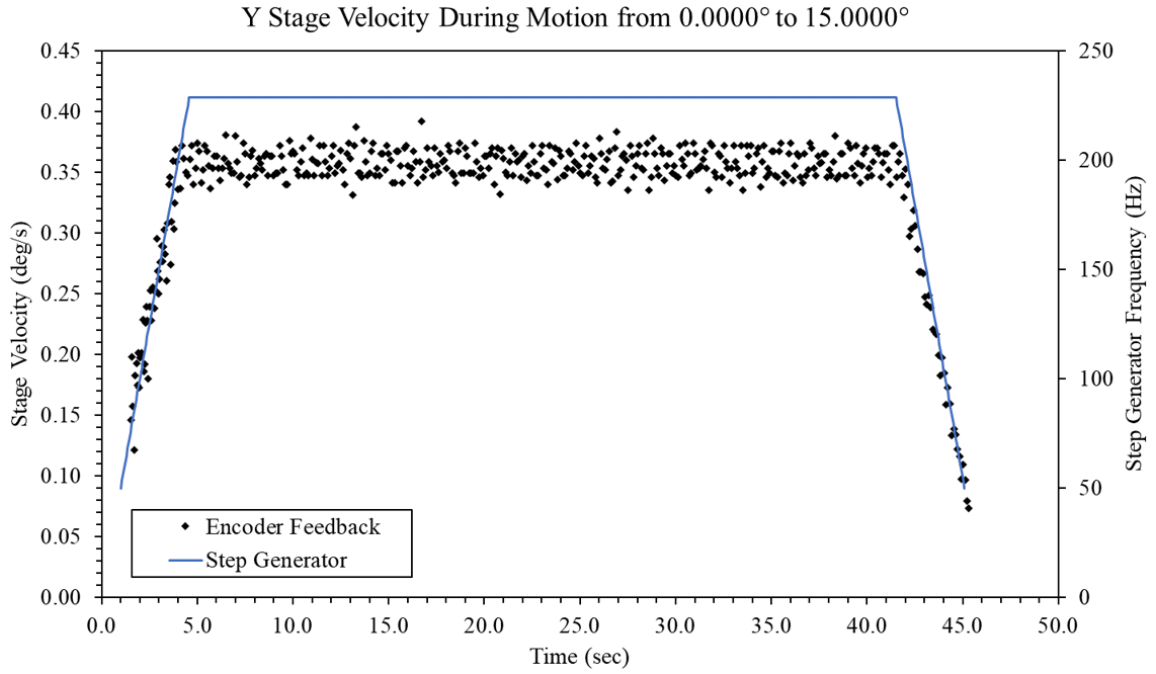


Figure 8.8: Ramp profile test featuring the velocity response of the ψ stage moving from 0.0000° to 15.0000°.

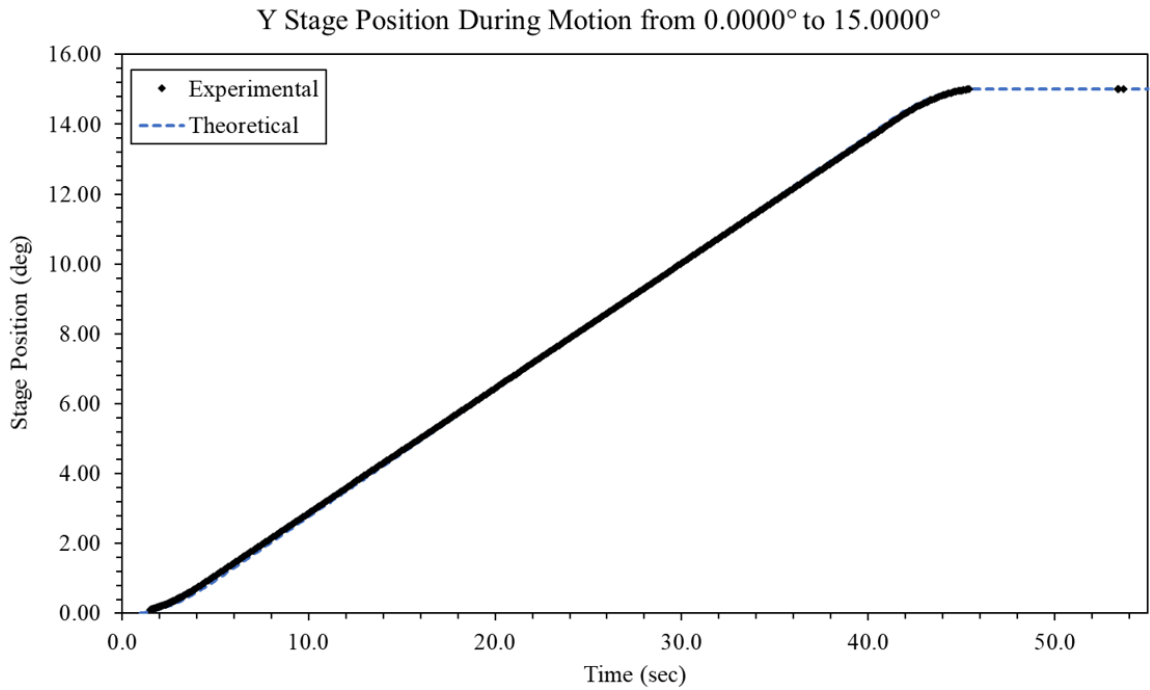


Figure 8.9: Ramp profile test featuring the position response of the ψ stage moving from 0.0000° to 15.0000°.

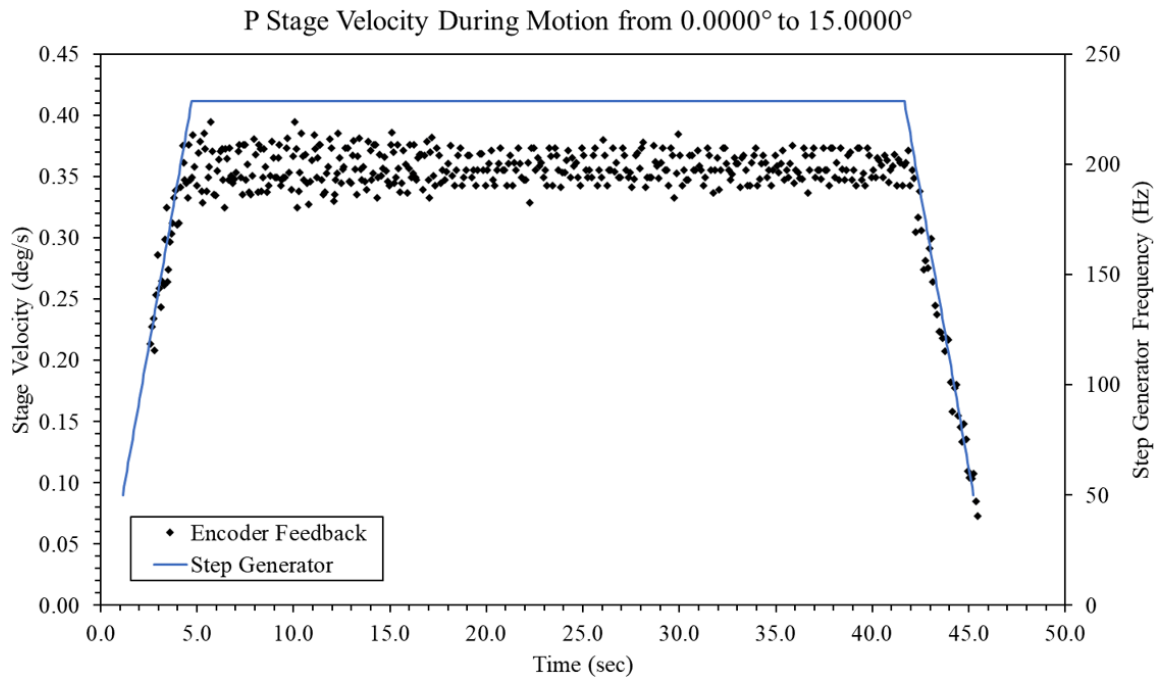


Figure 8.10: Ramp profile test featuring the velocity response of the θ stage moving from 0.0000° to 15.0000°.

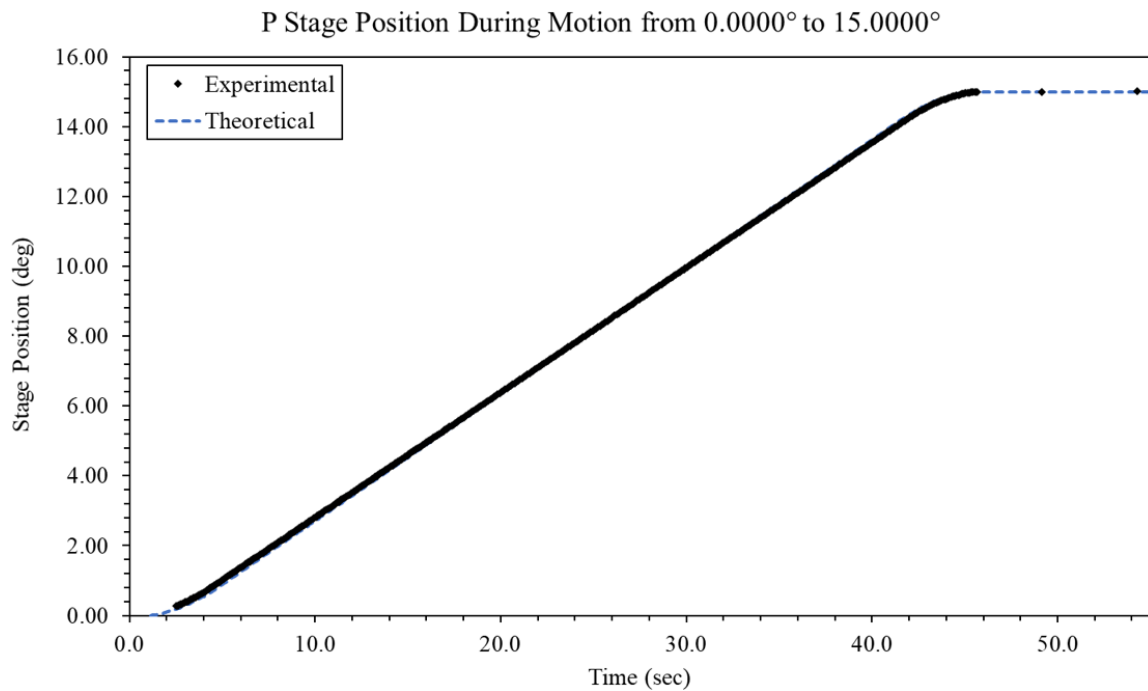


Figure 8.11: Ramp profile test featuring the position response of the θ stage moving from 0.0000° to 15.0000°.

8.3 Translation Compensation

A Matlab script was written to calculate and simulate the translation compensation for both pitch and yaw movements. To do this accurately, knowledge of the spacial location and orientation of the top and bottom mirrors was required. Because three points define a plane, a total of six vectors were necessary to define the position of the two mirrors with respect to the iris center (the origin). The mirror vectors and laser beamline vectors were defined using the CAD model of the optical GSE assembly and they are presented in Table 8.1. The points used to define the mirror vectors and the coordinate frame are labeled in Figure 8.12.

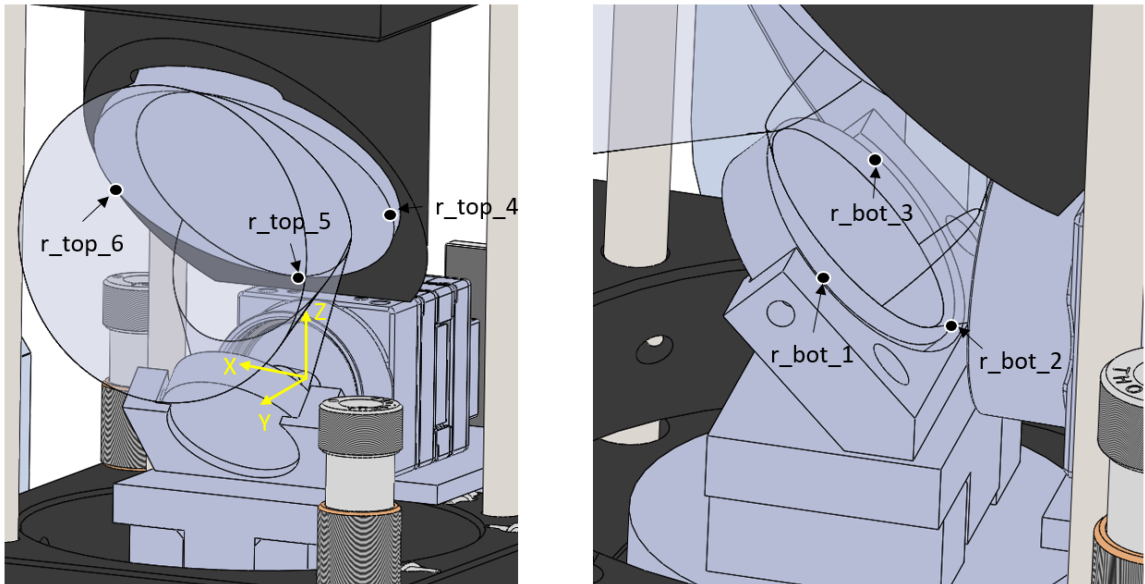


Figure 8.12: Labels of the points used to define the mirror vectors with respect to the iris center.

Table 8.1: Vectors defining the 3D location and orientation of the top and bottom mirrors with respect to the iris center.

Vector	X (mm)	Y (mm)	Z (mm)
r_bot_1	-12.700	20.882	2.312
r_bot_2	0.000	11.901	-6.669
r_bot_3	12.700	20.882	2.312
r_top_4	-25.400	23.324	37.204
r_top_5	0.000	5.364	19.244
r_top_6	25.400	23.324	37.204
beam1	0.000	80.000	32.450
beam2	0.000	18.570	32.450

Quaternions were used to handle the 3D rotation and translation of the vectors [13]. The quaternions were defined by a scalar and vector component. For the rotation of an arbitrary vector $\vec{u} = [a, b, c]$ about a unit vector $\vec{v} = [d, e, f]$ by an angle θ ,

$$u = (0, \vec{u}) \quad (8.2)$$

$$q = (\cos \theta/2, d \sin \theta/2, e \sin \theta/2, f \sin \theta/2) \quad (8.3)$$

$$q^* = (\cos \theta/2, -d \sin \theta/2, -e \sin \theta/2, -f \sin \theta/2) \quad (8.4)$$

$$u' = quq^* \quad (8.5)$$

where u is the quaternion representation of \vec{u} , q is the unit length rotation quaternion, q^* is the conjugate of q , and u' is the rotated quaternion. By using quaternion multiplication, the mirror vectors were rotated about the iris center. Next, the transmission of the laser beam through the periscope was calculated by determining the intersection points and reflection vectors from the two mirrors. The reflection of a

beam vector \vec{v} from a mirror plane is defined as

$$\vec{v}' = \vec{v} - 2(\vec{v} \cdot \hat{n})\hat{n} \quad (8.6)$$

where \hat{n} is the unit normal vector of mirror plane. Similarly, the reflection calculation may be performed using quaternions by

$$v' = nvn \quad (8.7)$$

where v' is the reflected ray quaternion, n is the mirror's unit normal quaternion, and v is the incident ray quaternion. Once the reflected ray vector is obtained from the top mirror, the intersection point of the reflected ray on the bottom mirror may be determined. To find the intersection point of a line defined by $P_0 = (x_0, y_0, z_0)$ and $P_1 = (x_1, y_1, z_1)$ on the plane $ax + by + cz = d$, where $P_2 = (x_2, y_2, z_2)$ is a point on the plane, the following two equations may be solved

$$t = \frac{ax_0 - ax_2 + by_0 - by_2 + cz_0 - cz_2}{ax_0 - ax_1 + by_0 - by_1 + cz_0 - cz_1} \quad (8.8)$$

$$P_{int} = (x_0 + t(x_1 - x_0), y_0 + t(y_1 - y_0), z_0 + t(z_1 - z_0)) \quad (8.9)$$

where t is the intersection constant and P_{int} is the point of intersection. It is important to distinguish that the equation for a plane is defined by its normal vector $n = (a, b, c)$ and a point on the plane. Equations 8.2 through 8.9 were implemented in the algorithm to calculate the translation compensation.

Multiple simulations were performed to understand the translation requirements of the manipulator. The first simulation was of the optics rotated in pitch by 15° and the results are shown in Figure 8.13. An upward compensation of 12.3056 mm was calculated for this motion. Next, a simulation of the optics rotated in pitch by -15°

was conducted, which is found in Figure 8.14, and required a downward compensation of 10.0942 mm. Afterwards, simulations of the manipulator rotated in yaw by both 15° and -15° was performed, which required a horizontal compensation of 11.1999 mm and -11.1999 mm, respectively. The results of the yaw simulations are found in Figure 8.15 and Figure 8.16. Finally, a simulation of the optical GSE rotating North West on a 15° circular field angle is pictured in Figure 8.17. This last simulation was performed to verify that the two rotation axes are independent of their translation counterparts, which was indeed the case. Therefore, the X stage compensates for the ψ stage and the Z stage compensates for the θ stage without any coupling. During operation, field angles may be reached by calculating the required pitch and yaw compensation separately and treating them as components.

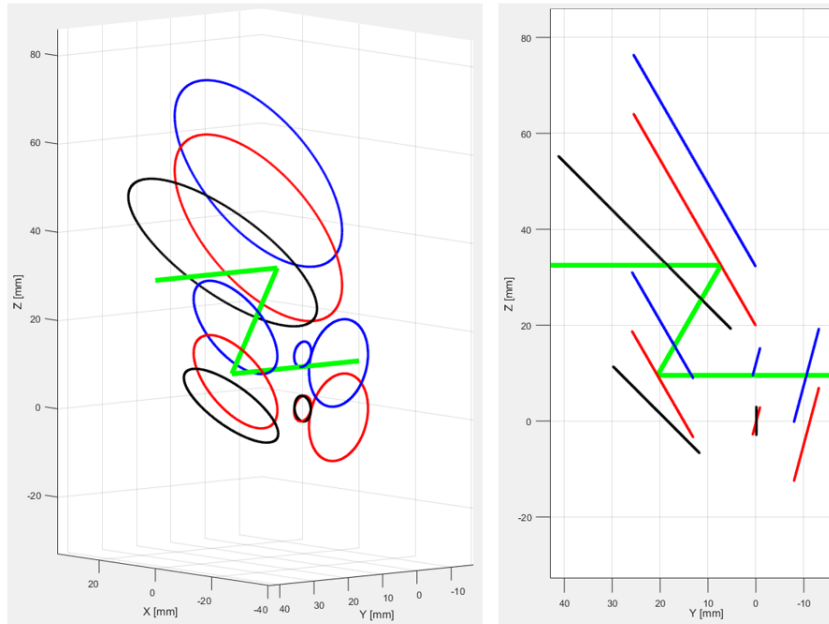


Figure 8.13: Optical simulation of the manipulator rotated in pitch by 15° . A positive vertical compensation of 12.3056 mm was calculated. Black represents the initial position of the optics at boresight, Red represents the optics after rotation, and Blue represents the optics after rotation and translation.

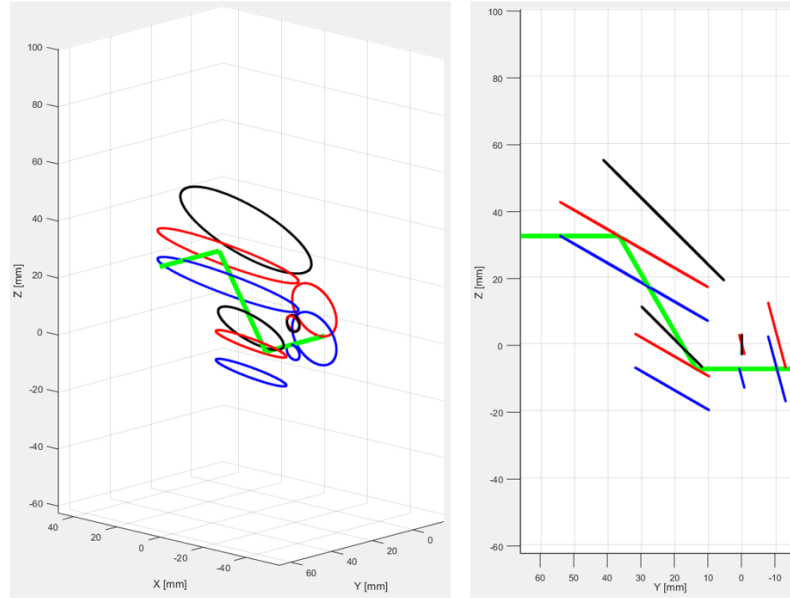


Figure 8.14: Optical simulation of the manipulator rotated in pitch by -15° . A negative vertical compensation of 10.0942 mm was calculated. Black represents the initial position of the optics at boresight, Red represents the optics after rotation, and Blue represents the optics after rotation and translation.

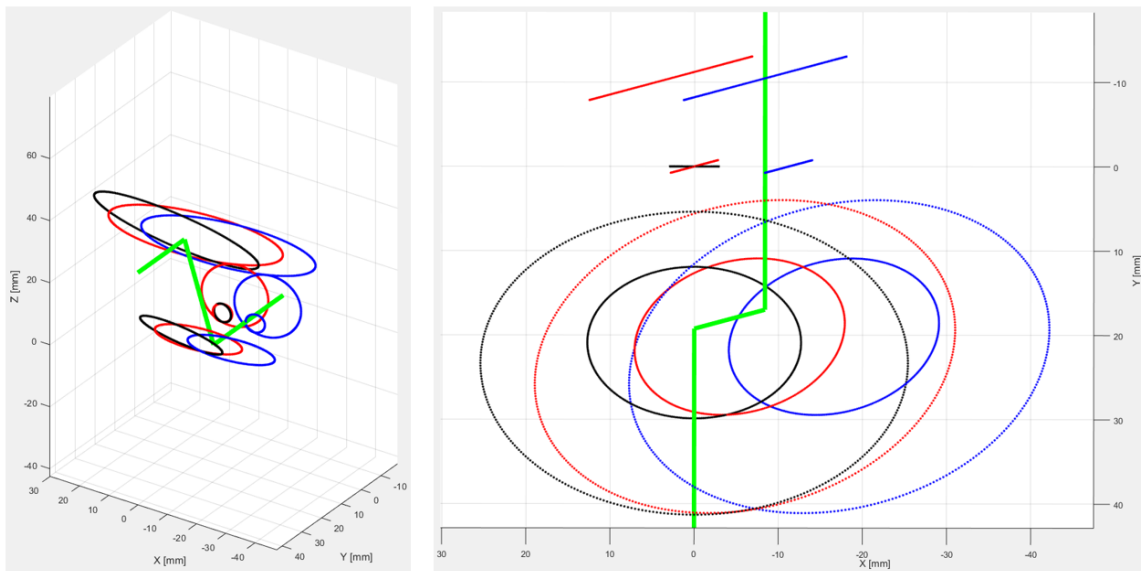


Figure 8.15: Optical simulation of the manipulator rotated in yaw by 15° . A positive horizontal compensation of 11.1999 mm was calculated. Black represents the initial position of the optics at boresight, Red represents the optics after rotation, and Blue represents the optics after rotation and translation.

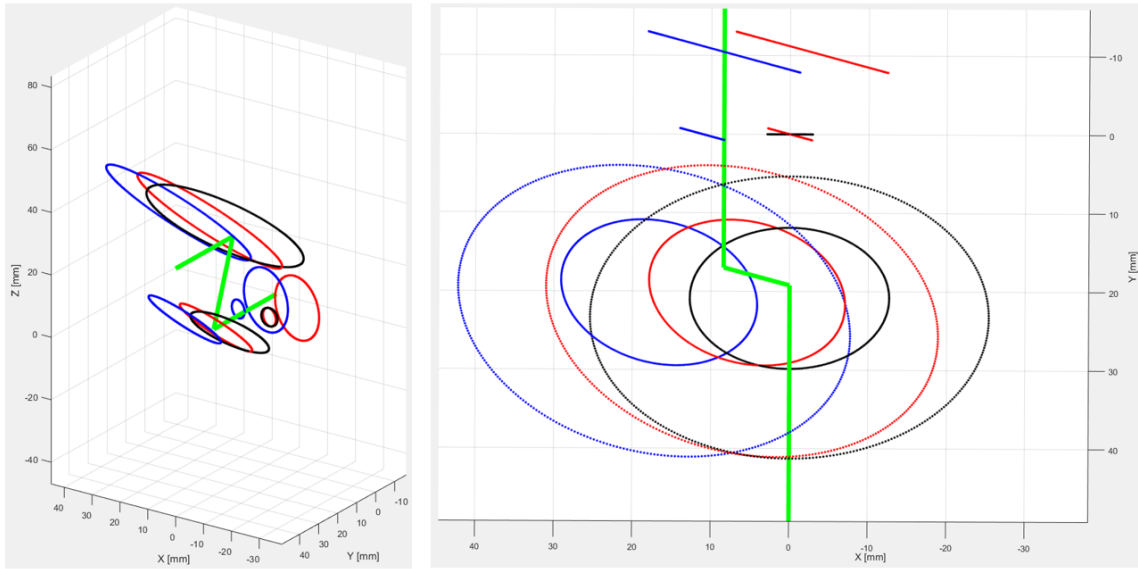


Figure 8.16: Optical simulation of the manipulator rotated in yaw by -15° . A negative vertical compensation of 12.3056 mm was calculated. Black represents the initial position of the optics at boresight, Red represents the optics after rotation, and Blue represents the optics after rotation and translation.

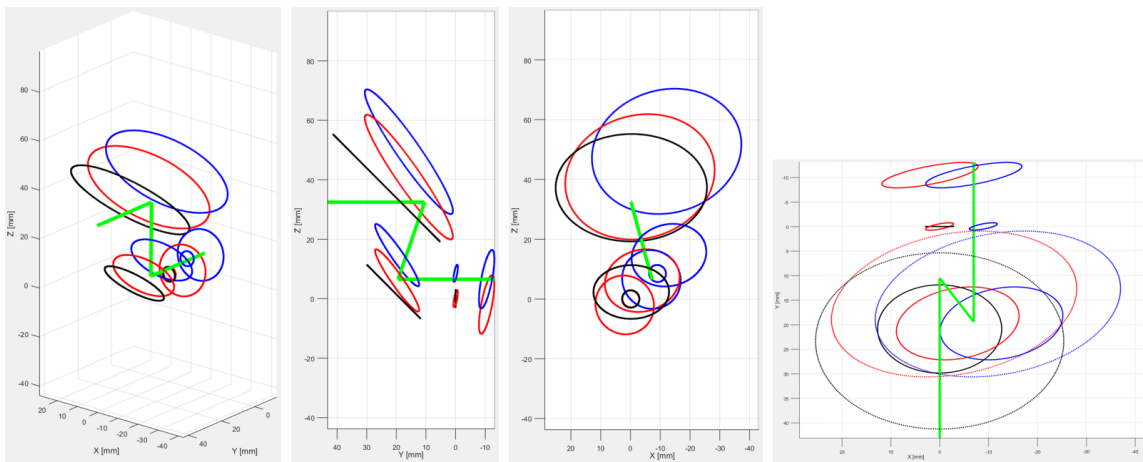


Figure 8.17: Matlab simulation of the optical GSE rotating about the iris 10.606° in both pitch and yaw. Black represents the initial position of the optics at boresight, Red represents the optics after rotation, and Blue represents the optics after rotation and translation.

Chapter 9

EXPERIMENTAL RESULTS

This chapter presents and discusses the experimental results of the manipulator characterization. The first section discusses the optical alignment, which was performed using precision gauge blocks. The mirror quaternions were then determined by measuring the location and orientation of the optical components with the FARO laser tracker. The next section presents the repeatability of the instrument moving to its boresight position after returning from various orientations. The last section then presents the images and corresponding analysis of the FOV sweep tests. Ultimately, the performance of the manipulator was evaluated based on the location of the laser centroid in the test images within a few microns. Reference Figure 9.1 for the experimental test setup.

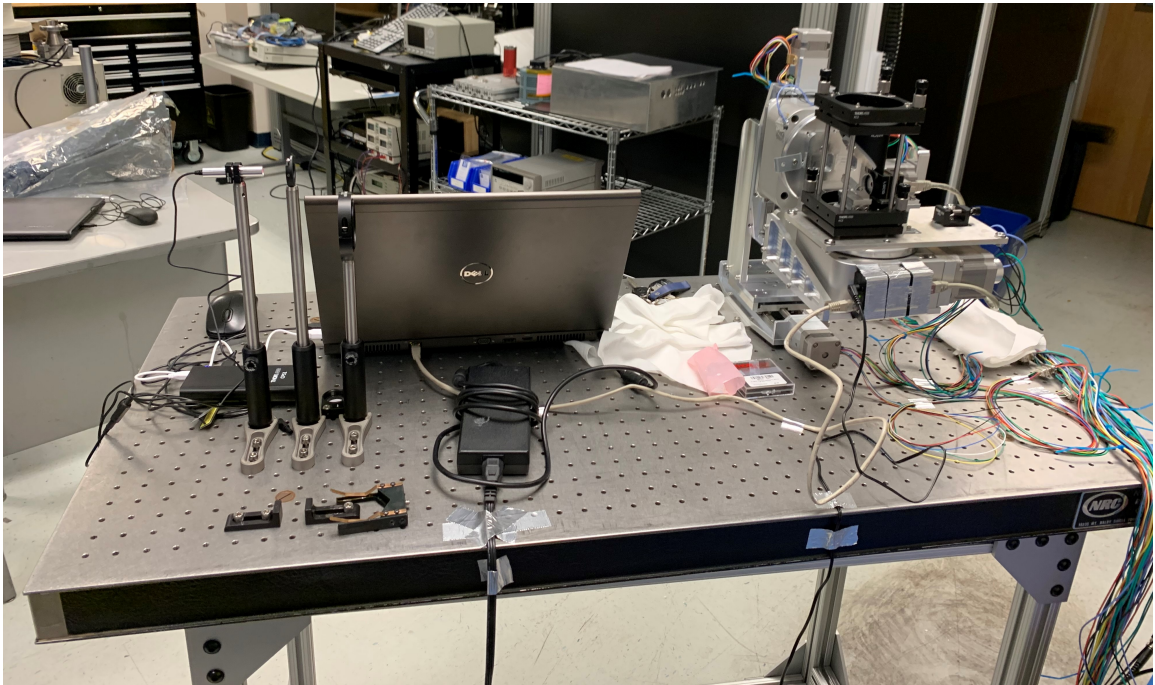


Figure 9.1: Experimental test setup of the manipulator on the GSE cart.

9.1 Optical Alignment

9.1.1 Mechanical Registration

The first step in the alignment process was to register the optical mounts to the datum plate. Precision gauge blocks were used to establish the distance between surfaces as close to the CAD model as possible. First, the iris plate was set into place. As stated by the camera manufacturer, the C-Mount flange back distance is 17.53 mm. This means the iris must be located 10.823 mm in front of the CCD plane, or 6.707 mm behind the front of the C-Mount flange, for a 30° FOV. Reference Figure 9.2 for images of the iris alignment.

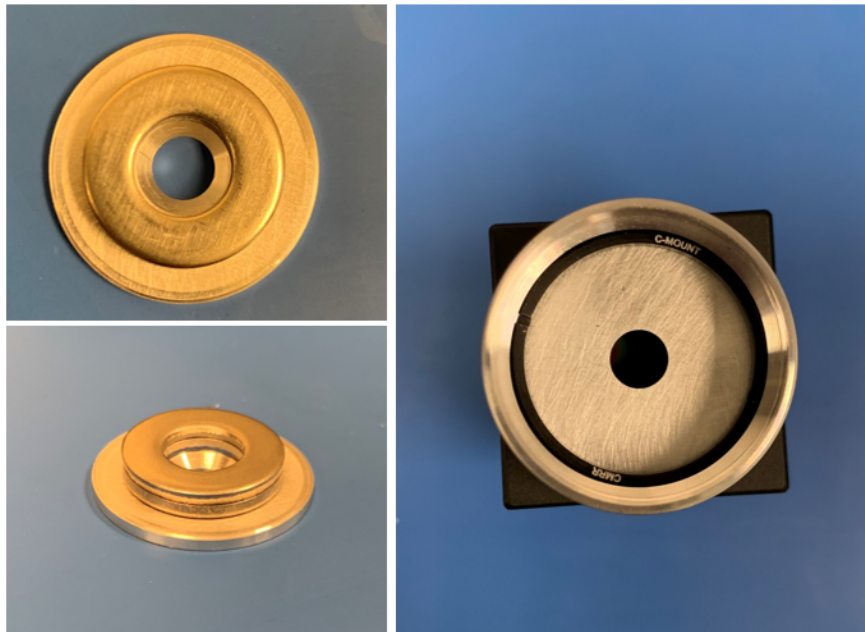


Figure 9.2: The iris was shimmed in the back and held in place by a C-Mount retaining ring. The distance from the front of the CCD flange to the iris plane was measured to be 6.75 mm, which implies the FOV would theoretically be a little smaller than 30°.

After the iris was set in place, the CCD was fastened to its mount using three M3 low-profile screws. The distance between the CCD flange and bracket face was then

established using precision gauge blocks in a stackup of 31.118 mm, or 1.2251 in, which is shown in Figure 9.3. The jig was helpful in squaring the CCD with the bracket that registered to the datum plate. Next, the heights of the tip/tilt stages for the top and bottom mirrors were measured and set to the values shown in Figure 9.4. After the mirror stages were in place, the bottom mirror mount base was squared to the CCD mount. Finally, the distance between the bottom mirror T-slot mount and CCD mount was set, as seen in Figure 9.5. This concluded the mechanical registration of the optical components. The next step in the alignment process was to measure the location and orientation of the top and bottom mirrors with the laser tracker.

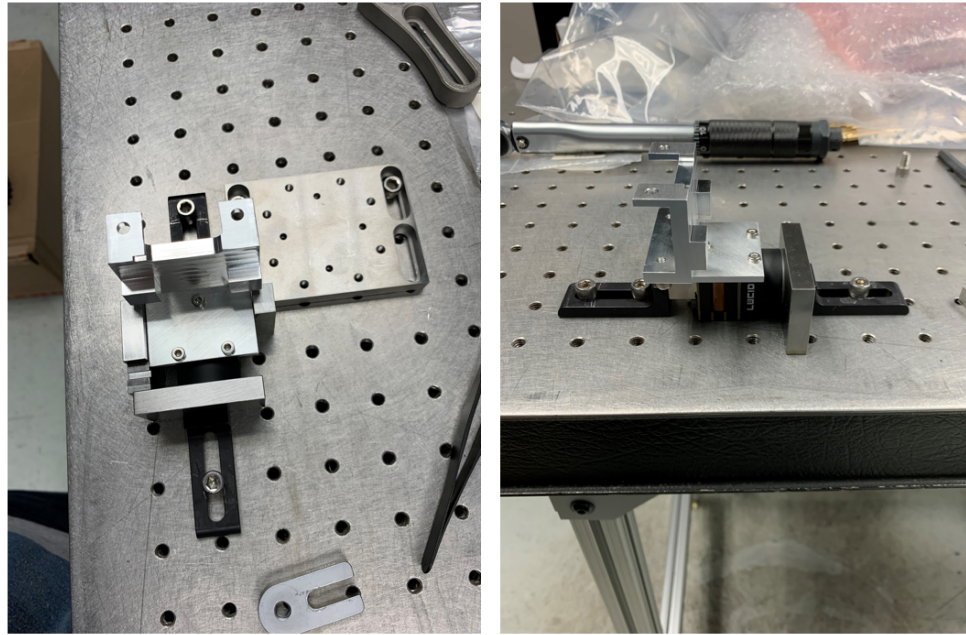


Figure 9.3: The CCD mount and bracket were aligned using a jig on the optical breadboard and precision gauge blocks.

9.1.2 FARO Laser Tracker Measurements

After the optics components were assembled as close to the CAD model as possible, the manipulator was aligned such that the optics datum was orthogonal to the laser

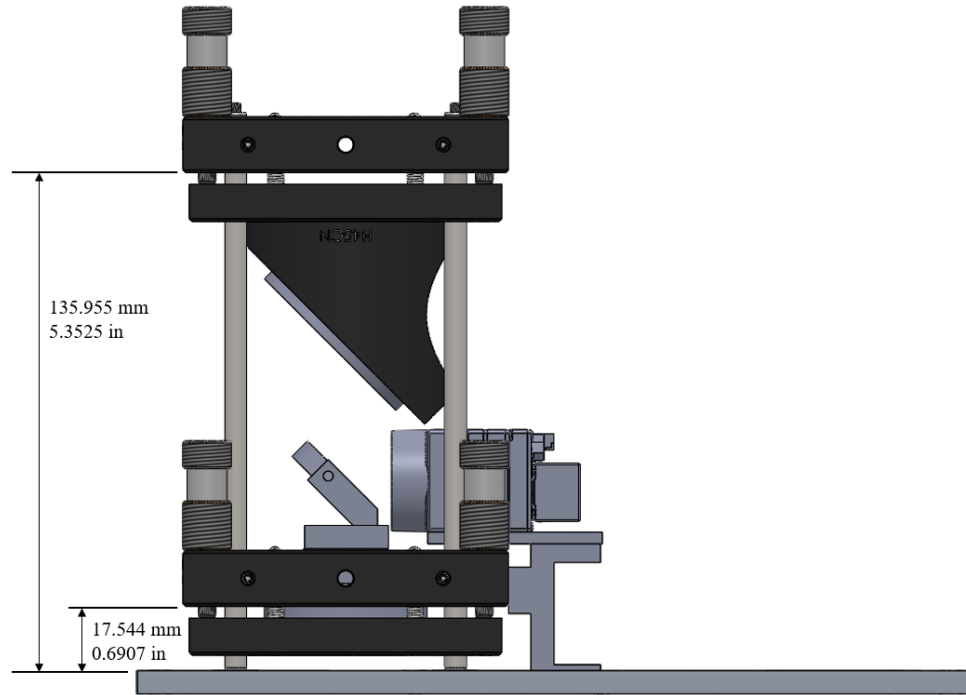


Figure 9.4: CAD measurements for the Thorlabs tip/tilt stages that were set using gauge blocks.

beam. Reference Chapter 7.1.1 for the process that was followed. Next, the FARO laser tracker was used to measure the orientation of the top mirror and the bottom mirrors. The first order of business was to establish the working coordinate frame. The origin was placed in the rear of the optics datum by placing the SMR target into the magnetic mounts. Unfortunately, only three of the four SMR mounts were visible from where the laser tracker was located. A couple photos of the FARO laser tracker setup are presented in Figure 9.6, an image of the SMR target on the optics datum is shown in Figure 9.7, and an illustration of the working coordinate frame is found in Figure 9.8.

Measurements of the optics GSE were taken once the working coordinate system was established. The first process was to measure the orientation of the top mirror with respect to the origin and ensure its orientation was as close to 45° as possible. Although the specific iterations won't be covered in grave detail, it is sufficient to say

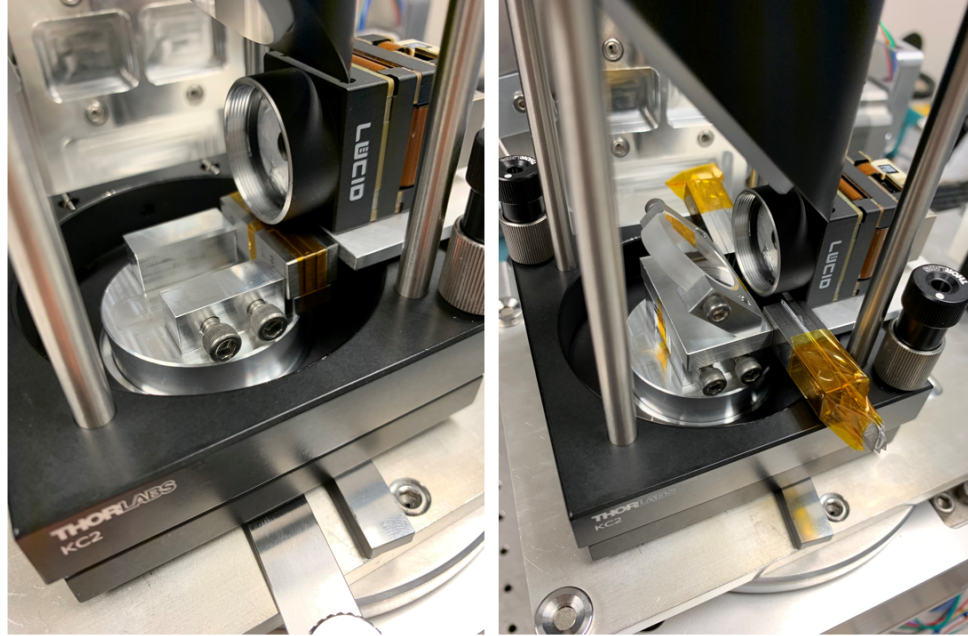


Figure 9.5: The bottom mirror base mount was first squared to the CCD mount (left) and then the distance from the bottom mirror T-slot mount to the CCD mount was set (right).

that it took 9 iterations before the top mirror was properly oriented. On a high level, the alignment process for the top mirror was:

1. Use the FARO tracker to measure the top mirror plane with 6-7 points
2. Retrieve the angle offset of the top mirror plane w/r origin in the Spatial Analyzer program
3. Measure the distance from the reflected spot to the laser pinhole and calculate the tip/tilt angle adjustment (reference Figure 9.9)
4. Adjust the top mirror tip/tilt stage to the new position
5. Repeat until top mirror is $45^\circ \pm 2$ arcmin w/r to the ψ axis, and $0^\circ \pm 2$ arcmin w/r to the X and Z axes



Figure 9.6: Image of the FARO laser tracker (left) and a view of the optical GSE with the laser tracker in the background (right).

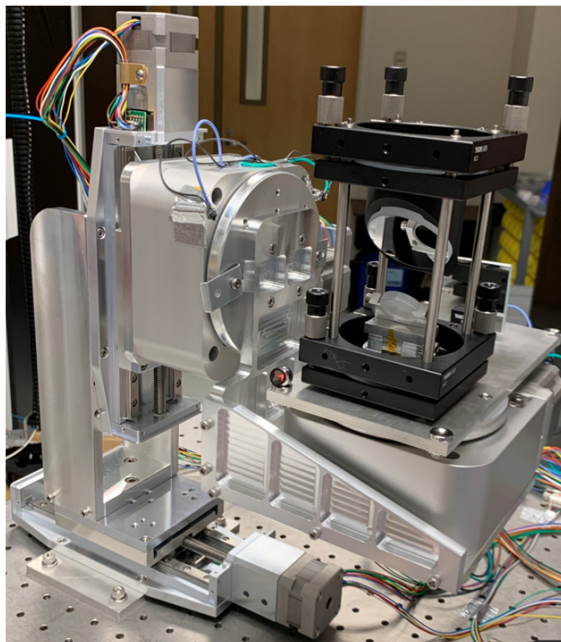


Figure 9.7: Image of the SMR target placed in a magnetic mount on the optics datum.

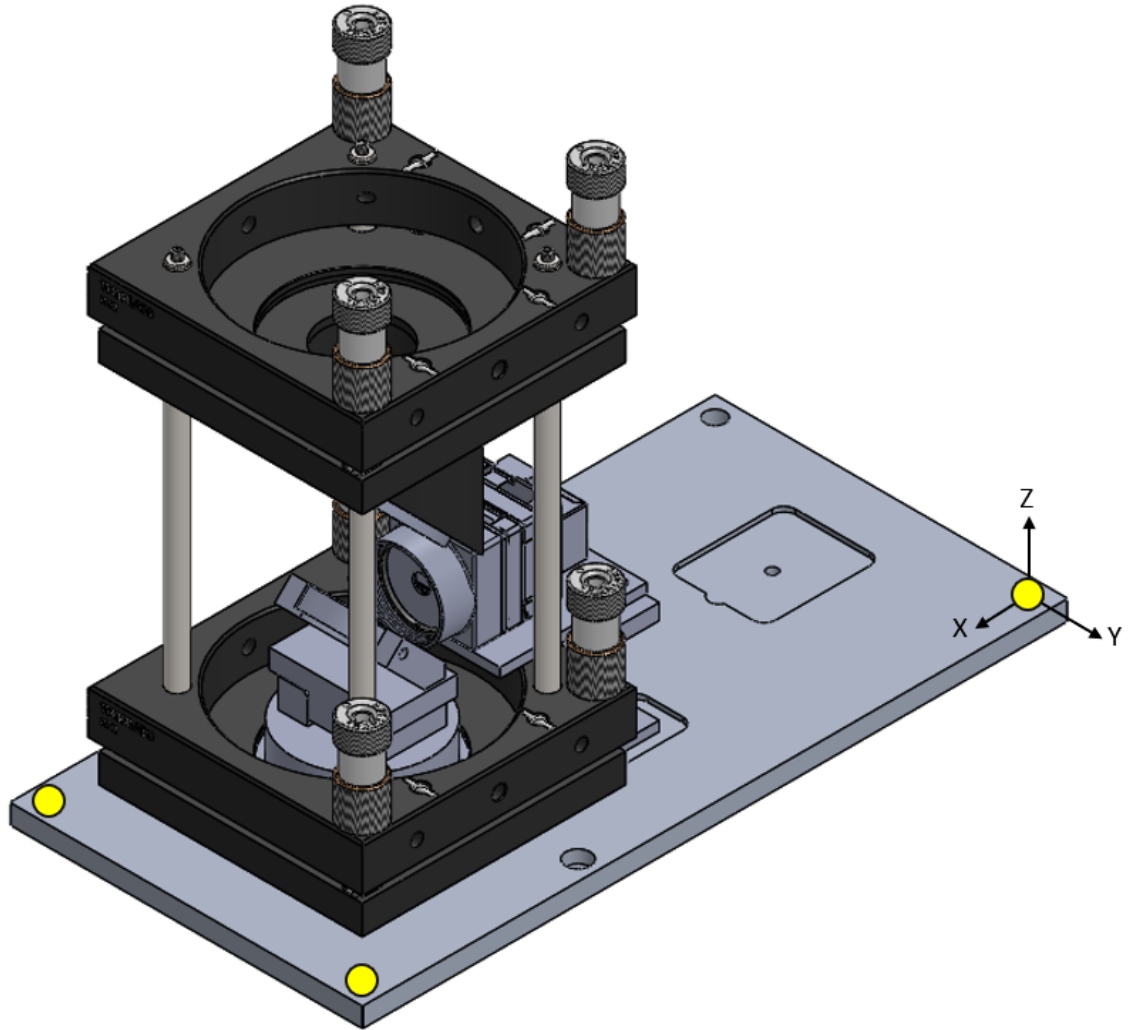


Figure 9.8: Illustration of the working coordinate frame that was defined by metrology. The yellow circles represent the SMR target positions that were used to define the frame.

After the top mirror was defined relative to the origin using metrology, parallelism between the two mirror planes was established by adjusting the bottom mirror. This was achieved by slowly correcting the tip and tilt knobs until the laser reflection was coincident with the pinhole. Parallelism was confidently established between the two mirrors because the optics datum was originally aligned to be orthogonal to the incident beam and the top mirror was measured to be in the proper orientation.



Figure 9.9: Measurement of the reflected spot during the alignment process for the top mirror. The measurement was used to calculate the required tip/tilt adjustment of the mirror stage.

Finally, the laser tracker was used to measure the bottom mirror plane after its adjustment.

9.1.3 Defining the Quaternions

The process to define the mirrors' quaternions began after the mirrors were measured with the FARO laser tracker. The Spatial Analyzer report, which may be found in Appendix F, produced the equations of the mirror planes with respect to the optics datum origin. However, the translation compensation algorithm required the mirror quaternions to be defined with respect to the iris center. Thus, a few sets of

measurements of the optical components were taken with digital calipers to define the 6 required mirror vectors. The first measurement set, found in Figure 9.10 and Figure 9.11, defined the location of the iris center with respect to the working coordinate frame. The next measurement set, shown in Figure 9.12 and Figure 9.13, defined the location of the 3 points of the bottom mirror with respect to the working coordinate system. Finally, the third measurement set defined the location of the 3 top mirror points, which is illustrated in Figure 9.14 through Figure 9.16.

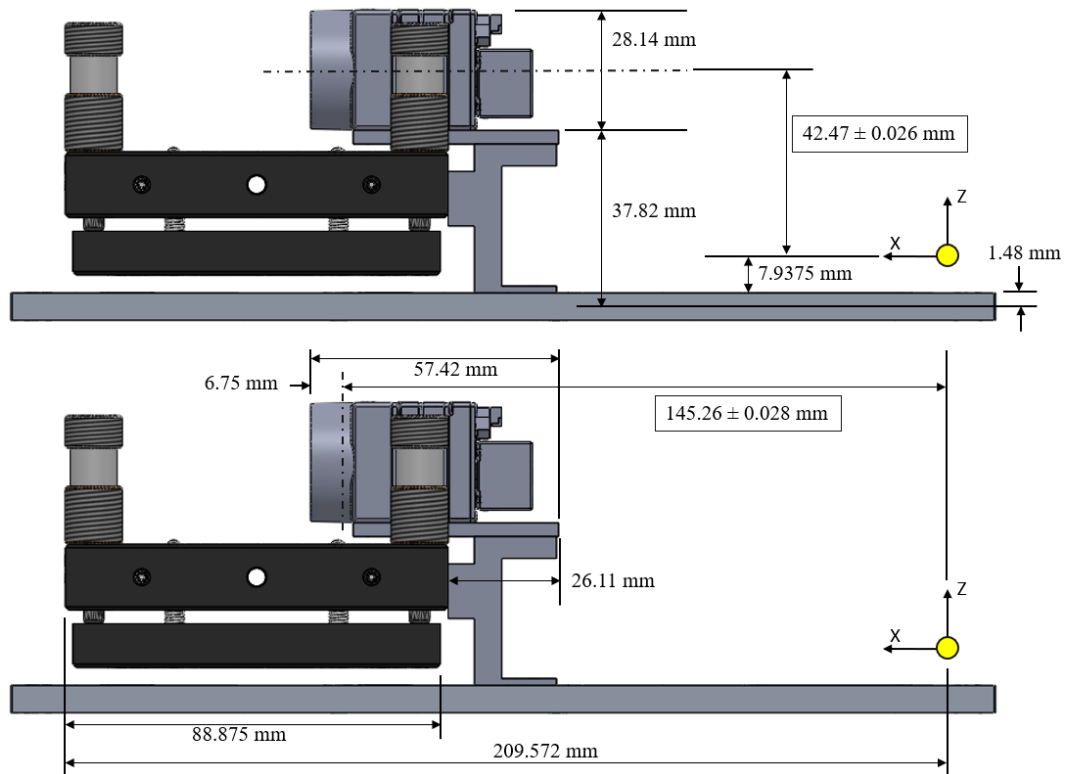


Figure 9.10: Diagram of the X CSYS and Z CSYS measurements taken to locate the iris center with respect to the origin. The Z CSYS component (top) was 42.47 mm and the X CSYS component (bottom) was 145.26 mm.

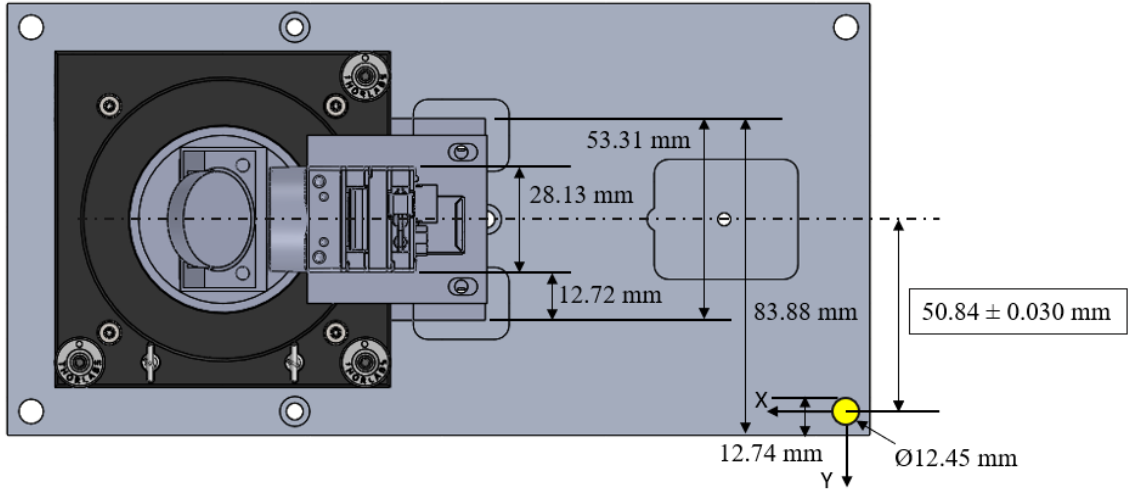


Figure 9.11: Diagram of the ψ CSYS measurements taken to locate the iris center with respect to the origin. The ψ CSYS component was 50.84 mm.

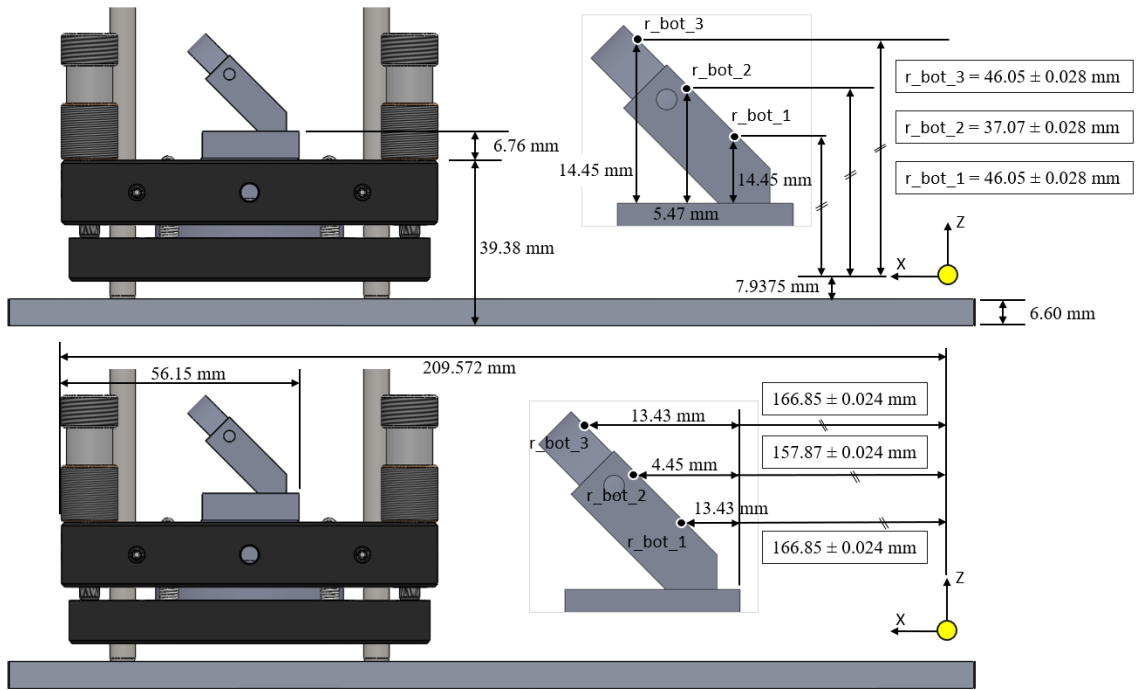


Figure 9.12: Diagram of the Z CSYS (top) and X CSYS (bottom) measurements taken to locate the 3 bottom mirror points with respect to the origin.

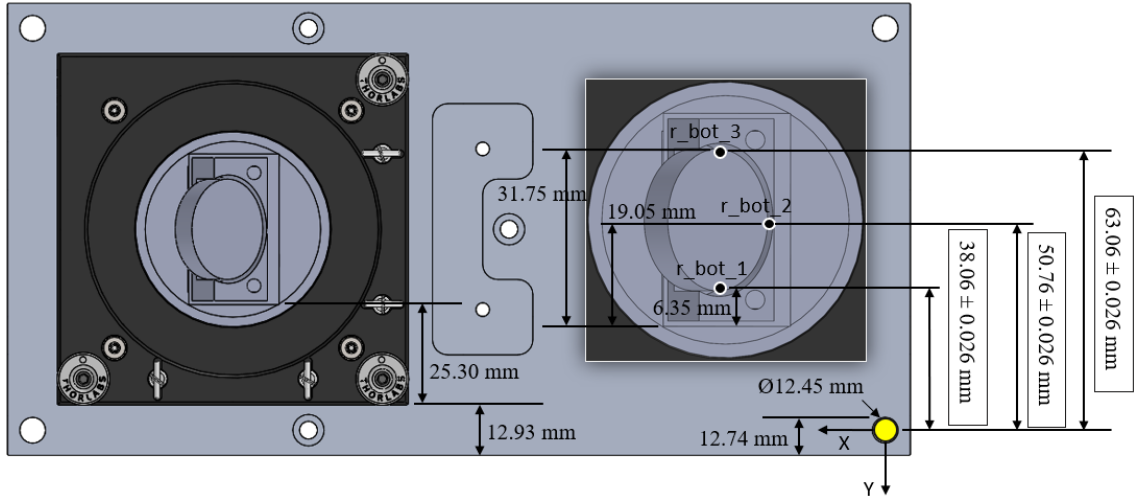


Figure 9.13: Diagram of the ψ CSYS measurements taken to locate the 3 bottom mirror points with respect to the origin.

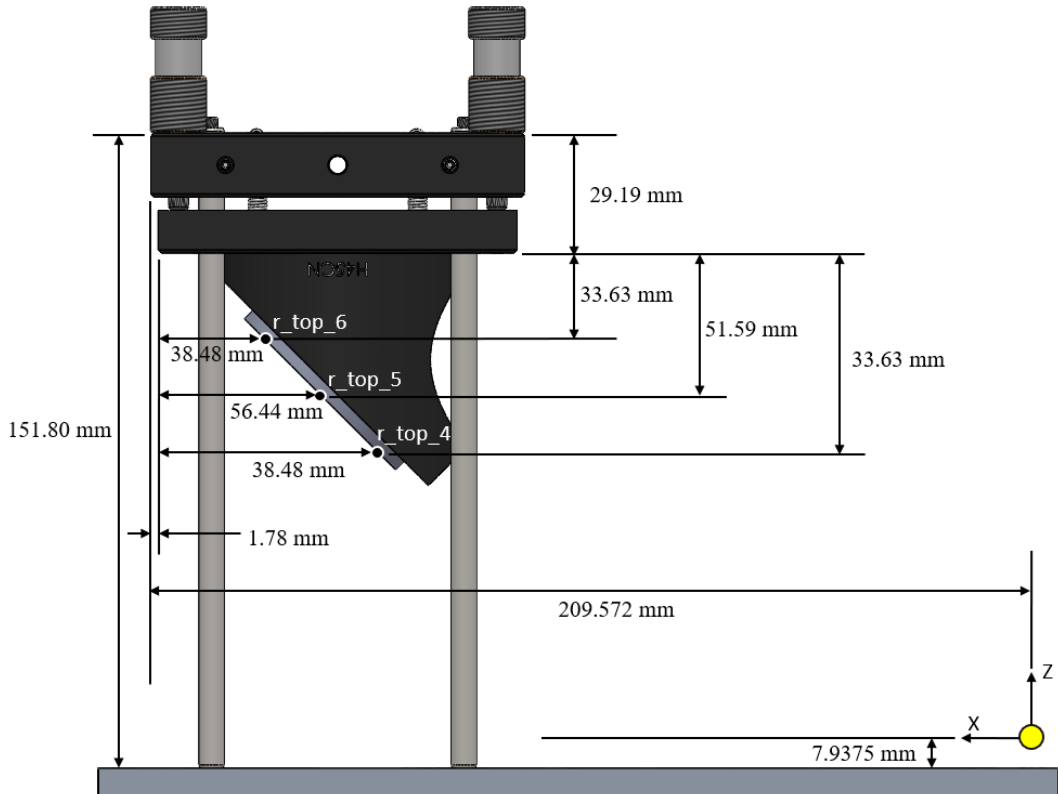


Figure 9.14: Diagram of the Z CSYS and X CSYS measurements taken to locate the 3 top mirror points with respect to the origin.

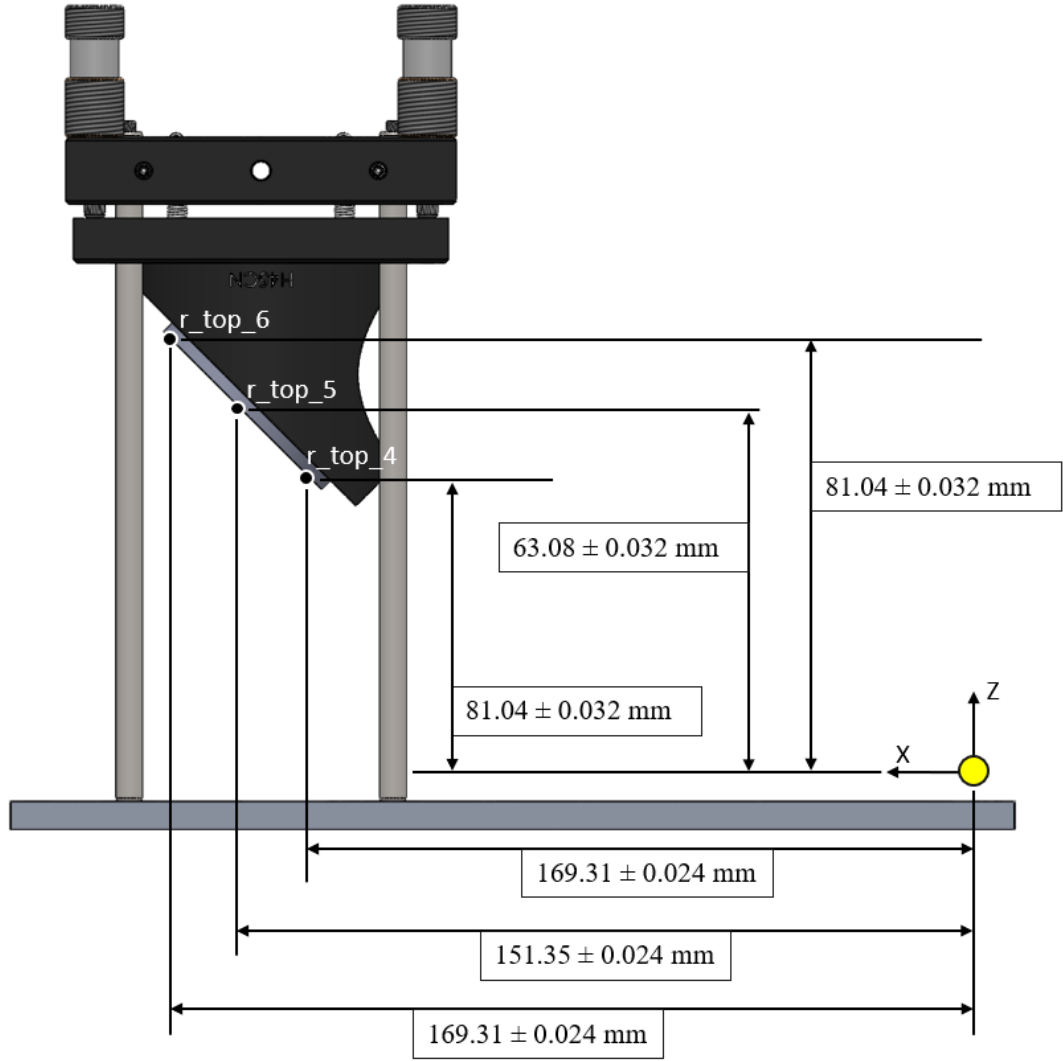


Figure 9.15: Diagram of the simplified Z CSYS and X CSYS measurements of the top mirror points with respect to the origin.

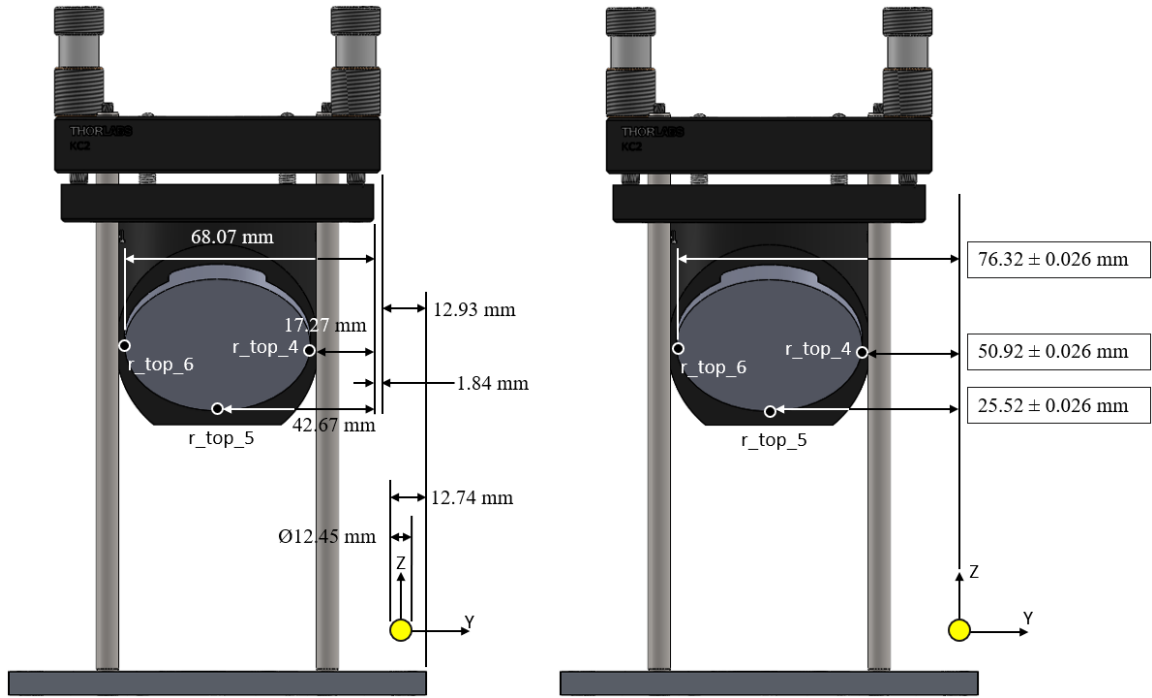


Figure 9.16: Diagram of the ψ CSYS measurements taken to locate the 3 top mirror points with respect to the origin.

When the bottom mirror plane was defined by the Spacial Analyzer program, the plane offset that automatically accounts for the SMR target thickness was flipped. This was not fixed in the program due to technical difficulties, so the bottom mirror plane was manually offset by 12.7 mm, which was the diameter of the SMR target. This was a valid assumption to manually offset as the SMRs are centered to < 0.0005 inches. An illustration of the bottom mirror offset is shown in Figure 9.17. The last step taken to define the mirror quaternions was to project the caliper measurements of the top and bottom mirror points onto the planes measured by metrology. To project the caliper measurements onto each of the mirror planes, equations 8.8 and 8.9 were solved using the mirror's normal vector, caliper measurements, and a metrology point on the mirror plane. The measured mirror quaternions are defined in Table 9.1.

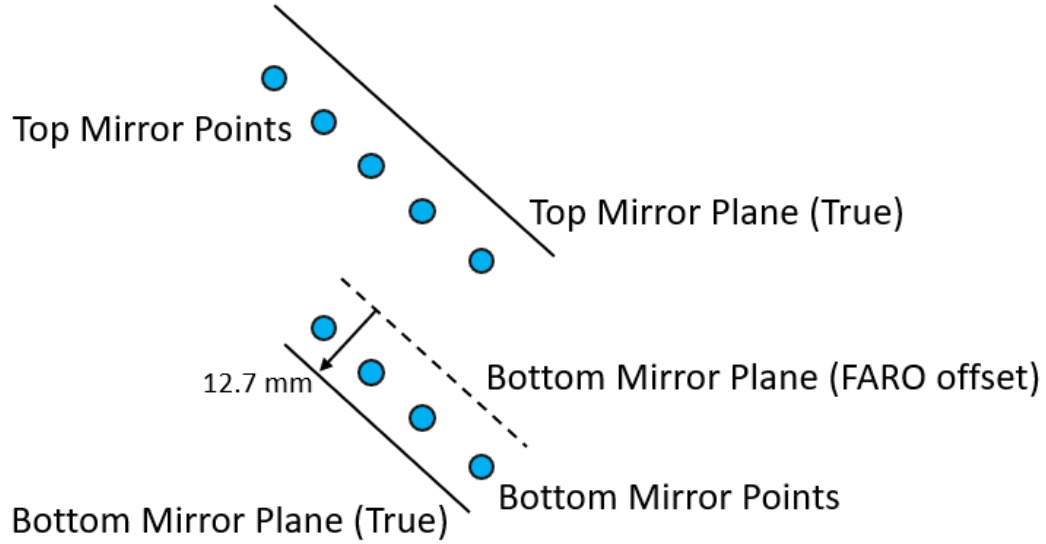


Figure 9.17: The bottom mirror plane was incorrectly defined by the Spatial Analyzer program. The bottom mirror plane was translated by 12.7 mm along its normal vector to properly establish the location of the bottom mirror in 3D space.

Table 9.1: Quaternions that defined the 3D location and orientation of the top and bottom mirrors with respect to the iris center.

Point	SA CSYS - Absolute				SA CSYS - Relative to Iris				MUVI CSYS - Relative to Iris			
	Scalar [mm]	i [mm]	j [mm]	k [mm]	Scalar [mm]	i [mm]	j [mm]	k [mm]	Scalar [mm]	i [mm]	j [mm]	k [mm]
Iris Center	0.000	145.257	-50.840	42.473	0.000	0.000	0.000	0.000	0.000	0.000	0.000	0.000
rbot1 Projected	0.000	166.924	-38.121	46.169	0.000	21.666	12.719	3.696	0.000	-12.719	21.666	3.696
rbot2 Projected	0.000	157.530	-50.389	36.602	0.000	12.273	0.451	-5.871	0.000	-0.451	12.273	-5.871
rbot3 Projected	0.000	166.545	-63.065	45.555	0.000	21.287	-12.225	3.082	0.000	12.225	21.287	3.082
rtop4 Projected	0.000	169.084	-25.407	80.406	0.000	23.827	25.433	37.933	0.000	-25.433	23.827	37.933
rtop5 Projected	0.000	151.063	-50.593	62.380	0.000	5.806	0.247	19.908	0.000	-0.247	5.806	19.908
rtop6 Projected	0.000	169.099	-75.997	80.449	0.000	23.842	-25.157	37.976	0.000	25.157	23.842	37.976
Beam1	0.000	200.000	-50.840	74.499	0.000	54.743	0.000	32.026	0.000	0.000	54.743	32.026
Beam2	0.000	163.234	-50.840	74.499	0.000	17.977	0.000	32.026	0.000	0.000	17.977	32.026

9.2 Finding the Spot Centroid

The centroid of the laser spot was calculated by a Matlab script that analyzed the pixel intensity in the X and Z axes. The algorithm found the average midpoint of

the centroid by iterating through the point spread function to encompass 2 standard deviations of the encircled energy (EE), as depicted in Figure 9.18. The lower intensity bound of 85 was determined by finding the percentage of total integrated flux under the curve for 95% of the encircled energy, which is illustrated in Figure 9.21. The sensitivity of the metric was evaluated by looking at how the centroid calculations shifted between 1σ , 2σ , 3σ , and 4σ of encircled energy. The results, shown in Figure 9.19 and Figure 9.20, depict large spread between the centroid calculation with 1σ EE that dramatically improves at 2σ , and is nearly unchanged at 3σ and 4σ . Overall, the standard error of the spot centroid calculation encompassing 2σ of encircled energy was about $1\mu\text{m}$.

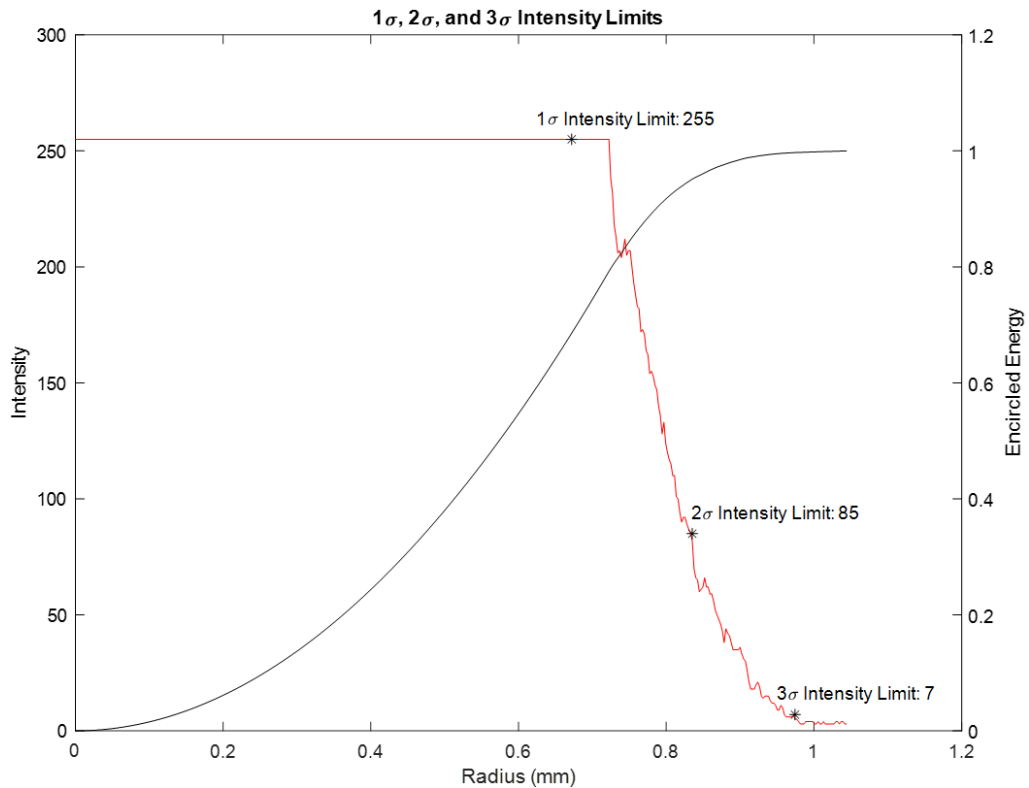


Figure 9.18: Point spread function (PSF) of the laser spot and encircled energy with indication of 68%, 95%, and 99% of the total energy contained in the PSF.

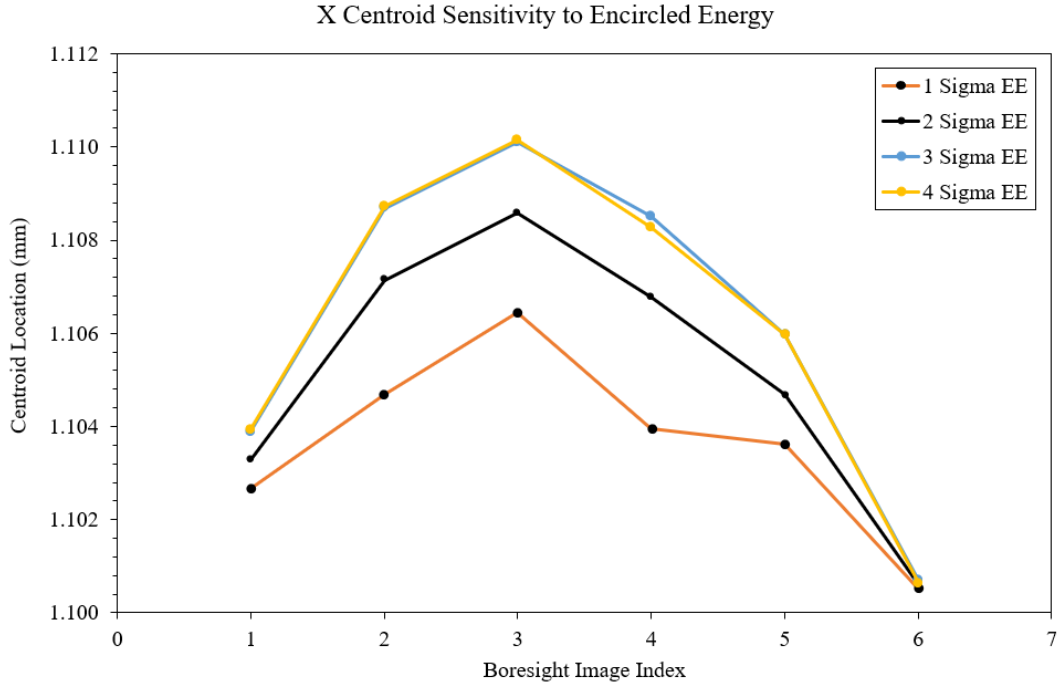


Figure 9.19: Sensitivity of the X centroid calculation with respect to 1σ , 2σ , 3σ , and 4σ of encircled energy.

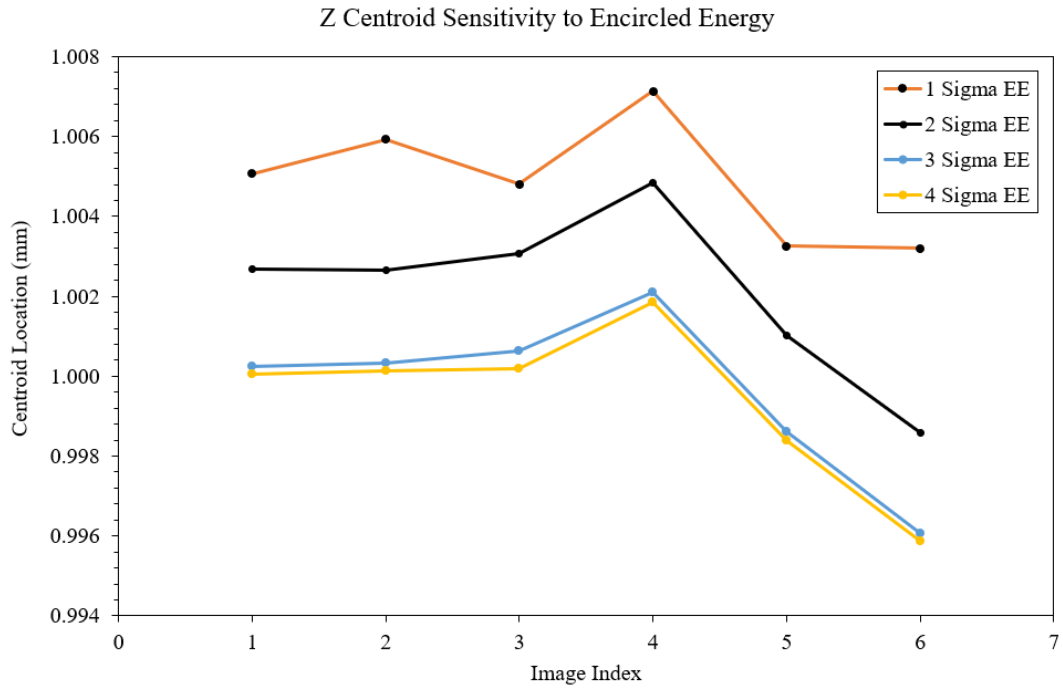


Figure 9.20: Sensitivity of the Z centroid calculation with respect to 1σ , 2σ , 3σ , and 4σ of encircled energy.

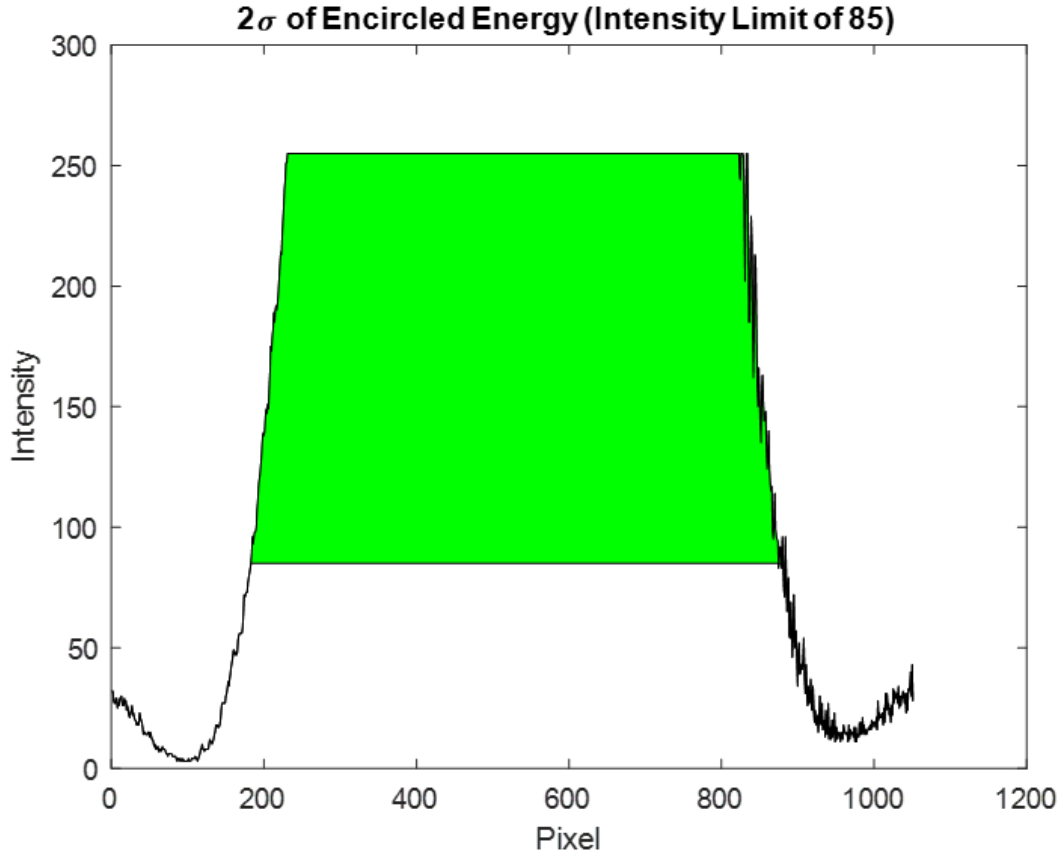


Figure 9.21: Illustration of the algorithm using 95% encircled energy to calculate the centroid of the spot. Note: the Phoenix 200S camera resolution was $2.4\mu\text{m}/\text{pixel}$.

9.3 Boresight Test

An initial boresight image was captured after the optical GSE was aligned. Subsequent boresight images were taken during the 15° and 7° FOV sweeps. These boresight images were compared against each other to understand the positioning repeatability of the manipulator. The 11 boresight images are shown in Figure 9.22, in addition to the spot centroid location on the initial boresight image. A graphical comparison of the difference between the mean and median data of the spot centroid's X and Z coordinates may be seen in Figure 9.23 and Figure 9.24, respectively. This comparison

was necessary because the diffraction of light waves through the aperture resulted in outliers that biased the mean value. The median value was used to locate the spot centroid due to its resistance to outliers. A summary of the data for the boresight repeatability test is located in Table 9.2. Overall, the boresight location was found to be located $(x,z) = (1.2646, 1.1254)$ mm relative to the boundary box, with a standard deviation of $(x,z) = (3.2, 5.3)$ μm . Thus, the manipulator met the pointing resolution of less than 1 arcmin corresponding to the $6.82 \mu\text{m}/\text{arcmin}$ requirement described in Chapter 3.1.1.

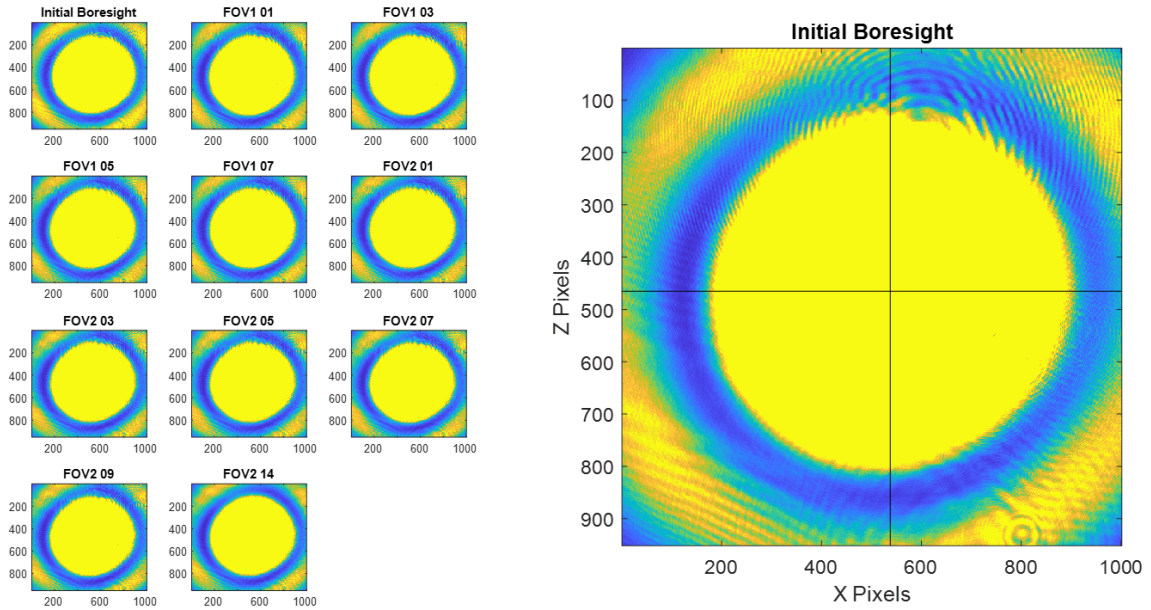


Figure 9.22: Assortment of images of the boresight location for the various field angle tests (left) and the centroid location overlaid on the initial boresight image (right).

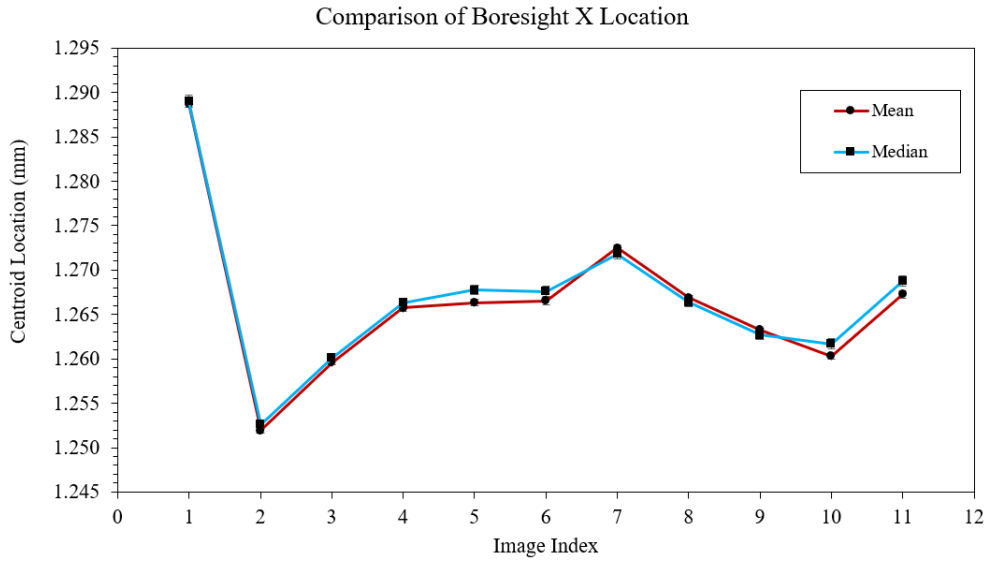


Figure 9.23: Deviation of the boresight spot location in the X axis.

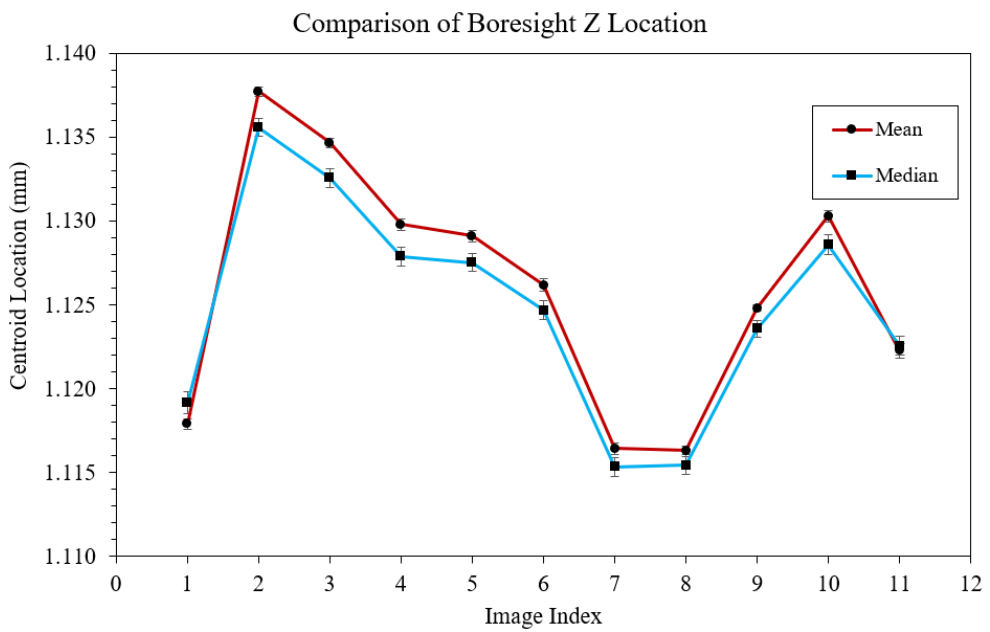


Figure 9.24: Deviation of the boresight spot location in the Z axis.

Table 9.2: Position data for the boresight locations from various tests.

		Image													
		Initial	FOV1 01	FOV1 03	FOV1 05	FOV1 07	FOV2 01	FOV2 03	FOV2 05	FOV2 07	FOV2 09	FOV2 14			
Instrument Target	Pitch (deg)	0.0000	0.0000	0.0000	0.0000	0.0000	0.0000	0.0000	0.0000	0.0000	0.0000	0.0000	0.0000	0.0000	
	Yaw (deg)	0.0000	0.0000	0.0000	0.0000	0.0000	0.0000	0.0000	0.0000	0.0000	0.0000	0.0000	0.0000	0.0000	
Target Position (Matlab Sim)	X (mm)	0.0000	0.0000	0.0000	0.0000	0.0000	0.0000	0.0000	0.0000	0.0000	0.0000	0.0000	0.0000	0.0000	
	Z (mm)	0.0000	0.0000	0.0000	0.0000	0.0000	0.0000	0.0000	0.0000	0.0000	0.0000	0.0000	0.0000	0.0000	
Actual Position (Encoder)	Y (deg)	0.0000	0.0000	0.0000	0.0000	0.0000	0.0000	0.0000	0.0000	0.0000	0.0000	0.0000	0.0000	0.0000	
	P (deg)	0.0000	0.0000	0.0000	0.0000	0.0000	0.0000	0.0000	0.0000	0.0000	0.0000	0.0000	0.0000	0.0000	
	X (mm)	0.0000	0.0000	0.0004	0.0004	0.0004	0.0004	0.0004	0.0004	0.0004	0.0004	0.0004	0.0004	0.0004	
	Z (mm)	0.0000	0.0000	0.0000	0.0000	0.0000	0.0004	0.0036	0.0036	0.0036	0.0036	0.0036	0.0036	0.0036	
Mean	Y (deg)	0.0000	0.0000	0.0000	0.0013	0.0013	0.0013	0.0013	0.0013	0.0013	0.0013	0.0013	0.0013	0.0013	
	P (deg)	0.0000	0.0000	0.0000	0.0000	0.0000	0.0000	0.0025	0.0025	0.0025	0.0025	0.0025	0.0025	0.0025	
Median	X (mm)	1.2896	1.2529	1.2606	1.2666	1.2672	1.2674	1.2736	1.2736	1.2680	1.2643	1.2613	1.2682		
	Z (mm)	1.1166	1.1369	1.1338	1.1283	1.1263	1.1238	1.1149	1.1164	1.1255	1.1279	1.1178			
Std. Error	X (mm)	0.0003	0.0003	0.0003	0.0003	0.0003	0.0004	0.0003	0.0002	0.0002	0.0002	0.0003			
	Z (mm)	0.0007	0.0005	0.0005	0.0005	0.0006	0.0006	0.0006	0.0005	0.0005	0.0005	0.0006			
2σ Encircled Energy															

9.4 Field of View Sweep Test

A rectangular 7° sweep was conducted to observe the performance of the manipulator and quantify the alignment of the optics GSE assembly. The manipulator was positioned at each of the nine locations labeled in Figure 7.3 of Chapter 7.1.2. The manipulator was moved to the boresight orientation after each of the cardinal points to characterize the pointing resolution, which was described in the previous section. The fourteen images captured for this test may be seen in Figure 9.25. Variations in the shape of the spot were observed when the manipulator was positioned at composite field angles. This effect may have been caused by microlenses in front of the CMOS detector plane responding to the off-axis beam. Consequently, the median value of the spot centroid algorithm was used to reject outliers imposed by this phenomenon. The data may be found in Table 9.3 and plots of the median location of the X and Z spot centroid coordinates are shown in Figure 9.26 and Figure 9.27, respectively. These figures depict shifts of the spot centroid when the manipulator rotated to different field angles, but it remained steady at the boresight location. Although small, these deviations indicate misalignment of the optics GSE assembly relative to the manipulator's rotation center. For example, the detector plane may not be exactly where the manufacturer claims given build tolerances or the location of the iris is not coincident to the intersection of the θ and ψ stage rotation axes. These discrepancies were quantified using the analytical model of the optics assembly and they are described in Chapter 10.

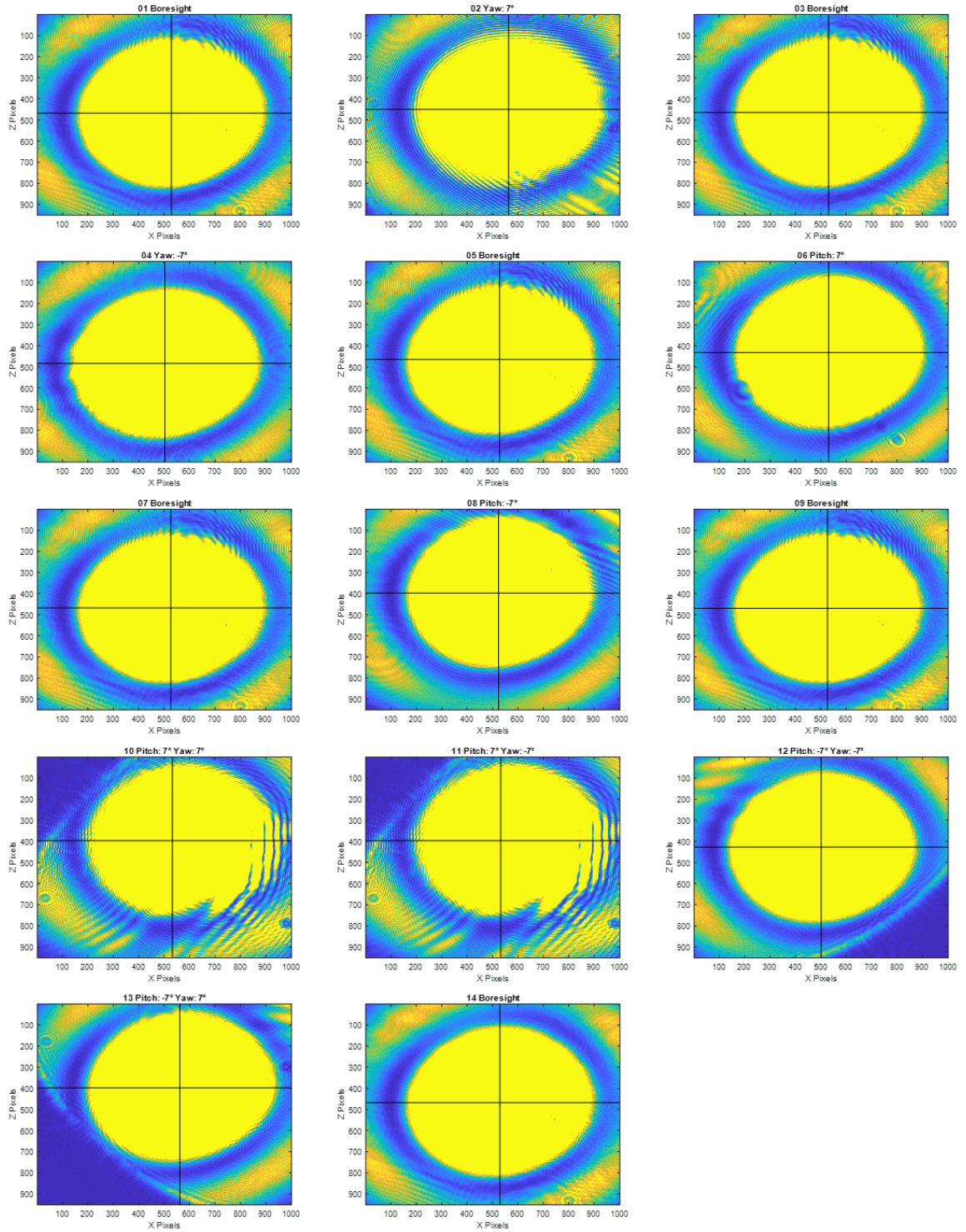


Figure 9.25: Assortment of images for the 7° field angle sweep test.

Table 9.3: Position data of the spot location during the 7° FOV sweep.

		Image													
		1	2	3	4	5	6	7	8	9	10	11	12	13	14
Instrument Target	Pitch (deg)	0.0000	0.0000	0.0000	0.0000	0.0000	7.0000	0.0000	-7.0000	0.0000	7.0000	7.0000	-7.0000	-7.0000	0.0000
	Yaw (deg)	0.0000	7.0000	0.0000	-7.0000	0.0000	0.0000	0.0000	0.0000	0.0000	7.0000	-7.0000	-7.0000	7.0000	0.0000
Target Position (Matlab Sim)	X (mm)	0.0000	5.2268	0.0000	-5.2657	0.0000	0.0000	0.0000	0.0000	0.0000	5.2268	-5.2657	-5.2657	5.2268	0.0000
	Z (mm)	0.0000	0.0000	0.0000	0.0000	0.0000	5.6269	0.0000	-4.8834	0.0000	5.6269	5.6269	-4.8834	-4.8834	0.0000
	Y (deg)	0.0000	7.0000	0.0000	-7.0000	0.0000	0.0000	0.0000	0.0000	0.0000	7.0000	-7.0000	-7.0000	7.0000	0.0000
	P (deg)	0.0000	0.0000	0.0000	0.0000	0.0000	7.0000	0.0000	-7.0000	0.0000	0.0000	7.0000	-7.0000	-7.0000	0.0000
Actual Position (Encoder)	X (mm)	0.0004	5.2288	0.0004	-5.2641	0.0004	0.0004	0.0004	0.0004	0.0004	5.2288	-5.2645	-5.2645	5.2288	0.0004
	Z (mm)	0.0036	0.0036	0.0036	0.0036	0.0036	5.6301	0.0004	-4.8891	0.0036	5.6305	5.6305	-4.8816	-4.8816	0.0028
	Y (deg)	0.0013	6.9987	0.0013	-6.9988	0.0025	0.0025	0.0025	0.0025	0.0025	7.0000	-6.9975	-6.9975	7.0000	0.0025
	P (deg)	0.0025	0.0025	0.0025	0.0025	0.0025	7.0025	0.0025	-6.9988	0.0025	7.0025	7.0025	-7.0000	-7.0000	0.0025
Mean	X (mm)	1.2671	1.3536	1.2732	1.2055	1.2676	1.2731	1.2639	1.2564	1.2610	1.3047	1.3047	1.2043	1.3475	1.2679
	Z (mm)	1.1249	1.0786	1.1158	1.1595	1.1168	1.0341	1.1255	0.9525	1.1287	0.9536	0.9536	1.0242	0.9516	1.1192
Median	X (mm)	1.2674	1.3530	1.2726	1.2092	1.2671	1.2739	1.2636	1.2568	1.2624	1.3026	1.3026	1.2035	1.3476	1.2687
	Z (mm)	1.1251	1.0752	1.1160	1.1560	1.1168	1.0292	1.1249	0.9484	1.1284	0.9506	0.9506	1.0209	0.9481	1.1140
Std. Error	X (mm)	0.0004	0.0007	0.0003	0.0006	0.0003	0.0004	0.0002	0.0004	0.0003	0.0028	0.0028	0.0003	0.0007	0.0004
	Z (mm)	0.0006	0.0005	0.0006	0.0004	0.0005	0.0005	0.0005	0.0005	0.0005	0.0006	0.0004	0.0004	0.0006	0.0006
2σ Encircled Energy															

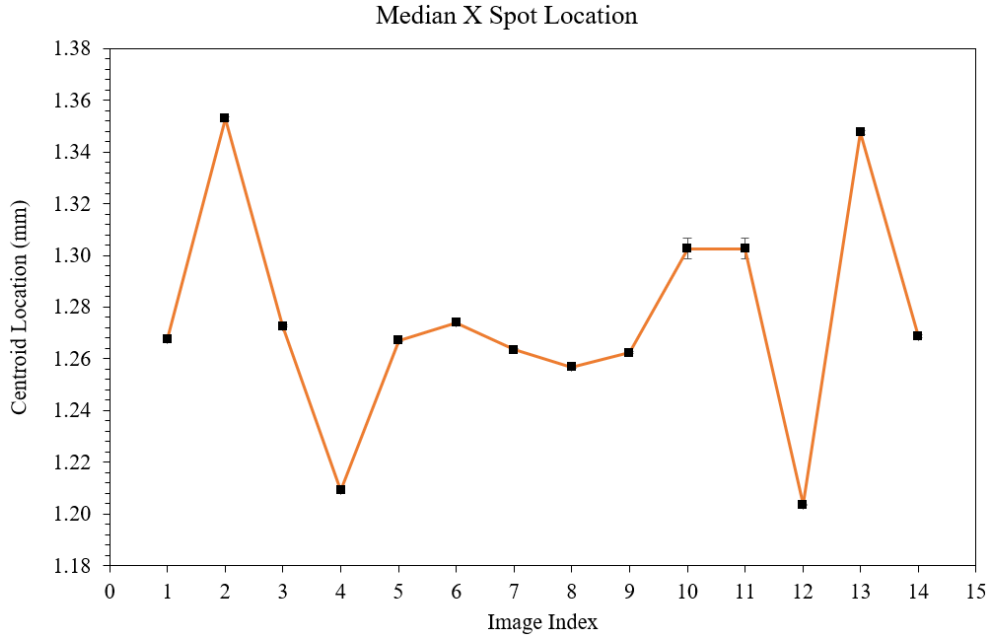


Figure 9.26: X spot location during the first 7° FOV sweep.

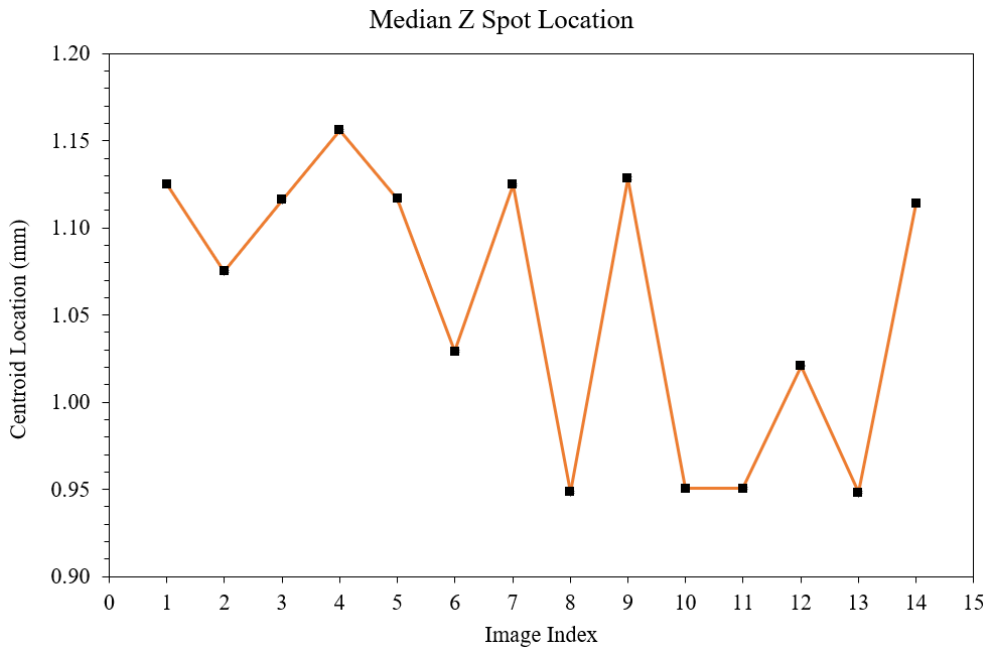


Figure 9.27: Z spot location during the first 7° FOV sweep.

Chapter 10

COMPARISON OF RESULTS

The analytical and experimental results are compared in this chapter to quantify systematic errors. The inherent offset of the detector plane and the center of rotation of the optical GSE is described by replicating the experimental data with the analytical model. A final test is presented that successfully decoupled the systematic errors.

10.1 Adjustment for Systematic Errors

Whether they are large or small, positioning errors are always present in mechanical systems. The difficulty is confidently quantifying these systematic errors with an analytical model. The following section describes the approach to quantify errors in the optical GSE assembly to decouple these errors from the performance characterization of the manipulator.

10.1.1 Detector Plane Offset

Given a fixed iris diameter, the intersection of field angle rays on the detector plane should be static if the detector plane is located exactly at the convergence point of the rays. However, if the detector plane is slightly offset, whether it be due to assembly or machining tolerances in the system, there will be consistent drift of the spot in the image. These effects may be seen in Figure 10.1 and Figure 10.2 for positive and negative field angles, respectively.

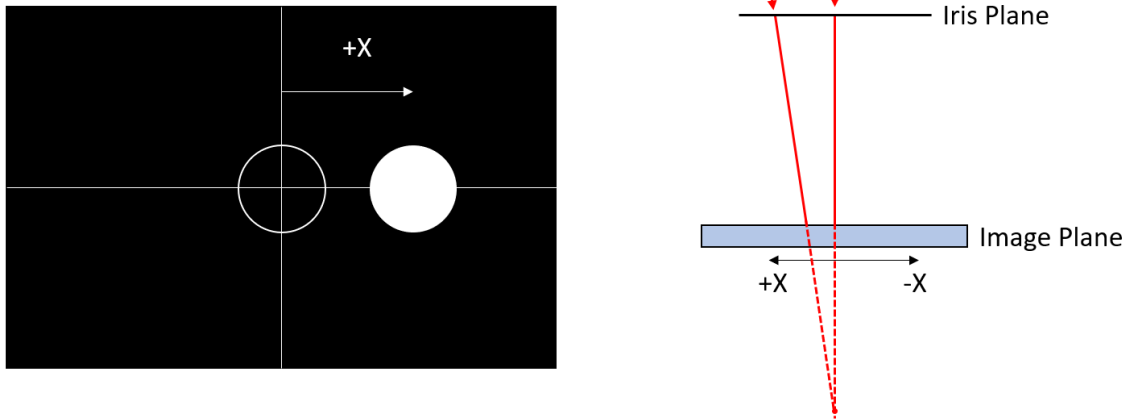


Figure 10.1: Illustration of the spot shift along the X axis for a positive field angle.

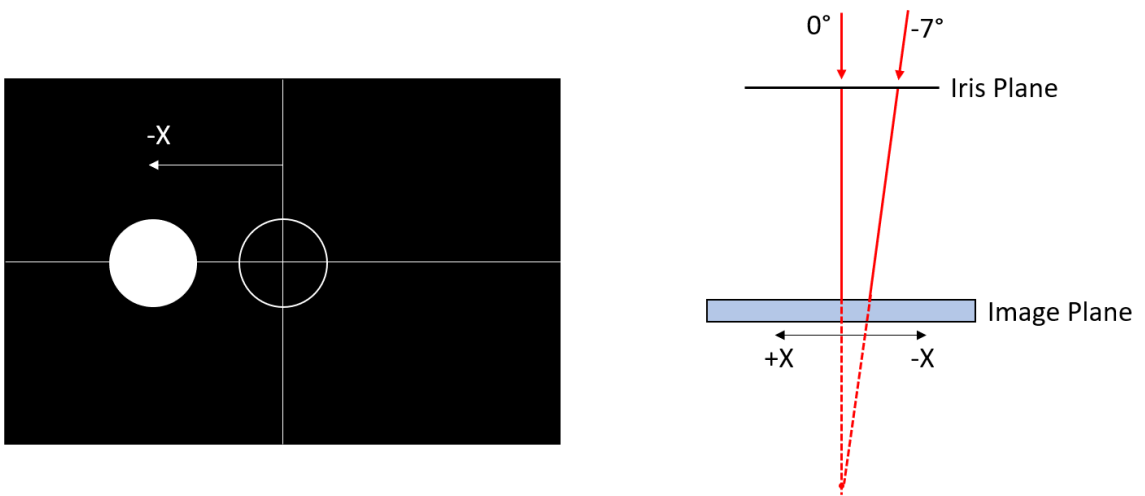


Figure 10.2: Illustration of the spot shift along the X axis for a negative field angle.

Fortunately, the detector plane offset does not invalidate the test results. The only repercussion is that the FOV is slightly bigger or smaller than the nominal 30° requirement and that depends on whether the image plane is behind or ahead of the ray convergence point. It was observed in the experimental data that the detector

plane was offset ahead of this point, consistent with a positive spot translation for a positive field angle. Thus for this experimental setup, the FOV would be slightly larger than 30° . The analytical model of the optics assembly was modified to account for the location of the detector plane. Multiple simulations were run with various detector offset values to replicate the experimental test results for the X axis, which is shown in Figure 10.3. Ultimately, the offset of the detector plane was determined to be approximately 1.181 mm closer to iris than initially regarded.

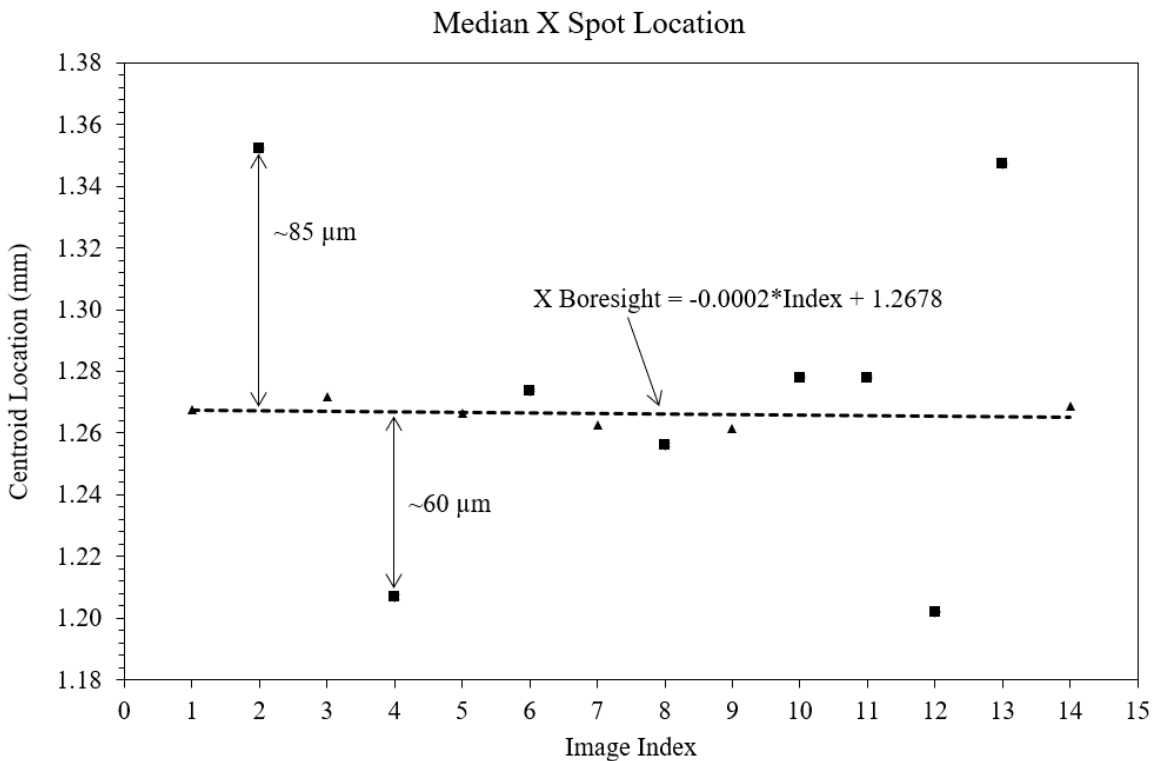


Figure 10.3: Deviations along the X spot location were used to characterize the detector plane offset.

10.1.2 Center of Rotation

The rotation center of the manipulator is located at the intersection of the θ and ψ stage axes. Consequently, additional translation compensation is required if the center of the imaging iris does not coincide with the rotation center because the optical lever arm changes. The analytical model of the optics GSE was used to determine the location of the rotation center relative to the center of the iris corresponding to the measured errors between the analytical and experimental data shown in Table 10.1. Multiple simulations were run with various center of rotation values to replicate the experimental test results for the Z axis, which is shown in Figure 10.4. The center of rotation was found to be approximately $[x, y, z] = [-0.014, -0.490, -0.106]$ mm relative to the center of the iris.

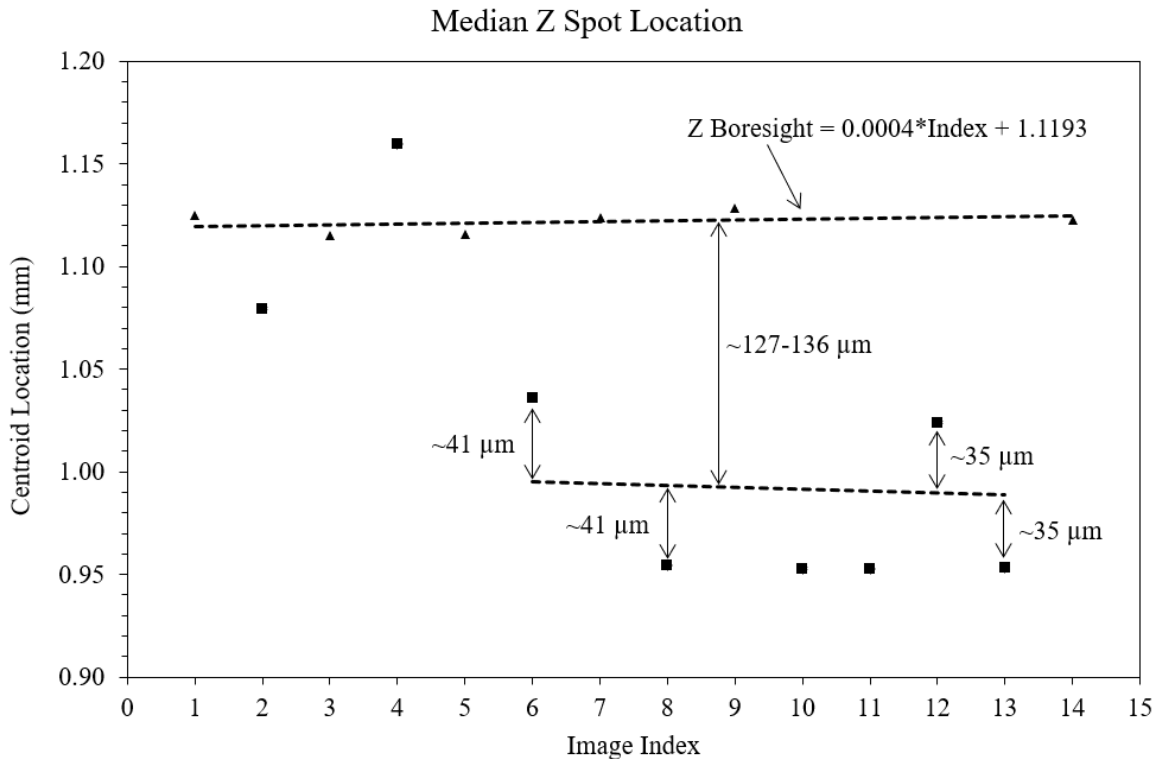


Figure 10.4: Deviations along the Z axis were used to characterize the center of rotation.

Table 10.1: Errors between the theoretical and measured spot locations before the center of rotation adjustment was applied.

Index	X Spot Location			Z Spot Location		
	Measured (mm)	Theoretical (mm)	Error (μm)	Measured (mm)	Theoretical (mm)	Error (μm)
2	1.3521	1.2674	85	1.0795	1.1201	-41
4	1.2068	1.2670	-60	1.1596	1.1209	39
6	1.2738	1.2666	7	1.0361	1.1217	-86
8	1.2561	1.2662	-10	0.9544	1.1225	-168
10	1.2780	1.2658	12	0.9527	1.1233	-171
11	1.2780	1.2656	12	0.9527	1.1237	-171
12	1.2020	1.2654	-63	1.0240	1.1241	-100
13	1.3472	1.2652	82	0.9533	1.1245	-171

10.2 Post-Adjustment Test Results

After the detector plane offset and center of rotation were quantified, the translation compensation within the analytical model was adjusted to remove these systematic errors. A final FOV sweep test was conducted to evaluate the effectiveness of the adjustment and the results are shown in Figure 10.5 and Figure 10.6. Before the error adjustment, the standard deviation of the X and Z spot centroid location was $296 \mu\text{m}$ and $85 \mu\text{m}$, respectively. After the adjustment, the standard deviation of the X and Z spot centroid location was $6 \mu\text{m}$ and $12 \mu\text{m}$, respectively. Therefore, the systematic error was cut down by a factor of 49 and 7 for the X and Z coordinates, respectively. It was observed in the position feedback data that the positioning error of the X stage was 1.4 microns and the Z stage was 2.7 microns. Once the systematic error is understood and accommodated, the resolution of the optical performance measurements is narrowed close to the resolution of the actuators themselves.

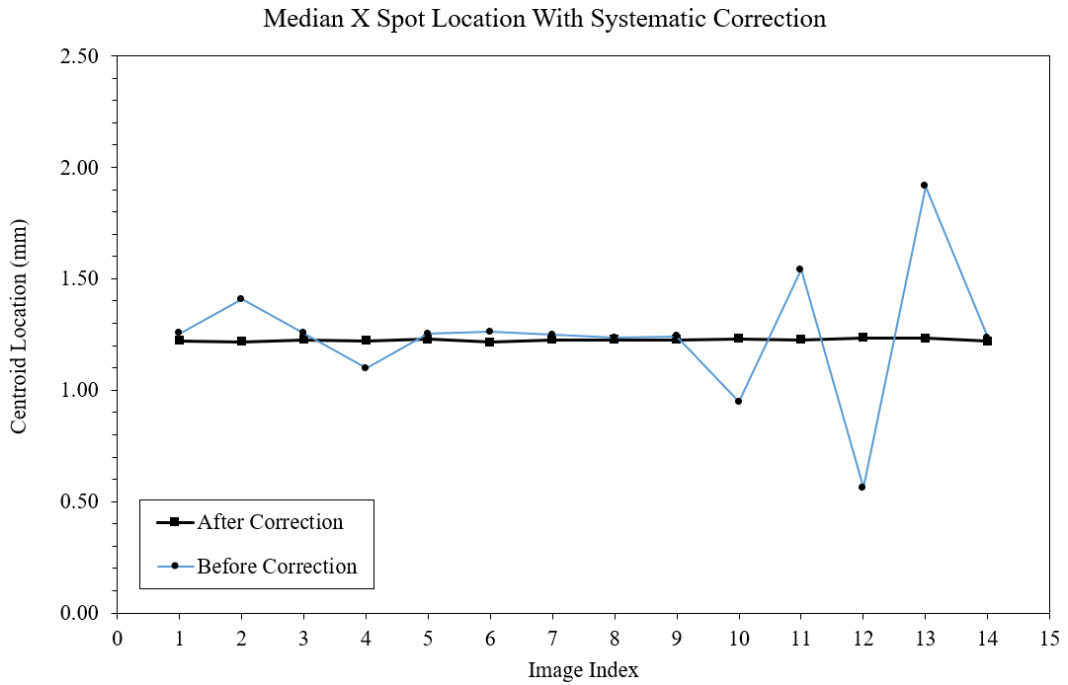


Figure 10.5: X spot location before and after the adjustment for systematic errors.

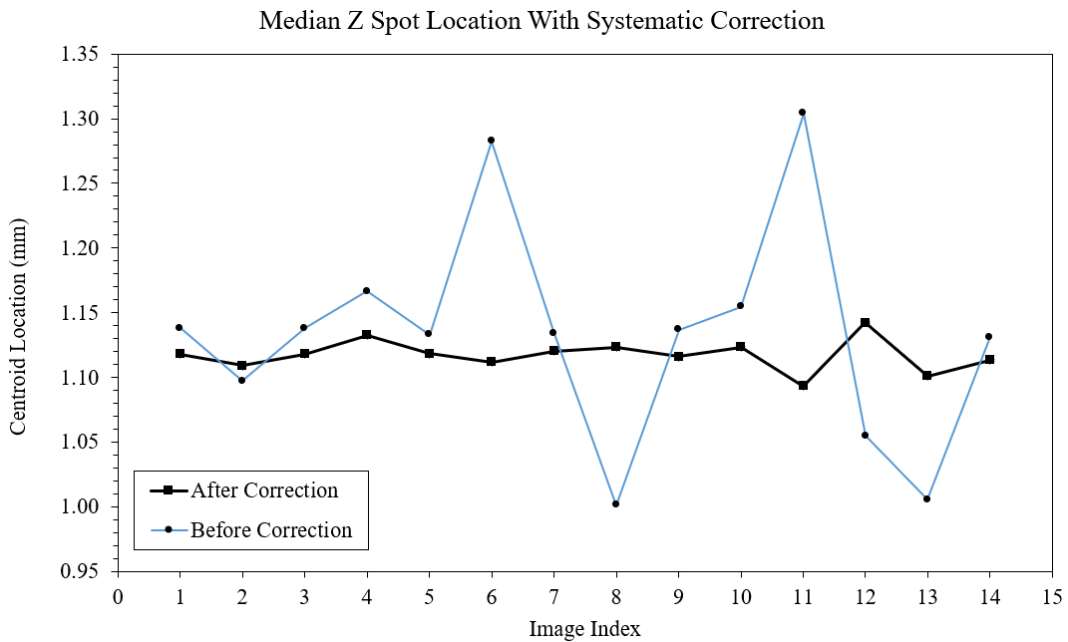


Figure 10.6: Z spot location before and after the adjustment for systematic errors.

Chapter 11

CONCLUSION

The objective of this thesis was to design, build, and characterize a vacuum-compatible manipulator to calibrate ultraviolet imagers for space. Precision positioning stages were implemented with customized adapter plates to comprise a 4 DOF manipulator that met the vacuum requirements for the SSL UV vacuum facility. A custom PCB was designed and implemented to control the manipulator with respect to input from a customized graphical user interface. In addition to hardware and software implementation, a complete optical simulation was developed in the Matlab environment. In the simulation, quaternion mathematics calculated the required translation compensation to accommodate various optical lever arms for a given instrument field angle.

The analytical model was verified by experimental testing, which utilized a monochromatic CMOS sensor to measure the location of a laser spot. The pointing resolution of the manipulator, characterized from boresight tests, was measured to be $(x,z) = (3.2, 5.3) \mu\text{m}$. The pointing resolution in angle space met the science requirement of $6.82 \mu\text{m}/\text{arcmin}$. Field of view sweeps were used to tune the analytical model of the optical GSE, which reduced the systematic errors by a factor of 49 and 7 for the X and Z coordinates, respectively. From these tests, the center of rotation and detector plane offset were quantified and used to refine the translation compensation calculation. By using the translation stages to counteract systematic errors, the performance of the manipulator was improved to be close to the resolution of the actuators.

11.1 Future Work

The knowledge gained from this thesis provided strong insight for future work. Once implemented, the following list of actions will make the operation and performance of the manipulator even more reliable and effective for operating the manipulator inside the vacuum chamber.

Fault Detection and Correction

Although outside the scope of this thesis, implementing detailed fault detection and correction (FDC) would significantly improve the reliability of the manipulator as it operates inside the vacuum chamber. The system could automatically identify issues and handle non-critical errors without requiring much attention from the operator.

PCB Current and Temperature Readings

Additional feedback data needs to be monitored when the manipulator and instrument are inside the vacuum chamber. As of now, the feedback data stream only provides insight on the position of the stages. To better understand the complete operational conditions of the manipulator, measurement of the current draw and temperature of the actuators should be added to the custom PCB.

Rotational Limit Switch Mounts

Non-vacuum limit switches for the rotation stages were temporarily mounted with hot glue to commission the manipulator. It is recommended to replace the limit switches with vacuum-compatible limit switches and implement custom mounting brackets to better secure the switches onto the manipulator. Fastening the limit switches to brackets will reduce the failure risk of the limit switches becoming detached during operation.

Vacuum Chamber Interface

The mounting interface between the vacuum chamber rails and manipulator needs to be designed. The requirement is simple, since four 1/4-20 fasteners are all that is required to mount the manipulator to the chamber.

Electronics Enclosure

The enclosure to house the stepper motor power supply and custom PCB was not integrated due to time constraints. Most of the hardware was ordered and shipped to SSL, except the PCB mounting standoffs and screws. Holes for the fan, power switch, and electrical harnesses will need to be cut out of the enclosure box before installing the components.

Electrical Harness to Vacuum Chamber

Currently, the electrical connectors attached to the Newmark stage harnesses are not vacuum compatible according to the manufacturer's disclaimer. These connectors need to be replaced with vacuum compatible hardware and may be integrated with a bulkhead.

BIBLIOGRAPHY

- [1] V. Angelopoulos. The themis mission. *Space Science Reviews*, 141, 2008.
- [2] B. Aschenbach, H. Brauning, K.-H. Stephan, and J. Trumper. X-ray test facilities at max-planck-institut garching. *SPIE*, 0184, 1979.
- [3] W. Berg. *The Theory and Application of Precision Mechanical Components*. Russell E. Sacken, Inc., East Rockaway, 2 edition, 1965.
- [4] W. Bertrand. Effects of spacecraft material outgassing on optical systems in the vacuum ultraviolet. *Arnold Engineering Development Center*, 1995.
- [5] W. Campbell, R. Marriott, and J. Park. Outgassing data for selecting spacecraft materials. *NASA Reference Publication*, 1984.
- [6] T. Chonis, B. Gallagher, J. S. Knight, D. S. Acton, K. Smith, and et al. Characterization and calibration of the james webb space telescope mirror actuators fine stage motion. *SPIE*, 10698, 2018.
- [7] A. David. Direct drive linear motors: Overview and selection process, 2018. www.zaber.com/technical-articles/direct-drive-linear-motors.
- [8] J. Grillo, B. Hill, and T. Hajjar. Ultraviolet imager application for a cube satellite. *Cal Poly Digital Commons*, 2018.
- [9] J. Grillo, B. Hill, T. Hajjar, and et al. Characterizing multifunctional materials to mitigate vibrations induced on spacecraft optical equipment. *Composites and Advanced Materials Conference*, 2018.
- [10] R. Halstead. Working in a vacuum, 2002. <https://www.machinedesign.com/archive/article/21814944/working-in-a-vacuum>.

- [11] T. Immel, S. England, S. Mende, and et al. The ionospheric connection explorer mission: Mission goals and design. *Space Science Reviews*, 214, 2018.
- [12] B. Jakosky, R. Lin, J. Grebowsky, and et al. The mars atmosphere and volatile evolution (maven) mission. *Space Science Reviews*, 195, 2015.
- [13] Y.-B. Jia. Quaternions, 2019.
- [14] N. Karasikov, G. Peled, R. Yasinov, M. Gissin, and A. Feinstein. Piezo-based motion stages for heavy duty operation in clean environments. *SPIE*, 10539, 2018.
- [15] J. Loicq, P. Blain, C. Kintziger, R. Desselle, and et al. V-uv spectrographic imager (fuv) for icon mission: from optical design to vacuum calibration. *International Conference on Space Optics*, 10562(36), 2016.
- [16] J. Loicq, P. Blain, C. Kintziger, R. Desselle, Y. Stockman, and et al. Alignment and calibration of the icon-fuv instrument: development of a vacuum uv facility. *SPIE*, 9905, 2016.
- [17] S. Mende, H. Frey, K. Rider, C. Chou, S. Harris, O. Siegmund, S. England, C. Wilkins, W. Craig, T. Immel, P. Turin, N. Darling, J. Loicq, P. Blain, B. Syrstad, B. Thompson, R. Burt, C. J, P. Sevilla, and S. Ellis. The far ultra-violet imager on the icon mission. *Space Science Reviews*, 2017.
- [18] Newmark Systems, Inc. *NLS4 Series Linear Stage Datasheet*.
- [19] Newmark Systems, Inc. *RM-5 Series Rotary Stage Datasheet*.
- [20] J. Quinones. Applying acceleration and deceleration profiles to bipolar stepper motors, 2012.
- [21] E. Rainville, P. Rainville, and J. Wagner. Deployable cover for cubesat fuv imager. *Cal Poly Digital Commons*, 2019.

- [22] Servo - how it works.
<http://arcbotics.com/products/sparki/parts/servo/>.
- [23] Stepper motors in precision motion control and positioning.
<https://www.pi-usa.us/en/tech-blog/stepper-motors-in-precision-motion-control-and-positioning/>.
- [24] Texas Instruments. *SN65LVDS349 Quad High-Speed Differential Receiver Datasheet*, Sep. 2010. Rev. SLLSE23.
- [25] 1- and 2-axis motorized goniometer stages. https://www.thorlabs.com/newgrouppage9.cfm?objectgroup_ID=2461&pn=GNL10-Z8.
- [26] Trinamic Motion Control. *TMC5072 Stepper Driver Datasheet*, May 2017. Rev. 1.22.
- [27] Trinamic Motion Control. *TMC2160 Stepper Driver Datasheet*, Feb. 2019. Rev. 1.03.
- [28] M. Walter. How accurate is microstepping really?, 2016.
<https://hackaday.com/2016/08/29/how-accurate-is-microstepping-really/>.
- [29] B. Welsh, P. Jelinsky, and R. Malina. The berkeley extreme ultraviolet calibration facility. *SPIE*, 0982, 1988.

APPENDICES

Appendix A

MANIPULATOR USER'S MANUAL

MANIPULATOR USER'S MANUAL

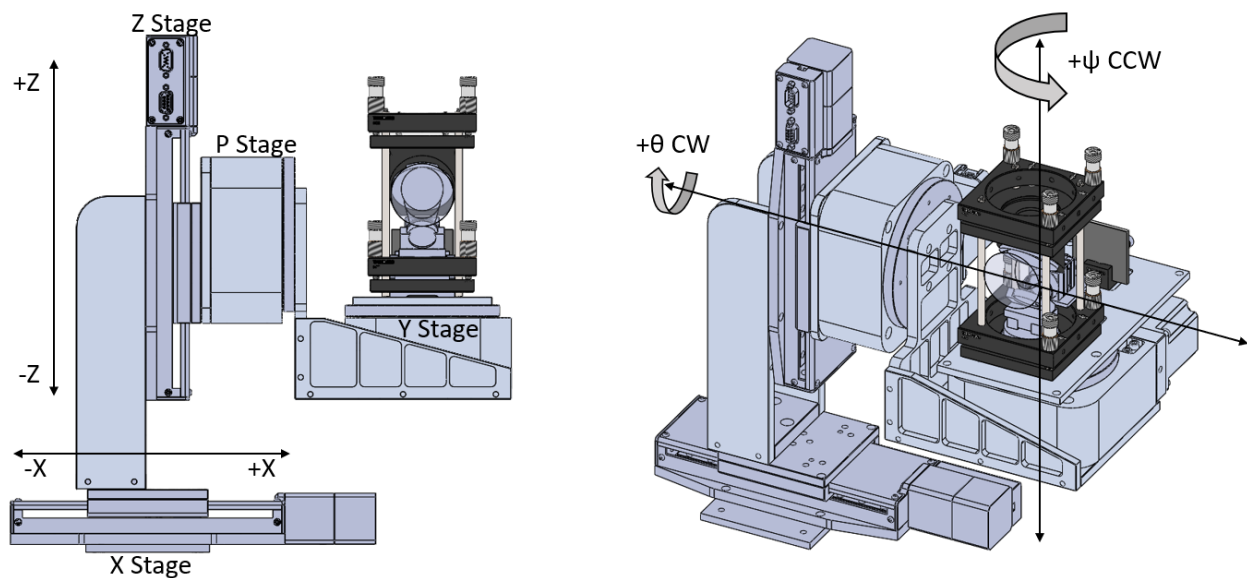
Jason L. Grillo

California Polytechnic State University, San Luis Obispo

1. FAMILIARIZATION

The purpose of this guide is to provide step-by-step instructions to operate the vacuum-compatible manipulator for the MUVI instrument. The GUI was built using the Tkinter python library, which is compatible with both Windows and Mac operating systems. The guide is written for a Windows platform, but the procedures throughout the document are similar for Mac OS.

Before getting started, the MUVI manipulator coordinate system is shown below.



2. OPERATIONAL NUANCES

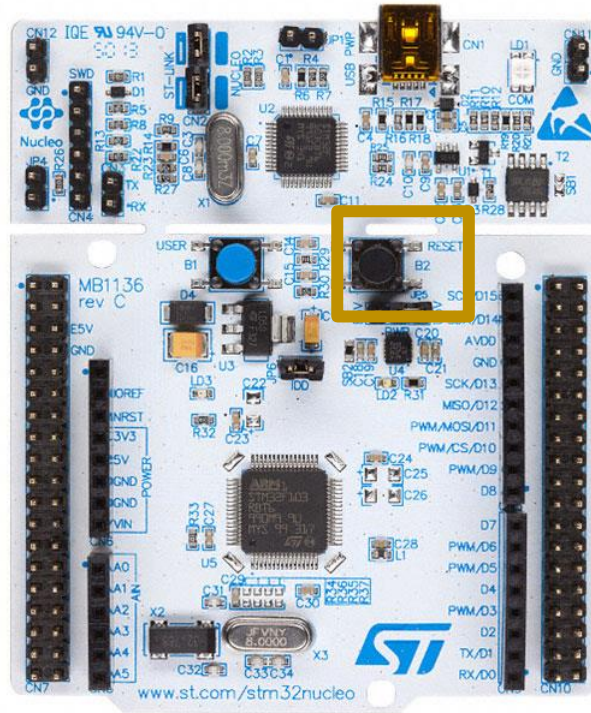
There are a few things the user must be aware of before operating the manipulator. Because the GUI/manipulator was developed with a short turn around, certain nuances have not been user-proofed from a software perspective. It may be possible to resolve these nuances with further GUI development.

2.1 Common Issues

Common bugs during GUI operation are documented in the following subsections.

2.1.1 Microcontroller Freezes with Bad GUI Command Timing

If GUI commands are sent too quickly, or if general input timing is out of sync, the microcontroller will error into an unknown state, meaning the microcontroller needs to be hard reset. The hard-reset button on the microcontroller is black and located to the right of the blue user input button, as shown in the figure below.



2.1.2 Microcontroller Cannot be Hard Reset if Limit Switches are Closed

It was found during testing that the microcontroller is unable to reset itself if a limit switch is closed when the hard-reset button is pressed. For the linear translation stages, the HD15 feedback harnesses must be physically disconnected from the PCB before pressing the hard-reset button. For the rotary stages, the user may simply unplug the limit switch jumpers from the PCB. After the microcontroller is successfully reset, the harnesses may be re-connected.

2.1.3 Only One Linear Stage may be Enabled at a Time

The linear stages draw about 0.9 A of current when they idle, and upwards of 2.2 A during operation. If both linear stages are enabled while another stage is moving, the bench supply will reach its current limit and the supply voltage will rapidly drop. A good rule of thumb is to only enable and move one linear stage motor at a time. Both rotary stage motors may be enabled at the same time.

2.2 Do's and Don'ts for Reliable Operation

- **DO NOT** – Consecutively click GUI buttons
- **DO** – Wait until the microcontroller prints feedback (encoder + limit switch) data before clicking another GUI button. When the microcontroller receives a command, it first sends a command acknowledgement, then it processes the command before executing the command. For reliable operation, it is recommended to wait at least a couple seconds after the microcontroller begins the execute the command before sending further commands. The microcontroller prints feedback data during normal operation, and GUI commands should only be sent at this time.

- **DO NOT** - Enable multiple motors at the same time
- **DO** – It is best practice to only enable and move one motor at a time.

For example, if the X and Y stages need to be moved to new targets the procedure would be:

1. Enable X motor
 - i. Wait for acknowledgement
 - ii. Wait for feedback data to display in the Manipulator Log
2. Move X motor
 - i. Wait for stage to finish both the coarse and fine movements
 - ii. Wait for feedback data to display in the Manipulator Log
3. Disable X motor (linear stage motors automatically disable after 30 seconds of being enabled, unless they are performing an operation)
 - i. Wait for acknowledgement
 - ii. Wait for feedback data to display in the Manipulator Log
4. Enable Y motor
 - i. Wait for acknowledgement
 - ii. Wait for feedback data to display in the Manipulator Log
5. Move Y motor
 - i. Wait for stage to finish both the coarse and fine movements
 - ii. Wait for feedback data to display in the Manipulator Log
6. Disable Y motor
 - i. Wait for acknowledgement
 - ii. Wait for feedback data to display in the Manipulator Log

3. OPENING THE GUI

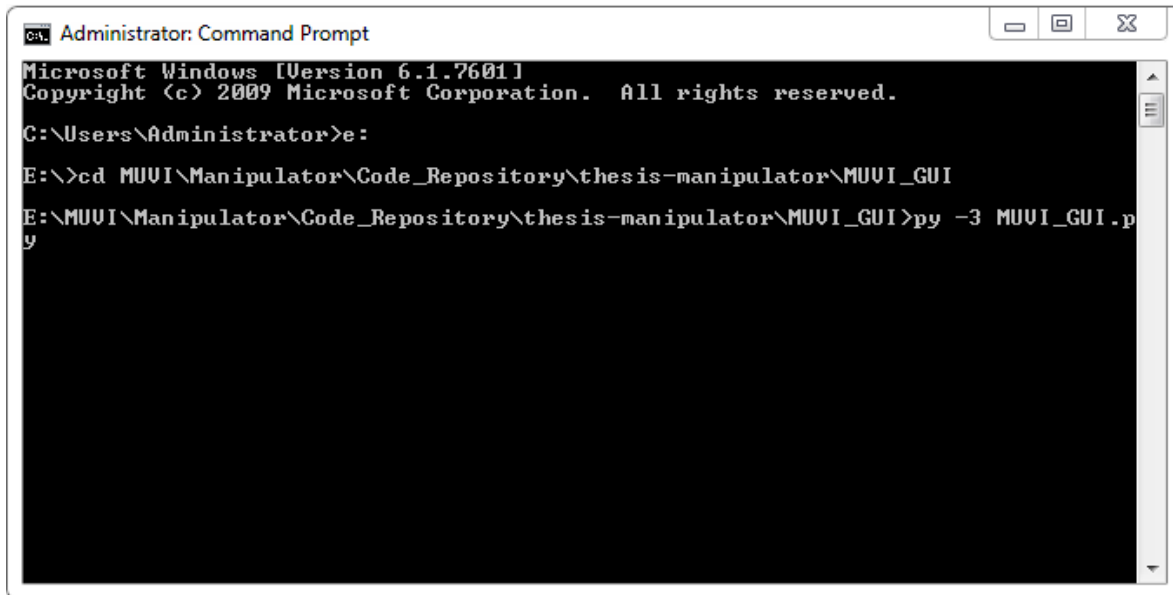
3.1 Command Prompt

The GUI is opened by executing the MUVI_GUI.py script.

1. Open the Windows Command Prompt.
2. Navigate to the directory that contains the MUVI_GUI.py script.

For example, the SSL lab machine requires the following commands to be entered:

- i. E:
- ii. `cd MUVI\Manipulator\Code_Repository\thesis-manipulator\MUVI_GUI`
3. Execute the MUVI_GUI.py script with the following command: ***py -3 MUVI_GUI.py***



```
Administrator: Command Prompt
Microsoft Windows [Version 6.1.7601]
Copyright (c) 2009 Microsoft Corporation. All rights reserved.

C:\Users\Administrator>e:
E:\>cd MUUI\Manipulator\Code_Repository\thesis-manipulator\MUUI_GUI
E:\MUUI\Manipulator\Code_Repository\thesis-manipulator\MUUI_GUI>py -3 MUUI_GUI.py
```

3.2 GUI Layout

The GUI contains five major sections that include two logs, stage feedback panels, stage control panels, and an instrument test panel. Each section is described below.

3.2.1 Manipulator Log

The Manipulator Log contains the print statements from the microcontroller that runs the RTOS handling motor commands and position feedback data. Because the microcontroller continuously prints its feedback data, the Manipulator Log does not print duplicate lines. When a command is sent from the GUI to the microcontroller, a command acknowledgement will be printed in this log. It is imperative that the user waits to send additional commands until feedback data is printed in the Manipulator Log after the acknowledgment is received.

3.2.2 GUI Log

The GUI Log documents the status of the GUI during automated sequences and prints the commands issued to the microcontroller. The timestamp of the GUI Log and Manipulator Log is consistent, meaning that the user may observe when a command was acknowledged by the microcontroller after it was sent by the GUI.

3.2.3 Status Panel

The position feedback for each stage is shown in this section. The speed of the stage is estimated from the change in position over the change in time between data readings. The current stage position may be marked and stored for later use. Limit switch feedback is displayed here as well.

3.2.4 Control Panel

The control panel is the main section of the GUI that issues commands to the microcontroller. There is a frame for each stage that allows the user to enable/disable the stage motor, set the stage target, and establish a new datum. Users may run automated sequences that enable, or zero, or

move all the stages. Additional functions include a stop button, a reset system button, and an input line to manually send commands to the microcontroller.

3.2.5 Test Panel

The user may upload custom motion and instrument parameters and run automated test sequences. The automated test sequences shown in this section are not completed for the MUVI manipulator.

MUVI Manipulator User Interface

Mechanical Engineering
CAL POLY

4 DOF Manipulator Interface

SSL UC Berkeley

Save Data and Close

Manipulator Log

Status Panel

X Translation: Position: None mm, Speed: None mm/s, Mark: None mm, -Limit, +Limit, Mark Position

Z Translation: Position: None mm, Speed: None mm/s, Mark: None mm, -Limit, +Limit, Mark Position

Yaw Rotation: Position: None deg, Speed: None deg/s, Mark: None deg, -Limit, +Limit, Mark Position

Pitch Rotation: Position: None deg, Speed: None deg/s, Mark: None deg, -Limit, +Limit, Mark Position

Control Panel

STOP

Send Command: m;p;1000;1;50;1500;50

Send

Move Stages

Enable All

Zero All

Reset System

X Translation: Enable: OFF, Target: 0.0000 mm, Jog Size: 0.0000 mm, Jog -, Jog +, Put Mark to Target, Set New Datum

Z Translation: Enable: OFF, Target: 0.0000 mm, Jog Size: 0.0000 mm, Jog -, Jog +, Put Mark to Target, Set New Datum

Yaw Rotation: Enable: OFF, Target: 0.0000 deg, Jog Size: 0.0000 deg, Jog -, Jog +, Put Mark to Target, Set New Datum

Pitch Rotation: Enable: OFF, Target: 0.0000 deg, Jog Size: 0.0000 deg, Jog -, Jog +, Put Mark to Target, Set New Datum

Test Panel

Load Motion Parameters

Load Instrument Parameters

Config File:

FOV Sweep

Boresight

Stray Light Sweep

Pitch (θ): 0.0000 deg

Yaw (ψ): 0.0000 deg

Move Instrument

Capture Image

Manipulator Log

GUI Log

Created by: Jason Grillo
 Cal Poly Mechanical Engineering
 In Collaboration with UC Berkeley Space Sciences Laboratory
 © 2019, All Rights Reserved

4. LOADING PARAMETERS

Test Panel

Load Motion Parameters

Load Instrument Parameters

Config File:

FOV Sweep

Boresight

Stray Light Sweep

Pitch (θ): deg Yaw (ψ): deg

Move Instrument

Capture Image

4.1 Load Motion Parameters

The motion parameters define variables that are unique to each stage. A list of the different parameters and their descriptions is shown in the table below. The motion parameters should be loaded every time a new GUI session is created and before commanding stage movements.

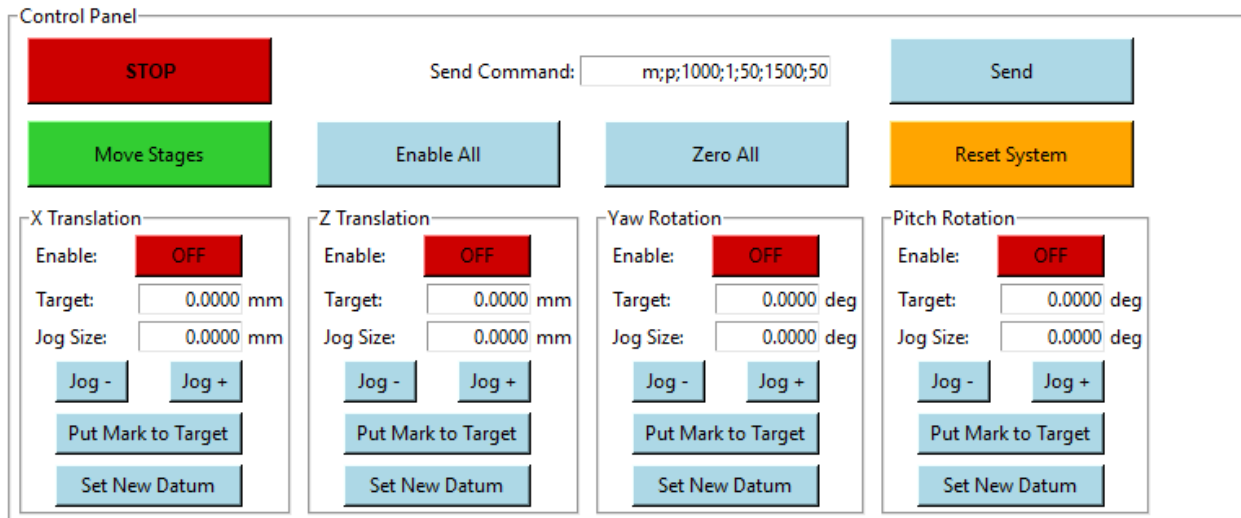
Parameter	Description
direction	Configures the positive coordinate direction for the stage. Value = 1 to keep default direction. Value = -1 to switch the positive/negative coordinates.
init_speed	Defines the initial frequency (Hz) at which the ramp profile generator begins.
max_speed	Defines the maximum allowable frequency (Hz) the step generator may achieve.
accel	Defines the acceleration rate (Hz/s) of the ramp profile.
mot_SPR	The stepper motor's number of full steps per revolution.
pitch	The linear stage's lead screw pitch (mm of travel per full revolution)
gear_ratio	The rotary stage's worm gear ratio.
enc_CPR	The encoder's number of Counts per Revolution
overshoot	The number of steps to overshoot the target for backlash mitigation purposes.
move1_uS	The number of microsteps for the first (coarse) movement.
move2_uS	The number of microsteps for the second (fine) movement.
restore_encoder	The last encoder value of the previous GUI session. This removes the need to zero the stages whenever the GUI is closed.
MC_period	The period at which the microcontroller Hub Task Function operates (ms).

4.2 Load Instrument Parameters

The instrument parameters define variables that are unique to the instrument, independent of the stage hardware that comprises the manipulator. A list of the different parameters and their descriptions is shown in the table below. The instrument parameters should be loaded every time a new GUI session is created and before commanding stage movements.

Parameter	Description
datum_offset	Defines the number of stage units (mm or deg) the datum is from the zeroing hard stop
travel	Defines the range of travel for the stage (mm or deg)
iris_diameter	The diameter of the entrance pupil that defines the FOV (mm)
FOV	Defines the instrument's FOV (deg)
r_bot1	Quaternion defined from the iris center to the bottom mirror (point 1)
r_bot2	Quaternion defined from the iris center to the bottom mirror (point 2)
r_bot3	Quaternion defined from the iris center to the bottom mirror (point 3)
r_top4	Quaternion defined from the iris center to the top mirror (point 1)
r_top5	Quaternion defined from the iris center to the top mirror (point 2)
r_top6	Quaternion defined from the iris center to the top mirror (point 3)
beam1	Quaternion defining the laser beam (point 1)
beam2	Quaternion defining the laser beam (point 2)

5. ZEROING THE STAGES



5.1 When to Zero

Zeroing the stages allows the GUI to know the absolute position of the stage relative to a hard stop. The stages do not need to be zeroed upon every GUI startup if the Load Motion Parameters feature is used to restore the last known stage position. However, it is recommended to zero a stage if confidence in the position of a stage is reduced.

5.2 Zeroing Procedure

1. Enable the stage/s to zero and disable the remaining stage/s. Only enabled stages will be zeroed.
2. Once the desired stages are enabled, click the “Zero All” button.
3. The GUI log documents the status of the zeroing sequence and will indicate when the zeroing procedure is finished. Normal GUI operation may continue after the zeroing procedure is complete.

6. POSITIONING THE STAGES

Control Panel

STOP

Send Command: Send

Move Stages Enable All Zero All Reset System

X Translation Z Translation Yaw Rotation Pitch Rotation

Enable: OFF Enable: OFF Enable: OFF Enable: OFF

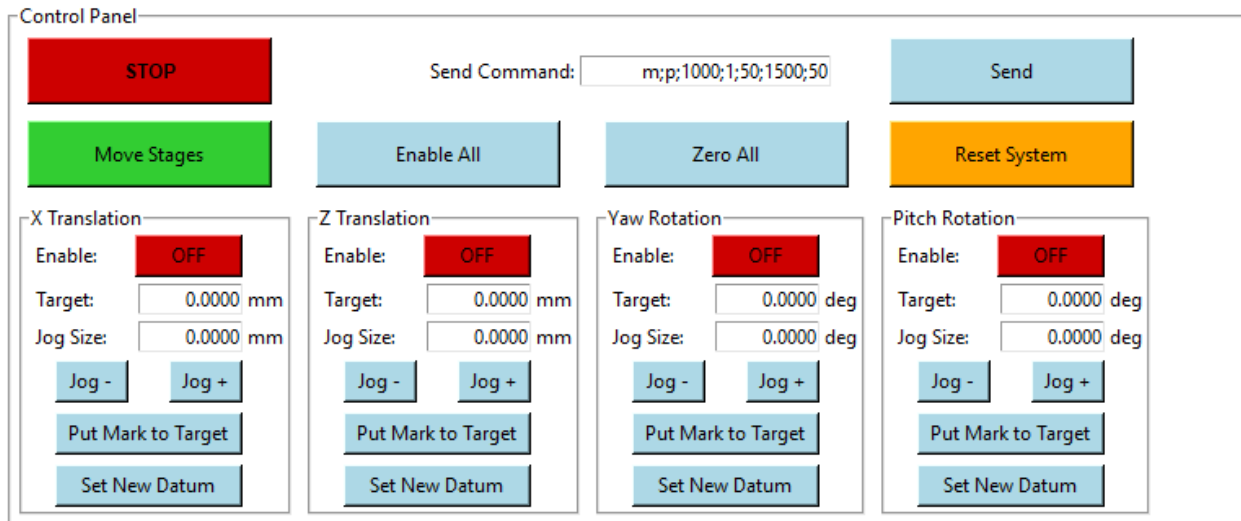
Target: 0.0000 mm Target: 0.0000 mm Target: 0.0000 deg Target: 0.0000 deg

Jog Size: 0.0000 mm Jog Size: 0.0000 mm Jog Size: 0.0000 deg Jog Size: 0.0000 deg

Jog - Jog + Jog - Jog + Jog - Jog + Jog - Jog +

Put Mark to Target Put Mark to Target Put Mark to Target Put Mark to Target

Set New Datum Set New Datum Set New Datum Set New Datum



6.1 Setting the Target

The desired target position may be typed in the “Target” input box. The target is an absolute position from the datum. Floating point and integer values are supported.

6.1.1 Jogging

The target value may be automatically incremented (Jog +) or decremented (Jog -) by the value specified in the “Jog Size” input box. This feature removes the need of an external calculator when the target needs to be adjusted.

6.2 Moving the Stages

1. Enable the stage/s to move and disable the remaining stage/s. Only enabled stages will be moved to their target position.
2. Once the desired stages are enabled, click the “Move Stages” button.
3. The GUI log documents the status of the move sequence and will indicate when it is finished moving the stage/s. Normal GUI operation may continue after the move sequences are complete.

6.3 Stopping

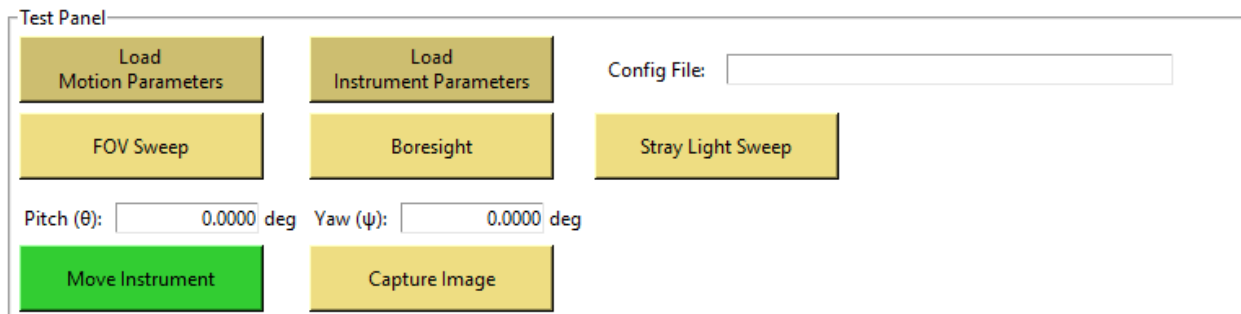
The stages may be stopped during a movement by pressing the “STOP” button. This sends an abort command to the microcontroller that disables all the stepper motors. It is recommended to use this feature because it effectively shuts down all the motors simultaneously and abandons the operation. The GUI is reset to its idle state after the “STOP” button is pressed.

An alternative method to stop a stage during its movement is to disable a motor individually. However, only that stage will be disabled – all other enabled stages would continue their operation.

6.4 Establishing a New Datum

A new datum may be established by using the “Set New Datum” button. Once clicked, the current position (which is relative to the previous datum) is added to the datum offset parameter to establish the new datum position relative to the zeroing hard stop.

7. RUNNING TESTS



7.1 Setup Manipulator

Before running an automated sequence, ensure the Motion Parameters and Instrument Parameters are loaded into the GUI.

7.2 Automated Test Sequences

Predetermined tests may be run by clicking the “FOV Sweep” or “Boresight” or “Stray Light Sweep” buttons. Although they are not currently setup, these buttons would orient the manipulator at various field angles and capture images with minimal user input.

7.3 Instrument Field Angles

The input boxes labeled “Pitch (θ)” and “Yaw (ψ)” may be used to specify the field angle orientation of the manipulator. Once the “Move Instrument” button is pressed, the field angle target is fed through the translation compensation algorithm (translated to Python from Matlab), and the individual stage targets are returned. The user would then press the “Capture Image” button to take an image once the manipulator is at the field angle. Although this feature is not currently operational, its implementation would require minimal development.

8. CLOSING THE GUI

There are two ways of closing the GUI. The first is to exit by pressing the traditional window “X” in the top right corner. By doing this, the GUI session is terminated, and all test data is lost. It is recommended to use the “Save Data and Close” button, which writes and saves the Manipulator Log to a CSV file before terminating the GUI session.

9. SOFTWARE DEVELOPMENT

Updating the software that runs the GUI and microcontroller is straightforward. The code repository is located on a GitHub server that controls revisions. Follow the guidelines below for updating the software for the MUVI manipulator. The GitHub repository may be opened online: <https://github.com/jgrillo20/vacuum-manipulator>

9.1 Pull Latest Code Revision (master → local)

To make sure the local software directory is up to date with the master branch, simply force pull the master branch into the local directory. Before doing this, it is imperative that software changes that have not been pushed to the master branch are either saved in a separate directory or pushed to master, since the force pull will overwrite the local directory.

1. Open the Command Prompt and navigate to the parent directory containing the GitHub project.
 - i. For example, on the SSL lab machine the manipulator project is in *E:\MUVI\Manipulator\Code_Repository\thesis-manipulator*
2. Once the path is set, type the following git commands to pull the master branch:
 - i. `git fetch --all`
 - ii. `git reset --hard origin/master`
3. Now the local directory will be reset to contain the master branch. Software may now be written or changed using whichever IDE the user prefers.

9.2 Push Modified Code (local → master)

After the software has been modified, uploading the changes to the master branch consists of the following steps.

1. Open the Command Prompt and navigate to the parent directory containing the GitHub project.
 - i. For example, on the SSL lab machine the manipulator project is in *E:\MUVI\Manipulator\Code_Repository\thesis-manipulator*
2. Once the path is set, type the following git commands to push code to the master branch:
 - iii. `git add .`
 - iv. `git commit -am “Type upload description here”`
 - v. `git push origin master`
3. The master branch will now be updated with the changes

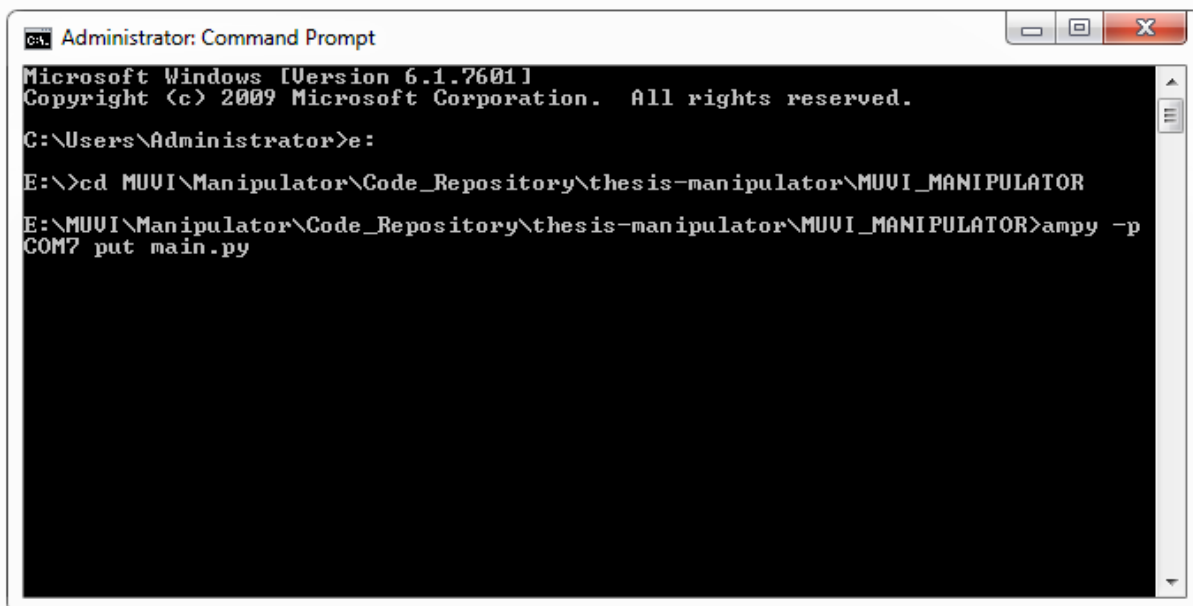
9.3 Load Code onto Nucleo Microcontroller

The Nucleo microcontroller may be programmed by using the Ampy tool from Adafruit. This tool allows a host computer to load files and run code on a MicroPython board. After installing Ampy, follow this procedure.

1. Open the Command Prompt and navigate to the MUVI_MANIPULATOR directory
2. To load a file onto the microcontroller, simply enter:

ampy -p <com port name> put <filename>.py

where <com port name> is the name of the serial port assigned to the microcontroller and <filename> is the name of the python file to upload. See example below where the file “main.py” is uploaded through COM7.

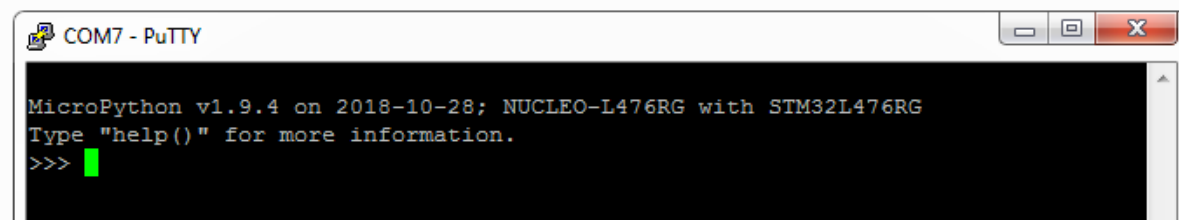


```
Administrator: Command Prompt
Microsoft Windows [Version 6.1.7601]
Copyright (c) 2009 Microsoft Corporation. All rights reserved.

C:\Users\Administrator>e:
E:\>cd MUVI\Manipulator\Code_Repository\thesis-manipulator\MUUI_MANIPULATOR
E:\MUUI\Manipulator\Code_Repository\thesis-manipulator\MUUI_MANIPULATOR>ampy -p
COM7 put main.py
```

9.3.1 Open Nucleo Serial Port (Software Reset)

Sometimes it is useful to open the serial port to see what the microcontroller is doing. To open the serial port, open PuTTY, set the serial line to the appropriate port, and the baudrate to 115200. If the microcontroller is not running the RTOS, as shown in the below example, simply press CTRL+D to perform a software reset.



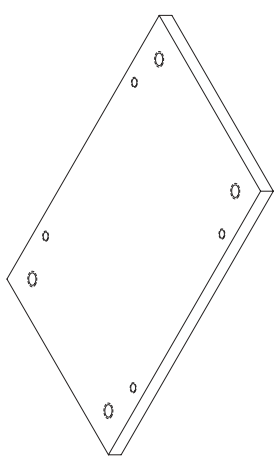
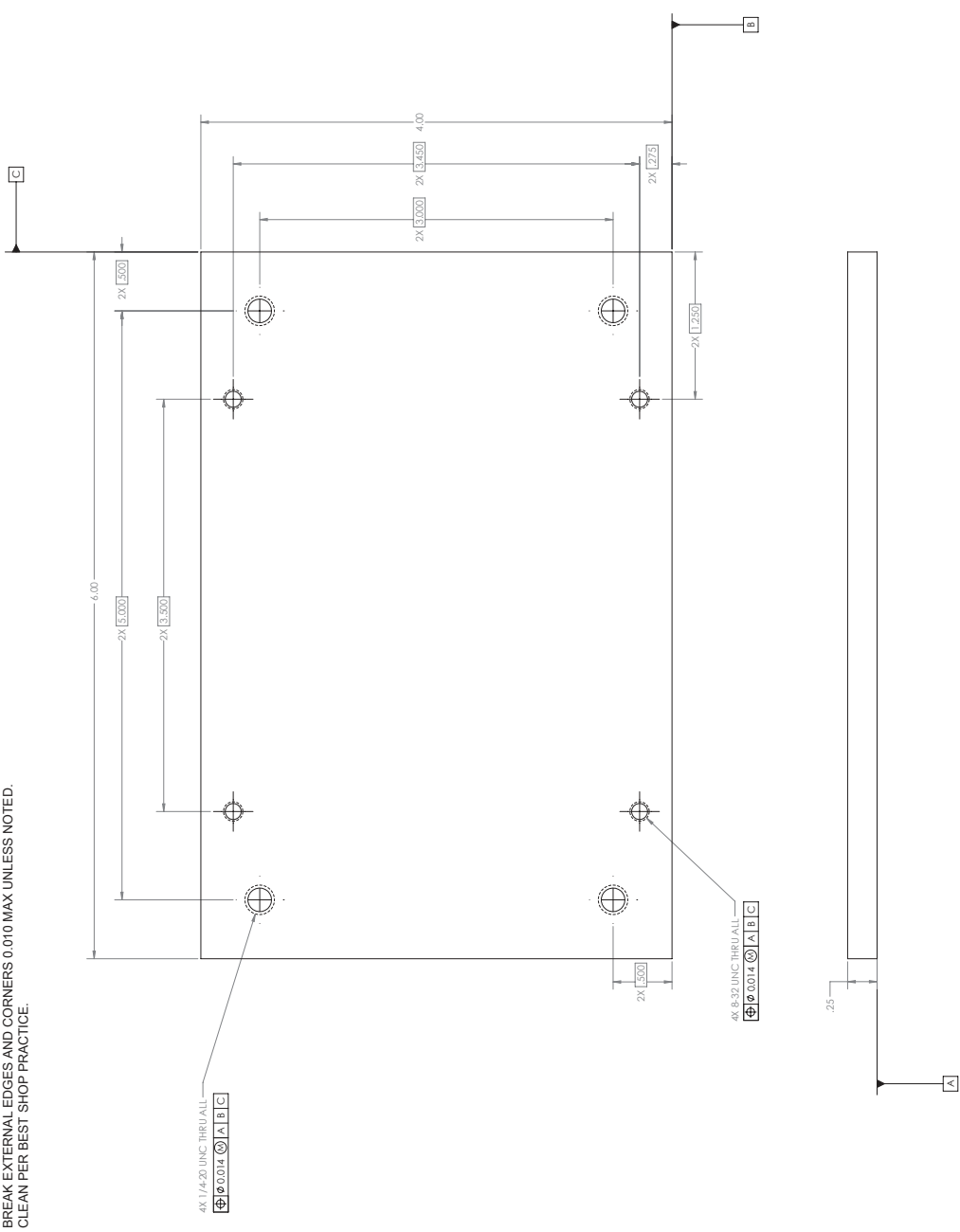
```
COM7 - PuTTY
MicroPython v1.9.4 on 2018-10-28; NUCLEO-L476RG with STM32L476RG
Type "help()" for more information.
>>> █
```


Appendix B

MECHANICAL DRAWINGS

1 2 3 4 5 6 7 8

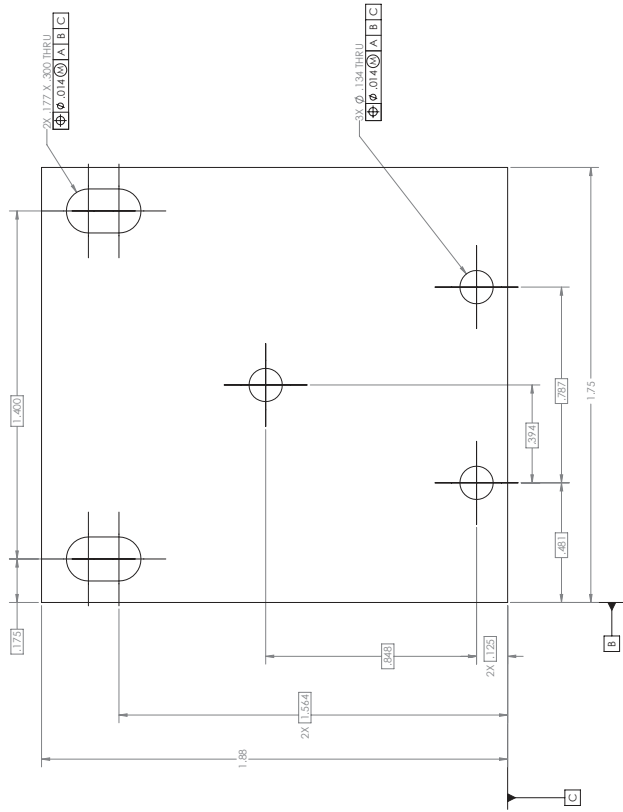
NOTES:
 1. BREAK EXTERNAL EDGES AND CORNERS 0.010 MAX UNLESS NOTED.
 2. CLEAN PER BEST SHOP PRACTICE.



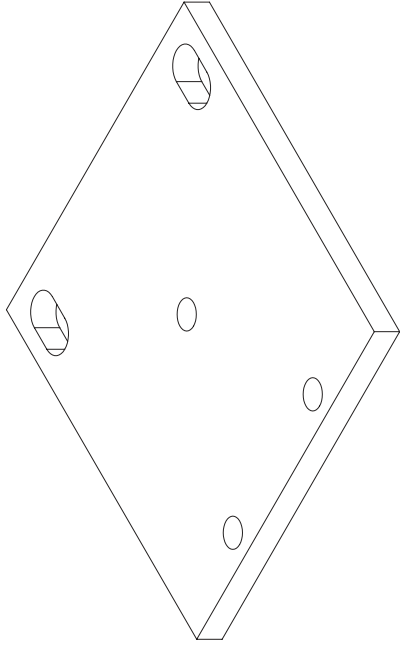
FOR REFERENCE ONLY

SPACE SCIENCES LABORATORY		NAME		DATE	
7 GAUSSWAY		ASG		08/21/18	
BRIDGECG.0210					
TITLE:		STAGE ADAPTER PLATE		REV	
SIZE DWG. NO.:		D		MMU1_MAN_GSE.001	
SCALE 1:1		WEIGHT 0.19 KG		SHEET 1 OF 1	
QTY: 1		APPROVAL:		DATE:	
DRAWN:		CHECKED:		DATE:	
DESIGNED:		APPROVED:		DATE:	
MATERIALS:		PARTS:		DATE:	
DIMENSIONS:		TOLERANCES:		DATE:	
FINISHES:		SURFACES:		DATE:	
COATINGS:		TREATMENTS:		DATE:	
ASSEMBLY:		DISASSEMBLY:		DATE:	
TESTING:		INSPECTION:		DATE:	
REVISIONS:		REVISIONS:		DATE:	
REVISIONS:		REVISIONS:		DATE:	
REVISIONS:		REVISIONS:		DATE:	

- NOTES:
 1. BREAK EXTERNAL EDGES AND CORNERS 0.010 MAX UNLESS NOTED.
 2. CLEAN PER BEST SHOP PRACTICE.



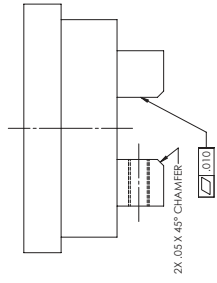
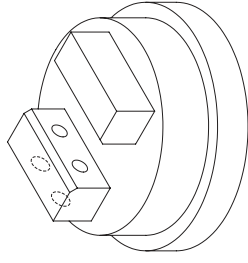
FOR REFERENCE ONLY



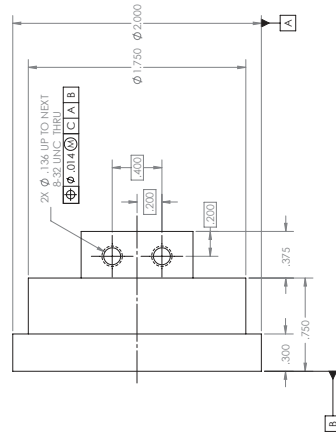
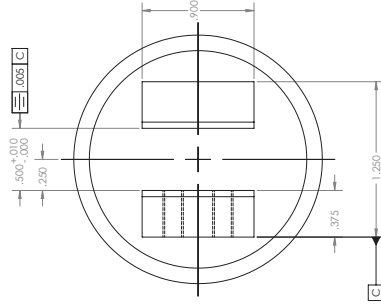
DRAWN BY		DATE		SPACE SCIENCES LABORATORY	
CHECKED BY		REV		7 GAUSSWAY	
APP'D BY		REV		BRIELLE, G. 2/10	
TITLE:		QTY: 1		REV	
CAMERA MOUNT ADAPTER		SCALE: 4:1		D IMU/1MAN_GSE.011 -	
SIZE (DWG. NO.):		WEIGHT: 0.19 KG		SHEET 1 OF 1	
D IMU/1MAN_GSE.011					
SCALE: 4:1					
WEIGHT: 0.19 KG					
SHEET 1 OF 1					

MATERIALS		FINISHES		TOLERANCES	
ITEM NO.	DESCRIPTION	FINISH	TOLERANCE	ITEM NO.	DESCRIPTION
1	ALUMINUM 6061-T6	ANODIZED	±0.005	1	ALUMINUM 6061-T6
2	STAINLESS STEEL	POLISHED	±0.005	2	STAINLESS STEEL
3	COPPER	PLATED	±0.005	3	COPPER
4	BRASS	PLATED	±0.005	4	BRASS
5	STEEL	PLATED	±0.005	5	STEEL
6	ALUMINUM 6061-T6	ANODIZED	±0.005	6	ALUMINUM 6061-T6
7	STAINLESS STEEL	POLISHED	±0.005	7	STAINLESS STEEL
8	COPPER	PLATED	±0.005	8	COPPER
9	BRASS	PLATED	±0.005	9	BRASS
10	STEEL	PLATED	±0.005	10	STEEL

- NOTES:
 1. BREAK EXTERNAL EDGES AND CORNERS 0.010 MAX UNLESS NOTED.
 2. CLEAN PER BEST SHOP PRACTICE.



FOR REFERENCE ONLY



NO.	DATE	BY	CHKD.
1	08/15/18	MMU	MMU
2			
3			
4			
5			
6			
7			
8			
9			
10			

FOR REFERENCE ONLY
 THIS DRAWING IS THE PROPERTY OF
 SPACE SCIENCES LABORATORY
 AND IS NOT TO BE REPRODUCED OR
 TRANSMITTED IN ANY FORM OR BY
 ANY MEANS, ELECTRONIC OR MECHANICAL,
 INCLUDING PHOTOCOPYING, RECORDING,
 OR BY ANY INFORMATION STORAGE AND
 RETRIEVAL SYSTEM.

SPACE SCIENCES LABORATORY
 7 GAUSSWAY
 BERKELEY, CA 94720

TITLE:
 BOTTOM MIRROR MOUNT

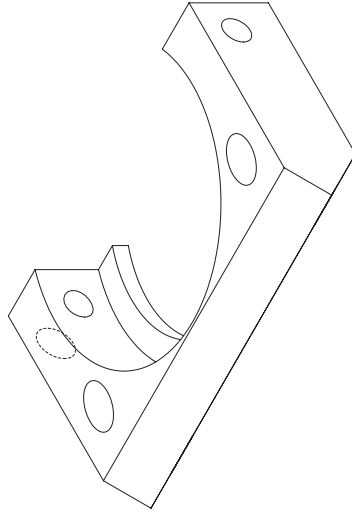
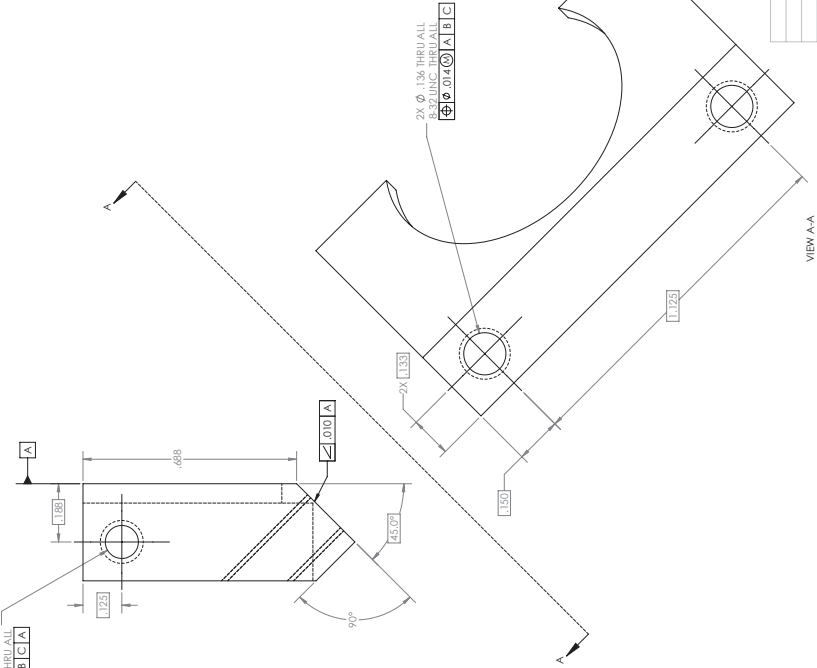
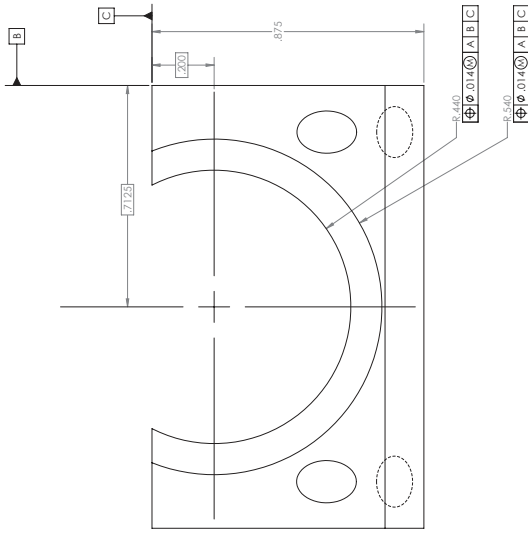
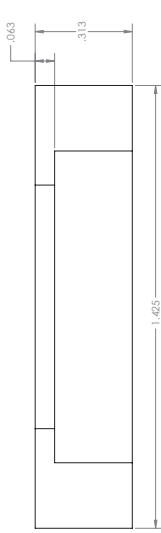
SIZE: DWG. NO. D IMU1_MAN_GSE_012
 SCALE: 2:1 WEIGHT: 0.19 KG

QTY: 1

REV: -

SHEET 1 OF 1

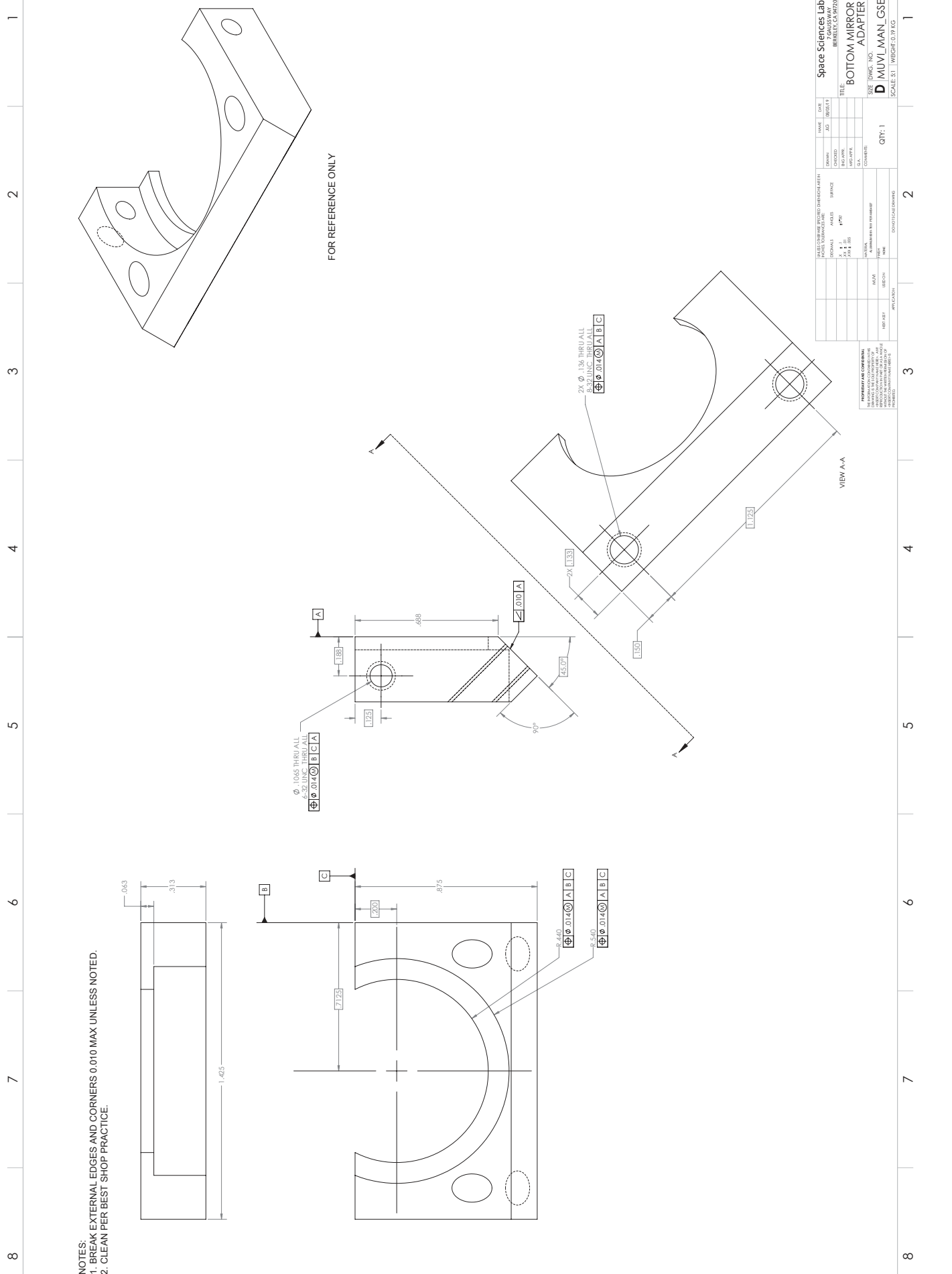
- NOTES:
 1. BREAK EXTERNAL EDGES AND CORNERS 0.010 MAX UNLESS NOTED.
 2. CLEAN PER BEST SHOP PRACTICE.



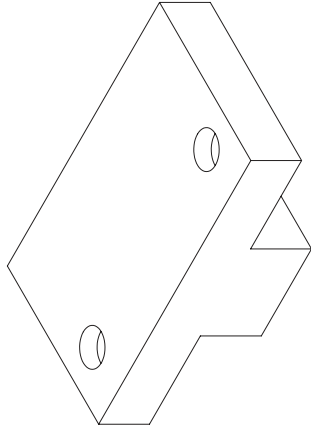
FOR REFERENCE ONLY

SPACE SCIENCES LABORATORY		DATE	10/15/18
7 GAUSSWAY		ISSUED	
BRIELLE, G. 2/10		REV	
TITLE: BOTTOM MIRROR MOUNT ADAPTER			
SIZE: DWG. NO. D IMUVMAN_GSE_013			
SCALE: S:1 WEIGHT: 0.19 KG			
APPLICATOR		QTY: 1	REV
PART		DESCRIPTION	REV
SUBPART		DESCRIPTION	REV
MATERIAL		DESCRIPTION	REV
FINISH		DESCRIPTION	REV
TOLERANCES UNLESS OTHERWISE SPECIFIED:			
FRACTIONS	DECIMALS	ANGLES	SURFACE
XX	XX	XX	XX
XX	XX	XX	XX
XX	XX	XX	XX
XX	XX	XX	XX
XX	XX	XX	XX

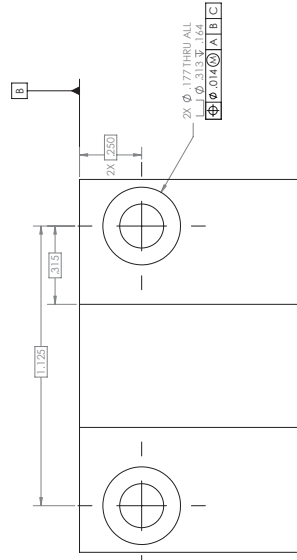
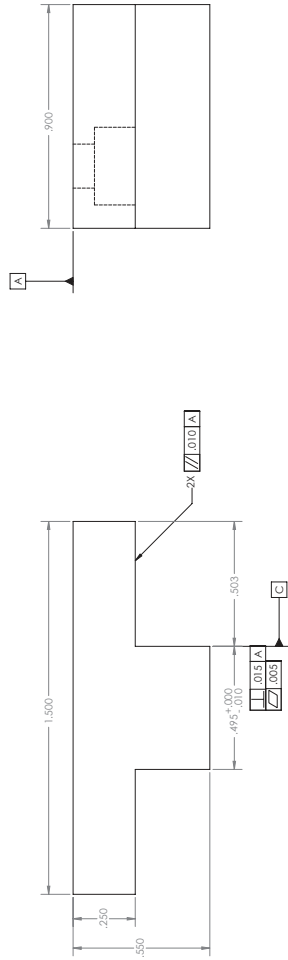
FOR FABRICATOR CONSIDERATION:
 DIMENSIONS TO BE USED FOR FABRICATING THE PART SHALL BE THE DIMENSIONS SHOWN ON THIS DRAWING UNLESS OTHERWISE SPECIFIED.



- NOTES:
 1. BREAK EXTERNAL EDGES AND CORNERS 0.010 MAX UNLESS NOTED.
 2. CLEAN PER BEST SHOP PRACTICE.



FOR REFERENCE ONLY



A

B

SPACE SCIENCES LABORATORY		DATE	11/20/18
7 GAUSSWAY		ASG	11/20/18
BIRRELL, G.S. 210		DESIGNED BY	
TITLE: BOTTOM MIRROR MOUNT SLIDER		DESIGNED BY	
SIZE	DWG. NO.	QTY:	1
D	IMUVMAN_GSE_014	REV	-
SCALE	4:1	WEIGHT	0.19 KG
SHEET 1 OF 1			

APPROVAL	DESIGNED BY	DATE
APPROVAL	DESIGNED BY	DATE

APPROVAL	DESIGNED BY	DATE
APPROVAL	DESIGNED BY	DATE

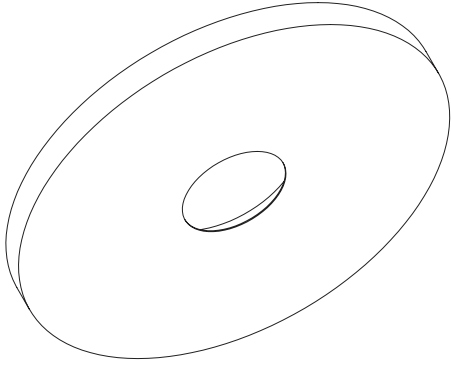
APPROVAL	DESIGNED BY	DATE
APPROVAL	DESIGNED BY	DATE

APPROVAL	DESIGNED BY	DATE
APPROVAL	DESIGNED BY	DATE

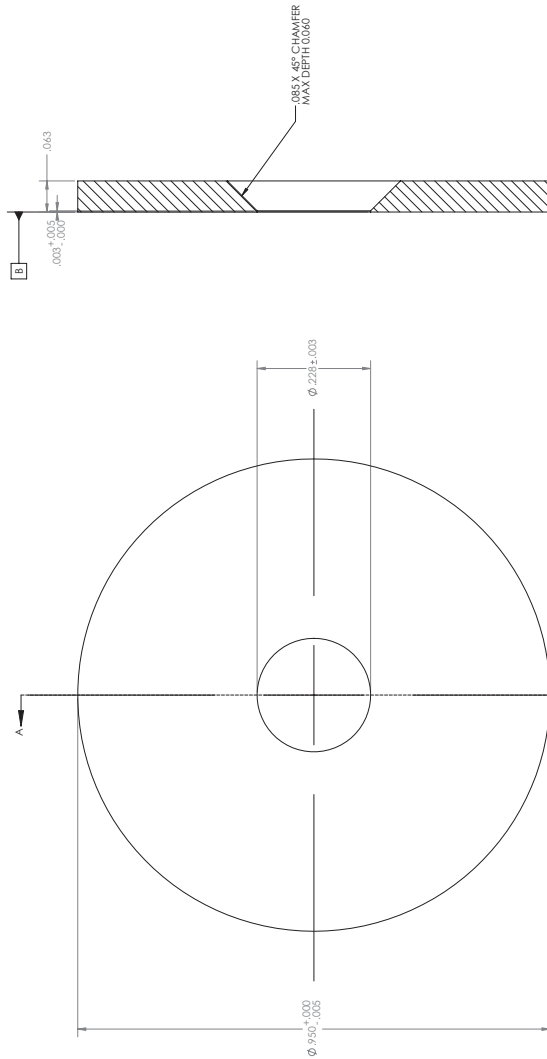
APPROVAL	DESIGNED BY	DATE
APPROVAL	DESIGNED BY	DATE

APPROVAL	DESIGNED BY	DATE
APPROVAL	DESIGNED BY	DATE

- NOTES:
 1. BREAK EXTERNAL EDGES AND CORNERS 0.010 MAX UNLESS NOTED.
 2. CLEAN PER BEST SHOP PRACTICE.



FOR REFERENCE ONLY

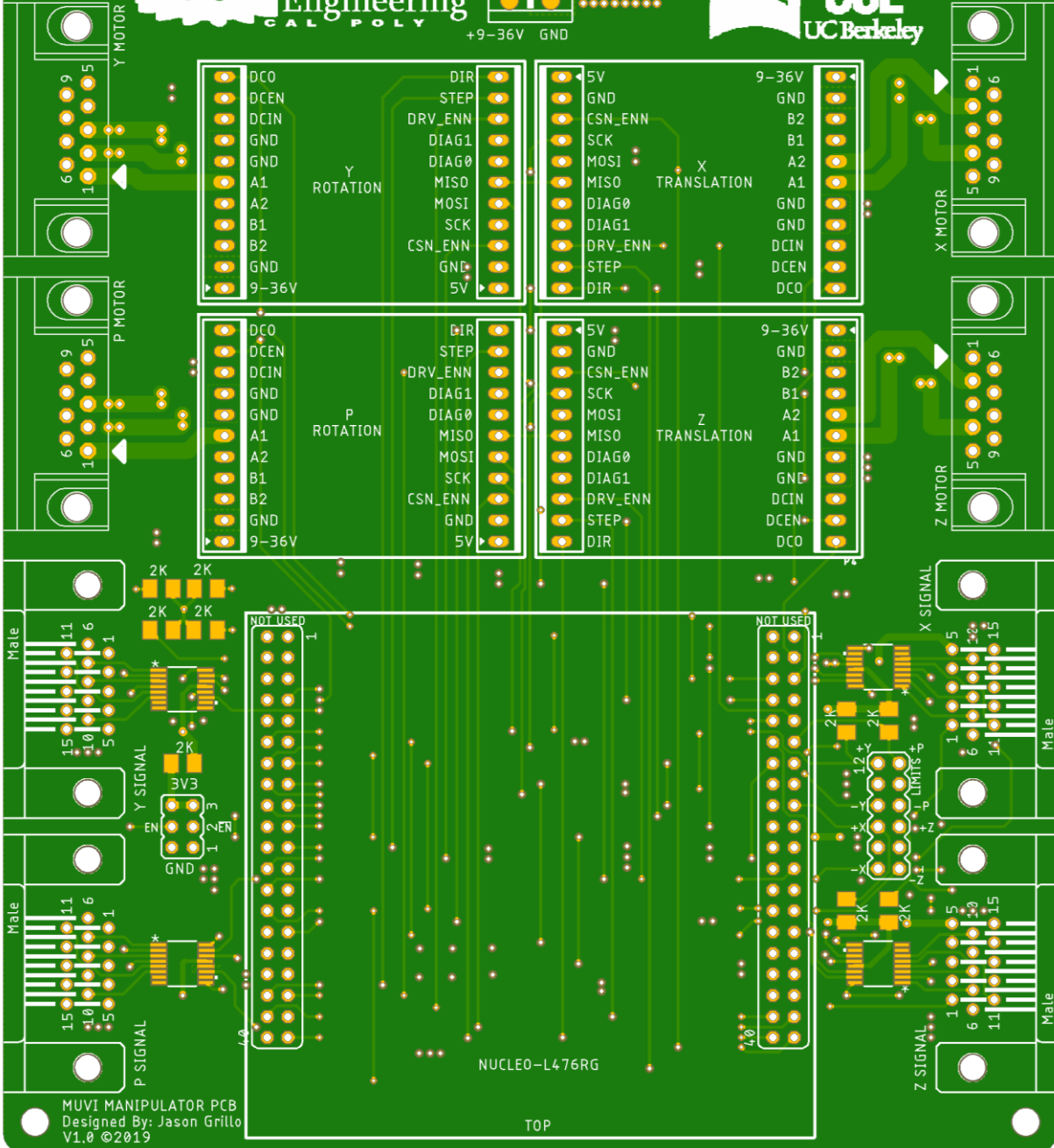
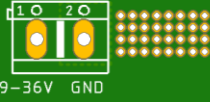


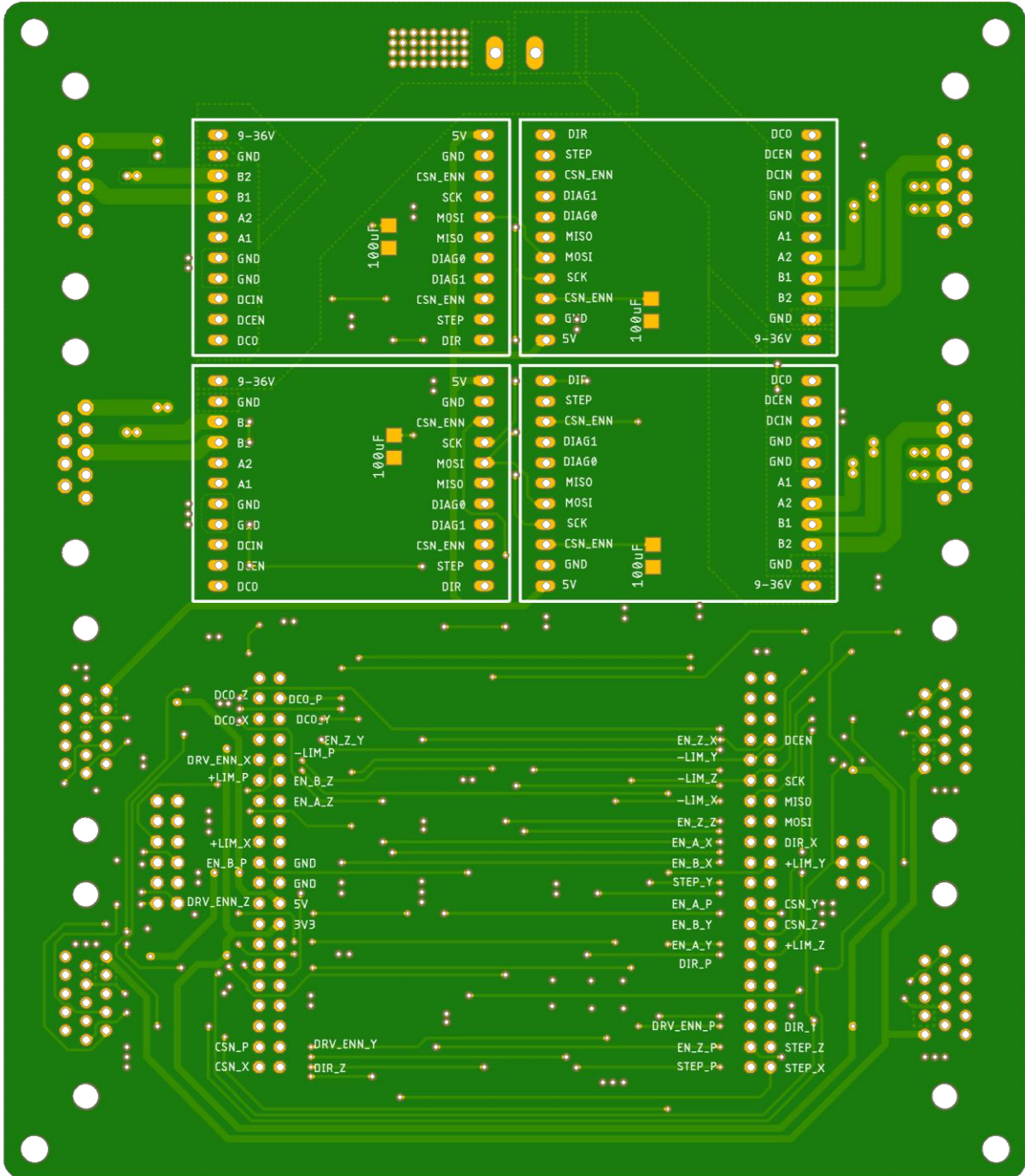
SECTION A-A

DRAWN BY		DATE		SPACE SCIENCES LABORATORY	
CHECKED BY		AGE		7 GAUSSWAY	
APPROVED BY		REV		BRENDEL, G.S/210	
MATERIAL		QUANTITY		TITLE	
FINISH		SPECIFICATION		INTERNAL IRIS PLATE	
TOLERANCES		DIMENSIONS		SIZE DWG. NO.	
DIMENSIONS		DIMENSIONS		D IMUVMAN_GSE_015	
DIMENSIONS		DIMENSIONS		SCALE B:1 WEIGHT:0.19 KG	
DIMENSIONS		DIMENSIONS		SHEET 1 OF 1	

Appendix C

ELECTRICAL SCHEMATICS





Appendix D

SOFTWARE

The GUI and RTOS software that was developed for this project may be found at <https://github.com/jgrillo20/vacuum-manipulator>. The following Matlab code is attached below:

1. Optical GSE Simulation
2. Ramp Profile Simulation
3. Spot Centroid Algorithm

Contents

- MUVI Manipulator Full Optical GSE Simulation
- Define Unit Coordinate Vectors and Ray Intersection Distance
- Define Rotation Quaternions
- Define Component Offset Quaternions Relative to Origin (mm)
- Define Initial Mirror Quaternions (mm)
- Calculate Initial Boresight Location on Detector Plane
- Calculate Rotated Quaternions
- Calculate Normal Vectors
- Calculate Beam Line Through Rotated Optics Assembly
- Calculate Translation Compensation
- Translate Mirrors
- Calculate Beam Line Through Rotated and Translated Optics Assembly
- Re-Calculate Translation Compensation Based on Center of Rotation Offset
- Plot Results

MUVI Manipulator Full Optical GSE Simulation

Written by: Jason Grillo 11/12/2019

```
clear all, close all, clc

% PLOT = 'True';
PLOT = 'False';
```

Define Unit Coordinate Vectors and Ray Intersection Distance

```
unitx = [-1 0 0];
unity = [0 -1 0];
unitz = [0 0 1];
origin = [0 0 0];

% Distance from the origin (iris center) to the ray intersection point
l_focus = 10.823; % mm
```

Define Rotation Quaternions

```
% Multiplier if you want a circular field angle (unit circle vectors)
% unit_circ = [sqrt(2)/2, sqrt(2)/2];
unit_circ = [1,1];

psi = 7*unit_circ(1); % YAW - deg of rotation
theta = -7*unit_circ(2); % PITCH - deg of rotation

% Define rotation quaternions for pitch
```

```

q = [cosd(theta/2) unitx*sind(theta/2)];
q_star = [cosd(theta/2) -unitx*sind(theta/2)];

% Define rotation quaternions for yaw
q_y = [cosd(psi/2) unitz*sind(psi/2)];
q_star_y = [cosd(psi/2) -unitz*sind(psi/2)];

```

Define Component Offset Quaternions Relative to Origin (mm)

```

center_rotation = [0 -0.014 -0.490 -0.106]; % the center of rotation defined relative to the
origin (iris center)
detector_offset = [0 0 .145/tand(7) 0]; % the offset of the detector from its nominal position
boresight_offset = [0 -.0195 0 0.1045]; % the spot centroid offset of the boresight beam

```

Define Initial Mirror Quaternions (mm)

```

% CAD Values
% r_bot1 = [0 -12.7 20.882 2.312] + center_rotation;
% r_bot2 = [0 0 11.901 -6.669] + center_rotation;
% r_bot3 = [0 12.7 20.882 2.312] + center_rotation;
% r_top4 = [0 -25.4 23.324 37.204] + center_rotation;
% r_top5 = [0 0 5.364 19.244] + center_rotation;
% r_top6 = [0 25.4 23.324 37.204] + center_rotation;
% beam1 = [0 0 80 32.45] + center_rotation + boresight_offset;
% beam2 = [0 0 18.57 32.45] + center_rotation + boresight_offset;
r_FOV1 = [0 0 12.359 -6.211] + center_rotation;
r_FOV2 = [0 -7.876 18.57 0] + center_rotation;
r_FOV3 = [0 0 29.329 10.759] + center_rotation;
r_FOV4 = [0 0 5.501 19.381] + center_rotation;
r_FOV5 = [0 -16.571 18.57 32.45] + center_rotation;
r_FOV6 = [0 0 41.206 55.086] + center_rotation;
r_iris1 = [0 -2.9 0 0] + center_rotation;
r_iris2 = [0 0 0 -2.9] + center_rotation;
r_iris3 = [0 0 0 2.9] + center_rotation;
r_detc1 = [0 -10 -1_focus 0] + center_rotation + detector_offset;
r_detc2 = [0 0 -1_focus -10] + center_rotation + detector_offset;
r_detc3 = [0 0 -1_focus 10] + center_rotation + detector_offset;

% Measured Values
r_bot1 = [0 -12.7191 21.6663 3.6961] + center_rotation;
r_bot2 = [0 -0.4506 12.2728 -5.8707] + center_rotation;
r_bot3 = [0 12.2255 21.2872 3.0825] + center_rotation;
r_top4 = [0 -25.4325 23.8267 37.9334] + center_rotation;
r_top5 = [0 -0.2472 5.8059 19.9078] + center_rotation;
r_top6 = [0 25.1571 23.8419 37.9761] + center_rotation;
beam1 = [0 0 54.7426 32.3248] + center_rotation + boresight_offset;
beam2 = [0 0 17.9768 32.3248] + center_rotation + boresight_offset;

% Convert to Image Coordinate System
% The quaternions were defined with different axes than the
% manipulator/image CSYS.. this will correct that discrepancy
image_coord_cys = [1 -1 -1 1];
r_bot1 = image_coord_cys.*r_bot1;

```

```

r_bot2 = image_coord_cys.*r_bot2;
r_bot3 = image_coord_cys.*r_bot3;
r_top4 = image_coord_cys.*r_top4;
r_top5 = image_coord_cys.*r_top5;
r_top6 = image_coord_cys.*r_top6;
beam1 = image_coord_cys.*beam1;
beam2 = image_coord_cys.*beam2;
r_iris1 = image_coord_cys.*r_iris1;
r_iris2 = image_coord_cys.*r_iris2;
r_iris3 = image_coord_cys.*r_iris3;
r_detc1 = image_coord_cys.*r_detc1;
r_detc2 = image_coord_cys.*r_detc2;
r_detc3 = image_coord_cys.*r_detc3;

% Calculate geometry for plotting in 3D
p1 = [r_iris1(2:4);r_bot1(2:4);r_top4(2:4);r_detc1(2:4)];
p2 = [r_iris2(2:4);r_bot2(2:4);r_top5(2:4);r_detc2(2:4)];
p3 = [r_iris3(2:4);r_bot3(2:4);r_top6(2:4);r_detc3(2:4)];

[center, rad, v1, v2] = circlefit3d(p1,p2,p3);

```

Calculate Initial Boresight Location on Detector Plane

```

% Calculate Normal Vectors
bot_mirror_norm = cross(r_bot1(2:4)-r_bot2(2:4),r_bot3(2:4)-r_bot2(2:4));
top_mirror_norm = cross(r_top4(2:4)-r_top5(2:4),r_top6(2:4)-r_top5(2:4));
detector_norm = cross(r_detc1(2:4)-r_detc2(2:4),r_detc3(2:4)-r_detc2(2:4));

bot_mirror_norm = bot_mirror_norm/norm(bot_mirror_norm);
top_mirror_norm = top_mirror_norm/norm(top_mirror_norm);
detector_norm = detector_norm/norm(detector_norm);

% Calculate Beam Line Intersection Point on Top Mirror
norm_vect = top_mirror_norm;
P0 = beam1(2:4);
P1 = beam2(2:4);
P2 = r_top4(2:4);

[top_ints_pt_init, beam_top_refl_init] = vect_ints_plane(norm_vect,P0,P1,P2);

% Calculate Beam Line Intersection Point on Bottom Mirror
norm_vect = bot_mirror_norm;
P0 = top_ints_pt_init;
P1 = top_ints_pt_init + beam_top_refl_init(2:4);
P2 = r_bot1(2:4);

[bot_ints_pt_init,beam_bot_refl_init] = vect_ints_plane(norm_vect,P0,P1,P2);

% Calculate Beam Line Intersection Point on Detector Plane
norm_vect = detector_norm;
P0 = bot_ints_pt_init;
P1 = bot_ints_pt_init + beam_bot_refl_init(2:4);
P2 = r_detc2(2:4);

[spot_boresight, ~] = vect_ints_plane(norm_vect,P0,P1,P2);

```

```
% Define Boresight intersection point as a quaternion to rotate it, etc.
spot_boresight = [0 spot_boresight];
```

Calculate Rotated Quaternions

```
r_bot1_prime = quatmultiply(quatmultiply(q,r_bot1),q_star);
r_bot2_prime = quatmultiply(quatmultiply(q,r_bot2),q_star);
r_bot3_prime = quatmultiply(quatmultiply(q,r_bot3),q_star);
r_top4_prime = quatmultiply(quatmultiply(q,r_top4),q_star);
r_top5_prime = quatmultiply(quatmultiply(q,r_top5),q_star);
r_top6_prime = quatmultiply(quatmultiply(q,r_top6),q_star);
r_FOV1_prime = quatmultiply(quatmultiply(q,r_FOV1),q_star);
r_FOV2_prime = quatmultiply(quatmultiply(q,r_FOV2),q_star);
r_FOV3_prime = quatmultiply(quatmultiply(q,r_FOV3),q_star);
r_FOV4_prime = quatmultiply(quatmultiply(q,r_FOV4),q_star);
r_FOV5_prime = quatmultiply(quatmultiply(q,r_FOV5),q_star);
r_FOV6_prime = quatmultiply(quatmultiply(q,r_FOV6),q_star);
r_iris1_prime = quatmultiply(quatmultiply(q,r_iris1),q_star);
r_iris2_prime = quatmultiply(quatmultiply(q,r_iris2),q_star);
r_iris3_prime = quatmultiply(quatmultiply(q,r_iris3),q_star);
r_detc1_prime = quatmultiply(quatmultiply(q,r_detc1),q_star);
r_detc2_prime = quatmultiply(quatmultiply(q,r_detc2),q_star);
r_detc3_prime = quatmultiply(quatmultiply(q,r_detc3),q_star);
spot_boresight_prime = quatmultiply(quatmultiply(q,spot_boresight),q_star);

r_bot1_prime = quatmultiply(quatmultiply(q_y,r_bot1_prime),q_star_y);
r_bot2_prime = quatmultiply(quatmultiply(q_y,r_bot2_prime),q_star_y);
r_bot3_prime = quatmultiply(quatmultiply(q_y,r_bot3_prime),q_star_y);
r_top4_prime = quatmultiply(quatmultiply(q_y,r_top4_prime),q_star_y);
r_top5_prime = quatmultiply(quatmultiply(q_y,r_top5_prime),q_star_y);
r_top6_prime = quatmultiply(quatmultiply(q_y,r_top6_prime),q_star_y);
r_FOV1_prime = quatmultiply(quatmultiply(q_y,r_FOV1_prime),q_star_y);
r_FOV2_prime = quatmultiply(quatmultiply(q_y,r_FOV2_prime),q_star_y);
r_FOV3_prime = quatmultiply(quatmultiply(q_y,r_FOV3_prime),q_star_y);
r_FOV4_prime = quatmultiply(quatmultiply(q_y,r_FOV4_prime),q_star_y);
r_FOV5_prime = quatmultiply(quatmultiply(q_y,r_FOV5_prime),q_star_y);
r_FOV6_prime = quatmultiply(quatmultiply(q_y,r_FOV6_prime),q_star_y);
r_iris1_prime = quatmultiply(quatmultiply(q_y,r_iris1_prime),q_star_y);
r_iris2_prime = quatmultiply(quatmultiply(q_y,r_iris2_prime),q_star_y);
r_iris3_prime = quatmultiply(quatmultiply(q_y,r_iris3_prime),q_star_y);
r_detc1_prime = quatmultiply(quatmultiply(q_y,r_detc1_prime),q_star_y);
r_detc2_prime = quatmultiply(quatmultiply(q_y,r_detc2_prime),q_star_y);
r_detc3_prime = quatmultiply(quatmultiply(q_y,r_detc3_prime),q_star_y);
spot_boresight_prime = quatmultiply(quatmultiply(q_y,spot_boresight_prime),q_star_y);

p1_prime = [r_iris1_prime(2:4);r_bot1_prime(2:4);r_top4_prime(2:4);r_detc1_prime(2:4)];
p2_prime = [r_iris2_prime(2:4);r_bot2_prime(2:4);r_top5_prime(2:4);r_detc2_prime(2:4)];
p3_prime = [r_iris3_prime(2:4);r_bot3_prime(2:4);r_top6_prime(2:4);r_detc3_prime(2:4)];

[center_prime, rad_prime, v1_prime, v2_prime] = circlefit3d(p1_prime,p2_prime,p3_prime);
```

Calculate Normal Vectors

```
bot_mirror_norm = cross(r_bot1_prime(2:4)-r_bot2_prime(2:4),r_bot3_prime(2:4)-r_bot2_prime(2:
```



```

4));
top_mirror_norm = cross(r_top4_prime(2:4)-r_top5_prime(2:4),r_top6_prime(2:4)-r_top5_prime(2:4));
detector_norm = cross(r_detc1_prime(2:4)-r_detc2_prime(2:4),r_detc3_prime(2:4)-r_detc2_prime(2:4));

bot_mirror_norm = bot_mirror_norm/norm(bot_mirror_norm);
top_mirror_norm = top_mirror_norm/norm(top_mirror_norm);
detector_norm = detector_norm/norm(detector_norm);

```

Calculate Beam Line Through Rotated Optics Assembly

```

% Calculate Beam Line Intersection Point on Top Mirror
norm_vect = top_mirror_norm;
P0 = beam1(2:4);
P1 = beam2(2:4);
P2 = r_top4_prime(2:4);

[top_ints_pt, beam_top_refl] = vect_ints_plane(norm_vect,P0,P1,P2);

% Calculate Beam Line Intersection Point on Bottom Mirror
norm_vect = bot_mirror_norm;
P0 = top_ints_pt;
P1 = top_ints_pt + beam_top_refl(2:4);
P2 = r_bot1_prime(2:4);

[bot_ints_pt, beam_bot_refl] = vect_ints_plane(norm_vect,P0,P1,P2);

```

Calculate Translation Compensation

```

% beam_offset = [0 0 0]; % use this to find the beam offset below..
beam_offset = [0.016011058488824 0 0.132012539768716];

trans_comp_z = abs(bot_ints_pt(3)) + abs(l_focus*sind(theta)) - beam_offset(3);
trans_comp_x = abs(bot_ints_pt(1)) + abs(l_focus*sind(psi)) - beam_offset(1);

```

Translate Mirrors

```

r_iris1_comp = r_iris1_prime(2:4);
r_iris2_comp = r_iris2_prime(2:4);
r_iris3_comp = r_iris3_prime(2:4);
r_bot1_comp = r_bot1_prime(2:4);
r_bot2_comp = r_bot2_prime(2:4);
r_bot3_comp = r_bot3_prime(2:4);
r_top4_comp = r_top4_prime(2:4);
r_top5_comp = r_top5_prime(2:4);
r_top6_comp = r_top6_prime(2:4);
r_detc1_comp = r_detc1_prime(2:4);
r_detc2_comp = r_detc2_prime(2:4);
r_detc3_comp = r_detc3_prime(2:4);
spot_boresight_comp = spot_boresight_prime(2:4);

```

```

if theta > 0

```

```

r_iris1_comp = r_iris1_comp + [0 0 trans_comp_z];
r_iris2_comp = r_iris2_comp + [0 0 trans_comp_z];
r_iris3_comp = r_iris3_comp + [0 0 trans_comp_z];
r_bot1_comp = r_bot1_comp + [0 0 trans_comp_z];
r_bot2_comp = r_bot2_comp + [0 0 trans_comp_z];
r_bot3_comp = r_bot3_comp + [0 0 trans_comp_z];
r_top4_comp = r_top4_comp + [0 0 trans_comp_z];
r_top5_comp = r_top5_comp + [0 0 trans_comp_z];
r_top6_comp = r_top6_comp + [0 0 trans_comp_z];
r_detc1_comp = r_detc1_comp + [0 0 trans_comp_z];
r_detc2_comp = r_detc2_comp + [0 0 trans_comp_z];
r_detc3_comp = r_detc3_comp + [0 0 trans_comp_z];
spot_boresight_comp = spot_boresight_comp + [0 0 trans_comp_z];
else
r_iris1_comp = r_iris1_comp - [0 0 trans_comp_z];
r_iris2_comp = r_iris2_comp - [0 0 trans_comp_z];
r_iris3_comp = r_iris3_comp - [0 0 trans_comp_z];
r_bot1_comp = r_bot1_comp - [0 0 trans_comp_z];
r_bot2_comp = r_bot2_comp - [0 0 trans_comp_z];
r_bot3_comp = r_bot3_comp - [0 0 trans_comp_z];
r_top4_comp = r_top4_comp - [0 0 trans_comp_z];
r_top5_comp = r_top5_comp - [0 0 trans_comp_z];
r_top6_comp = r_top6_comp - [0 0 trans_comp_z];
r_detc1_comp = r_detc1_comp - [0 0 trans_comp_z];
r_detc2_comp = r_detc2_comp - [0 0 trans_comp_z];
r_detc3_comp = r_detc3_comp - [0 0 trans_comp_z];
spot_boresight_comp = spot_boresight_comp - [0 0 trans_comp_z];
end

if psi < 0
r_iris1_comp = r_iris1_comp - [trans_comp_x 0 0];
r_iris2_comp = r_iris2_comp - [trans_comp_x 0 0];
r_iris3_comp = r_iris3_comp - [trans_comp_x 0 0];
r_bot1_comp = r_bot1_comp - [trans_comp_x 0 0];
r_bot2_comp = r_bot2_comp - [trans_comp_x 0 0];
r_bot3_comp = r_bot3_comp - [trans_comp_x 0 0];
r_top4_comp = r_top4_comp - [trans_comp_x 0 0];
r_top5_comp = r_top5_comp - [trans_comp_x 0 0];
r_top6_comp = r_top6_comp - [trans_comp_x 0 0];
r_detc1_comp = r_detc1_comp - [trans_comp_x 0 0];
r_detc2_comp = r_detc2_comp - [trans_comp_x 0 0];
r_detc3_comp = r_detc3_comp - [trans_comp_x 0 0];
spot_boresight_comp = spot_boresight_comp - [trans_comp_x 0 0];
else
r_iris1_comp = r_iris1_comp + [trans_comp_x 0 0];
r_iris2_comp = r_iris2_comp + [trans_comp_x 0 0];
r_iris3_comp = r_iris3_comp + [trans_comp_x 0 0];
r_bot1_comp = r_bot1_comp + [trans_comp_x 0 0];
r_bot2_comp = r_bot2_comp + [trans_comp_x 0 0];
r_bot3_comp = r_bot3_comp + [trans_comp_x 0 0];
r_top4_comp = r_top4_comp + [trans_comp_x 0 0];
r_top5_comp = r_top5_comp + [trans_comp_x 0 0];
r_top6_comp = r_top6_comp + [trans_comp_x 0 0];
r_detc1_comp = r_detc1_comp + [trans_comp_x 0 0];
r_detc2_comp = r_detc2_comp + [trans_comp_x 0 0];
r_detc3_comp = r_detc3_comp + [trans_comp_x 0 0];
spot_boresight_comp = spot_boresight_comp + [trans_comp_x 0 0];

```

```

end
p1_comp = [r_iris1_comp;r_bot1_comp;r_top4_comp; r_detc1_comp];
p2_comp = [r_iris2_comp;r_bot2_comp;r_top5_comp; r_detc2_comp];
p3_comp = [r_iris3_comp;r_bot3_comp;r_top6_comp; r_detc3_comp];

[center_comp, rad_comp, v1_comp, v2_comp] = circlefit3d(p1_comp,p2_comp,p3_comp);

```

Calculate Beam Line Through Rotated and Translated Optics Assembly

```

% Calculate Beam Line Intersection Point on Top Mirror
norm_vect = top_mirror_norm;
P0 = beam1(2:4);
P1 = beam2(2:4);
P2 = r_top4_comp;

[top_ints_pt_trans, beam_top_refl_trans] = vect_ints_plane(norm_vect,P0,P1,P2);

% Calculate Beam Line Intersection Point on Bottom Mirror
norm_vect = bot_mirror_norm;
P0 = top_ints_pt_trans;
P1 = top_ints_pt_trans + beam_top_refl_trans(2:4);
P2 = r_bot1_comp;

[bot_ints_pt_trans, beam_bot_refl_trans] = vect_ints_plane(norm_vect,P0,P1,P2);

% Calculate Beam Line Intersection Point on Detector Plane After Rotation
norm_vect = detector_norm;
P0 = bot_ints_pt;
P1 = bot_ints_pt + beam_bot_refl(2:4);
P2 = r_detc1_prime(2:4);

[detc_ints_pt, ~] = vect_ints_plane(norm_vect,P0,P1,P2);

% Calculate Beam Line Intersection Point on Detector Plane After Rotation
% and Translation
norm_vect = detector_norm;
P0 = bot_ints_pt_trans;
P1 = bot_ints_pt_trans + beam_bot_refl_trans(2:4);
P2 = r_detc1_comp;

[detc_ints_pt_trans, ~] = vect_ints_plane(norm_vect,P0,P1,P2);

del_beam_boresight = 1000*(detc_ints_pt_trans - spot_boresight_comp);
del_beam_boresight(1) = -1*del_beam_boresight(1); % convert x coord to image coord sys
disp('----- Initial Compensation -----')
fprintf('Spot Centroid from Boresight: %.2f %.2f %.2f (microns)\n',del_beam_boresight);
fprintf('Delta between Laser Spot and Boresight: \n%.1f microns\n',sqrt(del_beam_boresight(1)
^2+del_beam_boresight(2)^2+del_beam_boresight(3)^2));

```

```

----- Initial Compensation -----
Spot Centroid from Boresight: 92.41 11.73 -186.50 (microns)
Delta between Laser Spot and Boresight:
208.5 microns

```

Re-Calculate Translation Compensation Based on Center of Rotation Offset

```
% center_rot_comp = [0 0 0]; % use this to find the beam offset below..
center_rot_comp = del_beam_boresight./1000;

if theta > 0
    trans_comp_z = trans_comp_z + center_rot_comp(3);
else
    trans_comp_z = trans_comp_z - center_rot_comp(3);
end

if psi > 0
    trans_comp_x = trans_comp_x - center_rot_comp(1);
else
    trans_comp_x = trans_comp_x + center_rot_comp(1);
end

% -----
% Translate Mirrors
r_iris1_comp = r_iris1_prime(2:4);
r_iris2_comp = r_iris2_prime(2:4);
r_iris3_comp = r_iris3_prime(2:4);
r_bot1_comp = r_bot1_prime(2:4);
r_bot2_comp = r_bot2_prime(2:4);
r_bot3_comp = r_bot3_prime(2:4);
r_top4_comp = r_top4_prime(2:4);
r_top5_comp = r_top5_prime(2:4);
r_top6_comp = r_top6_prime(2:4);
r_detc1_comp = r_detc1_prime(2:4);
r_detc2_comp = r_detc2_prime(2:4);
r_detc3_comp = r_detc3_prime(2:4);
spot_boresight_comp = spot_boresight_prime(2:4);

if theta > 0
    r_iris1_comp = r_iris1_comp + [0 0 trans_comp_z];
    r_iris2_comp = r_iris2_comp + [0 0 trans_comp_z];
    r_iris3_comp = r_iris3_comp + [0 0 trans_comp_z];
    r_bot1_comp = r_bot1_comp + [0 0 trans_comp_z];
    r_bot2_comp = r_bot2_comp + [0 0 trans_comp_z];
    r_bot3_comp = r_bot3_comp + [0 0 trans_comp_z];
    r_top4_comp = r_top4_comp + [0 0 trans_comp_z];
    r_top5_comp = r_top5_comp + [0 0 trans_comp_z];
    r_top6_comp = r_top6_comp + [0 0 trans_comp_z];
    r_detc1_comp = r_detc1_comp + [0 0 trans_comp_z];
    r_detc2_comp = r_detc2_comp + [0 0 trans_comp_z];
    r_detc3_comp = r_detc3_comp + [0 0 trans_comp_z];
    spot_boresight_comp = spot_boresight_comp + [0 0 trans_comp_z];
else
    r_iris1_comp = r_iris1_comp - [0 0 trans_comp_z];
    r_iris2_comp = r_iris2_comp - [0 0 trans_comp_z];
    r_iris3_comp = r_iris3_comp - [0 0 trans_comp_z];
    r_bot1_comp = r_bot1_comp - [0 0 trans_comp_z];
    r_bot2_comp = r_bot2_comp - [0 0 trans_comp_z];
    r_bot3_comp = r_bot3_comp - [0 0 trans_comp_z];
    r_top4_comp = r_top4_comp - [0 0 trans_comp_z];
    r_top5_comp = r_top5_comp - [0 0 trans_comp_z];
    r_top6_comp = r_top6_comp - [0 0 trans_comp_z];
end
```

```

r_detc1_comp = r_detc1_comp - [0 0 trans_comp_z];
r_detc2_comp = r_detc2_comp - [0 0 trans_comp_z];
r_detc3_comp = r_detc3_comp - [0 0 trans_comp_z];
spot_boresight_comp = spot_boresight_comp - [0 0 trans_comp_z];
end

if psi < 0
    r_iris1_comp = r_iris1_comp - [trans_comp_x 0 0];
    r_iris2_comp = r_iris2_comp - [trans_comp_x 0 0];
    r_iris3_comp = r_iris3_comp - [trans_comp_x 0 0];
    r_bot1_comp = r_bot1_comp - [trans_comp_x 0 0];
    r_bot2_comp = r_bot2_comp - [trans_comp_x 0 0];
    r_bot3_comp = r_bot3_comp - [trans_comp_x 0 0];
    r_top4_comp = r_top4_comp - [trans_comp_x 0 0];
    r_top5_comp = r_top5_comp - [trans_comp_x 0 0];
    r_top6_comp = r_top6_comp - [trans_comp_x 0 0];
    r_detc1_comp = r_detc1_comp - [trans_comp_x 0 0];
    r_detc2_comp = r_detc2_comp - [trans_comp_x 0 0];
    r_detc3_comp = r_detc3_comp - [trans_comp_x 0 0];
    spot_boresight_comp = spot_boresight_comp - [trans_comp_x 0 0];
else
    r_iris1_comp = r_iris1_comp + [trans_comp_x 0 0];
    r_iris2_comp = r_iris2_comp + [trans_comp_x 0 0];
    r_iris3_comp = r_iris3_comp + [trans_comp_x 0 0];
    r_bot1_comp = r_bot1_comp + [trans_comp_x 0 0];
    r_bot2_comp = r_bot2_comp + [trans_comp_x 0 0];
    r_bot3_comp = r_bot3_comp + [trans_comp_x 0 0];
    r_top4_comp = r_top4_comp + [trans_comp_x 0 0];
    r_top5_comp = r_top5_comp + [trans_comp_x 0 0];
    r_top6_comp = r_top6_comp + [trans_comp_x 0 0];
    r_detc1_comp = r_detc1_comp + [trans_comp_x 0 0];
    r_detc2_comp = r_detc2_comp + [trans_comp_x 0 0];
    r_detc3_comp = r_detc3_comp + [trans_comp_x 0 0];
    spot_boresight_comp = spot_boresight_comp + [trans_comp_x 0 0];
end

p1_comp = [r_iris1_comp;r_bot1_comp;r_top4_comp; r_detc1_comp];
p2_comp = [r_iris2_comp;r_bot2_comp;r_top5_comp; r_detc2_comp];
p3_comp = [r_iris3_comp;r_bot3_comp;r_top6_comp; r_detc3_comp];

[center_comp, rad_comp, v1_comp, v2_comp] = circlefit3d(p1_comp,p2_comp,p3_comp);

% -----
% Calculate Beam Line Through Rotated and Translated Optics Assembly

% Calculate Beam Line Intersection Point on Top Mirror
norm_vect = top_mirror_norm;
P0 = beam1(2:4);
P1 = beam2(2:4);
P2 = r_top4_comp;

[top_ints_pt_trans, beam_top_refl_trans] = vect_ints_plane(norm_vect,P0,P1,P2);

% Calculate Beam Line Intersection Point on Bottom Mirror
norm_vect = bot_mirror_norm;
P0 = top_ints_pt_trans;
P1 = top_ints_pt_trans + beam_top_refl_trans(2:4);
P2 = r_bot1_comp;

```

```

[bot_ints_pt_trans, beam_bot_refl_trans] = vect_ints_plane(norm_vect,P0,P1,P2);

% Calculate Beam Line Intersection Point on Detector Plane After Rotation
norm_vect = detector_norm;
P0 = bot_ints_pt;
P1 = bot_ints_pt + beam_bot_refl(2:4);
P2 = r_detcl_prime(2:4);

[detc_ints_pt, ~] = vect_ints_plane(norm_vect,P0,P1,P2);

% Calculate Beam Line Intersection Point on Detector Plane After Rotation
% and Translation
norm_vect = detector_norm;
P0 = bot_ints_pt_trans;
P1 = bot_ints_pt_trans + beam_bot_refl_trans(2:4);
P2 = r_detcl_comp;

[detc_ints_pt_trans, ~] = vect_ints_plane(norm_vect,P0,P1,P2);

del_beam_boresight = 1000*(detc_ints_pt_trans - spot_boresight_comp);
del_beam_boresight(1) = -1*del_beam_boresight(1); % convert x coord to image coord sys
disp('----- Final Compensation -----')
fprintf('Spot Centroid from Boresight: %.2f %.2f %.2f (microns)\n',del_beam_boresight);
fprintf('Delta between Laser Spot and Boresight: \n%.1f microns\n',sqrt(del_beam_boresight(1)
^2+del_beam_boresight(2)^2+del_beam_boresight(3)^2));

disp('----- Compensation Values -----');
fprintf('X: %.4f \tZ: %.4f \n',trans_comp_x,trans_comp_z);

```

```

----- Final Compensation -----
Spot Centroid from Boresight: 2.04 -0.39 1.10 (microns)
Delta between Laser Spot and Boresight:
2.4 microns
----- Compensation Values -----
X: 4.6459      Z: 4.9223

```

Plot Results

```

if strcmp(PLOT,'True')
    figure;hold on;
    % Plot Origin
    % plot3([origin(1) unitx(1)],[origin(2) unitx(2)],[origin(3) unitx(3)],'LineWidth',5);
    % plot3([origin(1) unity(1)],[origin(2) unity(2)],[origin(3) unity(3)],'LineWidth',5);
    % plot3([origin(1) unitz(1)],[origin(2) unitz(2)],[origin(3) unitz(3)],'LineWidth',5);
    plot3(center_comp(4,1),center_comp(4,2),center_comp(4,3),'k.')
    % Plot Initial Beamline
    plot3([beam1(2) top_ints_pt_init(1)],[beam1(3) top_ints_pt_init(2)],[beam1(4) top_ints_pt_init(3)],'-','LineWidth',1,'Color','k');
    plot3([top_ints_pt_init(1) bot_ints_pt_init(1)],[top_ints_pt_init(2) bot_ints_pt_init(2)],[top_ints_pt_init(3) bot_ints_pt_init(3)],'-','LineWidth',1,'Color','k');
    plot3([bot_ints_pt_init(1) spot_boresight(2)],[bot_ints_pt_init(2) spot_boresight(3)],[bot_ints_pt_init(3) spot_boresight(4)],'-','LineWidth',1,'Color','k');
    % Plot Beamline After Rotation

```

```

    plot3([beam1(2) top_ints_pt(1)], [beam1(3) top_ints_pt(2)], [beam1(4) top_ints_pt(3)], '-', '
LineWidth', 1, 'Color', 'r');
    plot3([top_ints_pt(1) bot_ints_pt(1)], [top_ints_pt(2) bot_ints_pt(2)], [top_ints_pt(3) bot
_ints_pt(3)], '-', 'LineWidth', 1, 'Color', 'r');
    plot3([bot_ints_pt(1) detc_ints_pt(1)], [bot_ints_pt(2) detc_ints_pt(2)], [bot_ints_pt(3) d
etc_ints_pt(3)], '-', 'LineWidth', 1, 'Color', 'r');
    % Plot Beamline After Rotation and Translation
    plot3([beam1(2) top_ints_pt_trans(1)], [beam1(3) top_ints_pt_trans(2)], [beam1(4) top_ints_
pt_trans(3)], '-', 'LineWidth', 1, 'Color', 'b');
    plot3([top_ints_pt_trans(1) bot_ints_pt_trans(1)], [top_ints_pt_trans(2) bot_ints_pt_trans
(2)], [top_ints_pt_trans(3) bot_ints_pt_trans(3)], '-', 'LineWidth', 1, 'Color', 'b');
    plot3([bot_ints_pt_trans(1) detc_ints_pt(1)], [bot_ints_pt_trans(2) detc_ints_pt(2)], [bot_
ints_pt_trans(3) detc_ints_pt(3)], '-', 'LineWidth', 1, 'Color', 'b');
    % Plot FOV
    % plot3([origin(1) r_FOV1(2)], [origin(2) r_FOV1(3)], [origin(3) r_FOV1(4)], 'LineWidth', 2, '
Color', 'b');
    % plot3([origin(1) r_FOV1_prime(2)], [origin(2) r_FOV1_prime(3)], [origin(3) r_FOV1_prime(4
)], 'LineWidth', 2, 'Color', 'b');
    % plot3([origin(1) r_FOV2(2)], [origin(2) r_FOV2(3)], [origin(3) r_FOV2(4)], 'LineWidth', 2, '
Color', 'r');
    % plot3([origin(1) r_FOV2_prime(2)], [origin(2) r_FOV2_prime(3)], [origin(3) r_FOV2_prime(4
)], 'LineWidth', 2, 'Color', 'r');
    % plot3([origin(1) r_FOV3(2)], [origin(2) r_FOV3(3)], [origin(3) r_FOV3(4)], 'LineWidth', 2, '
Color', 'g');
    % plot3([origin(1) r_FOV3_prime(2)], [origin(2) r_FOV3_prime(3)], [origin(3) r_FOV3_prime(4
)], 'LineWidth', 2, 'Color', 'g');
    % plot3([origin(1) r_FOV4(2)], [origin(2) r_FOV4(3)], [origin(3) r_FOV4(4)], 'LineWidth', 2, '
Color', 'b');
    % plot3([origin(1) r_FOV4_prime(2)], [origin(2) r_FOV4_prime(3)], [origin(3) r_FOV4_prime(4
)], 'LineWidth', 2, 'Color', 'b');
    % plot3([origin(1) r_FOV5(2)], [origin(2) r_FOV5(3)], [origin(3) r_FOV5(4)], 'LineWidth', 2, '
Color', 'r');
    % plot3([origin(1) r_FOV5_prime(2)], [origin(2) r_FOV5_prime(3)], [origin(3) r_FOV5_prime(4
)], 'LineWidth', 2, 'Color', 'r');
    % plot3([origin(1) r_FOV6(2)], [origin(2) r_FOV6(3)], [origin(3) r_FOV6(4)], 'LineWidth', 2, '
Color', 'g');
    % plot3([origin(1) r_FOV6_prime(2)], [origin(2) r_FOV6_prime(3)], [origin(3) r_FOV6_prime(4
)], 'LineWidth', 2, 'Color', 'g');
    % Plot Mirror Normal Vector
    % plot3([r_bot2_prime(2) (r_bot2_prime(2)+bot_mirror_norm(1))], [r_bot2_prime(3) (r_bot2_p
rime(3)+bot_mirror_norm(2))], [r_bot2_prime(4) (r_bot2_prime(4)+bot_mirror_norm(3))], 'LineWidt
h', 3, 'Color', 'c');
    % plot3([top_ints_pt(1) (top_ints_pt(1)+top_mirror_norm(1))], [top_ints_pt(2) (top_ints_pt
(2)+top_mirror_norm(2))], [top_ints_pt(3) (top_ints_pt(3)+top_mirror_norm(3))], 'LineWidth', 3, '
Color', 'c');

    % Plot Mirrors and Iris
    % Default (Boresight)
    for i=1:1000
        a = i/180*pi;
        x = center(:,1)+sin(a)*rad.*v1(:,1)+cos(a)*rad.*v2(:,1);
        y = center(:,2)+sin(a)*rad.*v1(:,2)+cos(a)*rad.*v2(:,2);
        z = center(:,3)+sin(a)*rad.*v1(:,3)+cos(a)*rad.*v2(:,3);
        plot3(x,y,z, 'k. ');
    end
    % Rotated by Theta
    for i=1:1000

```

```

    a = i/180*pi;
    x_prime = center_prime(:,1)+sin(a)*rad_prime.*v1_prime(:,1)+cos(a)*rad_prime.*v2_prime(:,1);
    y_prime = center_prime(:,2)+sin(a)*rad_prime.*v1_prime(:,2)+cos(a)*rad_prime.*v2_prime(:,2);
    z_prime = center_prime(:,3)+sin(a)*rad_prime.*v1_prime(:,3)+cos(a)*rad_prime.*v2_prime(:,3);
    plot3(x_prime,y_prime,z_prime,'r.');
```

end

% Translated for Compensation

```

for i=1:1000
    a = i/180*pi;
    x_comp = center_comp(:,1)+sin(a)*rad_comp.*v1_comp(:,1)+cos(a)*rad_comp.*v2_comp(:,1)
;
    y_comp = center_comp(:,2)+sin(a)*rad_comp.*v1_comp(:,2)+cos(a)*rad_comp.*v2_comp(:,2)
;
    z_comp = center_comp(:,3)+sin(a)*rad_comp.*v1_comp(:,3)+cos(a)*rad_comp.*v2_comp(:,3)
;
    plot3(x_comp,y_comp,z_comp,'b.');
```

end

```

grid on;
rotate3d on;
axis equal;
xlabel('X [mm]');
ylabel('Y [mm]');
zlabel('Z [mm]');
set(gca,'CameraPosition',[-40 80 50]);
end
```


Contents

- [Ramp Profile Simulation](#)
- [Declare Variables](#)
- [Simulated Ramp](#)
- [Plot](#)

Ramp Profile Simulation

Written by: Jason Grillo

```
clear all, close all, clc
```

Declare Variables

```
num_steps = 2*4800;
uS = 8;
init_sp = 50;
max_sp = 500;
accel = 50;

accel_phase = 0.2;
steps_accel = min(num_steps*accel_phase,max_sp*init_sp/accel);
steps_decel = num_steps-steps_accel;

del_t = 0.073;
t = transpose(0:del_t:200);

speed = zeros(length(t),1) + init_sp;
steps_taken = zeros(length(t),1);
```

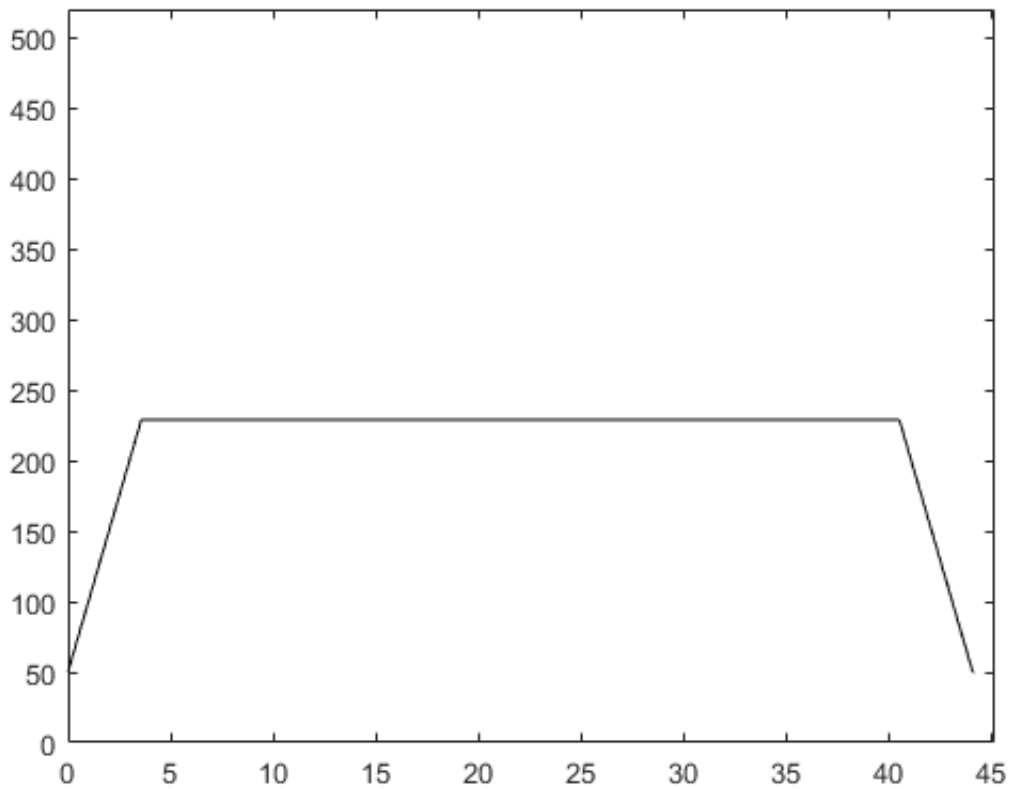
Simulated Ramp

```
for i=2:length(t)
    if steps_taken(i-1) < num_steps
        if steps_taken(i-1) < steps_accel
            speed(i) = speed(i-1) + del_t*accel;
            if speed(i) > max_sp
                speed(i) = max_sp;
            end
        elseif steps_taken(i-1) < steps_decel
            speed(i) = speed(i-1);
        else
            speed(i) = speed(i-1) - del_t*accel;
        end
        steps_taken(i) = steps_taken(i-1) + round(speed(i)*del_t);
    else
        stop_index = i;
        break
    end
end
```

```
steps_taken = steps_taken./2;
```

Plot

```
figure;  
plot(t(1:stop_index),speed(1:stop_index), 'k')  
axis([0 t(stop_index)+1 0 max_sp+20])
```



Contents

- [MUVI Manipulator Spot Centroid](#)
- [Load Image](#)
- [Find Centroid](#)
- [Image](#)

MUVI Manipulator Spot Centroid

Written by: Jason Grillo

```
clear all, close all, clc
```

Load Image

```
path = 'G:\Cal Poly\Thesis\Vacuum_Manipulator\Tests\FOV_Sweep_5';
filename = strcat(path, '\13_y_p7_p_m7.png');
image_title = '13 - Yaw: +7°, Pitch: -7°';

% heights = 1325:2225;
% widths = 2275:3275;
heights = 1400:2350;
widths = 2200:3250;

offset_x = 0;
offset_z = 0;

heights = heights + offset_z;
widths = widths + offset_x;

rbg = imread(filename);
rbg = rbg(heights,widths);
```

Find Centroid

```
intensity_lim = 85; % 2sigma of encircled energy
% intensity_lim = 150;
% intensity_lim = 200;

fill_color = 'g';

% Find Width
row_offset = 425;
cents_width = zeros((length(heights)-2*row_offset),1);

for i = row_offset:(length(heights)-row_offset)
    [~,~,cents_width(i-(row_offset-1))] = find_spot_centroid(rbg(i,:),intensity_lim);
end
cents_width = cents_width + offset_x;

% Find Height
row_offset = 450;
cents_heights = zeros((length(widths)-2*row_offset)+1,1);

for i = row_offset:(length(widths)-row_offset)
    [~,~,cents_heights(i-(row_offset-1))] = find_spot_centroid(rbg(:,i),intensity_lim);
end
cents_heights = cents_heights + offset_z;
```

Image

```
figure;
image(imread(filename));
hold on
line([widths(1) widths(1)], [heights(1) heights(length(heights))], 'Color', 'y')
line([widths(length(widths)) widths(length(widths))], [heights(1) heights(length(heights))], 'Color', 'y')
line([widths(1) widths(length(widths))], [heights(1) heights(1)], 'Color', 'y')
line([widths(1) widths(length(widths))], [heights(length(heights)) heights(length(heights))], 'Color', 'y')
plot(median(cents_width)+widths(1), median(cents_heights)+heights(1), 'r*')
% plot(2997.8,1817.9, 'r*')
% plot(2725,1875, 'b*')

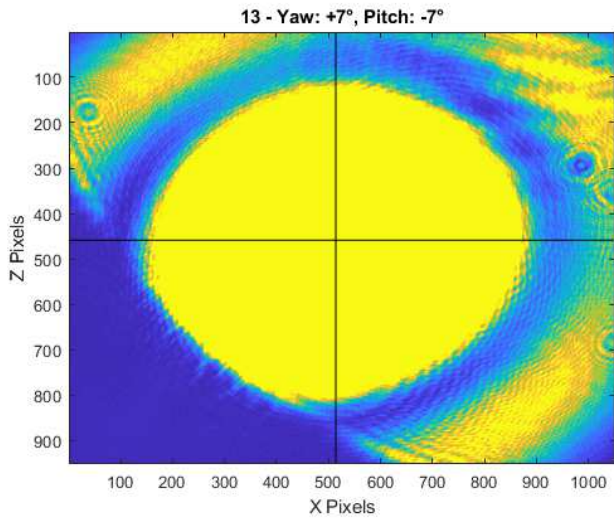
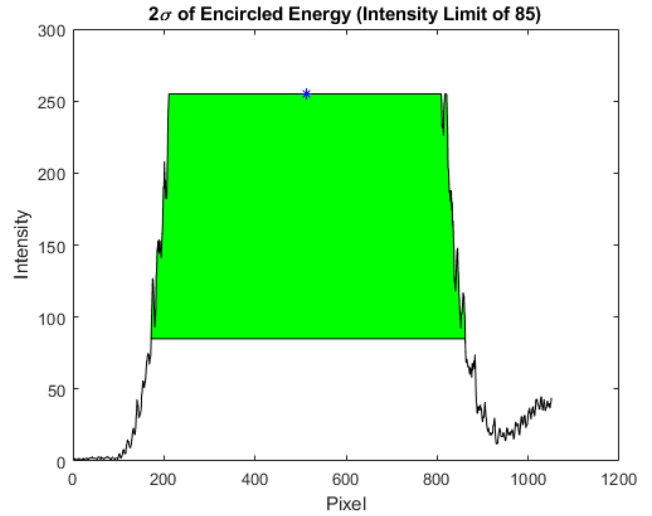
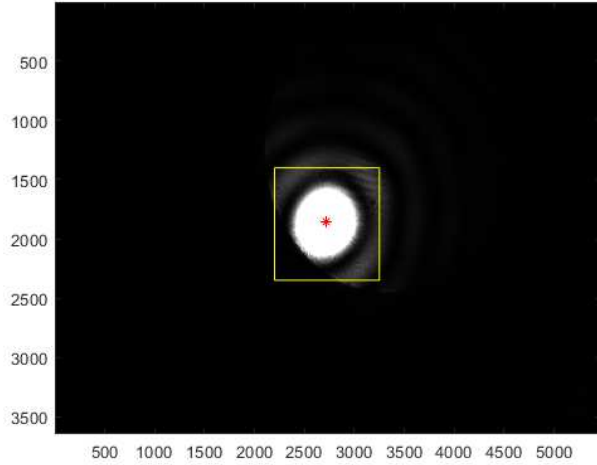
% referenced: https://stackoverflow.com/questions/6245626/matlab-filling-in-the-area-between-two-sets-of-data-lines-in-one-figure?noredirect=1&lq=1
row_lim = 468;
figure;
x = 1:length(rbg(row_lim,:));
y1 = rbg(row_lim,:);
y2 = ones(1,length(y1));
y2 = intensity_lim.*y2;
[start_y2,end_y2,~] = find_spot_centroid(rbg(row_lim,:),intensity_lim);
y2(1:round(min(start_y2))) = rbg(row_lim,1:round(min(start_y2)));
y2(round(max(end_y2)):length(y2)) = rbg(row_lim,round(max(end_y2)):length(y2));
X=[x,flip1r(x)]; % create continuous x value array for plotting
Y=[y1,flip1r(y2)]; % create y values for out and then back
plot(x,y1,'k');
hold on
fill(X,Y,fill_color); % plot filled area
plot(median(cents_width),255, 'b*')
```

```

title('2\sigma of Encircled Energy (Intensity Limit of 85)');
xlabel('Pixel')
ylabel('Intensity')

figure;
image(rgb)
hold on
plot([0 length(rgb(1,:))],[median(cents_heights) median(cents_heights)], 'k')
plot([median(cents_width) median(cents_width)],[0 length(rgb(:,1))], 'k')
title(image_title)
xlabel('X Pixels')
ylabel('Z Pixels')

```



```

function [start_vals, end_vals, centroid] = find_spot_centroid(intensity, i_level)
% This function calculates the average location of a laser spot centroid by
% finding the location of maximum intensity. Assuming a symmetric spot, the
% average of multiple intensity measurements are used to calculate the
% centroid location.

intensity = double(intensity);

dx_data = 1:length(intensity);
dx_int = 1:0.05:length(intensity);
intensity_int = interp1(dx_data, intensity, dx_int);

int_end = length(intensity_int);
peak_start = find(intensity_int==255,1,'first'); % index of first highest intensity
peak_end = find(intensity_int==255,1,'last'); % index of last highest intensity
peak_mid = round((peak_end + peak_start)/2); % average index of the two peaks

begin_i = i_level;
start_vals = zeros(255-begin_i,1);
end_vals = zeros(255-begin_i,1);

for i = begin_i:255
    [~, index_start] = min(abs(intensity_int(1:peak_mid)-i));
    [~, index_end] = min(abs(intensity_int(peak_mid:int_end)-i));
    start_vals(i-(begin_i-1)) = dx_int(index_start);
    end_vals(i-(begin_i-1)) = dx_int(peak_mid + index_end);
end

centroid_vals = (end_vals + start_vals)/2;
centroid_vals(length(centroid_vals)+1) = dx_int(peak_mid);
centroid_vals = rmoutliers(centroid_vals,'median');

centroid = mean(centroid_vals);
end

```

Not enough input arguments.

Error in find_spot_centroid (line 7)
intensity = double(intensity);

Appendix E

BILL OF MATERIALS

Appendix E
Bill of Materials

Aspect	Supplier	Part Description	Part No.	Qty	Price	Extended
Electronics	Amazon	TP-Link PoE Injector	TP-Link TL-POE150S	1	\$ 20.00	\$ 20.00
	Amazon	Soldering Tool Accessories		- 1	\$ 13.99	\$ 13.99
	Amazon	Flux Pen		- 1	\$ 10.10	\$ 10.10
	Amazon	18 AWG Wire		- 1	\$ 13.89	\$ 13.89
	Amazon	20 AWG Wire		- 2	\$ 15.79	\$ 31.58
	Amazon	30 AWG Wire		- 1	\$ 12.99	\$ 12.99
	Amazon	Heat Shrink		- 1	\$ 6.99	\$ 6.99
	Amazon	DB9 Solder Connectors		- 1	\$ 7.65	\$ 7.65
	Amazon	HD15 Solder Connectors		- 1	\$ 9.45	\$ 9.45
	Amazon	Electronics Development Kit		- 2	\$ 17.00	\$ 34.00
	Amazon	24V 15A Power Supply		- 1	\$ 23.00	\$ 23.00
	DigiKey	Hammond Electrical Enclosure	HM2765-ND	1	\$ 37.44	\$ 37.44
	DigiKey	24VDC Fan	1053-1244-ND	1	\$ 5.22	\$ 5.22
	DigiKey	Rocker Switch	EG4777-ND	4	\$ 1.12	\$ 4.48
	DigiKey	double row header pin	952-2125-ND	2	\$ 0.46	\$ 0.92
	DigiKey	double row jumper pin	952-2121-ND	2	\$ 0.24	\$ 0.48
	DigiKey	2kohm resistor 1206	RNCP1206FTD1K00CT-ND	13	\$ 0.10	\$ 1.30
	DigiKey	Nucleo-64 STM32L476	497-15881-ND	1	\$ 20.00	\$ 20.00
	DigiKey	Stepper Driver BOB	1460-1337-ND	4	\$ 20.00	\$ 80.00
	DigiKey	HD15 Connector	181-115RME-ND	5	\$ 3.43	\$ 17.15
	DigiKey	D9 Connector	AE10921-ND	5	\$ 0.77	\$ 3.85
	DigiKey	Screw Terminal	ED2600-ND	2	\$ 0.86	\$ 1.72
	DigiKey	Female Header Pins	SAM1213-11-ND	10	\$ 1.09	\$ 10.90
	DigiKey	Male Header Pins	SAM1031-11-ND	10	\$ 0.90	\$ 9.00
	DigiKey	μ C Female Header Pins	S6106-ND	4	\$ 1.26	\$ 5.04
	DigiKey	Differential Receiver IC	296-33593-5-ND	5	\$ 11.31	\$ 56.55
	Oshpark	Custom PCB	uv_manipulator_pcb	3	\$ 288.10	\$ 288.10
					Subtotal	\$ 725.79

Aspect	Supplier	Part Description	Part No.	Qty	Price	Extended
Hardware	McMaster Carr	Vented #8-32 5/8" Fastener	93235A196	1	\$ 8.86	\$ 8.86
	McMaster Carr	Vented #8-32 1/2" Fastener	93235A194	4	\$ 7.50	\$ 30.00
	McMaster Carr	Vented #8-32 5/16" Fastener	93235A190	2	\$ 6.75	\$ 13.50
	McMaster Carr	Vented #10-32 5/16" Fastener	93235A239	1	\$ 5.36	\$ 5.36
	McMaster Carr	M6x1.0 14mm Fastener	91292A070	1	\$ 11.10	\$ 11.10
	McMaster Carr	M3x0.5 5mm Fastener	92855A304	1	\$ 1.68	\$ 1.68
	McMaster Carr	#4-40 1/4" Fastener	92196A106	1	\$ 3.92	\$ 3.92
	McMaster Carr	#6-32 1/4" Fastener	92196A144	1	\$ 4.70	\$ 4.70
	McMaster Carr	#8-32 1/4" Fastener	92196A190	1	\$ 6.04	\$ 6.04
	McMaster Carr	1/4-20 Nitronic 60 Helicoils	96246A242	2	\$ 7.28	\$ 14.56
	McMaster Carr	#8-32 Nitronic 60 Helicoils	96246A144	6	\$ 8.10	\$ 48.60
	McMaster Carr	1/4-20 Helicoil Installation Tool	90261A155	1	\$ 91.01	\$ 91.01
	McMaster Carr	#8-32 Helicoil Installation Tool	90261A153	1	\$ 96.63	\$ 96.63
	McMaster Carr	1/4-20 Helicoil Break-Off Tool	92955A111	1	\$ 70.84	\$ 70.84
	McMaster Carr	#8-32 Helicoil Break-Off Tool	92955A107	1	\$ 70.84	\$ 70.84
	McMaster Carr	Low Scratch Nylon Brush	7187T29	1	\$ 3.40	\$ 3.40
	McMaster Carr	4-40 x 1/4" Low Profile Screw	93615A110	1	\$ 13.00	\$ 13.00
	McMaster Carr	4-40 x 1" Female Hex Standoff	91115A522	4	\$ 2.34	\$ 9.36
					Subtotal	\$ 503.40

Aspect	Supplier	Part Description	Part No.	Qty	Price	Extended
Stages	Newmark	100mm Linear Stage	NLS4-4-12V	2	\$ 4,860.00	\$ 9,720.00
	Newmark	360deg Rotation Stage	RM-5-111V	2	\$ 5,350.00	\$ 10,700.00
					Subtotal	\$ 20,420.00

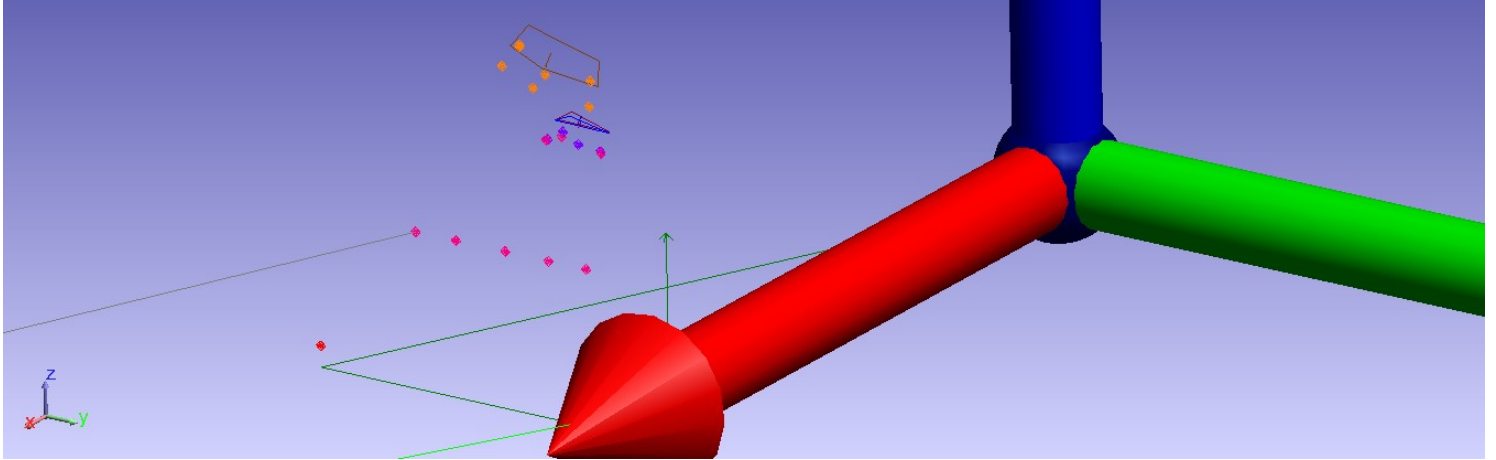
Aspect	Supplier	Part Description	Part No.	Qty	Price	Extended
Optics GSE	Edmunds	Phoenix 1" Monochrome Camera	PHX200S-MC	1	\$ 595.00	\$ 595.00
	Thorlabs	2in Kinematic Mount	KC2	2	\$ 202.77	\$ 405.54
	Thorlabs	45° 2in Mirror Mount	H45CN	1	\$ 46.61	\$ 46.61
	Thorlabs	C-Mount Retaining Ring	CMRR	2	\$ 12.30	\$ 24.60
	Thorlabs	ER Assembly Rods for 60mm Cage	ER6-P4	1	\$ 32.87	\$ 32.87
	Thorlabs	Plate Mount	FP01	1	\$ 47.28	\$ 47.28
	Thorlabs	2in Aluminum Square Mirror	ME2S-G01	1	\$ 32.04	\$ 32.04
	Thorlabs	8in Optical Post	TR8	3	\$ 8.53	\$ 25.59
Thorlabs	4in Pedestal Post Holder	PH4E	3	\$ 26.27	\$ 78.81	
Subtotal						\$ 1,288.34

Aspect	Supplier	Part Description	Part No.	Qty	Price	Extended	Length (in)
GSE Cart	8020	37" T-Slot	1515-S	4	\$ 0.53	\$ 78.44	37
	8020	33" T-Slot (5/16 tapped bottom)	1515-S	4	\$ 0.53	\$ 69.96	33
	8020	17" T-Slot	1515-S	4	\$ 0.53	\$ 36.04	17
	8020	angle plate large	4351	8	\$ 7.10	\$ 56.80	-
	8020	angle plate small	4350	8	\$ 5.60	\$ 44.80	-
	8020	L-bracket for shelf	4504	4	\$ 4.10	\$ 16.40	-
	8020	5/16-18 leveling foot	2194	4	\$ 12.10	\$ 48.40	-
	Thorlabs	Passive Isolation Mounts	PWA074	1	\$ 497.98	\$ 497.98	-
Subtotal						\$ 848.82	

Appendix F

FARO LASER TRACKER REPORT

Jason_Thesis_110119



Transform			
A::0 - Faro Tracker			
# Meas.	87		
Scale Factor	1.000000		
Position (mm)	X	Y	Z
	2832.70	10.23	544.46
Rotation (deg)	Rx	Ry	Rz
	0.9478°	-1.3346°	-5.6987°

Observations										
A::0 - Faro Tracker										
Collection	Group	Target	Azimuth	Elevation	Distance (mm)	Offset1 (mm)	Offset2 (mm)	Date & Time	User	Ac
Jason_Thesis	Datum_Plate	SMR1	-187.9993°	99.4225°	2885.28	6.35	6.35	11/01/19 17:08:11		
Jason_Thesis	Datum_Plate	SMR1	-186.0386°	99.4539°	2884.57	6.35	6.35	11/01/19 17:13:33		
Jason_Thesis	Datum_Plate	SMR2	-186.0682°	100.3268°	2672.95	6.35	6.35	11/01/19 17:14:00		
Jason_Thesis	Datum_Plate	SMR3	-188.2780°	100.2860°	2675.37	6.35	6.35	11/01/19 17:14:17		
Jason_Thesis	+X_Line_Check	SMR1	-185.9287°	100.1075°	2700.35	6.35	6.35	11/01/19 17:19:16		
Jason_Thesis	+X_Line_Check	SMR4	-185.9222°	99.8648°	2757.98	6.35	6.35	11/01/19 17:20:32		
Jason_Thesis	+X_Line_Check	SMR5	-185.9128°	99.4407°	2863.90	6.35	6.35	11/01/19 17:22:47		
Jason_Thesis	M1	SMR1	-186.9060°	99.0062°	2712.55	6.35	6.35	11/01/19 17:28:37		
Jason_Thesis	M1	SMR2	-187.2884°	98.9889°	2712.10	6.35	6.35	11/01/19 17:29:02		
Jason_Thesis	M1	SMR3	-187.1161°	98.9222°	2707.05	6.35	6.35	11/01/19 17:29:25		
Jason_Thesis	M2	SMR1	-186.9698°	98.3443°	2687.89	6.35	6.35	11/01/19 17:32:10		
Jason_Thesis	M2	SMR2	-186.8049°	98.6968°	2711.97	6.35	6.35	11/01/19 17:32:29		
Jason_Thesis	M2	SMR3	-187.3687°	98.7631°	2717.73	6.35	6.35	11/01/19 17:32:38		
Jason_Thesis	M2	SMR4	-187.4543°	98.4037°	2692.96	6.35	6.35	11/01/19 17:32:46		
Jason_Thesis	M2	SMR5	-187.1608°	98.3332°	2687.47	6.35	6.35	11/01/19 17:32:53		
Jason_Thesis	M2	SMR6	-187.0945°	98.5765°	2704.04	6.35	6.35	11/01/19 17:32:58		
Jason_Thesis	M2	SMR7	-187.0956°	98.7931°	2719.16	6.35	6.35	11/01/19 17:33:06		
Jason_Thesis	M2-ADJ1	SMR1	-187.1156°	98.3150°	2686.29	6.35	6.35	11/01/19 17:47:14		
Jason_Thesis	M2-ADJ1	SMR2	-186.7616°	98.4865°	2697.41	6.35	6.35	11/01/19 17:47:22		
Jason_Thesis	M2-ADJ1	SMR3	-186.8522°	98.7235°	2714.09	6.35	6.35	11/01/19 17:47:29		
Jason_Thesis	M2-ADJ1	SMR4	-187.2898°	98.7691°	2718.22	6.35	6.35	11/01/19 17:47:36		
Jason_Thesis	M2-ADJ1	SMR5	-187.4318°	98.5684°	2704.45	6.35	6.35	11/01/19 17:47:45		
Jason_Thesis	M2-ADJ1	SMR6	-187.3784°	98.3893°	2691.90	6.35	6.35	11/01/19 17:47:52		
Jason_Thesis	M2-ADJ2	SMR1	-187.1221°	98.2918°	2685.01	6.35	6.35	11/01/19 17:53:36		
Jason_Thesis	M2-ADJ2	SMR2	-186.8488°	98.4002°	2691.82	6.35	6.35	11/01/19 17:53:42		
Jason_Thesis	M2-ADJ2	SMR3	-186.7801°	98.6888°	2711.84	6.35	6.35	11/01/19 17:53:48		
Jason_Thesis	M2-ADJ2	SMR4	-187.0031°	98.7652°	2717.62	6.35	6.35	11/01/19 17:53:55		
Jason_Thesis	M2-ADJ2	SMR5	-187.3540°	98.7191°	2715.13	6.35	6.35	11/01/19 17:54:01		
Jason_Thesis	M2-ADJ2	SMR6	-187.4723°	98.5815°	2705.71	6.35	6.35	11/01/19 17:54:07		
Jason_Thesis	M2-ADJ2	SMR7	-187.4284°	98.3900°	2692.28	6.35	6.35	11/01/19 17:54:15		
Jason_Thesis	M2-ADJ3	SMR1	-187.1333°	98.2747°	2683.00	6.35	6.35	11/01/19 17:58:27		
Jason_Thesis	M2-ADJ3	SMR2	-186.8455°	98.3933°	2690.46	6.35	6.35	11/01/19 17:58:34		
Jason_Thesis	M2-ADJ3	SMR3	-186.8276°	98.6556°	2708.28	6.35	6.35	11/01/19 17:58:41		
Jason_Thesis	M2-ADJ3	SMR4	-187.0769°	98.7849°	2717.65	6.35	6.35	11/01/19 17:58:52		
Jason_Thesis	M2-ADJ3	SMR5	-187.3835°	98.6766°	2710.86	6.35	6.35	11/01/19 17:59:38		

Jason_Thesis_110119

Observations										
A::0 - Faro Tracker										
Collection	Group	Target	Azimuth	Elevation	Distance (mm)	Offset1 (mm)	Offset2 (mm)	Date & Time	User	Ac
Jason_Thesis	M2-ADJ3	SMR6	-187.4951°	98.4977°	2698.92	6.35	6.35	11/01/19 17:59:44		
Jason_Thesis	M2-ADJ3	SMR7	-187.2510°	98.3083°	2685.52	6.35	6.35	11/01/19 17:59:50		
Jason_Thesis	M2-ADJ4	SMR1	-187.1565°	98.2774°	2683.18	6.35	6.35	11/01/19 18:05:46		
Jason_Thesis	M2-ADJ4	SMR2	-186.8183°	98.4110°	2691.47	6.35	6.35	11/01/19 18:05:52		
Jason_Thesis	M2-ADJ4	SMR3	-186.8932°	98.7404°	2713.93	6.35	6.35	11/01/19 18:06:01		
Jason_Thesis	M2-ADJ4	SMR4	-187.2473°	98.7843°	2717.62	6.35	6.35	11/01/19 18:06:07		
Jason_Thesis	M2-ADJ4	SMR5	-187.4861°	98.6378°	2708.10	6.35	6.35	11/01/19 18:06:14		
Jason_Thesis	M2-ADJ4	SMR6	-187.4611°	98.4151°	2692.98	6.35	6.35	11/01/19 18:06:21		
Jason_Thesis	M2-ADJ5	SMR1	-187.1129°	98.2986°	2684.37	6.35	6.35	11/01/19 18:13:14		
Jason_Thesis	M2-ADJ5	SMR2	-186.7152°	98.5610°	2701.29	6.35	6.35	11/01/19 18:13:22		
Jason_Thesis	M2-ADJ5	SMR3	-186.9073°	98.7668°	2715.63	6.35	6.35	11/01/19 18:13:27		
Jason_Thesis	M2-ADJ5	SMR4	-187.2577°	98.7871°	2717.68	6.35	6.35	11/01/19 18:13:33		
Jason_Thesis	M2-ADJ5	SMR5	-187.4218°	98.6533°	2708.89	6.35	6.35	11/01/19 18:13:40		
Jason_Thesis	M2-ADJ5	SMR6	-187.4907°	98.5184°	2699.92	6.35	6.35	11/01/19 18:13:46		
Jason_Thesis	M2-ADJ5	SMR7	-187.2902°	98.3105°	2685.51	6.35	6.35	11/01/19 18:13:53		
Jason_Thesis	M2-ADJ6	SMR1	-187.1281°	98.3330°	2686.51	6.35	6.35	11/01/19 18:21:20		
Jason_Thesis	M2-ADJ6	SMR2	-186.7948°	98.4965°	2696.84	6.35	6.35	11/01/19 18:21:28		
Jason_Thesis	M2-ADJ6	SMR3	-186.9033°	98.7155°	2711.79	6.35	6.35	11/01/19 18:21:34		
Jason_Thesis	M2-ADJ6	SMR4	-187.2250°	98.7982°	2718.06	6.35	6.35	11/01/19 18:21:52		
Jason_Thesis	M2-ADJ6	SMR5	-187.4162°	98.7035°	2712.01	6.35	6.35	11/01/19 18:21:59		
Jason_Thesis	M2-ADJ6	SMR6	-187.1526°	98.6318°	2706.55	6.35	6.35	11/01/19 18:22:05		
Jason_Thesis	M2-ADJ6	SMR7	-187.4880°	98.4736°	2696.67	6.35	6.35	11/01/19 18:22:11		
Jason_Thesis	M2-ADJ7	SMR1	-187.0891°	98.2980°	2684.35	6.35	6.35	11/01/19 18:27:34		
Jason_Thesis	M2-ADJ7	SMR2	-186.7836°	98.4717°	2695.42	6.35	6.35	11/01/19 18:27:40		
Jason_Thesis	M2-ADJ7	SMR3	-186.8957°	98.7488°	2714.28	6.35	6.35	11/01/19 18:27:45		
Jason_Thesis	M2-ADJ7	SMR4	-187.2272°	98.8024°	2718.33	6.35	6.35	11/01/19 18:28:02		
Jason_Thesis	M2-ADJ7	SMR5	-187.4878°	98.6556°	2708.31	6.35	6.35	11/01/19 18:28:08		
Jason_Thesis	M2-ADJ7	SMR6	-187.1911°	98.5882°	2703.76	6.35	6.35	11/01/19 18:28:13		
Jason_Thesis	M2-ADJ7	SMR7	-187.3993°	98.4004°	2691.60	6.35	6.35	11/01/19 18:28:19		
Jason_Thesis	M2-ADJ8	SMR1	-187.1791°	98.3282°	2685.95	6.35	6.35	11/01/19 18:30:15		
Jason_Thesis	M2-ADJ8	SMR2	-186.7775°	98.5153°	2697.50	6.35	6.35	11/01/19 18:30:22		
Jason_Thesis	M2-ADJ8	SMR3	-186.9712°	98.8223°	2718.64	6.35	6.35	11/01/19 18:30:29		
Jason_Thesis	M2-ADJ8	SMR4	-187.4477°	98.7555°	2715.31	6.35	6.35	11/01/19 18:30:35		
Jason_Thesis	M2-ADJ8	SMR5	-187.5066°	98.5687°	2702.85	6.35	6.35	11/01/19 18:30:40		
Jason_Thesis	M2-ADJ8	SMR6	-187.4559°	98.3683°	2689.29	6.35	6.35	11/01/19 18:30:45		
Jason_Thesis	M2-ADJ8	SMR7	-187.1920°	98.3156°	2685.11	6.35	6.35	11/01/19 18:30:52		
Jason_Thesis	M2-ADJ9	SMR1	-187.1576°	98.3111°	2684.97	6.35	6.35	11/01/19 18:33:17		
Jason_Thesis	M2-ADJ9	SMR2	-186.8125°	98.5101°	2697.49	6.35	6.35	11/01/19 18:33:23		
Jason_Thesis	M2-ADJ9	SMR3	-187.0352°	98.7532°	2714.37	6.35	6.35	11/01/19 18:33:30		
Jason_Thesis	M2-ADJ9	SMR4	-187.3881°	98.6904°	2710.96	6.35	6.35	11/01/19 18:33:35		
Jason_Thesis	M2-ADJ9	SMR5	-187.4873°	98.5419°	2701.15	6.35	6.35	11/01/19 18:33:41		
Jason_Thesis	M2-ADJ9	SMR6	-187.1688°	98.5407°	2700.30	6.35	6.35	11/01/19 18:33:47		
Jason_Thesis	M2-ADJ9	SMR7	-187.1746°	98.3253°	2685.94	6.35	6.35	11/01/19 18:33:54		
Jason_Thesis	M1-ADJ1	SMR1	-186.9217°	99.0013°	2713.47	6.35	6.35	11/01/19 18:40:03		
Jason_Thesis	M1-ADJ1	SMR2	-187.0614°	98.9763°	2712.06	6.35	6.35	11/01/19 18:40:10		
Jason_Thesis	M1-ADJ1	SMR3	-187.0973°	98.8886°	2706.10	6.35	6.35	11/01/19 18:40:16		
Jason_Thesis	M1-ADJ1	SMR4	-187.2913°	98.9879°	2713.20	6.35	6.35	11/01/19 18:40:39		
Jason_Thesis	M1-MOUNT	SMR1	-186.4038°	99.5066°	2671.86	6.35	6.35	11/01/19 18:52:05		
Jason_Thesis	M1-MOUNT	SMR2	-186.6744°	99.5026°	2671.97	6.35	6.35	11/01/19 18:52:11		
Jason_Thesis	M1-MOUNT	SMR3	-186.9906°	99.4975°	2672.19	6.35	6.35	11/01/19 18:52:17		
Jason_Thesis	M1-MOUNT	SMR4	-187.3496°	99.4911°	2672.55	6.35	6.35	11/01/19 18:52:22		
Jason_Thesis	M1-MOUNT	SMR5	-187.6412°	99.4858°	2672.92	6.35	6.35	11/01/19 18:52:27		

Frame			
A::WORLD			
	X	Y	Z
Translation (mm)	2832.70	10.23	544.46
Rotation	0.9478°	-1.3346°	-5.6987°
X Axis	0.994788	-0.099269	0.023291
Y Axis	0.098899	0.994960	0.016536
Z Axis	-0.024815	-0.014147	0.999592
Proj. Ang.	Rx from Y	Ry from Z	Rz from X
X	166.7961°	88.6588°	-5.6987°
Y	0.9522°	80.5078°	84.3234°
Z	90.8108°	-1.4221°	-150.3128°

Jason_Thesis_110119

Frame A::Datum_Frame_Boresight_1			
	X	Y	Z
Translation (mm)	0.00	0.00	0.00
Rotation	0.0000°	0.0000°	0.0000°
X Axis	1.000000	0.000000	0.000000
Y Axis	0.000000	1.000000	0.000000
Z Axis	0.000000	0.000000	1.000000
Proj. Ang.	Rx from Y	Ry from Z	Rz from X
X	0.0000°	90.0000°	0.0000°
Y	0.0000°	0.0000°	90.0000°
Z	90.0000°	0.0000°	0.0000°

Line A::+X_Line_Check			
	X	Y	Z
Begin (mm)	186.86	6.23	4.60
End (mm)	20.14	6.27	4.62
Direction (mm)	-1.000000	0.000277	0.000126
Proj. Ang.	Rx from Y	Ry from Z	Rz from X
(deg)	24.5005°	-89.9928°	179.9842°
Length (mm)	166.72		

Plane A::Datum_Plate_Boresight1				
	A	B	C	D
(mm)	0.000000	0.000000	1.000000	6.350000
Proj. Ang.	Rx from Y	Ry from Z	Rz from X	
(deg)	90.0000°	0.0000°	0.0000°	

Plane A::M1				
	A	B	C	D
(mm)	-0.698537	-0.003070	0.715567	71.441229
Proj. Ang.	Rx from Y	Ry from Z	Rz from X	
(deg)	90.2458°	-44.3100°	-179.7482°	

Plane A::M2				
	A	B	C	D
(mm)	0.697844	0.003026	-0.716243	-59.400686
Proj. Ang.	Rx from Y	Ry from Z	Rz from X	
(deg)	-89.7579°	135.7454°	0.2484°	

Plane A::M2-ADJ1				
	A	B	C	D
(mm)	0.696377	0.002655	-0.717671	-58.955961
Proj. Ang.	Rx from Y	Ry from Z	Rz from X	
(deg)	-89.7881°	135.8628°	0.2184°	

Jason_Thesis_110119

Plane A::M2-ADJ2				
	A	B	C	D
(mm)	0.695770	0.003164	-0.718258	-58.629338
Proj. Ang. (deg)	Rx from Y -89.7476°	Ry from Z 135.9111°	Rz from X 0.2606°	

Plane A::M2-ADJ3				
	A	B	C	D
(mm)	0.702652	0.001891	-0.711531	-61.035600
Proj. Ang. (deg)	Rx from Y -89.8477°	Ry from Z 135.3597°	Rz from X 0.1542°	

Plane A::M2-ADJ4				
	A	B	C	D
(mm)	0.705262	0.003835	-0.708936	-61.716696
Proj. Ang. (deg)	Rx from Y -89.6901°	Ry from Z 135.1489°	Rz from X 0.3115°	

Plane A::M2-ADJ5				
	A	B	C	D
(mm)	0.705411	0.003529	-0.708790	-61.840942
Proj. Ang. (deg)	Rx from Y -89.7147°	Ry from Z 135.1369°	Rz from X 0.2866°	

Plane A::M2-ADJ6				
	A	B	C	D
(mm)	0.707088	0.003331	-0.707117	-62.412673
Proj. Ang. (deg)	Rx from Y -89.7301°	Ry from Z 135.0012°	Rz from X 0.2699°	

Plane A::M2-ADJ7				
	A	B	C	D
(mm)	0.709223	0.014715	-0.704831	-62.343246
Proj. Ang. (deg)	Rx from Y -88.8040°	Ry from Z 134.8220°	Rz from X 1.1886°	

Plane A::M2-ADJ8				
	A	B	C	D
(mm)	0.707904	-0.002349	-0.706304	-63.146849
Proj. Ang. (deg)	Rx from Y -90.1905°	Ry from Z 134.9352°	Rz from X -0.1901°	

Plane A::M2-ADJ9				
	A	B	C	D

Jason_Thesis_110119

Plane A::M2-ADJ9				
	A	B	C	D
(mm)	0.707468	-0.000382	-0.706746	-62.799345
Proj. Ang. (deg)	Rx from Y -90.0309°	Ry from Z 134.9707°	Rz from X -0.0309°	

Plane A::M1-ADJ1				
	A	B	C	D
(mm)	0.709306	0.006561	-0.704870	-72.934224
Proj. Ang. (deg)	Rx from Y -89.4667°	Ry from Z 134.8203°	Rz from X 0.5299°	

Geometry Fit Results (Datum_Plate) (Summary) 11/1/2019 5:15:07 PM				
Working Frame	A::WORLD	Units:	(mm)/(deg)	
Plane Fit Results:	X	Y	Z	
Normal	0.023291	0.016536	0.999592	
Position	-2683.30	-318.88	-483.24	
Rotation (deg)	Rx 1.1149	Ry -1.1985	Rz 172.4376	
Proj. Ang. (deg)	Rx from Y 89.0522	Ry from Z 1.3348	Rz from X 35.3748	
DEVIATION STATS				
Mean	-0.00	RMS	0.00	
Max	0.00	Min	0.00	
Max	-0.00	Min	-0.00	
Total Number	3			
Points Used	3			
Probing Direction was used to override normal determination.				
All offsets set to	6.35			

Geometry Fit Results (Datum_Plate) (Details) 11/1/2019 5:15:07 PM			
	Points Used	Weight	Error
Jason_Thesis::Datum_Plate::SMR1		1.00	-0.00
Jason_Thesis::Datum_Plate::SMR2		1.00	-0.00
Jason_Thesis::Datum_Plate::SMR3		1.00	-0.00

Geometry Fit Results (+X_Line_Check) (Summary) 11/1/2019 5:20:57 PM			
Working Frame	A::Datum_Frame_Boresight_1	Units:	(mm)/(deg)
Line Fit Results:		X	Y Z

Jason_Thesis_110119

Geometry Fit Results (+X_Line_Check) (Summary)				
11/1/2019 5:20:57 PM				
Begin Point		186.86	6.26	4.61
End Point		37.32	6.06	4.59
Direction		-0.999999	-0.001352	-0.000098
Proj. Ang. (deg)		Rx from Y -175.8651	Ry from Z -90.0056	Rz from X -179.9226
DEVIATION STATS				
Mean		0.06	RMS	0.06
		Magnitude		
Max		0.09	Min	0.04
		Signed		
Max		0.09	Min	0.04
Total Number		3		
Points Used		3		

Geometry Fit Results (+X_Line_Check) (Details)			
11/1/2019 5:20:57 PM			
	Points Used		
	Name	Weight	Error
	Jason_Thesis::+X_Line_Check::SMR1	1.00	0.05
	Jason_Thesis::+X_Line_Check::SMR2	1.00	0.04
	Jason_Thesis::+X_Line_Check::SMR4	1.00	0.09

Geometry Fit Results (+X_Line_Check)1 (Summary)				
11/1/2019 5:24:40 PM				
Working Frame	A::Datum_Frame_Boresight_1	Units:	(mm)/(deg)	
Line Fit Results:				
		X	Y	Z
Begin Point		186.86	6.23	4.60
End Point		20.14	6.27	4.62
Direction		-1.000000	0.000277	0.000126
Proj. Ang. (deg)		Rx from Y 24.5005	Ry from Z -89.9928	Rz from X 179.9842
DEVIATION STATS				
Mean		0.03	RMS	0.04
		Magnitude		
Max		0.05	Min	0.02
		Signed		
Max		0.05	Min	0.02
Total Number		3		
Points Used		3		

Geometry Fit Results (+X_Line_Check)1 (Details)			
11/1/2019 5:24:40 PM			
	Points Used		
	Name	Weight	Error
	Jason_Thesis::+X_Line_Check::SMR1	1.00	0.03
	Jason_Thesis::+X_Line_Check::SMR4	1.00	0.05

Jason_Thesis_110119

Geometry Fit Results (M1) (Summary)			
11/1/2019 5:30:25 PM			
Working Frame	A::Datum_Frame_Boresight_1	Units:	(mm)/(deg)
Plane Fit Results:	X	Y	Z
Normal	0.698537	0.003070	-0.715567
Position	163.02	-49.49	59.09
	Rx	Ry	Rz
Rotation (deg)	136.7698	10.8561	101.5812
Proj. Ang.	Rx from Y	Ry from Z	Rz from X
(deg)	-89.7542	135.6900	0.2518
DEVIATION STATS			
Mean	-0.00	RMS	0.00
	Magnitude		
Max	0.00	Min	0.00
	Signed		
Max	-0.00	Min	-0.00
Total Number	3		
Points Used	3		
Probing Direction was used to override normal determination.			
All offsets set to	6.35		

Geometry Fit Results (M1) (Details)			
11/1/2019 5:30:25 PM			
	Points Used		
	Name	Weight	Error
	Jason_Thesis::M1::SMR1	1.00	-0.00
	Jason_Thesis::M1::SMR2	1.00	-0.00
	Jason_Thesis::M1::SMR3	1.00	-0.00

Geometry Fit Results (M2) (Summary)			
11/1/2019 5:33:45 PM			
Working Frame	A::Datum_Frame_Boresight_1	Units:	(mm)/(deg)
Plane Fit Results:	X	Y	Z
Normal	0.697844	0.003026	-0.716243
Position	167.05	-51.16	79.60
	Rx	Ry	Rz
Rotation (deg)	158.9733	-39.8846	31.1894
Proj. Ang.	Rx from Y	Ry from Z	Rz from X
(deg)	-89.7579	135.7454	0.2484
DEVIATION STATS			
Mean	-0.00	RMS	0.02
	Magnitude		
Max	0.03	Min	0.01
	Signed		
Max	0.03	Min	-0.02
Total Number	7		
Points Used	7		
Probing Direction was used to override normal determination.			
All offsets set to	6.35		

Jason_Thesis_110119

Geometry Fit Results (M2) (Details)			
11/1/2019 5:33:45 PM			
Points Used	Name	Weight	Error
	Jason_Thesis::M2::SMR1	1.00	-0.01
	Jason_Thesis::M2::SMR2	1.00	-0.02
	Jason_Thesis::M2::SMR3	1.00	-0.02
	Jason_Thesis::M2::SMR4	1.00	-0.01
	Jason_Thesis::M2::SMR5	1.00	0.01
	Jason_Thesis::M2::SMR6	1.00	0.03
	Jason_Thesis::M2::SMR7	1.00	0.03

Geometry Fit Results (M2-ADJ1) (Summary)			
11/1/2019 5:48:23 PM			
Working Frame	A::Datum_Frame_Boresight_1	Units:	(mm)/(deg)
Plane Fit Results:	X	Y	Z
Normal	0.696377	0.002655	-0.717671
Position	167.88	-51.28	80.56
Rotation (deg)	Rx	Ry	Rz
Proj. Ang. (deg)	176.6076	-44.0337	5.0929
	Rx from Y	Ry from Z	Rz from X
	-89.7881	135.8628	0.2184
DEVIATION STATS			
Mean	-0.00	RMS	0.01
	Magnitude		
Max	0.01	Min	0.00
	Signed		
Max	0.01	Min	-0.01
Total Number Points Used	6		
	6		
Probing Direction was used to override normal determination.			
All offsets set to	6.35		

Geometry Fit Results (M2-ADJ1) (Details)			
11/1/2019 5:48:23 PM			
Points Used	Name	Weight	Error
	Jason_Thesis::M2-ADJ1::SMR1	1.00	-0.01
	Jason_Thesis::M2-ADJ1::SMR2	1.00	0.00
	Jason_Thesis::M2-ADJ1::SMR3	1.00	0.01
	Jason_Thesis::M2-ADJ1::SMR4	1.00	-0.01
	Jason_Thesis::M2-ADJ1::SMR5	1.00	0.00
	Jason_Thesis::M2-ADJ1::SMR6	1.00	0.01

Plane M2 to Plane M2-ADJ1
11/1/2019 5:49:45 PM
Angle = 0.1193°

Plane M2 to Plane M2-ADJ1
11/1/2019 5:50:34 PM
Angle = 0.1193°

Jason_Thesis_110119

Geometry Fit Results (M2-ADJ2) (Summary)			
11/1/2019 5:54:34 PM			
Working Frame	A::Datum_Frame_Boresight_1	Units:	(mm)/(deg)
Plane Fit Results:	X	Y	Z
Normal	0.695770	0.003164	-0.718258
Position	167.24	-51.57	80.15
	Rx	Ry	Rz
Rotation (deg)	177.0641	-44.0114	4.4821
Proj. Ang.	Rx from Y	Ry from Z	Rz from X
(deg)	-89.7476	135.9111	0.2606
DEVIATION STATS			
Mean	-0.00	RMS	0.02
	Magnitude		
Max	0.05	Min	0.00
	Signed		
Max	0.03	Min	-0.05
Total Number	7		
Points Used	7		
Probing Direction was used to override normal determination.			
All offsets set to	6.35		

Geometry Fit Results (M2-ADJ2) (Details)			
11/1/2019 5:54:34 PM			
Points Used	Name	Weight	Error
	Jason_Thesis::M2-ADJ2::SMR1	1.00	-0.05
	Jason_Thesis::M2-ADJ2::SMR2	1.00	0.03
	Jason_Thesis::M2-ADJ2::SMR3	1.00	-0.00
	Jason_Thesis::M2-ADJ2::SMR4	1.00	0.00
	Jason_Thesis::M2-ADJ2::SMR5	1.00	-0.02
	Jason_Thesis::M2-ADJ2::SMR6	1.00	0.01
	Jason_Thesis::M2-ADJ2::SMR7	1.00	0.03

Geometry Fit Results (M2-ADJ3) (Summary)			
11/1/2019 6:00:04 PM			
Working Frame	A::Datum_Frame_Boresight_1	Units:	(mm)/(deg)
Plane Fit Results:	X	Y	Z
Normal	0.702652	0.001891	-0.711531
Position	170.39	-51.54	82.35
	Rx	Ry	Rz
Rotation (deg)	178.1033	-44.6086	2.8541
Proj. Ang.	Rx from Y	Ry from Z	Rz from X
(deg)	-89.8477	135.3597	0.1542
DEVIATION STATS			
Mean	-0.00	RMS	0.01
	Magnitude		
Max	0.01	Min	0.00
	Signed		
Max	0.01	Min	-0.01
Total Number	7		

Jason_Thesis_110119

Geometry Fit Results (M2-ADJ3) (Summary)			
11/1/2019 6:00:04 PM			
Proj. Ang.	Rx from Y	Ry from Z	Rz from X
Points Used	7		
Probing Direction was used to override normal determination.			
All offsets set to	6.35		

Geometry Fit Results (M2-ADJ3) (Details)			
11/1/2019 6:00:04 PM			
Points Used	Name	Weight	Error
	Jason_Thesis::M2-ADJ3::SMR1	1.00	0.01
	Jason_Thesis::M2-ADJ3::SMR2	1.00	-0.01
	Jason_Thesis::M2-ADJ3::SMR3	1.00	-0.01
	Jason_Thesis::M2-ADJ3::SMR4	1.00	0.01
	Jason_Thesis::M2-ADJ3::SMR5	1.00	0.00
	Jason_Thesis::M2-ADJ3::SMR6	1.00	-0.01
	Jason_Thesis::M2-ADJ3::SMR7	1.00	0.00

Geometry Fit Results (M2-ADJ4) (Summary)			
11/1/2019 6:06:46 PM			
Working Frame	A::Datum_Frame_Boresight_1	Units:	(mm)/(deg)
Plane Fit Results:	X	Y	Z
Normal	0.705262	0.003835	-0.708936
Position	168.73	-53.08	80.51
	Rx	Ry	Rz
Rotation (deg)	177.2226	-44.7838	4.2512
Proj. Ang.	Rx from Y	Ry from Z	Rz from X
(deg)	-89.6901	135.1489	0.3115
DEVIATION STATS			
Mean	-0.00	RMS	0.01
	Magnitude		
Max	0.01	Min	0.00
	Signed		
Max	0.01	Min	-0.01
Total Number	6		
Points Used	6		
Probing Direction was used to override normal determination.			
All offsets set to	6.35		

Geometry Fit Results (M2-ADJ4) (Details)			
11/1/2019 6:06:46 PM			
Points Used	Name	Weight	Error
	Jason_Thesis::M2-ADJ4::SMR1	1.00	-0.01
	Jason_Thesis::M2-ADJ4::SMR2	1.00	0.01
	Jason_Thesis::M2-ADJ4::SMR3	1.00	0.00
	Jason_Thesis::M2-ADJ4::SMR4	1.00	-0.01
	Jason_Thesis::M2-ADJ4::SMR5	1.00	0.00
	Jason_Thesis::M2-ADJ4::SMR6	1.00	0.01

Jason_Thesis_110119

Geometry Fit Results (M2-ADJ5) (Summary)			
11/1/2019 6:14:10 PM			
Working Frame	A::Datum_Frame_Boresight_1	Units:	(mm)/(deg)
Plane Fit Results:	X	Y	Z
Normal	0.705411	0.003529	-0.708790
Position	168.15	-52.79	79.83
	Rx	Ry	Rz
Rotation (deg)	172.6127	-44.3796	10.7885
Proj. Ang.	Rx from Y	Ry from Z	Rz from X
(deg)	-89.7147	135.1369	0.2866
DEVIATION STATS			
Mean	-0.00	RMS	0.00
	Magnitude		
Max	0.01	Min	0.00
	Signed		
Max	0.01	Min	-0.01
Total Number	7		
Points Used	7		
Probing Direction was used to override normal determination.			
All offsets set to	6.35		

Geometry Fit Results (M2-ADJ5) (Details)			
11/1/2019 6:14:10 PM			
	Points Used		
Name	Weight	Error	
Jason_Thesis::M2-ADJ5::SMR1	1.00	-0.00	
Jason_Thesis::M2-ADJ5::SMR2	1.00	0.00	
Jason_Thesis::M2-ADJ5::SMR3	1.00	-0.00	
Jason_Thesis::M2-ADJ5::SMR4	1.00	0.01	
Jason_Thesis::M2-ADJ5::SMR5	1.00	0.00	
Jason_Thesis::M2-ADJ5::SMR6	1.00	-0.01	
Jason_Thesis::M2-ADJ5::SMR7	1.00	0.00	

Plane M2-ADJ4 to Plane M2-ADJ5
11/1/2019 6:16:27 PM
Angle = 0.0212°

Geometry Fit Results (M2-ADJ6) (Summary)			
11/1/2019 6:22:32 PM			
Working Frame	A::Datum_Frame_Boresight_1	Units:	(mm)/(deg)
Plane Fit Results:	X	Y	Z
Normal	0.707088	0.003331	-0.707117
Position	166.28	-52.23	77.76
	Rx	Ry	Rz
Rotation (deg)	175.9432	-44.8550	6.0120
Proj. Ang.	Rx from Y	Ry from Z	Rz from X
(deg)	-89.7301	135.0012	0.2699
DEVIATION STATS			
Mean	-0.00	RMS	0.01
	Magnitude		

Jason_Thesis_110119

Geometry Fit Results (M2-ADJ6) (Summary)				
11/1/2019 6:22:32 PM				
Proj. Ang.	Rx from Y	Ry from Z	Rz from X	
Max	Signed	0.02	Min	0.00
Max		0.02	Min	-0.01
Total Number		7		
Points Used		7		
Probing Direction was used to override normal determination.				
All offsets set to				
		6.35		

Geometry Fit Results (M2-ADJ6) (Details)				
11/1/2019 6:22:32 PM				
	Points Used	Name	Weight	Error
		Jason_Thesis::M2-ADJ6::SMR1	1.00	0.00
		Jason_Thesis::M2-ADJ6::SMR2	1.00	-0.01
		Jason_Thesis::M2-ADJ6::SMR3	1.00	0.00
		Jason_Thesis::M2-ADJ6::SMR4	1.00	-0.01
		Jason_Thesis::M2-ADJ6::SMR5	1.00	-0.00
		Jason_Thesis::M2-ADJ6::SMR6	1.00	0.02
		Jason_Thesis::M2-ADJ6::SMR7	1.00	-0.01

Geometry Fit Results (M2-ADJ7) (Summary)				
11/1/2019 6:28:40 PM				
Working Frame	A::Datum_Frame_Boresight_1	Units:	(mm)/(deg)	
Plane Fit Results:	X	Y	Z	
Normal	0.709223	0.014715	-0.704831	
Position	167.79	-52.05	79.29	
	Rx	Ry	Rz	
Rotation (deg)	172.6116	-44.7055	11.6329	
Proj. Ang.	Rx from Y	Ry from Z	Rz from X	
(deg)	-88.8040	134.8220	1.1886	
DEVIATION STATS				
Mean	-0.00	RMS	0.09	
	Magnitude			
Max	0.16	Min	0.01	
	Signed			
Max	0.16	Min	-0.10	
Total Number	7			
Points Used	7			
Probing Direction was used to override normal determination.				
All offsets set to				
		6.35		

Geometry Fit Results (M2-ADJ7) (Details)				
11/1/2019 6:28:40 PM				
	Points Used	Name	Weight	Error
		Jason_Thesis::M2-ADJ7::SMR1	1.00	-0.01
		Jason_Thesis::M2-ADJ7::SMR2	1.00	0.08
		Jason_Thesis::M2-ADJ7::SMR3	1.00	-0.03

Jason_Thesis_110119

Geometry Fit Results (M2-ADJ7) (Details)			
11/1/2019 6:28:40 PM			
Jason_Thesis::M2-ADJ7::SMR4	1.00	-0.08	
Jason_Thesis::M2-ADJ7::SMR5	1.00	0.16	
Jason_Thesis::M2-ADJ7::SMR6	1.00	-0.03	
Jason_Thesis::M2-ADJ7::SMR7	1.00	-0.10	

Geometry Fit Results (M2-ADJ8) (Summary)				
11/1/2019 6:32:55 PM				
Working Frame	A::Datum_Frame_Boresight_1	Units:	(mm)/(deg)	
Plane Fit Results:		X	Y	Z
Normal		0.707904	-0.002349	-0.706304
Position		170.55	-54.94	81.72
		Rx	Ry	Rz
Rotation (deg)		172.9032	-44.6219	9.8608
Proj. Ang.		Rx from Y	Ry from Z	Rz from X
(deg)		-90.1905	134.9352	-0.1901
DEVIATION STATS				
Mean		-0.00	RMS	0.01
		Magnitude		
Max		0.01	Min	0.00
		Signed		
Max		0.01	Min	-0.01
Total Number		7		
Points Used		7		
Probing Direction was used to override normal determination.				
All offsets set to		6.35		

Geometry Fit Results (M2-ADJ8) (Details)			
11/1/2019 6:32:55 PM			
	Points Used		
	Name	Weight	Error
	Jason_Thesis::M2-ADJ8::SMR1	1.00	-0.01
	Jason_Thesis::M2-ADJ8::SMR2	1.00	-0.01
	Jason_Thesis::M2-ADJ8::SMR3	1.00	0.01
	Jason_Thesis::M2-ADJ8::SMR4	1.00	-0.00
	Jason_Thesis::M2-ADJ8::SMR5	1.00	-0.01
	Jason_Thesis::M2-ADJ8::SMR6	1.00	0.01
	Jason_Thesis::M2-ADJ8::SMR7	1.00	0.01

Geometry Fit Results (M2-ADJ9) (Summary)				
11/1/2019 6:36:27 PM				
Working Frame	A::Datum_Frame_Boresight_1	Units:	(mm)/(deg)	
Plane Fit Results:		X	Y	Z
Normal		0.707468	-0.000382	-0.706746
Position		170.41	-52.92	81.76
		Rx	Ry	Rz
Rotation (deg)		176.8344	-44.9417	4.4460
Proj. Ang.		Rx from Y	Ry from Z	Rz from X
(deg)		-90.0309	134.9707	-0.0309
DEVIATION STATS				

Jason_Thesis_110119

Geometry Fit Results (M2-ADJ9) (Summary)				
11/1/2019 6:36:27 PM				
Proj. Ang.	Rx from Y	Ry from Z	Rz from X	
Mean	-0.00	RMS		0.01
	Magnitude			
Max	0.01	Min		0.00
	Signed			
Max	0.01	Min		-0.01
Total Number	7			
Points Used	7			
Probing Direction was used to override normal determination.				
All offsets set to 6.35				

Geometry Fit Results (M2-ADJ9) (Details)			
11/1/2019 6:36:27 PM			
Points Used	Name	Weight	Error
	Jason_Thesis::M2-ADJ9::SMR1	1.00	-0.01
	Jason_Thesis::M2-ADJ9::SMR2	1.00	0.00
	Jason_Thesis::M2-ADJ9::SMR3	1.00	0.00
	Jason_Thesis::M2-ADJ9::SMR4	1.00	-0.01
	Jason_Thesis::M2-ADJ9::SMR5	1.00	0.01
	Jason_Thesis::M2-ADJ9::SMR6	1.00	0.00
	Jason_Thesis::M2-ADJ9::SMR7	1.00	0.00

Geometry Fit Results (M1-ADJ1) (Summary)				
11/1/2019 6:41:17 PM				
Working Frame	A::Datum_Frame_Boresight_1	Units:	(mm)/(deg)	
Plane Fit Results:	X	Y	Z	
Normal	0.709306	0.006561	-0.704870	
Position	162.23	-49.04	59.32	
	Rx	Ry	Rz	
Rotation (deg)	136.5654	13.9080	104.7747	
Proj. Ang. (deg)	Rx from Y	Ry from Z	Rz from X	
	-89.4667	134.8203	0.5299	
DEVIATION STATS				
Mean	-0.00	RMS		0.02
	Magnitude			
Max	0.03	Min		0.00
	Signed			
Max	0.01	Min		-0.03
Total Number	4			
Points Used	4			
Probing Direction was used to override normal determination.				
All offsets set to 6.35				

Geometry Fit Results (M1-ADJ1) (Details)			
11/1/2019 6:41:17 PM			
Points Used	Name	Weight	Error
	Jason_Thesis::M1-ADJ1::SMR1	1.00	0.01

Jason_Thesis_110119

Geometry Fit Results (M1-ADJ1) (Details)

11/1/2019 6:41:17 PM

Jason_Thesis::M1-ADJ1::SMR2	1.00	-0.03
Jason_Thesis::M1-ADJ1::SMR3	1.00	0.00
Jason_Thesis::M1-ADJ1::SMR4	1.00	0.01

Plane: M2-ADJ9 to vertices of Plane: M1-ADJ1

11/1/2019 6:42:14 PM

Min = 10.02 (mm), Avg = 10.07 (mm), Max = 10.14 (mm), Points = 3

Plane M1-ADJ1 to Plane M2-ADJ9

11/1/2019 6:42:54 PM

Angle = 0.4253°

Point Group

Jason_Thesis::Datum_Plate

Point Name	X (mm)	Y (mm)	Z (mm)
SMR1	0.00	0.00	0.00
SMR2	215.81	-0.00	0.00
SMR3	215.70	-101.51	0.00

Point Group

Jason_Thesis::+X Line Check

Point Name	X (mm)	Y (mm)	Z (mm)
SMR1	186.86	6.21	4.63
SMR4	128.08	6.27	4.56
SMR5	20.14	6.27	4.64

Point Group

Jason_Thesis::M1

Point Name	X (mm)	Y (mm)	Z (mm)
SMR1	165.57	-40.26	52.74
SMR2	166.30	-58.13	53.38
SMR3	170.49	-50.03	57.51

Point Group

Jason_Thesis::M2

Point Name	X (mm)	Y (mm)	Z (mm)
SMR1	184.44	-43.29	87.73
SMR2	163.43	-35.77	67.32
SMR3	158.96	-62.24	62.85
SMR4	180.53	-65.86	83.82
SMR5	184.98	-52.16	88.20
SMR6	170.54	-49.24	74.12
SMR7	157.46	-49.45	61.37

Jason_Thesis_110119

Point Group Jason_Thesis::M2-ADJ1			
Point Name	X (mm)	Y (mm)	Z (mm)
SMR1	185.95	-50.05	89.27
SMR2	176.00	-33.68	79.65
SMR3	161.61	-38.00	65.67
SMR4	158.43	-58.55	62.53
SMR5	170.51	-64.99	74.21
SMR6	181.34	-62.32	84.71

Point Group Jason_Thesis::M2-ADJ2			
Point Name	X (mm)	Y (mm)	Z (mm)
SMR1	187.03	-50.34	90.55
SMR2	180.89	-37.70	84.56
SMR3	163.46	-34.61	67.73
SMR4	158.64	-45.10	63.00
SMR5	161.13	-61.52	65.37
SMR6	169.43	-66.91	73.35
SMR7	181.05	-64.65	84.58

Point Group Jason_Thesis::M2-ADJ3			
Point Name	X (mm)	Y (mm)	Z (mm)
SMR1	188.89	-50.83	91.68
SMR2	182.18	-37.53	85.11
SMR3	166.74	-36.80	69.87
SMR4	158.86	-48.54	62.03
SMR5	165.02	-62.82	68.09
SMR6	175.47	-67.85	78.41
SMR7	186.82	-56.31	89.62

Point Group Jason_Thesis::M2-ADJ4			
Point Name	X (mm)	Y (mm)	Z (mm)
SMR1	188.75	-51.90	91.50
SMR2	181.29	-36.27	84.13
SMR3	161.95	-39.90	64.88
SMR4	159.09	-56.53	61.96
SMR5	167.56	-67.57	70.31
SMR6	180.60	-66.17	83.28

Point Group Jason_Thesis::M2-ADJ5			
Point Name	X (mm)	Y (mm)	Z (mm)
SMR1	187.70	-49.89	90.35
SMR2	172.74	-31.51	75.55
SMR3	160.51	-40.57	63.34
SMR4	159.06	-57.01	61.81
SMR5	166.82	-64.57	69.49

Jason_Thesis_110119

Point Group Jason_Thesis::M2-ADJ5			
Point Name	X (mm)	Y (mm)	Z (mm)
SMR6	174.65	-67.65	77.28
SMR7	186.89	-58.13	89.50

Point Group Jason_Thesis::M2-ADJ6			
Point Name	X (mm)	Y (mm)	Z (mm)
SMR1	185.88	-50.62	88.39
SMR2	176.67	-35.20	79.27
SMR3	163.86	-40.35	66.41
SMR4	158.74	-55.48	61.24
SMR5	164.16	-64.35	66.61
SMR6	168.60	-51.96	71.07
SMR7	177.48	-67.48	79.92

Point Group Jason_Thesis::M2-ADJ7			
Point Name	X (mm)	Y (mm)	Z (mm)
SMR1	187.69	-48.79	90.40
SMR2	177.86	-34.68	80.67
SMR3	161.68	-40.02	64.42
SMR4	158.52	-55.58	61.00
SMR5	167.51	-67.64	69.45
SMR6	171.03	-53.73	73.56
SMR7	181.75	-63.27	84.24

Point Group Jason_Thesis::M2-ADJ8			
Point Name	X (mm)	Y (mm)	Z (mm)
SMR1	186.46	-52.97	88.68
SMR2	176.16	-34.39	78.29
SMR3	158.08	-43.58	60.18
SMR4	161.39	-65.87	63.58
SMR5	172.20	-68.43	74.43
SMR6	183.85	-65.86	86.08
SMR7	187.21	-53.56	89.39

Point Group Jason_Thesis::M2-ADJ9			
Point Name	X (mm)	Y (mm)	Z (mm)
SMR1	187.26	-51.97	89.65
SMR2	176.16	-36.02	78.51
SMR3	161.77	-46.55	64.12
SMR4	165.05	-63.03	67.42
SMR5	173.62	-67.51	75.98
SMR6	174.02	-52.65	76.38
SMR7	186.44	-52.77	88.81

Jason_Thesis_110119

Point Group Jason_Thesis::M1-ADJ1			
Point Name	X (mm)	Y (mm)	Z (mm)
SMR1	164.64	-41.01	52.79
SMR2	165.96	-47.53	54.12
SMR3	171.12	-49.16	59.25
SMR4	165.22	-58.30	53.23

Point Group Jason_Thesis::M1-MOUNT			
Point Name	X (mm)	Y (mm)	Z (mm)
SMR1	209.51	-16.00	37.51
SMR2	209.55	-28.45	37.49
SMR3	209.58	-43.00	37.49
SMR4	209.60	-59.52	37.49
SMR5	209.62	-72.95	37.49